The University of Nottingham

Nottingham

The University of Nottingham

School of Mechanical, Materials and Manufacturing

Engineering

Next Generation Corrosion

Protection for the Automotive

Industry

by Niamh C. Hosking, BEng

Thesis submitted to The University of Nottingham

for the degree of Doctor of Philosophy

21st November 2007

CONTENTS

Contents

Contents

Contents

Next Generation Corrosion Protection for the Automotive Industry

ABSTRACT

Vehicle bodies are generally constructed from galvanized steel, which, together with phosphate and e-coat paint treatments, ensures corrosion resistance. The use of these materials alone cannot provide adequate corrosion protection to certain features that are inherent to vehicle body construction but are also vulnerable to corrosion, such as cut edges of panels and creviced joints. The use of further corrosion protection measures, (e.g. sealers, lacquers and waxes), is undesirable because they require additional manufacturing processes, increase weight and reduce recyclability of the vehicle. The potential benefits of using zinc-magnesium alloy coated steel (ZMG) as a substitute for conventional galvanized steel were investigated in this work. Cyclic corrosion testing in sodium chloride and acid rain-based environments was conducted on panels of ZMG and conventional galvanized steel and the resistance of each material to red rust initiation and propagation was assessed. ZMG offered approximately a 3-fold improvement in red rust resistance compared to galvanized steel in the sodium chloride test but ZMG's corrosion benefit was attenuated in the acid rain environment. Cyclic corrosion testing was also conducted on painted test panels incorporating geometric features; enhanced edge and crevice corrosion resistance was also observed for panels constructed from ZMG. Corrosion products formed in each environment were characterized using a suite of analysis techniques and mechanisms to explain the enhanced corrosion resistance of ZMG were proposed based on these products and on the literature. An inhibiting corrosion protection mechanism was suggested for ZMG whereby cathodic activity was retarded via the precipitation of insulating, sparingly soluble magnesium hydroxide. Further inhibition of cathodic activity has been attributed to the specific oxide layer (possibly magnesium oxyhydroxide doped with zinc) present at the ZMG surface. The observed efficacy of the corrosion protection

mechanisms suggests that ZMG may allow improvement of the vehicle body corrosion protection system for vehicle weight and recyclability targets.

KEYWORDS:

PUBLICATIONS

1. N.C. Hosking, M.A. Ström, P.H. Shipway, C.D. Rudd: *Corrosion science*, v.49 n.9 (2007) 3669-3695.

2. N.C. Hosking, M.A. Ström, P.H. Shipway, C.D. Rudd: *Proc. EuroCorr*, (2007) 09/09/07-13/09/07 Freiburg, Germany: European Federation of Corrosion.

3. N.C. Hosking, A. Tönnessen, P.H. Shipway, C.D. Rudd: *Proc. 6th materials for lean weight vehicles conference*, (best paper award – session 5) (2005) 07/12/05-08/12/05 Coventry, UK: SMMT Ltd.

ACKNOWLEDGEMENTS

I would like to take this opportunity to thank my family, friends and colleagues for their support, encouragement and advice during this work. Special thanks are due to:

- My supervisors Prof. P.H. Shipway and Prof. C.D. Rudd for their guidance and support and the Head of School, Prof. T. Hyde, for the use of school facilities.

- My colleagues at the Materials Technology Centre of Ford Motor Company Ltd.(FMC); Lee Fretwell, George Marsh, Steve Scott, Stephen Gould, Mark Swain, Udo Müller, Jörg Sassmanhausen and my colleagues from the paint and corrosion team at Volvo Car Corporation (VCC); Göran Strannhage and Roy Johansson, who assisted with specimen preparation and corrosion testing and advised on analysis techniques.

- I am particularly indebted to Mats Ström of VCC who advised on corrosion testing and corrosion mechanisms.

- Serge Seron and Jurgen Cobbaut from ArcelorMittal Ltd.

- Keith Dinsdale, Martin Roe and Nigel Neate for assistance with XRD and SEM analysis and Emily Smith for running XPS analysis and helping with interpretations.

- Mr. Jian Chen and Dr. Hanshan Dong of the University of Birmingham for running GDOES analysis.

- Alan Harrison, Albert Tönnessen and Roger Davis of FMC for their support and for use of departmental facilities.

- Glenn Austin for wise words, patient listening and plenty of laughter.

- Nathan for his incredible encouragement and forbearance at becoming a PhD widower.

Chapter 1

INTRODUCTION

1.1. OVERVIEW

Sheet steel continues to be the prime construction material for mass produced vehicle bodies. Steel offers many advantages as an engineering construction material but is susceptible to corrosion, which is both unsightly and leads to thinning and perforation of the steel panel. The automotive engineer must incorporate a cost-effective corrosion protection strategy into the vehicle body design to guarantee its structural integrity over the vehicle lifetime. The use of zinc-coated (or galvanized) steel and phosphate and e-coat paint treatments are the primary defence against corrosive attack of steel-based vehicle bodies. Zinc coatings are applied by the steel producers and coils of galvanized steel are supplied to the vehicle manufacturers for assembly. Paint treatments are applied to the assembled vehicle body by the automotive manufacturer. Further corrosion protection materials such as anti-chip primers, sealers, waxes and lacquers are typically added to specific areas of the vehicle body during construction. These secondary corrosion protection measures are necessary because galvanized steel and paint alone do not provide adequate corrosion resistance at certain features of the vehicle body that are vulnerable to corrosion, such as creviced areas and panel cut edges. Secondary corrosion protection materials constitute additional weight, processing time, material complexity and cost to the overall vehicle. The premise of this work is that use of a more corrosion-resistant construction material for the vehicle body will enable reduction in use of secondary corrosion protection methodologies.

1.2. AUTOMOTIVE VEHICLE BODY CORROSION

1.2.1. Definition of Automotive Corrosion

Automotive body corrosion is categorized as either cosmetic or perforation corrosion. Cosmetic corrosion is corrosive attack which initiates at the exterior

surface [1] and it degrades the vehicle appearance, typically manifesting as unsightly red rust, white "rust" or paint blistering. Perforation corrosion occurs when the corrosive attack initiates at an interior surface of a body panel and penetrates the sheet, resulting in structural damage to the vehicle body. Most vehicle manufacturers offer a corrosion resistance warranty to their customers; currently in the UK, the warranty offered is typically a 3-year guarantee against cosmetic corrosion and up to a 12-year guarantee against perforation corrosion of the vehicle body. Automotive engineers must ensure that their corrosion protection system supports the warranty offered to the customer. Failure to do so is costly, both to short-term profitability in terms of repair bills and longer term profitability due to damage to the vehicle manufacturer's reputation.

1.2.2. History of Automotive Corrosion

The automotive industry has not always offered a guarantee against corrosive attack. Automobile corrosion became an issue of concern in the 1970s, when a large number of corrosion-related claims were made, particularly in Canada and the north-eastern parts of the United States [2-3]. Investigations pointed to the increased use of road salt for winter de-icing as a cause of the escalated corrosion defects. The "Anti-Corrosion Code and Owners Care Guide for Motor Vehicles" [4], announced in 1978 by the Canadian government, specified target guidelines for vehicle corrosion resistance performance (see Table 1.1). Compliance with the code was not compulsory for vehicle manufacturers, although consumers were urged to purchase only those vehicles that met or exceeded the minimum provisions stated.

Table 1.1: "Anti-corrosion code" guidelines for automotive corrosion resistance [4]

Corrosion type	Resistance stipulated	
	Vehicles sold 1978-1980	Vehicles sold from 1981
Cosmetic	12 months or 40,000 km	18 months or 60,000 km
Perforation	36 months or 120,000 km	60 months or 200,000 km

By November 1978 it was reported that most automotive manufacturers selling vehicles in Canada had responded positively to the code [5], agreeing to accept the

provisions of the code and, furthermore, several manufacturers introduced anti-corrosion warranties. Similar automotive corrosion problems were experienced in northern Europe and the Finnish government introduced legislation in the early 1980s to ensure a minimum corrosion resistance performance by all passenger vehicles [6]. Vehicle corrosion protection became the subject of intense investigation by automotive manufacturers and their suppliers as a result of these developments. The evolution of the vehicle body corrosion protection system is discussed briefly in the next section.

1.3. VEHICLE BODY CORROSION PROTECTION

The evolution of the automotive corrosion protection strategy has occurred over several years. Increased use of galvanized steel has been one of the most significant, and most expensive, changes in vehicle body design from the corrosion protection perspective since the 1980s. Kikuchi et al. [7] reported that the percentage of vehicle body panels constructed from galvanized steel increased from approximately 10% in 1985 to 40% in 1988 and to more than 70% in the 1990s. Guzman et al. [8] estimated in 2003 that 95% of the vehicle body was constructed from galvanized steel. Surveys of aged vehicles have confirmed that vehicle bodies with greater galvanized steel content exhibited superior corrosion resistance [3,9,10]. Dietz [12] reported in 1991 that galvanized steel costs between 20% and 40% more than non-zinc coated steel, with greater costs associated with galvanized steel produced by electrodeposition compared to hot-dipped galvanized steel (these processes are described in Chapter 4).

Use of galvanized steel alone is not sufficient to guarantee corrosion resistance over the warranty period because of localized corrosion effects experienced at specific areas of the vehicle body. These vulnerable areas include cut edges of panels and creviced features such as lap joints and hem flanges. Cut edges of galvanized steel panels are vulnerable to increased corrosive attack compared to open surfaces because the panels are cut to size after galvanizing, resulting in discontinuities of the zinc coating, as illustrated by Fig. 1.1. Furthermore, e-coat paint may not adhere well to sharp corners due to surface tension effects and shrinkage of the paint during curing.
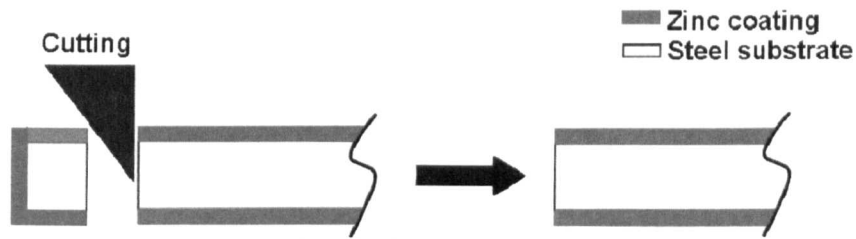
Fig. 1.1: Cut edge of galvanized steel panel. *Not to scale.*

Hem flanges are used to join outer and inner body panels (such as the door inner and outer panel) by wrapping the outer panel edge around the inner panel, as illustrated in Fig. 1.2. Historically, hem flanges and lapped joints constructed from non-zinc coated steel and without adequate drainage provision suffered from perforation corrosion due to corrosive attack initiating within the crevice area [10,11]. In addition, paint treatments may not be able to penetrate into creviced or recessed areas. Therefore, these vulnerable areas are protected against corrosion by the application of organic sealers, waxes, lacquer as well as the use of galvanized steel and paint treatments.
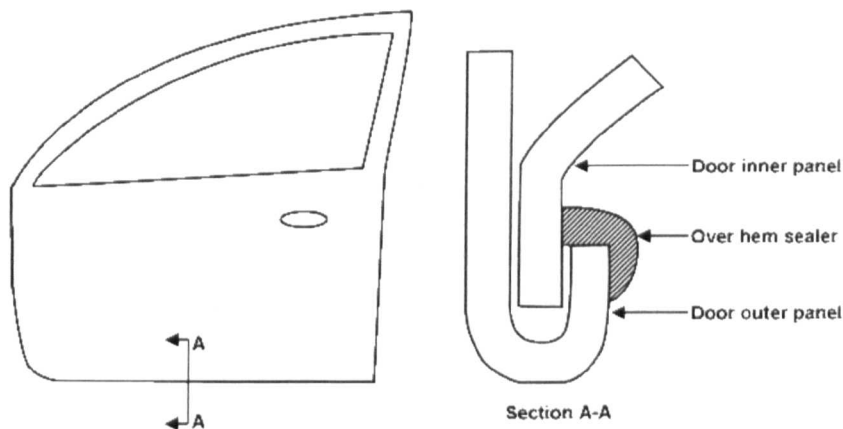
Fig. 1.2: Sealer application to the door assembly hem flange. *Not to scale.*

1.4. THEME OF THIS WORK

To date, the components of the corrosion protection system have generally been added one to another, resulting in several layers of corrosion protection materials at some areas of the vehicle body. Tailpipe emissions legislation and customer expectations of fuel economy performance continue to spur efforts to reduce overall vehicle weight and directives on recyclability require vehicle manufacturers to plan

the materials used in vehicle construction for recovery at the end of the vehicle life. The corrosion protection system must contribute to weight reduction and recyclable content targets and the continued use of secondary corrosion protection materials, especially sealer, is at loggerheads with these targets. It is desirable to construct the vehicle body from a material that itself provides adequate corrosion resistance to cut edge and crevice corrosion without the need for secondary corrosion protection materials. Zinc-magnesium alloy coated steel (ZMG) has been highlighted as a highly-corrosion resistant material [13-17] compared to conventional galvanized steel and several steel producers are developing processes to industrialize ZMG production for the automotive industry. The potential benefits of introducing ZMG as a construction material for vehicle bodies are investigated in this work.

1.5. OBJECTIVES

The overall objective of this work was to assess the potential of ZMG to become the next generation galvanized steel for the automotive industry. The following tasks were undertaken to meet the overall objective:

- Review the literature to select suitable corrosion test methods and corrosion resistance assessment techniques.

- Assess the corrosion benefit of ZMG versus conventional galvanized steel in both the open corrosion mode (general corrosion) and under localized corrosion influences, such as cut edges and crevices.

- Review the literature to clarify corrosion mechanisms that are relevant to vehicle body corrosion.

- Develop mechanisms for the corrosion protection offered by ZMG in the open corrosion mode and under localized corrosion conditions.

- Analyse the corrosion benefits and protection mechanisms generated to give a recommendation on whether ZMG should be considered as construction material for vehicle bodies in the future.

1.6. THESIS STRUCTURE

The underpinning basics of corrosion are outlined in Chapter 2. Corrosion test and analysis techniques are reviewed in Chapter 3 and the approach adopted in this work is described. Chapter 4 is a detailed review of zinc corrosion mechanisms that are relevant to automotive body panels. The experimental methods used in this work are presented in Chapter 5. The corrosion resistance of ZMG and conventional galvanized steel in a sodium chloride environment is investigated in Chapter 6 and a corrosion protection mechanism is proposed for ZMG. Chapter 7 investigates the corrosion resistance of ZMG and conventional galvanized steel in an acid rain environment and a mechanism is proposed to describe the corrosion behaviours observed. The corrosion behaviour of painted panels of ZMG in a sodium chloride environment is compared to similar panels of galvanized steel in Chapter 8. Corrosion mechanisms for ZMG at a paint defect (due to a scribe line), at cut edges and within crevices are proposed. The overall corrosion resistance and potential of ZMG to become the next generation galvanized steel for the automotive industry are discussed in Chapter 9 and recommendations for future work and the major conclusions of this work are presented.

Chapter 2

FUNDAMENTALS OF CORROSION

2.1. INTRODUCTION

The principles of metallic corrosion are discussed in this chapter. Corrosion occurs under many different conditions and is manifest in various ways. A general definition of corrosion is offered in Section 2.2. Different forms of corrosion and their respective corrosion mechanisms are introduced in Section 2.3. Aqueous solutions are the environments most frequently associated with corrosion problems. Automotive vehicles in the atmosphere encounter aqueous corrosion environments in times of high atmospheric relative humidity and rain fall. The underlying electrochemical, thermodynamic and kinetic principles of aqueous corrosion are discussed in Sections 2.4–2.6. Corrosion control methods are described in Section 2.7.

2.2. DEFINITION OF CORROSION

Many definitions of corrosion can be found in the literature. In this work, metallic corrosion, rather than general material corrosion, is considered and the definition offered by West [18] is presented:

Metallic corrosion is the surface wastage that occurs when metals

are exposed to a reactive environment.

The chemical compounds in the surface wastage are close to the metallic ores found in the earth's crust. Fontana [19] noted that corrosion could be considered as extractive metallurgy in reverse, as illustrated by Fig. 2.1. This observation highlights that many useful construction metals, such as iron, do not exist in their metallic state in nature; significant energy input in the blast furnace is required to separate iron from its ore. Upon exposure to the environment, metallic iron reverts to its natural, lowest energy state: the ore.
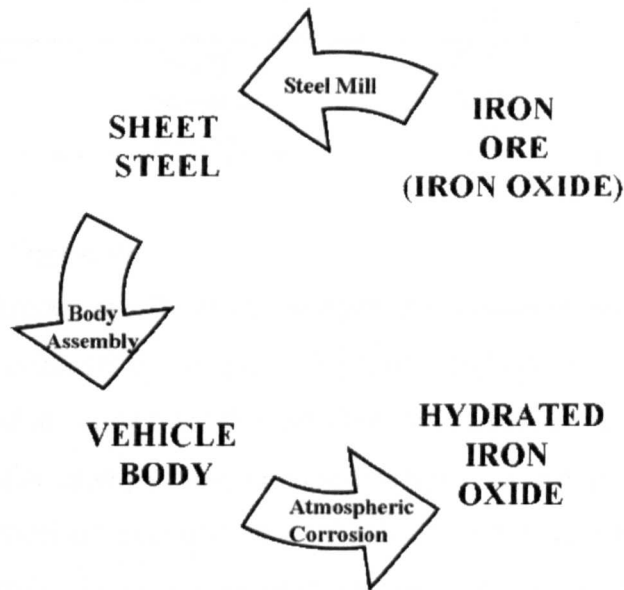
Fig. 2.1: Corrosion as extractive metallurgy in reverse (adapted from [19])

2.3. FORMS OF CORROSION

Corrosion may be classified according to how it manifests itself and the following eight forms of corrosion are cited in the literature [18-22]: uniform or general attack; galvanic or two-metal corrosion; crevice corrosion; pitting; intergranular corrosion; selective leaching or parting; erosion corrosion; and stress corrosion. Those forms of corrosion that are of greatest concern to the automotive body engineer are discussed in turn in the following sections.

2.3.1. Uniform Corrosion

Uniform attack is characterized by progressive and uniform thinning of the metallic component. The uniformity of the degradation allows the design engineer to make a corrosion allowance and adjust the component thickness accordingly. Uniform corrosion can be assessed by measurement of the mass loss of a metal in a particular corrosion environment. Mass or thickness loss rates of particular metals in various environments have been measured and compiled in handbooks, such as Slunder and Boyd's study of zinc corrosion [23]. Table 2.1 shows the variations in corrosion rate of steel and zinc in different environments.

Table 2.1: Corrosion rates of steel and zinc after one year exposure in different environments [23]

Location	Environment	Corrosion rate (mm/year)	
		steel	Zinc
Pennsylvania	Rural	0.279	0.001
New York	Industrial	0.869	0.005
California	Marine	0.371	0.008

2.3.2. Galvanic Corrosion

A potential difference usually exists between two dissimilar metals when they are immersed in a conductive solution. Galvanic corrosion occurs when two such metals are placed in contact and the potential difference produces an electron flow between them. For example, galvanic corrosion results in accelerated corrosion of zinc coupled to steel compared to zinc's corrosion rate when not part of a galvanic couple. Conversely, the corrosion attack of steel coupled to zinc is very low, as shown by Table 2.2 [19].

Table 2.2: Mass change of coupled & uncoupled steel and zinc immersed in sodium chloride solutions [19]

Electrolyte	Mass change (g) uncoupled		Mass change (g) coupled	
	steel	zinc	steel	Zinc
0.005 M NaCl	-0.10	-0.06	+0.02	-0.13
0.050 M NaCl	-0.15	-0.15	+0.01	-0.44

Coupling the metals in conductive solution generates an electrochemical cell, which is discussed in more detail in Section 2.4. Zinc acts as the anode and steel acts as the cathode. The tendency of a coupled metal to act as either a cathode or anode can be estimated from the galvanic series shown in Table 2.3. The data presented in Table 2.3 are based on potential measurements made in seawater and the positions of metals in the series may change depending on the environment encountered.

Galvanic corrosion is usually most severe at the junction between the two dissimilar metals, with attack decreasing as the distance from the junction increases. Severity of galvanic corrosion is also affected by the relative sizes of the cathodic and anodic areas. A large cathode coupled to a small anode generates an unfavourable ratio and results in greater corrosive attack of the anode. This is explained in terms of

current density, which is greater for a smaller electrode than for a large electrode at a given current flow. The increased current density at the anodic area generates a greater corrosion rate.

Table 2.3: Galvanic series of some commercial metals in seawater [19]

↑	Platinum
	Gold
	Graphite
Noble or Cathodic	Titanium
	Silver
	18-8 Stainless Steels (passive)
	Nickel (passive)
	Bronze (Cu-Sn)
	Copper
	Brass (Cu-Zn)
	Nickel (active)
	Tin
	Lead
	18-8 Stainless Steels (active)
	Mild Steel and Iron
Active or Anodic	Cadmium
	Commercially Pure Aluminium
↓	Zinc
	Magnesium

2.3.3. Crevice Corrosion

Severe localized corrosion can occur within crevices and other secluded areas on metal surfaces exposed to a corrosive environment. This type of attack is usually associated with small volumes of stagnant and deaerated solution encountered in situations such as lap joints, crevices under bolt heads and under surface deposits. A general definition of crevice corrosion is the attack which occurs because part of a metal surface is in a restricted environment compared to the rest of the metal which is exposed to a large volume of electrolyte [20]. Fig. 2.2 illustrates crevice

corrosion of a metal (*Me*) within a lap joint in a sodium chloride-containing (NaCl) electrolyte.
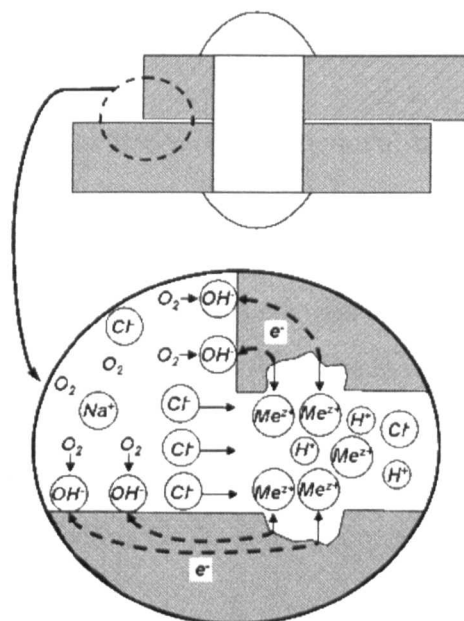
Fig. 2.2: Accelerated corrosion within a crevice at a lap joint [19]

Crevice corrosion occurs when a more aggressive corrodent develops due to deoxygenation and increased salt and acid concentrations of the solution within the crevice [21]. Deoxygenation results from the relatively slow convection and diffusion between the solution entrapped within a crevice and the bulk environment. The difference in oxygen concentrations within and without the crevice generates a galvanic cell, whereby the deoxygenated zone within the crevice acts as the anode and the surrounding surface acts as the cathode. Metal cations (Me^{z+}) are concentrated in the stagnant solution within a crevice, reacting with water to generate acidity $[H^+]$. Charge neutrality is maintained by the attraction of mobile anionic species such as Cl^-. These processes increase the severity of the corrodent and result in greater rates of metallic corrosion within crevices.

2.4. THE ELECTROCHEMICAL CELL

Aqueous metallic corrosion is almost always electrochemical in nature [22]. The metal surface is called the electrode and is the site for the corrosion reactions. The electrolyte is an ionically conducting liquid. The electrode and electrolyte

constitute an electrochemical cell and corrosion occurs when two or more electrochemical reactions take place on the electrode. Electrochemical cell processes are described in the following sections.

2.4.1. Electrode Processes

In an electrochemical cell, oxidation is the removal of electrons from atoms or groups of atoms whereas reduction is the balancing reaction whereby electrons are absorbed by an atom or group of atoms. Reduction-oxidation, or Redox, reactions can be represented by an electrochemical cell whereby reduction reactions occur at the anode and oxidation reactions occur at the cathode. Dissolution of a solid metal, *Me(s)*, as described by reaction (2.1) is an anodic reaction and a corresponding cathodic reaction is given by (2.2). The integer z is the valence of the metal species and *(aq)* denotes aqueous species.

$$Me(s) \rightarrow Me^{z+}(aq) + ze^- \tag{2.1}$$

$$Me^{z+}(aq) + ze^- \rightarrow Me(s) \tag{2.2}$$

The production of electrons during oxidation and consumption of electrons during reduction are coupled events; therefore the overall corrosion reaction is given by the combination of (2.1) and (2.2). Equivalent processes of oxidation and reduction occur together during the course of normal electrochemical reactions. The individual reactions are termed half-cell reactions and the overall process can be visualized as an electrochemical cell, as shown for zinc and copper in Fig. 2.3.
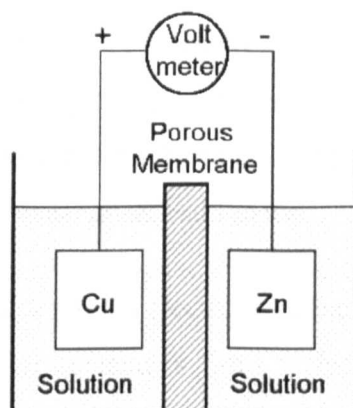
Fig. 2.3: Electrochemical cell with copper and zinc electrodes in solutions of their own ions [19].

The zinc electrode is in a solution of zinc ions and the copper electrode is immersed in a solution of copper ions; the copper and zinc ions are separated from each other by the porous membrane. The sign convention across the voltmeter shows that zinc acts as the anode, producing electrons, and copper acts as the cathode, consuming electrons.

2.4.2. Electrode to Electrolyte Interface

Redox reactions (2.1) and (2.2) involve aqueous metal species and species in the electrolyte reacting at or near the electrode. These reactions result in charging of the electrode surface relative to the solution, generating an electric field that extends into the solution. Water is polar and can be visualized as dipolar molecules that have a positive side (hydrogen atoms) and a negative side (oxygen atoms), as shown in Fig. 2.4a.
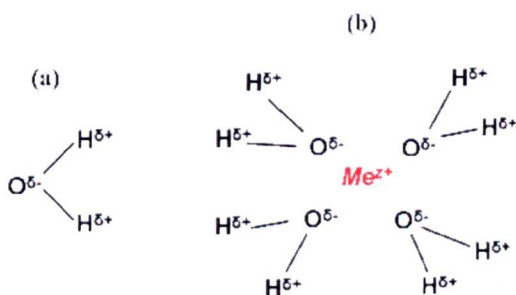
Fig. 2.4: (a) water as a dipolar molecule and (b) cage of molecules around metallic anion

The dipolar water molecules close to the electrode surface align themselves in the direction of the electric field. Oxidized metal species (Me^{z+}) go into solution according to reaction 2.1 and are surrounded by a cage of aligned water molecules, as shown in Fig. 2.4b. The attraction between the cation and the negative poles of the water molecules is strong enough for the water molecules to travel with the metal ion as it moves through the solvent. The tightly bound water molecules are referred to as the primary water sheath of the ion.

A net negative charge resides at the electrode surface as cations leave the surface of the electrode. Polar water molecules form a first row at the metal to aqueous solution interface, as shown schematically in Fig. 2.5.
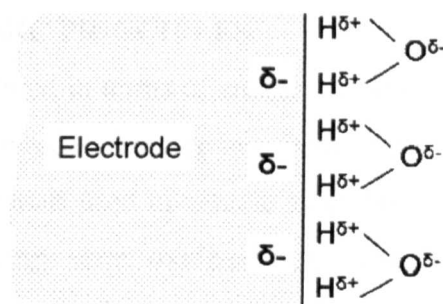
Fig. 2.5: Alignment of water molecules at an electrode surface

The electrode to solution interface is known as the double layer, as it is made up of two layers of charge; the negative charge of the electrode surface and the positive charge of the aligned water molecules. The compact layer of charge adjacent to the electrode surface is known as the Helmholtz layer. The local potential within the Helmholtz layer varies linearly with distance from the electrode surface. A more diffuse layer of charge, known as the Gouy-Chapman layer, lies outside the Helmholtz layer. It can be shown that the local potential within the Gouy-Chapman layer increases exponentially until it reaches the potential of the bulk solution.

The overall interface comprises a compact layer of charge residing at the interface between the electrode surface and the electrolyte and a diffuse zone of ions in the solutions phase, as shown in Fig. 2.6.
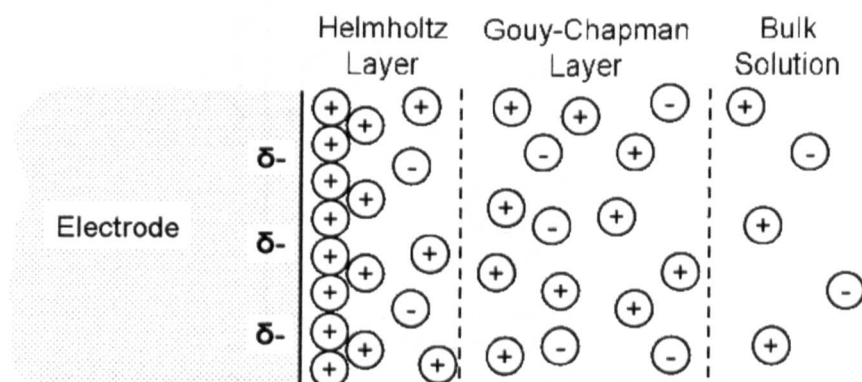
Fig. 2.6: Ionic double layer showing Helmholtz and Gouy-Chapman layers [20]

The significance of the electronic double layer is that is provides a barrier to the transfer of electrons. In effect, the double layer is an energy barrier that must be overcome for corrosion to occur.

2.5. THERMODYNAMIC PRINCIPLES

Corrosion can be considered in terms of energy changes; as noted in Section 2.2, a large energy input is required to separate iron from its ore. Although a useful life is realised from the steel panels used in vehicle assembly, eventually the iron reverts to its natural, lowest energy state; oxidized iron. The driving force for chemical reactions is expressed in thermodynamic treatments as the free energy.

2.5.1. Free Energy Concept

Consider the following reaction (2.3):

$$A + B \rightarrow C + D \tag{2.3}$$

Reactants A and B interact to form the new species, products C and D. The reactants must physically join together, forming an intermediate species AB, to produce C and D. AB is called the transition state and may exist for only the briefest of moments. It is the reorganisation of the transition state that leads directly to the products, C and D. A free energy profile, as shown in Fig. 2.7, describes the free energy changes occurring during reaction (2.3) via the transition state.
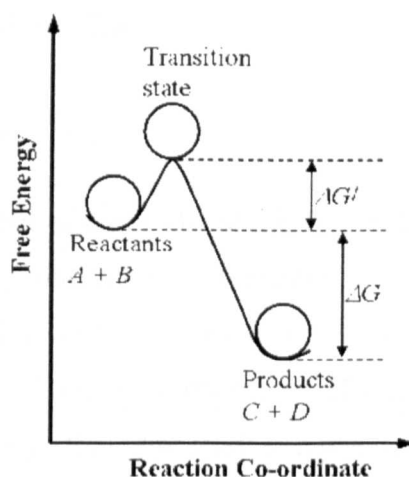
Fig. 2.7: Free energy profile for reaction (2.3) via the transition state [20]

The y-axis in the diagram is the free energy, G, and changes in free energy are denoted ΔG. The x-axis is called the reaction co-ordinate and can be considered as the extent to which the reaction has progressed. The transition state AB is at a higher free energy than the sum of the free energies of the reactants A and B, and

the difference is termed $\Delta G\ddagger$. The sum of the free energies of the products C and D must be less than A and B for a spontaneous reaction to occur, and this difference is termed ΔG; in other words, for a spontaneous reaction to occur, $\Delta G < 0$.

2.5.2. The Nernst Equation

The free energy of a system at constant temperature can be expressed as:

$$\Delta G = \Delta H - T\Delta S \tag{2.4}$$

where ΔG is the change in free energy (Gibbs free energy), ΔH is the change in enthalpy, T is the absolute temperature and ΔS is the change in entropy. It can be shown that

$$\Delta G = \Delta G^0 + RT \ln K_{eq} \tag{2.5}$$

where ΔG^0 is the standard free energy in the standard state, R is the gas constant and K_{eq} is the equilibrium constant.

Free energy differences are measurable as electrical potentials and flow of current, as described by Faraday's Law (2.6)

$$\Delta G = (-zF)E \tag{2.6}$$

The symbol z is the number of electrons transferred in the corrosion reaction. F is the charge transported by one mole of electrons and is of known value. The potential, E, is measured in volts. A negative sign is necessary to indicate the conventional assignment of negative charge to electrons. When a reaction is spontaneous, $\Delta G < 0$ and equation (2.6) leads to a positive measured potential.

Applying equation (2.6) to standard conditions gives:

$$\Delta G^0 = -zFE^0 \tag{2.7}$$

Substituting (2.6) and (2.7) into (2.5) gives the following expression for the non-equilibrium potential generated by the reactants:

$$E = E^0 - \frac{RT}{zF} \ln K_{eq} \qquad (2.8)$$

Equation (2.8) is known as the Nernst equation. Using the standard temperature, T = 298 K, R = 8.3143 J/molK and the value of F = 96485 C/mol, and converting to base 10 logarithms gives equation (2.9):

$$E = E^0 - \frac{0.059}{z} \log_{10} K_{eq} \qquad (2.9)$$

2.5.3. Calculating the Equilibrium Constant

The equilibrium constant, K_{eq}, may be expressed in terms of the concentrations of the reacting species. For example, for the following reaction:

$$jA + kB \rightarrow lC + mD \qquad (2.10)$$

the equilibrium concentration constant is given by (2.11).

$$K_{eq} = \frac{[C]^l [D]^m}{[A]^j [B]^k} \qquad (2.11)$$

2.5.4. Standard Electrode Potentials

At equilibrium conditions, E in equation (2.9) equals zero. Standard electrode potentials E^0 refer to oxidation and reduction reactions at standard conditions of 298 K in which all ions taking part in the electrode process are at unit activity, all gases at 1 atmosphere pressure and solids are in their most stable form. The half-reaction represented by the hydrogen ion reaction is used as a reference standard. Reaction (2.12) is assigned a standard electrode potential of zero. All other half-cell potentials can then be calculated with respect to this zero reference.

$$2H^+ + 2e^- \rightarrow H_2 \qquad (2.12)$$

The standard hydrogen electrode (SHE) potential is measured by using a platinum electrode immersed in a solution saturated with hydrogen gas at 1 atm. Table 2.4.

lists values of electrode potentials of various half-cell reactions with respect to the SHE.

Table 2.4: Standard potential of some half-cell reactions [24]

Electrode Reaction	E^0 (V)
$Au^{3+} + 3e^- \rightarrow Au$	1.50
$\frac{1}{2}Cl_2 + e^- \rightarrow Cl^-$	1.36
$Cu^{2+} + 2e^- \rightarrow Cu$	0.34
$2H^+ + 2e^- \rightarrow H2$	0.00
$Fe^{3+} + 3e^- \rightarrow Fe$	-0.04
$Ni^{2+} + 2e^- \rightarrow Ni$	-0.25
$Fe^{2+} + 2e^- \rightarrow Fe$	-0.44
$Zn^{2+} + 2e^- \rightarrow Zn$	-0.763
$Al^{3+} + 3e^- \rightarrow Al$	-1.66
$Mg^{2+} + 2e^- \rightarrow Mg$	-2.37
$Na^+ + e^- \rightarrow Na$	-2.71

Table 2.4 is also known as the electromotive force (EMF) series. The standard electrode potential values indicate the tendency of a metal to oxidize under standard state conditions. Those reactions with negative E^0 values are more likely to oxidize than those with positive values. This tendency is a thermodynamic quantity and does not consider kinetic factors that may limit a reaction because of physical factors such as protection by corrosion product layers. For example, the position of aluminium in the series indicates a strong tendency to oxidize; however, the passive surface of aluminium prevents this reaction from taking place readily.

2.5.5. The Sign Convention

Electrode reactions may proceed in two opposite directions; for example, the Fe^{2+}/Fe system may undergo oxidation ($Fe \rightarrow Fe^{2+} + 2e^-$) or reduction ($Fe^{2+} + 2e^- \rightarrow Fe$). The potential of the iron electrode is expressed with respect to the SHE = 0. The coupling of these two systems (Fe^{2+}/Fe and H^+/H_2), however, brings about the spontaneous oxidation of iron, as indicated by the lower position of the Fe^{2+}/Fe system in table 2.4. The opposite is true in the case of the Cu^{2+}/Cu system, which spontaneously reduces when coupled to the H^+/H_2 system. This difference in the spontaneous reaction direction with respect to

hydrogen can be represented by a sign. At the International Union of Pure and Applied Chemistry (IUPAC) meeting held in Stockholm in 1953, it was decided to choose the reduction reaction as the convention direction:

$$ox + ze^- \rightarrow red \qquad\qquad (2.13)$$
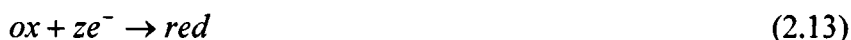
where *ox* represents the oxidized species, z is the number of electrons (e^-) and *red* is the reduced species. A negative sign in this reduction convention indicates a trend towards corrosion in the presence of H^+ ions. The ferrous cations have a greater tendency to exist in aqueous solution than H^+ cations. A positive sign indicates that the H^+ ion is more stable than Cu^{2+}, for example, in aqueous solution.

2.5.6. Pourbaix Diagrams

The Nernst equation was used by Pourbaix to construct Potential-pH or Pourbaix diagrams. Pourbaix diagrams are graphical representations of the domain of stability of metal ions, oxides and other species in solution. The lines that show limits between two domains express the value of the equilibrium potential between two species as a function of pH. These diagrams also give the equilibrium potential of acid-base reactions independent of the potentials. These equilibria are represented by vertical lines at specific pH values.

The equilibrium potentials and the pH lines that set the limits between the various stability domains are determined from the chemical equilibria between the chemical species considered. Pourbaix diagrams can be constructed for each of the following three types of reactions:

- Electrochemical reactions of pure charge transfer
- Electrochemical reactions involving both electrons and H^+
- Pure acid-base reactions

Reactions of Pure Charge Transfer

Pure charge transfer reactions involve only electrons and the reduced and oxidized species. They do not have protons (H^+) as reacting particles; consequently they are not influenced by pH. An example of this type of reaction is:

$$Fe^{2+} + 2e^- \rightarrow Fe \qquad (2.14)$$

The equilibrium potential is given by the Nernst equation (2.8) and in the case of the iron reaction at standard conditions, it can be written as:

$$E = E^0 - \frac{RT}{zF} \ln \frac{[Fe]}{[Fe^{2+}]} \qquad (2.15)$$

where E is the equilibrium potential for Fe^{2+} / Fe; E^0 is the standard potential for Fe^{2+} / Fe, $[Fe]$ is the concentration of Fe in the solution and $[Fe^{2+}]$ is the concentration of Fe^{2+} in the solution. The concentration of a solid metal is taken as unity, therefore (2.15) can be rewritten:

$$E = E^0 - \frac{RT}{zF} \ln \frac{1}{[Fe^{2+}]} = E^0 + \frac{RT}{zF} \ln[Fe^{2+}] \qquad (2.16)$$

The value of E^0 for reaction (2.14) is given in Table 2.4 as -0.44 V and the value of z for this reaction is 2. Substituting values for E^0, R, T, z and F and converting to base 10 logarithms in equation (2.16) gives:

$$E = -0.44 + 0.03 \log_{10}[Fe^{2+}] \qquad (2.17)$$

Equation (2.17) shows that the equilibrium potential depends only on the concentration of Fe^{2+}, not on the pH. It is customary to select four concentrations to evaluate E; 10^0, 10^{-2}, 10^{-4} and 10^{-6} g ion/L. This provides four horizontal lines, as shown in Fig. 2.8.
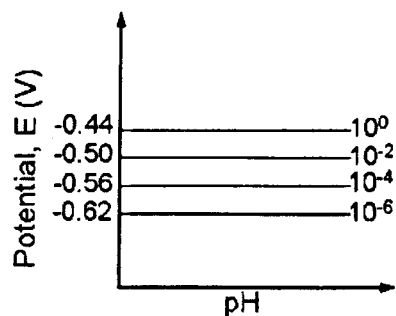
Fig. 2.8: Partial *E*-pH diagram for reaction (2.14)

The horizontal lines represent the potential at which Fe^{2+} ions and Fe metal can coexist for a given concentration of Fe^{2+} in the solution. The region above the line is the stability domain of Fe^{2+}, and below the line is the stability domain of Fe metal.

Reactions Involving Both Electrons and H^+

The reaction involving nickel and water to form nickel oxide is given by the electrochemical reaction:

$$Ni + H_2O \rightarrow NiO + 2H^+ + 2e^-$$

(2.18)
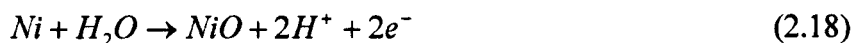
The standard potential E^0 can be calculated from the standard chemical potentials and equates to a value of +0.11V [22]. The equilibrium constant, K_{eq}, is given by (2.19), where the oxidized species are in the numerator and the reduced species in the denominator, in accordance with IUPAC convention:

$$K_{eq} = \frac{[Ni][H_2O]}{[NiO][H^+]^2}$$

(2.19)

The concentration of the solid species Ni and NiO are considered to be unity, as is the concentration of water in aqueous solution. The Nernst equation for reaction (2.18) can therefore be written as:

$$E = +0.11 + 0.03\log[H^+]^2$$

(2.20)

Because $pH = -\log[H^+]$, equation (2.20) may be rewritten as:

$$E = 0.11 - 0.06pH \qquad (2.21)$$

In this case, the equilibrium potential of *Ni* and *NiO* in aqueous solution is a decreasing function of pH, as represented by the partial E-pH diagram shown in Fig. 2.9.
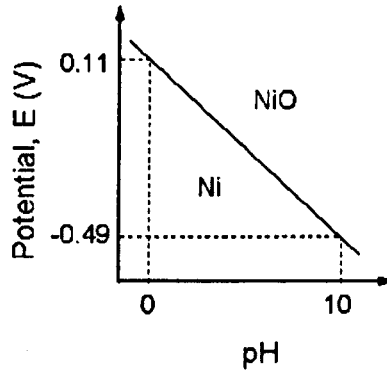
Fig. 2.9: Partial E-pH Diagram for reaction (2.18)

Pure Acid-Base Reactions

Pure acid-base reactions take place without the involvement of electrons; therefore the regions of stability for species undergoing such reactions do not depend on the potential. The limit is represented by a vertical line at a particular pH. For example, cobalt may be subject to an acid-base reaction:

$$Co^{2+} + H_2O \leftrightarrow CoO + 2H^+ \qquad (2.22)$$

The pH value of the line that separates Co^{2+} from CoO can be computed from the chemical equilibrium, with the general equation:

$$\Delta G^0 = -RT \ln K_{eq} \qquad (2.23)$$

derived from equation (2.5) and putting $G = -zFE$ with $E = 0$. Rearranging (2.23) gives

$$\log_{10} K_{eq} = \frac{-\Delta G^0}{2.3RT} \qquad (2.24)$$

The value of ΔG^0 can be calculated from the standard chemical potentials of the products and reactants (available in [22]); substituting standard values for R and T gives

$$\log_{10} K_{eq} = \log_{10} \frac{[CoO][H^+]^2}{[Co^{2+}][H_2O]} = -12.6 \qquad (2.25)$$

Taking the concentration of CoO and H_2O as unity and substituting $pH = -\log[H^+]$ gives:

$$-2pH - \log_{10}[Co^{2+}] = -12.6 \qquad (2.26)$$

Therefore, at concentration of $Co^{2+} = 1$, the equilibrium between CoO and Co^{2+} in acid-base reaction lies at a pH of 6.3, as shown in Fig. 2.10.
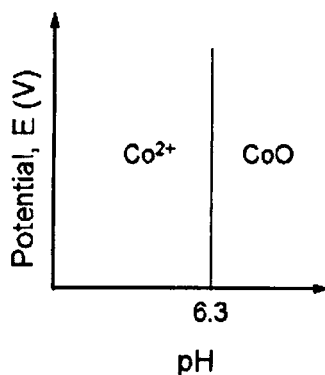
Fig. 2.10: Partial E-pH Diagram for reaction (2.22)

The three types of reactions described here form the basis for the more detailed diagrams presented in Pourbaix's atlas of chemical equilibria [25]. The Pourbaix diagrams for zinc and magnesium are of greatest interest in this research and are shown in Fig. 2.11a-b. Thermodynamic data to construct Pourbaix diagrams for corroding systems are available in many handbooks, such as [26].
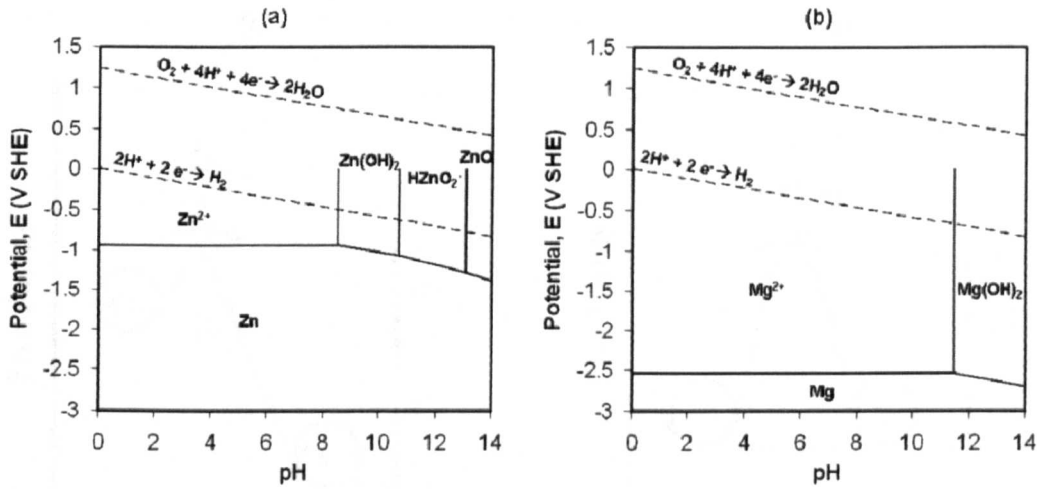
Fig. 2.11: Pourbaix diagram for the (a) zinc-water and (b) magnesium-water systems at 25°C [25]

2.6. KINETIC CONSIDERATIONS

The thermodynamic principles introduced in the previous section indicate the tendency of a given system to corrode. The rates or kinetics of corrosion are of major interest to the automotive design engineer. A corrosion system in equilibrium has zero net current flowing because the anodic current is equal in magnitude and opposite in direction to the cathodic current flow. Corrosion reactions not in equilibrium cause current to flow and the relationships between potential and current must be explored to appreciate corrosion kinetics.

2.6.1. Current Density

Consider two pieces of metal with areas of 10 mm^2 and 1 mm^2 respectively which are corroding in a cell. The smaller piece of metal will suffer mass loss 10-times more rapidly than the larger piece because the surface mass affected by corrosion is directly proportional to the rate of generation of electrons. The effects of area can be eliminated in corrosion current calculations by considering current density, i, commonly measured in A/cm^2 rather than absolute current (I, measured in A). The subscripts a and c are used to denote the anodic and cathodic currents. It is necessary to treat anodic and cathodic currents as having opposite signs when adding them.

(a)   (b)
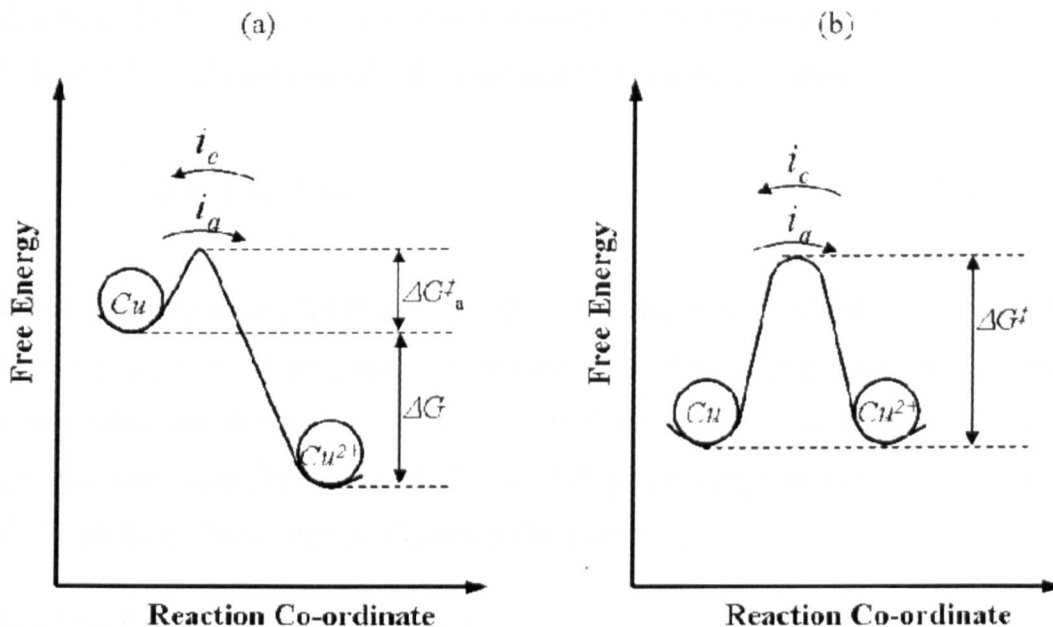
Fig. 2.12: Energy profile for copper (a) in pure water with $i_a > i_c$ and (b) in equilibrium with a solution of its divalent ions; $i_a = i_c = i_0$ [20]

Consider placing a piece of copper in a beaker of pure water. An energy profile, (Fig. 2.12a) can be drawn. Sufficient energy is available for a steady flow of copper atoms to pass over the energy barrier, $\Delta G_f^{\ddagger}$, and proceed to the Cu^{2+} ionic form. The copper begins to dissolve (corrode) and the concentration of copper ions in the water, initially zero, will increase, as described by reaction (2.27):

$$Cu(s) \rightarrow Cu^{2+}(aq) + 2e^-$$ (2.27)

There is a possibility for the copper ions in solution to pass back over the energy barrier and replate onto the metal. The rate of this process is governed by the activation free energy in the reverse direction (sum of ΔG and $\Delta G_{f a}^{\ddagger}$), a quantity initially greater than the free energy in the forward direction. However, this free energy barrier is reduced in magnitude as the energies of the copper metal and copper ions approach each other, increasing the extent of the backward reaction. At the same time, the rate of the forward reaction decreases because its activation free energy increases. Equilibrium is established when the rate of the decreasing forward reaction becomes equal to the rate of the increasing backward reaction, as

illustrated by Fig. 2.12b, where the free energy of activation is equal to $\Delta G_\ddagger$ and $\Delta G = 0$. For a divalent metal, *Me*, reaction (2.27) can be rewritten as:

$$Me \underset{i_c}{\overset{i_a}{\leftrightarrow}} Me^{2+} + 2e^- \qquad (2.28)$$

When the state of equilibrium is reached, the magnitude of the anodic current density is equal to the magnitude of the cathodic current density, (i.e. $i_a = i_c$). The measured current density, $i_{meas} = (i_a - i_c) = 0$. Current is flowing, but it is equal and opposite and cannot be measured. It is called the exchange current and is denoted by I_0 and the exchange current density is denoted by i_0.

Faraday's Law of Electrolysis states that:

$$Q = zFM \qquad (2.29)$$

where Q is the charge created by the ionisation of M mol of material. Differentiating (2.29) with respect to time gives:

$$\frac{dQ}{dt} = zF\frac{dM}{dt} \qquad (2.30)$$

The rate of flow of charge is the current, I, and if the passage of charge across unit area of cross-section is considered, the current density, i, can be used. The flux of substance, J, can be substituted for dM/dt, and equation (2.30) becomes:

$$i = zFJ \qquad (2.31)$$

The flux of substance is another name for corrosion rate per unit area: hence equation (2.31) shows that the corrosion rate is directly proportional to the current density.

2.6.2. Polarization

When a metal is not in equilibrium with a solution of its ions, the electrode potential differs from the equilibrium potential by an amount known as the polarization, (η). Referring to Fig. 2.12b, it is clear that the rate of the forward (anodic) reaction at

equilibrium is i_a and it equals the rate of the reverse (cathodic) reaction i_c. It is usually possible to treat the concentration of reactants (e.g. the solid metal for the anodic reaction) as constant. The rate of the forward reaction for which the activation free energy is $\Delta G_{\ddagger}^{\ddagger}$ is given by:

$$i_a = i_c = i_0 = A_0 \exp\left(\frac{-\Delta G_{\ddagger}^{\ddagger}}{RT}\right) \tag{2.32}$$

where A_0 is a constant.

When the forward reaction is faster than the reverse reaction ($i_a > i_c$) and an overall corrosion process occurs, equilibrium is destroyed and the free energies of the metal and its ions are at different levels (Fig. 2.12a). Fig. 2.13 is an overlay of Fig. 2.12a and Fig. 2.12b, showing that the energy of the metal increased and the energy of the environment decreased as the system moved towards the equilibrium state.
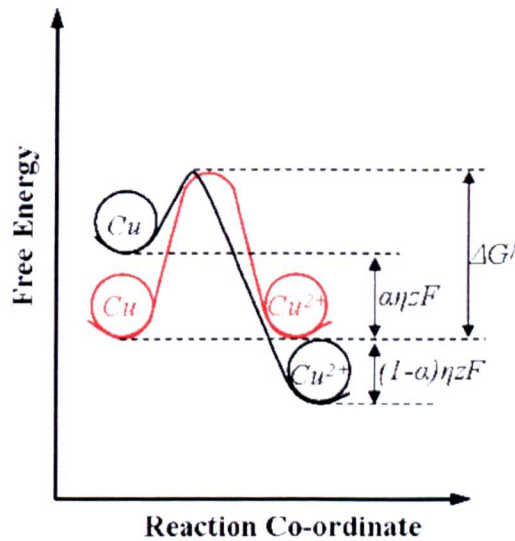
Fig. 2.13: Energy profiles for copper in pure water *(black curve)* at equilibrium and *(red curve)* with anodic polarization η [20].

The total polarization in Fig. 2.13 is η. The anodic polarization can be defined as $\alpha\eta$ where α is the symmetry coefficient, which describes the shape of the rate-controlling energy barrier. In single-step electron transfer processes representing a redox process, the cathodic polarization is equal to ($1-\alpha\eta$). The anodic polarization can be related to free energy by equation (2.6)

$$\Delta G^{\ddagger}_a = -zF(\alpha\eta)$$

(2.33)

The activation energy for the anodic reaction is given by:

$$\Delta G_a = \Delta G^{\ddagger} - \alpha\eta zF$$

(2.34)

The energy state of the metal increased and the activation energy reduced as the system moved from anodic behaviour to equilibrium. Equation 2.30 can be rewritten as:

$$i_a = A_0 \exp\left(\frac{-\Delta G^{\ddagger} + \alpha\eta zF}{RT}\right)$$

(2.35)

$$i_a = A_0 \exp\left(\frac{-\Delta G^{\ddagger}}{RT}\right)\exp\left(\frac{\alpha\eta zF}{RT}\right)$$

(2.36)

Substituting the exchange current density (2.32) into equation (2.36) gives:

$$i_a = i_0 \exp\left(\frac{\alpha\eta zF}{RT}\right)$$

(2.37)

A comparable expression for the cathodic current density is:

$$i_c = i_0 \exp\left(\frac{(1-\alpha)\eta zF}{RT}\right)$$

(2.38)

The bulk current flow, $i_{meas} = (i_a - i_c)$ is therefore given by the following expression, known as the Butler-Volmer equation:

$$i_{meas} = i_0\left[\exp\left(\frac{\alpha\eta zF}{RT}\right) - \exp\left(\frac{(1-\alpha)\eta zF}{RT}\right)\right]$$

(2.39)

2.6.3. Tafel Slopes

The anodic current density equation in (2.39) can be simplified to:

$$i_a = i_0 \exp(A'\eta)$$

(2.40)

Where $A' = \alpha z F / RT$. Taking logarithms of both sides:

$$\ln i_a = \ln i_0 + A'\eta \qquad (2.41)$$

Rearranging (2.41) and converting to base 10 logarithms gives:

$$\eta = \frac{2.303}{A'} \log_{10}\left(\frac{i_a}{i_0}\right) \qquad (2.42)$$

Letting $\beta = 2.303 / A'$ gives the Tafel equation which defines the relationship between reaction rate and polarization for a system under activation polarization:

$$\eta_a = \beta_a \log_{10}\left(\frac{i_a}{i_0}\right) \qquad (2.43)$$

Similarly, for the cathodic process at large cathodic polarizations;

$$\eta_c = \beta_c \log_{10}\left(\frac{i_c}{i_0}\right) \qquad (2.44)$$

where, similarly;

$$\beta_c = \frac{2.303RT}{(1-\alpha)zF} \qquad (2.45)$$

The constants β_a and β_c are called the anodic and cathodic Tafel constants. Equations (2.43) and (2.44) can be plotted as a graph of polarization (η) versus the logarithm of current density, as shown in Fig. 2.14.
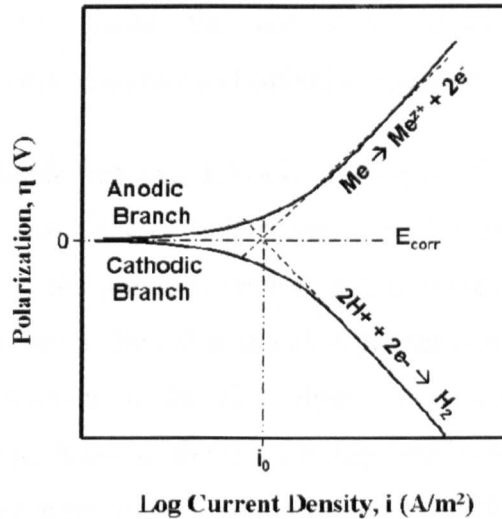
Log Current Density, i (A/m²)
Fig. 2.14: Idealised Tafel Plot

The measured current density is given by:

$$i_{meas} = i_a - i_c \qquad (2.46)$$

As the polarization is increased, i_a increases, i_c decreases and i_{meas} approaches i_a. Substituting (2.46) into the Tafel equation (2.43) gives:

$$\eta_a = \beta_a \log_{10}\left(\frac{i_{meas} + i_c}{i_0} \right) \qquad (2.47)$$

Linear Tafel behaviour is observed when $i_{meas} \gg i_c$. The anodic current density is comparable with i_0 at polarizations close to equilibrium and the measured value for the current density will be far removed from the true value of i_a and substantial deviations from linearity are obtained. The same arguments apply whether anodic or cathodic polarizations are used. Extrapolation of the linear portion of the polarization plots, as shown in Fig. 2.13, allows i_0 to be determined.

2.6.4. Diffusion Processes

The corrosion reaction itself is complex and consists of many steps. The overall corrosion reaction rate can be no faster than the slowest of these steps; the rate determining step. Each portion of the reaction sequence imparts a resistance to the

corrosion reaction, i.e. limits the corrosion current resulting from the thermodynamically favoured anodic and cathodic reactions.

The transport of cathode reactant (dissolved oxygen, for example) through a solution is relatively easy when small currents are involved and the activation process, as described in the previous section, is the rate-determining step. When large currents flow, however, the cell demands a greater charge transfer than can be accommodated by diffusion in the electrolyte. The speed of passage of the dissolved oxygen species becomes the slowest step, and is thus rate-determining. A corroding system under these conditions is referred to as diffusion-controlled.
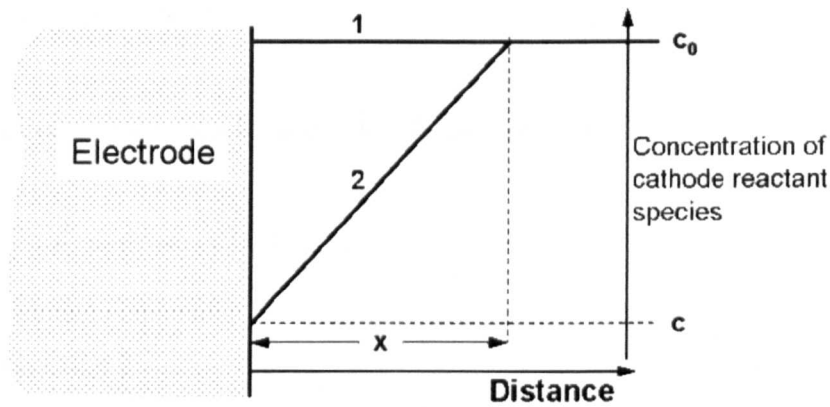
Fig. 2.15: Variation in cathode reaction species with distance from cathode [20]

Fig. 2.15 represents the variation of cathodic reactant concentration, c, with distance from the cathode, x. Under zero-current conditions, labelled 1 in Fig. 2.15, the concentration of species, c_0, will be uniform throughout the electrolyte. The concentration drops, as illustrated by line 2, when the cell is connected and current flows. A concentration gradient dc/dx is established.

Fick's First Law of Diffusion states that:

$$J = -D\frac{dc}{dx} \qquad\qquad (2.48)$$

where J is the flux of substance and D is a diffusion coefficient. It has already been seen from Faraday's Law of Electrolysis that $i = zFJ$ (2.31), thus (2.48) can be rewritten as:

$$i = -zFD \frac{dc}{dx} \qquad (2.49)$$

If the concentration gradient is assumed to be linear as shown in Fig. 2.15, then $dc/dx = (c_0 - c)/x$ and equation (2.49) becomes:

$$i = -zFD \frac{(c_0 - c)}{x} \qquad (2.50)$$

The maximum or limiting current, i_L, occurs when $c = 0$ and is given by:

$$i_L = -zDF \frac{c_0}{x} \qquad (2.51)$$

Using the Nernst equation for condition 1, (no current):

$$E_1 = E^0 + \frac{0.059}{z} \log_{10} c_0 \qquad (2.52)$$

and for condition 2:

$$E_2 = E^0 + \frac{0.059}{z} \log_{10} c \qquad (2.53)$$

Polarization is defined as the change of potential away from the equilibrium (no net current) condition; therefore $\eta = (E_2 - E_1)$ and subtracting (2.52) from (2.53) gives:

$$\eta = \frac{0.059}{z} \log_{10} \left(\frac{c}{c_0} \right) \qquad (2.54)$$

It can be shown that

$$\frac{c}{c_0} = \left(1 - \frac{i}{i_L} \right) \qquad (2.55)$$

Substituting (2.55) into (2.54) gives the relationship for the concentration polarization, η_c:

$$\eta_c = \frac{0.059}{z} \log_{10}\left(1 - \frac{i}{i_L}\right) \tag{2.56}$$

This equation shows that as $i \rightarrow i_L$, then $\eta \rightarrow \infty$. For small currents, $i_{meas} \rightarrow 0$ because $i_c \rightarrow i_a$ and non-linearity of the Tafel (E versus Log_{10} i) plot is obtained. The Tafel equation holds for intermediate currents, $i_{meas} \rightarrow i_c$, and linearity is observed. As the current increases still further the plot begins once more to deviate from linearity towards more negative values, approaching the limiting current density asymptotically.

2.6.5. Combined Polarization

Both activation and concentration polarization usually occur at an electrode. Activation polarization usually controls at low reaction rates, whereas concentration polarization becomes controlling at higher reaction rates. The total polarization, η_T, of an electrode is the sum of the contributions of activation polarization and concentration polarization:

$$\eta_T = \eta_a + \eta_c \tag{2.57}$$

As mentioned above, concentration polarization is not a factor during anodic dissolution, and the equation for the kinetics of anodic dissolution is given by:

$$\eta_{diss} = \beta \log_{10}\left(\frac{i}{i_o}\right) \tag{2.58}$$

During reduction processes such as hydrogen evolution or oxygen reduction, concentration polarization becomes important as the reduction rate approaches the limiting diffusion current density. The overall reaction for a reduction process is given by combining the Tafel equation (2.43) and the concentration polarization equation (2.56) with appropriate signs:

$$\eta_{red} = -\beta \log_{10}\left(\frac{i}{i_0}\right) + \frac{0.059}{z}\log_{10}\left(1 - \frac{i}{i_L}\right) \qquad (2.59)$$

Equations (2.58) and (2.59) are the basic equations of electrochemical reactions; (2.58) applies to most anodic dissolution reactions and (2.59) applies to all reduction reactions. Exceptions to (2.58) are metals which demonstrate active-passive behaviour.

2.6.6. Evans Diagrams and Mixed Potential Theory

Evans diagrams are produced by plotting a graph of potential versus the logarithm of current density and are used to illustrate the polarization of electrodes in a corrosion cell. The mixed-potential theory allows depiction of several corrosion reactions in a single Evans diagram, as shown in Fig. 2.16.
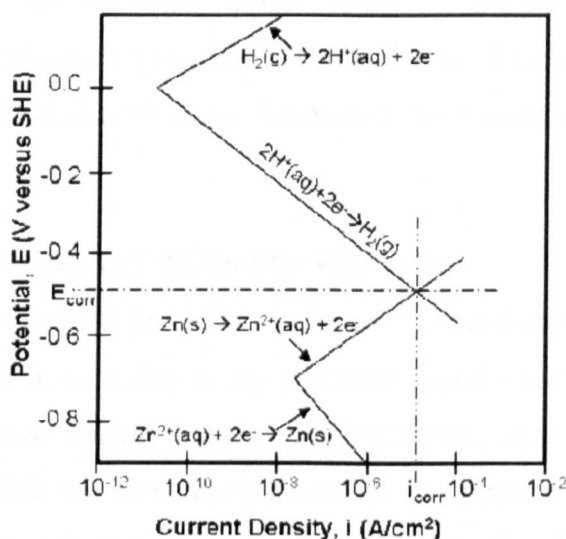
Fig. 2.16: Schematic representation of Evans Diagram for pure zinc in acid solution [19]

A zinc electrode in equilibrium with its ions is represented by a reversible potential corresponding to the zinc to zinc-ion electrode reaction, and a corresponding exchange current density. Likewise, a hydrogen electrode reaction occurring on a zinc surface under equilibrium conditions is represented by the reversible potential of the hydrogen electrode and the corresponding exchange current density for this reaction on a zinc metal surface. If a piece of zinc is inserted in hydrochloric acid containing zinc ions, the electrode cannot remain at either of these two reversible

potentials but must lie at some other potential. Zinc, since it is metallic, is an excellent conductor and its entire surface must be at a constant potential. This potential is achieved when the total rate of oxidation is equal to the total rate of reduction. It is seen from Fig. 2.16 that this condition is met at the intersection represented by a mixed or corrosion potential E_{corr}. At this point, the rate of zinc dissolution is equal to the rate of hydrogen evolution expressed in terms of current density. For every zinc ion released, two electrons are utilized in forming a hydrogen molecule. The current density corresponding to this point is usually called corrosion current density, i_{corr}, since it represents the rate of zinc dissolution, although it also represents the rate of hydrogen gas evolution.

Evans diagrams can be constructed for more complicated systems than that shown in Fig. 2.16. These diagrams are useful for explaining and predicting corrosion rates of metals in different environments. Evans diagrams combine thermodynamics and kinetics to form a whole picture of the corroding system; the potential axis is the thermodynamic factor and the current density is the kinetic factor.

2.7. CORROSION PROTECTION PRINCIPLES

The function of a corrosion protection system is to retard corrosion processes such that the component or assembly being protected offers a useful service life. The previous sections have shown that the factors affecting corrosion rate include the construction material, the service environment, the relative sizes of anodes and cathodes and these influences must be considered in the design of a corrosion protection system.

The automotive corrosion protection system includes material, design and environmental considerations. The use of protective metallic coatings on steel panels is the primary weapon in the automotive corrosion protection system and their protective mechanisms are introduced in the following sections. The protection afforded by the phosphate and e-coat paint treatments is discussed in Section 2.7.4.

2.7.1. Barrier Protection

A barrier coating serves to isolate the underlying metal from the corrosive environment. The barrier mechanism is effective as long as the coating is continuous. The continuity of the coating is particularly important with noble coatings (such as tin on steel) because if the substrate is exposed, it will act as the anode in the galvanic couple, as illustrated by Fig. 2.17, and will suffer accelerated corrosion. If the substrate is exposed at a defect or holiday in the noble coating, the unfavourable area effects will further accelerate corrosion of the substrate.
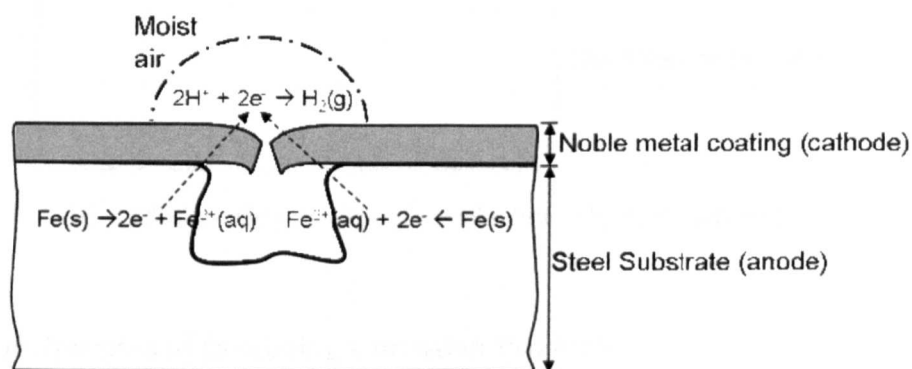
Fig. 2.17: Attack of the steel substrate at a discontinuity in the noble coating [22]

Application of sealer is an example of a non-metallic barrier coating often used in the automotive industry. The sealer serves to isolate the underlying metal from the corrosive environment, but similar to metallic coatings, it is effective only as long as it is applied to the precise location where it is required. Careful controls of sealer application and panel alignments are required to ensure robust corrosion protection by the barrier mechanism.

2.7.2. Galvanic or Cathodic Protection

Galvanic corrosion is exploited in engineered materials or systems where a sacrificial anode is used to protect the cathode against corrosion. For example, automotive body panels are constructed from galvanized steel panels because the zinc coating corrodes preferentially to the structural steel substrate. Magnesium is often connected to underground steel pipes to suppress their corrosion. This type of corrosion protection is termed cathodic protection, as the anode is sacrificed to protect the cathode. The protective action of a zinc coating on a steel substrate is

illustrated in Fig. 2.18. The advantage of galvanic versus barrier coatings is that the sacrificial coating continues to protect the steel substrate even at holidays in the coating. This is illustrated by the relatively light corrosion of the steel substrate, which occurs at a distance from the coating, compared to the accelerated attack of the substrate in Fig. 2.17.
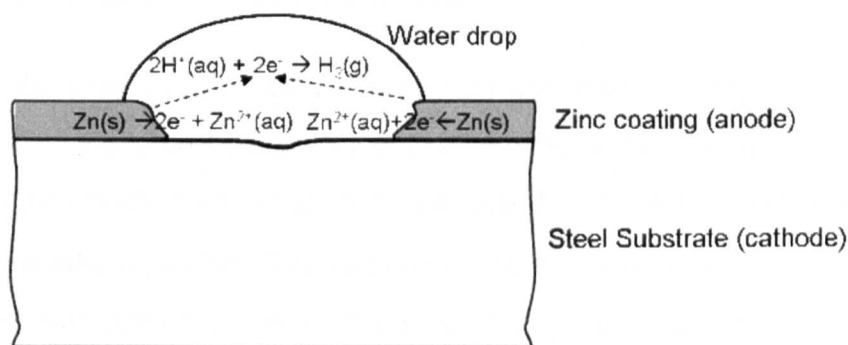
Fig. 2.18: Galvanic protection of a steel substrate by a zinc coating [22]

2.7.3. Precipitation of Insulating Corrosion Products

Reduced corrosion rates may develop when the corrosion products from a sacrificial coating are deposited onto the cathodic substrate and these products act as a barrier to further corrosion. In general, noble metals provide only barrier protection to steel. Zinc corrosion products however may offer protection to the steel substrate even after the galvanic action has extinguished, depending on the nature (such as solubility and porosity) of the product formed. Long-term atmospheric corrosion rate measurements of zinc confirm the ability of zinc corrosion products to retard the overall corrosion rates, because measured rates are significantly slower than those indicated by thermodynamic data. The mechanisms involved are discussed in detail in Chapter 4.

2.7.4. Phosphate & E-coat Treatments

Phosphating is an electrochemical process in which dissolution of the metal panel occurs at anodic sites and discharge of hydrogen, followed by hydrolysis and precipitation of insoluble phosphates takes place at cathodic sites [27]. The prime purpose of the zinc phosphate treatment applied to automobiles is to promote the adhesion of electrolytically deposited paint (e-coat) to the substrate material [28].

The presence of a crystalline zinc phosphate layer promotes paint adhesion by increasing the panel surface area, leading to an increased possibility of bond formation. Absorption of paint into micro-fissures in the crystalline layer generates greater inter-penetration of the phosphate and paint coatings. Zinc phosphate itself also gives corrosion protection to the underlying material as it constitutes a stable, insulating layer that inhibits the transfer of ions.

E-coat is the term given to the layer of paint deposited electrolytically onto the vehicle body. The e-coat paint is an epoxy-based resin and it coagulates onto the surface of the vehicle body (which acts as a cathode) as water decomposes to form OH^- at cathodic sites [29]. The function of the e-coat paint layer is to block the transfer of ions from the corroding environment to the steel substrate, thereby reducing the overall corrosion rate. In effect, e-coat offers a barrier to corrosion reactions. Unfortunately, small molecules such as water and oxygen can permeate the e-coat layer, even when it covers the entire metal surface [30]. Penetration of oxygen and water ions to the metallic surface allows corrosion to initiate underneath the paint layer. Defects in the e-coat layer such as porosity, scratches and "holidays" in the coating allow the transfer of ions, and therefore corrosion reactions, at a faster rate compared to intact e-coat. Thicker e-coat layers constitute a greater barrier to ions and therefore sites of reduced e-coat thickness may suffer increased corrosive attack. The porosity of the e-coat layer may be related to the pigment concentration of the e-coat, with reduced porosity associated with higher pigment concentration. At the same time, higher pigment concentration means higher viscosity, causing reduced flow of the e-coat in the deposition tank. The reduced flow may prevent adequate film build in recessed areas of the vehicle body structure and may reduce the appearance quality by "sagging" from vertical body panels. Each vehicle manufacturer selects an e-coat system that complements their overall corrosion protection strategy. The mechanisms of corrosion protection by paint treatments are reviewed in Chapter 4 and their influences on corrosion tests in this work are explored in Chapter 8.

2.8. SUMMARY

A metal's natural state is the lowest energy form. Metallic corrosion can be considered as the impetus to achieve a low energy state and thermodynamic principles apply to this reaction. Aqueous corrosion is generally electrochemical in nature and can be represented by an electrochemical cell, comprising electrodes connected by a conducting solution (electrolyte). The Nernst equation (2.8) combines thermodynamic principles with Faraday's Law of Electrolysis to relate equilibrium electrode potentials to pH. Pourbaix diagrams [25] are graphical representations of the Nernst equation and they describe the stability domains of different corrosion products (e.g. oxides, hydroxides, hydrides etc). Kinetics describe the rate of a given corrosion reaction. Electrochemical reactions can be assessed in terms of the rate of current flow between anodic and cathodic electrodes. Tafel experiments allow calculation of the corrosion current density, i_{corr}, which is directly proportional to the corrosion rate per unit area (equation 2.31). Evans diagrams combine thermodynamics and kinetics to illustrate the overall picture of a given corroding system; the potential axis is the thermodynamic factor and the current density is the kinetic factor. Metallic coatings are used to enhance the corrosion resistance of steel construction panels. The coatings may retard the corrosion of steel via sacrificial or barrier mechanisms and where solid corrosion products are formed, these may offer further protection to the substrate. Phosphate and e-coat paint treatments operate in tandem to provide an insulating, barrier coating on top of the automotive sheet. The efficacy of the paint barrier depends upon its insulating power, which in turn depends on the film thickness and porosity. In the next chapter, corrosion resistance test methods and assessments are discussed.

Chapter 3

CORROSION TESTS AND ANALYSIS

3.1. INTRODUCTION

The corrosion performance of a given material depends upon the environment it encounters. The corrosion resistance of a component depends upon its geometry as well as its construction material. A wealth of literature is available on corrosion testing of automotive materials, components and vehicles, with various researchers recommending different approaches to corrosion testing and analysis. The approach adopted depends on the expected corrosion environment and the availability of appropriate corrosion rate data from previous tests or from the literature, as well as practical considerations such as access to suitable equipment, testing time and budget. In this chapter, different types of corrosion test methods and test panels are discussed. Methods to assess corrosion resistance are discussed in Section 3.5 and the test and analysis approach adopted in this work is described in Section 3.6. A review of zinc corrosion mechanisms described in the literature is presented in Chapter 4. Details of the experimental methods used in this work are presented in Chapter 5.

3.2. LONG-TERM CORROSION DATA

Corrosion rate measurements of materials exposed outdoors and surveys of vehicles that have been in service for several years are valuable sources of long-term corrosion data and each of these sources is discussed in turn in the following sections. Long-term tests are often considered to be the highest quality data source because they give the actual service life of a material in a given environment. Exposure periods of several years are required to generate corrosion rate data for resistant materials such as painted, galvanized steel panels; accordingly, generating long-term data requires significant investment over an extended period.

3.2.1. Outdoor Exposure

Outdoor exposure allows weathering of test panels at natural rates in a given atmosphere. Various locations have been used as exposure sites and the corrosivity of the test site atmosphere may be classified according to average yearly humidity, temperature, rainfall and the atmospheric concentration of chloride and sulphate according to ISO 9223 [31]. For example, Kure Beach in North Carolina is a site for testing a material's corrosion resistance to an aggressive marine environment. Cramer et al. [32] reported corrosion rate data for a variety of metals exposed at 5 different test sites within the USA. Test panels for outdoor exposure are usually flat panels of painted or unpainted materials, mounted on racks and inclined at an angle of 30° from horizontal, as recommended in ASTM G-50 [33]. The angle of inclination is an important parameter in corrosion testing because it affects the deposition rates of atmospheric contaminants and the dwell time of precipitation. Handbooks of corrosion rate data of many materials at different exposure sites for various durations are available, for example Slunder and Boyd's compilation [23]. Comparison of cold rolled steel (CRS) and zinc corrosion rates at a particular test site indicate the increased service life that may be afforded by the use of zinc-coated steel rather than CRS. Some corrosion rate data from CRS and zinc panels exposed at various sites for 1 and 2 years are presented in Table 3.1.

Table 3.1: Average corrosion rates of steel and zinc at two exposure sites for 1 and 2 years [23].

Exposure site	Atmosphere	Steel corrosion rate (μm/year)		Zinc corrosion rate (μm/year)	
		year 1	year 2	year 1	year 2
Kure Beach	Marine	54.6	56.4	7.9	5.9
Montreal	Industrial	41.2	36.3	3.1	3.5

It is desirable to log weather conditions during outdoor exposures so that measured corrosion rates can be compared to published data and correlated to atmospheric conditions [23,31-32]. Analysis of corrosion rate data by geographic location allows the drafting of a "corrosion map", highlighting areas where severe corrosion may be expected, as shown in Fig. 3.1.
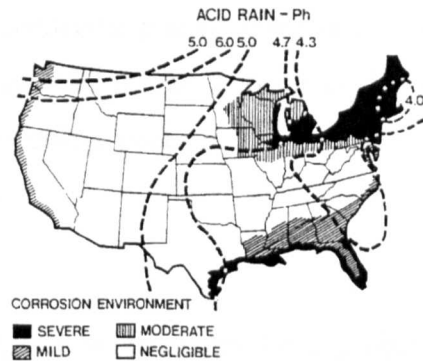
Fig. 3.1: Map showing corrosion environment types within the USA [34].

Corrosion rates in outdoor exposure may also be measured on test panels mounted onto vehicles [35-37] or trailers [3]. Test panels mounted in this way are exposed to the specific microclimates existing at discrete points on the vehicle and therefore give more accurate representations of the corrosion rates experienced by the corresponding vehicle panels than test panels exposed to the general macroclimate. Gao et al. [35] measured increased CRS and zinc corrosion rates at the rear bumper compared to those measured on the rooftop of a vehicle, as shown in Fig. 3.2.
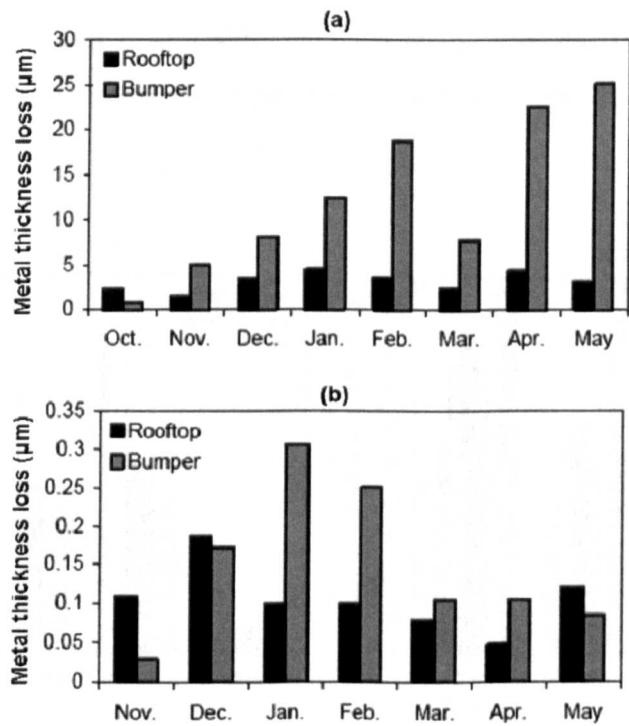
Fig. 3.2: Monthly corrosion rates of (a) cold rolled steel and (b) zinc at the vehicle roof and bumper [35]. *Note reduced y-scale on (b).*

Corrosion rate data from outdoor exposure expressed in metal thickness losses, such as in Fig. 3.2, can be used by the automotive engineer to specify the required thickness of a particular vehicle panel or the thickness of a corrosion protection layer.

3.2.2. Vehicle Surveys

Surveys of vehicles that have been in service for a number of years give information on the corrosion resistance of a particular vehicle. A committee was established by the society of automotive engineers (SAE) in the USA to conduct surveys of automotive body corrosion and to make the results available to the general public. Tiburcio et al. [3] reported that the first such survey was conducted in 1985 on 5–6 year old vehicles in the Detroit area and more recent surveys examined 7–8 year old vehicles. The surveys were "closed car" type, meaning only exterior panels were inspected and no information on inner, under-hood or under-body panels was generated. The number of corrosion imperfections observed on 7–8 year old vehicles decreased significantly between the 1993 survey and the 1998 survey, (see Fig. 3.3a), showing improved corrosion resistance of vehicles manufactured in 1990 versus those manufactured in 1982. Detailed analysis of the 1998 survey results showed increasing occurrence of imperfections in aging vehicles, (see Fig. 3.3b), as would be expected.
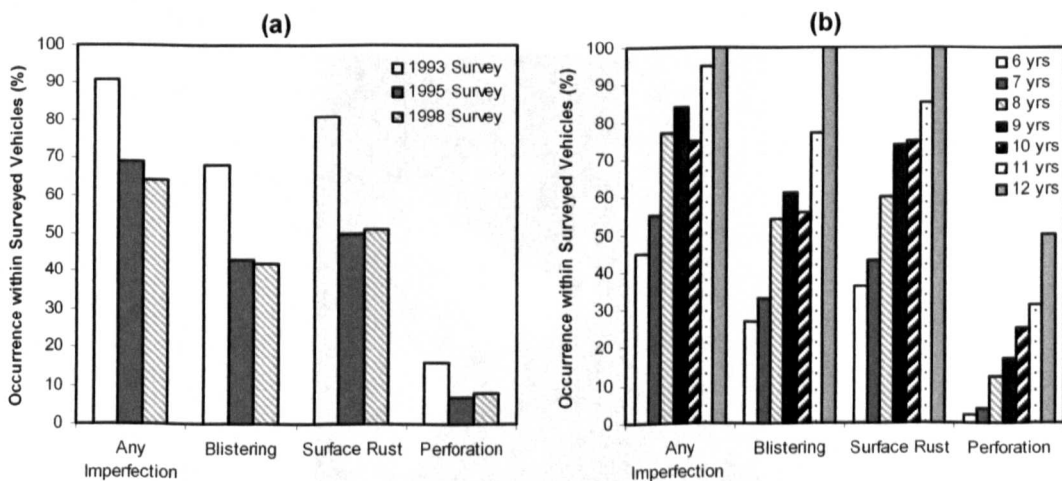
Fig. 3.3: Corrosion imperfections observed on (a) 7 – 8 year old vehicles surveyed in 1993, 1995 and 1998 and (b) vehicles from 6 – 12 years old surveyed in 1998 [3].

The 1998 survey results also highlighted that most imperfections observed on 6 year old vehicles were located on the hood outer panel (20% of all surveyed exhibited blistering or surface rust), and on the lower quarter panel adjacent to the rocker (14% of all surveyed), i.e. panels that are subject to mechanical damage due to stone and debris impingement during vehicle service.

Survey information is useful to automotive engineers because it indicates how well the corrosion protection system functions in service. The type of imperfection (surface rust, blister or perforation) observed and its location can be used to speculate the corrosion mechanism at work. Furthermore, the survey gives an independent comparison of the corrosion resistance of vehicles by different manufacturers. SAE survey results are available to the public; therefore it is in the manufacturers' interests to ensure that their vehicles achieve competitive corrosion resistance. Although the survey results give useful general information, they cannot be used for detailed assessment of vehicle corrosion mechanisms and corrosion rates in service because disassembly of a vehicle is usually required to view and analyse corroded areas. For example, perforation of an interior panel or inside an enclosed section such as the rocker cannot be observed during a closed car survey. Many manufacturers purchase used cars (e.g. from scrap yards) for tear-down and corrosion assessments after a given service interval. Fig. 3.4 shows tear-down analysis of a vehicle by drilling through spot welds.

Fig. 3.4: Vehicle disassembly for tear-down analysis. *Photo courtesy of Ford Motor Company Ltd. (FMC)*

Bednar [38] conducted detailed metallographic analysis of doors claimed from a scrap yard and Kurokawa et al. [39] sectioned and analysed doors 8 years after being assembled and fitted to a test vehicle. The data generated from such assessments are valuable because they can be used to investigate the corrosion mechanisms that actually occur on vehicles. These data are also essential for development of reliable accelerated corrosion tests and for interpretation of the results observed from those tests. Performing tear-down analysis also gives the automotive engineer a critical understanding of the correlation between vehicle body geometry, corrosion protection materials and the vehicle's ultimate corrosion resistance. However, surveys and tear-downs of full vehicles or sub-assemblies are expensive and time-consuming and unless the history of the vehicle's service life is known, uncertainty of whether it represents the average condition or an extreme condition persists. Another disadvantage of survey data is that they only become available after the vehicles have been in service for several years; too late to be input to the design of the surveyed vehicle and the data may be less relevant to current or future vehicles due to evolutions in designs, processes and materials.

3.3. ACCELERATED TEST METHODS

The purpose of accelerated corrosion testing is to assess the corrosion resistance of a system within a useful timeframe (i.e. within the product development lifecycle). All corrosion tests involve subjecting the test materials or components to some of the elements that are believed to contribute to corrosion in service, such as water, oxygen, sodium chloride, sulphates and nitrates. Corrosion is accelerated compared to natural conditions by using increased contaminant concentration, by adjusting the environmental conditions (temperature, relative humidity) and/or by adding some mechanical damage to coatings (e.g. scribe marks or stone chips to painted panels). Unfortunately, short tests and realistic corrosion results have generally been found to be mutually exclusive [40]. In the following sections, electrochemical, cabinet and proving ground tests are discussed in turn. The kind of data generated and the relative advantages and limitations of each methodology are briefly discussed.

3.3.1. Electrochemical Tests

Electrochemical principles can be used to measure corrosion potentials and corrosion rates of materials in a given aqueous environment (electrolyte). The test material is used as the working electrode (WE), a saturated calomel electrode (SCE) is typically used as the reference electrode (RE) and a platinum electrode is used as the auxiliary electrode (AE). Fig. 3.5 shows the experimental set up for an electrochemical polarization test using a three-electrode cell.
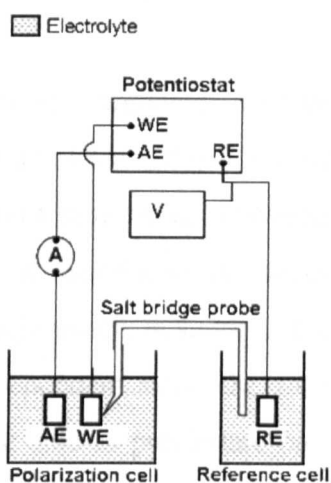
Fig. 3.5: Three-electrodes cell with ammeter (A), high impedance voltmeter (V) and potentiostat [41]

Standard test methods, for example ASTM G59 [42] and ASTM G71 [43], and computer-controlled potentiostats allow for repeatable and rapid analysis of a material's electrochemical behaviour. Polarization tests are based on the Tafel relationship (described in Section 2.6.3) and allow estimation of the polarization resistance R_P, of a material from the plot of potential (E) versus the current density (*log i*) close to (± 30 mV) the open circuit potential E_{corr} of the test material. Corrosion rates, measured in mm/year, can be calculated from the R_P values as described in the standard test method [42], or may be automatically calculated by the potentiostat control software. The tendency of coupled metals to corrode galvanically can be assessed by measurement of the galvanic current generated in a particular electrolyte using a zero resistance ammeter. Details of the polarization resistance test procedures carried out in this work are given in Chapter 5.

Scanning electrochemical techniques provide information on corroding systems in real time. The scanning vibrating electrode technique (SVET) has been used by researchers [44-46] to illustrate cathodic and anodic corrosion activity on the cut edges of panels whilst immersed in a corroding solution. The scanning Kelvin probe (SKP) was used by Fürbeth and Stratmann [47-49] to develop a mechanism for delamination of polymeric coatings from electrogalvanized steel. Many researchers have used electrochemical impedance spectrometry (EIS) or electrochemical noise (EN) methods to assess the integrity of organic coatings on steel substrates [50-51]. The mechanisms proposed by these authors are discussed in Chapter 4.

Electrochemical testing can be completed in relatively short times compared to natural exposures [52] and apart from the initial investment in equipment, it is a cheap and efficient corrosion test method. However, most electrochemical testing requires immersion of the test material in the electrolyte, which is not a condition usually encountered by vehicle panels in service. Indeed the corrosion resistance of zinc in the long term is dependent upon the formation of protective corrosion products, which may not be able to precipitate on immersed samples. Therefore longer-term corrosion rate data calculated or extrapolated from electrochemical test data may not be representative of natural service conditions. A further limitation of electrochemical tests is the inability to assess complex panel geometries; typically only small, flat specimens suitable for use as the working electrode in the electrochemical cell can be assessed.

3.3.2. Cabinet Tests

Cabinet testing is a generic term used here to describe accelerated tests carried out in climate-controlled cabinets. Cabinet tests can be used for samples ranging from simple flat panels to small components such as bolts, to full-size vehicle sub-assemblies such as doors, as shown in Fig. 3.6.
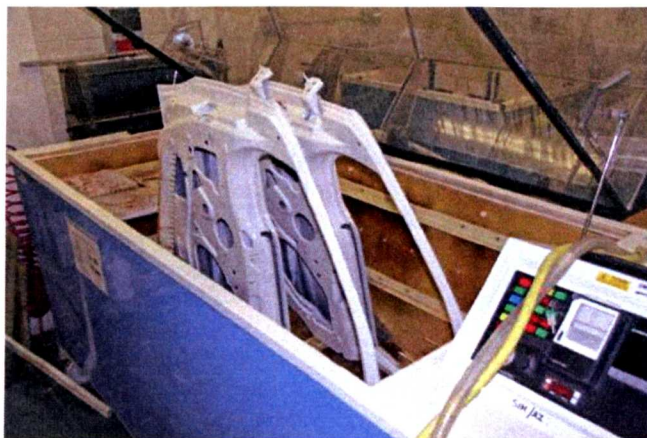
Fig. 3.6: Cyclic corrosion test cabinet. *Photo courtesy of FMC.*

Several standard cabinet test methods exist, such as the salt spray test, ASTM B117 [53], the modified salt fog test ASTM G85 [54], and the more recently-developed laboratory cyclic corrosion test SAE J2334 [55-56]. Test procedures have also been developed in-house by vehicle manufacturers. Effective cabinet testing requires awareness and understanding of the correlation between the corrosion rates and modes generated by the test and those likely to be experienced by the material or component in service.

The neutral salt spray or salt fog test [53] is still used by many automotive manufacturers and suppliers in spite of its inability to reproduce the corrosion behaviour of zinc-coated steels in the environment [34,40,57-59]. Ström et al. [59] produced "open corrosion" test samples of CRS and hot dip galvanized steel (HDG) by masking an area of the panel prior to paint shop treatments. Fig. 3.7 shows that HDG did not exhibit a corrosion benefit versus CRS when tested in a neutral salt spray test, but the corrosion benefit of HDG versus CRS was observed on similar test panels tested via a cyclic corrosion method, as shown in Fig. 3.8. This suggests that the salt spray test is not suitable even for comparative assessment of automotive panel corrosion resistance.
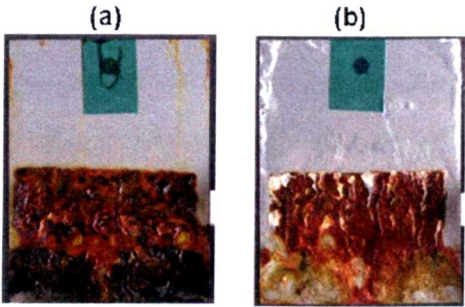
Fig. 3.7: Rust developed on (a) cold rolled steel and (b) hot-dip galvanized steel after 4 weeks of neutral salt spray testing [59].
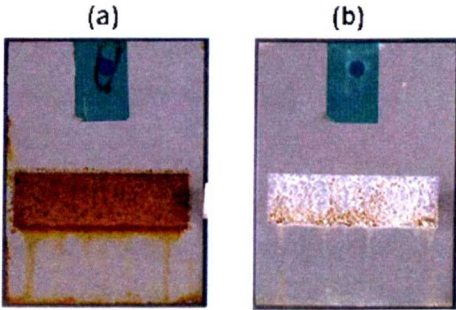
Fig. 3.8: Rust developed on (a) cold rolled steel and (b) hot-dip galvanized steel after 4 weeks of cyclic corrosion testing [59].

A cabinet test regime which is well understood in terms of it acceleration factor compared to natural corrosion rates and the corrosion modes it does and does not stimulate is a very useful tool to the automotive engineer. Townsend and McCune [60] reported on an inter-laboratory (round robin) test programme of zinc-coated, non-coated and phosphated panels according to SAE J2334. Controlling the relative humidity (RH) at 50% during the drying phase was critical to generation of correlation with on-vehicle tests. The specimen orientation and salt spray application method also affected the measured corrosion rate with greater rates associated with more vertical panels and immersion rather than spraying of salt solution [60].

Usually, cabinet testing is the precursor to more expensive proving ground or outdoor exposure testing. Test programmes can be designed and executed within reasonable (days or weeks) time frames and the tested materials can be assessed in a number of ways (discussed in Section 3.5). Modern test cabinets are programmable

and can be run automatically without interruption, making this kind of test method very accessible to the non-expert. However, extrapolation of long term corrosion rate data from any kind of accelerated test procedure should be undertaken only with awareness of the effects of the accelerating factors on the apparent corrosion rates. Continued effort is being invested in developing cabinet test methods that give greater correlation to actual corrosion rates and modes. The result of these studies is the proliferation of test procedures as modifications to "standard" procedures [61], the adoption of different test regimes by different vehicle manufacturers and the development of specific test methods for particular materials such as aluminium [62] and stainless steel [63].

3.3.3. Proving Ground Tests

Proving ground (PG) tests are commonly used to validate the corrosion resistance of a new vehicle prior to market launch, assessing both the vehicle design and the processes used to produce it. Each automotive manufacturer has developed its own vehicle test procedure although all PG tests include some form of salt application, climate chamber cycles, stone impingement and driving [61,64-67], as shown in Fig. 3.9.
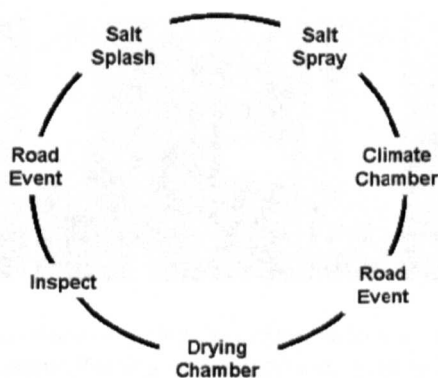
Fig. 3.9: Typical proving ground test cycle events [64].

Loads and damage due to road driving are included in the PG test making it more representative of the conditions that a vehicle will experience in service compared to cabinet or electrochemical tests. A PG test cycle devised by Hyundai Motor Company is given in Table 3.3 [65].

Table 3.3: Example of a proving ground test cycle (adapted from [65])

Event Type	Description	Parameters
Road driving	Vehicle driven over rough roads and on high speed track	Total driving time: 4 h Total distance: 130km/day
Salt spray and splash	Vehicle driven through a trough of salt solution.	Trough length: 50 m Driving speed: 40 km/h Solution depth: 50 mm Solution type: 5 wt.% NaCl
Salt soak	Vehicle parked in a climate chamber and sprayed with salt solution.	Time: 3 h Temperature: 35°C Wind fan speed: 70 kph
Climate soak	Vehicle parked in a climate chamber.	Time: 14 h Temperature: 49°C Humidity: 98% RH
Sunlight soak	Vehicle parked in a climate chamber.	Time: 3 h Temperature: 40°C Sun load: 1000 W/m^2

Table 3.3 represents 1 cycle, which takes 1 day to complete and the full test regime requires 100 cycles, so the total proving ground test duration is 100 days. Fig. 3.10 is a photograph of PG test events at FMC's proving ground in Lommel, Belgium.

Fig. 3.10: Test vehicle (*left and centre*) entering the climate chamber and (*right*) driving through salt mist at Lommel Proving Ground. *Photos courtesy of FMC.*

The vehicle is inspected at specific intervals during the test and full tear-down analysis is conducted at the end of the test period. Assessment of the overall corrosion resistance is made by analysing the progression of corrosion during the test and estimating a pass or fail grade [64]. It is desirable to achieve reliable validation of a vehicle's corrosion resistance with the minimum possible number of tests because running the PG test is expensive and resource-intensive, as well as lengthy (100 days in duration [65]). If the manufacturer wishes to test only a small

number of vehicles at the proving ground, then it is critical that the test generates results that can be used to make reliable corrosion resistance assessments. Significant effort has been invested by automotive manufacturers to demonstrate and improve the correlation between PG tests and real-world automotive corrosion. Wang et al. [64,66] noted that the microclimate (conditions at individual panel locations) and the macroclimate (geographical weather conditions) of the PG test themselves must be quantified to allow correlation of the PG test conditions to real world conditions. Ström et al. [59] emphasised that any acceleration of corrosion generates at best only indications of the vehicle corrosion performance and this notion must be reflected in how accelerated corrosion tests are interpreted by the automotive engineer.

3.4. TEST PANELS

Many researchers have suggested simplified test panels to assess corrosion resistance of some feature or other of the vehicle body without undertaking full vehicle tests, which are expensive and constitute a complex system with many variables. In the following sections different panel configurations used in the automotive industry are described.

3.4.1. Unpainted Panels

Unpainted panels are used at the initial stages of corrosion testing of a new construction material or to test a current material in a new environment. Flat, rectangular panels are useful geometries because the progression of corrosion on featureless panels can be assessed easily using image analysis. Cut edges of multi-layer material panels must be treated with lacquer, wax or isolated with tape to avoid early corrosion of the test panel. Alternatively, a specific area within the panel may be exposed as the test area by the application of lacquer, masking tape or by masking and applying paint treatments as shown in Fig. 3.7– 3.8 [59].

3.4.2. Painted Panels

The automotive paint system comprises several layers of varying thickness and with difference primary functions, as shown in Fig. 3.11 [29]. The primer, colour and clearcoat layers also offer barrier protection to the metallic substrate although

corrosion resistance is not their primary function. Painted test panels may be defined as full paint system with all layers included or just the pre-treatment stages of the paint system, depending on the objectives of the test programme.
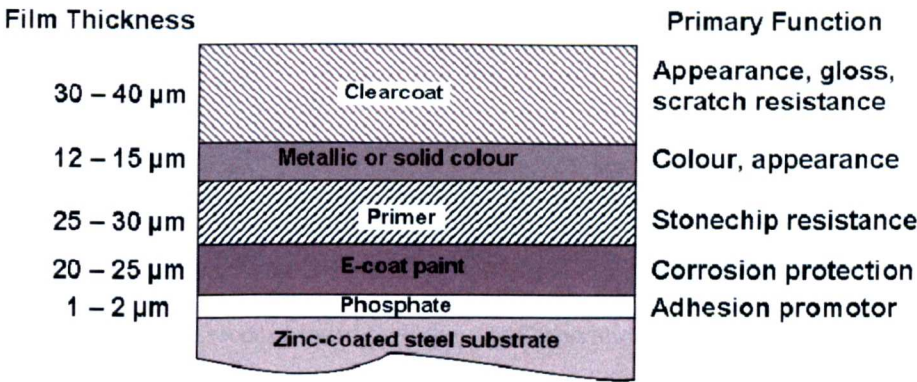
Fig. 3.11: Automotive paint system layers and their primary function [29]. *(Not to scale)*

The effectiveness of the protection offered by the paint system to the vehicle in service depends upon several factors including the intensity of damage to the paint by stone impingement and scratches. Defects are often introduced to painted test panels prior to corrosion testing to assess the system's resistance to corrosion from such mechanical damage. Fig. 3.12 is a photograph of a machine used to project gravel against a test panel. The severity of the resulting paint chips (number, size and penetration of chips) can be assessed according to ASTM D3170 [68].

Fig. 3.12: Painted panel chipping apparatus. *Photo courtesy of FMC.*

Scribe lines may be cut into painted test panels to simulate scratches. The scribe tool comprises a tool-steel grade blade (such as a parting tool) with a handle and

lateral support to aid consistent scribing from panel to panel. The scribe tool recommended by Volvo Car Corporation (VCC) is shown in Fig. 3.13 [69].

Fig. 3.13: Scribe tool recommended by Volvo Car Corporation [69]. *Photo courtesy of VCC.*

Subjecting panels with paint damage to corrosion tests allows assessment of the paint system's resilience. Red rust development at chipped areas of test panels with steel substrates gives clear visual evidence of the resistance of different paint systems to mechanical damage. Quantitative assessment of the painted panel's corrosion resistance can be achieved by measuring the "creep-back" (increase in scribe line width) and delamination of paint layers from scribe lines. Ström et al. [70] used scribe line creep data to correlate cabinet test procedures with outdoor exposures; Stephens [40] used similar data to compare corrosion results from several different cabinet test procedures. Townsend and McCune [60] used scribe line creep measurements to assess the reproducibility and repeatability of test method SAE J2334 in several different laboratories. The results of [60] showed that although the ranking of the test materials was similar between different laboratories and in agreement with on-vehicle tests, the scribe creep data exhibited rather poor inter-laboratory reproducibility. For example, one laboratory measured 1.2 mm scribe creep from a sample of electrogalvanized steel (EG) with 30 g/m^2 coating weight whilst another laboratory measured 6.2 mm scribe creep from a similar sample using the same test method. Even a simplified panel, tested according to a defined standard, was subject to large variations in apparent corrosion resistance by quantification of scribe line creep.

Other panel configurations have been used to assess corrosion from paint defects. For example, Stratmann and Fürbeth [47-79] induced paint delamination by over-

coating adhesive tape with a paint layer. The tape was lifted from the substrate after the paint had cured and a reservoir was constructed to allow retention of an electrolyte underneath the delaminated paint. This test panel design allowed the authors to monitor corrosion activity from the defect area in real time using a SKP.

3.4.3. Specific Panel Geometries

Edges and crevices are features of vehicle body construction that are associated with greater corrosion attack compared to open panel surfaces (see Section 2.3). Special test panels have been produced by different researchers to test the resistance of different materials to specific geometric features, such as the edge corrosion samples by Suzuki et al. [71], the lapped joint samples by Almeida and Morcillo [72-73] and the crevice samples devised by Ström et al. [59]. These panels are simplified versions of the geometries generated by vehicle body construction and are designed to assess the resistance of a given material to edge and crevice corrosion. Wakano et al. [74], Miki et al. [75] and Oldenburg et al. [76] constructed variations of "mini-door" specimens, incorporating a controlled-gap crevice [74], a hemmed edge [74-76], spot welds [74,76], a formed inner panel [74-76] and drain holes [76]. Roudabush et al. [77] conducted a literature review of different test panel geometries devised for crevice corrosion resistance assessments to propose a test panel that was subsequently refined and published as the SAE perforation test coupon shown in Fig. 3.14.
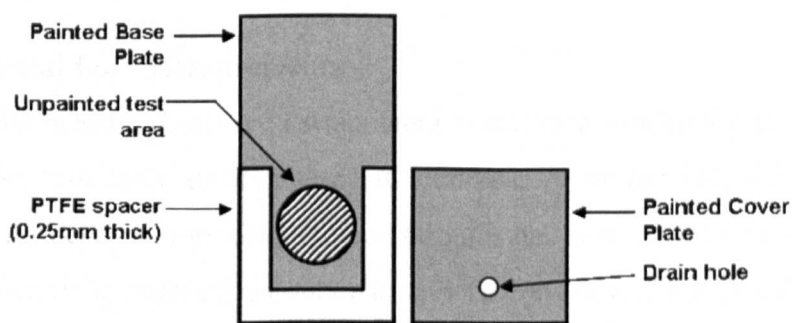
Fig. 3.14: SAE standard perforation test panel configuration [34,36,56,78].

Many researchers continue to design tailored test panels to assess a specific geometry or feature of interest (e.g. formed, welded and bonded panels) and to suit their own test and analysis equipment. Long-term corrosion rate data of the

standard test panel configuration is also required to allow correlation of laboratory test results to in-service lifetimes.

3.5. CORROSION RESISTANCE ASSESSMENTS

Corrosion resistance assessments may be devised to generate data on corrosion rates of a given material or may be designed to explain the corrosion mechanism at work. Visual observations and material loss measurements belong in the former category and corrosion product characterization belongs in the latter. Each of these approaches is discussed in turn in the following sections.

3.5.1. Visual Assessments

Visual observations are qualitative assessments of the appearance of a test object during and following corrosion testing and they allow ranking of materials in order of corrosion resistance [34,36-38,40,61,78-79]. Many researchers have used image analysis to quantify the percentage of corrosion-affected area (red rust coverage [36,37,61] or delaminated paint area [36,40]) to rank their test materials. Tools are available to enable consistent visual assessments, for example ASTM D610 [80] gives comparison charts to allow ranking of corrosion damage on painted steel substrates. Such qualitative assessments are useful to the automotive engineer because they relate to the visual impression of a corroding system, arguably the most direct representation of the customer's viewpoint. Unfortunately, visual assessments cannot be used to predict service life-times.

3.5.2. Material Loss Measurements

Material loss measurements are extrapolated to estimate service life-times, as mass or thickness loss rates are expressed in mm/year or g/year [34,35,57,78]. The maximum pit depth in corroding crevice samples has been used by several authors to rank materials in order of resistance to crevice corrosion [35-37,39,60,74-76,80]. Thickness loss measurements can be carried out using point-to-point micrometres or via cross-sectional analysis.

Careful preparation of the corroded samples is required prior to recording mass losses. ASTM G1 [81] describes cleaning protocols comprising chemical and mechanical steps for various metals. The cleaning process may remove some

portion of the substrate material and lead to overestimation of the actual material loss. This error can be estimated by applying the same cleaning process to uncorroded samples of the test material and correcting the mass loss results accordingly. Conversely, mass loss rates may be underestimated if the cleaning process does not remove all the corrosion products from the test sample. Ström et al. [59] suggested use of dry mass gain measurements to track crevice corrosion during a laboratory test procedure. This assessment required relatively mild corrosion acceleration and careful drying and weighing of corroding samples but no mechanical or chemical cleaning. The mass gain measurements were compared to point-to-point micrometre measurements of thickness loss and to ultrasonic thickness gauge measurements to ensure validity. The authors [59] produced graphs of accumulated dry mass gain versus corrosion exposure time of several material systems, allowing ranking of materials and illustrating the progression of corrosion over time.

Material loss measurements made on test panels subject to accelerated tests may be compared directly to long-term corrosion data available in handbooks [23] and therefore can be used to estimate the acceleration factor of a given test procedure. There are many sources of error in the cleaning and weighing procedures required for mass loss measurements, as discussed above. A further concern with such assessments is that a low mass or thickness loss rate may be recorded from a large sample suffering from severe localized corrosion (e.g. pitting attack), leading to inadequate corrosion protection provision. Similar to the visual assessment methods, material loss measurements give little information about the corrosion mechanism at work, but rather rate or track the corrosion attack. In practice, most researchers provide several assessment criteria for a single corroding system to give a more robust analysis of its corrosion resistance.

3.5.3. Corrosion Product Analysis

Corrosion product analysis is useful for establishing the corrosion mechanism(s) involved in a corroding system. Corrosion products may be protective or non-protective in nature, depending on their morphology, stability and solubility in the corroding environment, (see Chapter 4). Formation of one particular corrosion

product versus another allows estimation of the corrosion reactions taking place and therefore establishment of the corrosion mechanism. Some of the analysis techniques used to determine corrosion products present on a corroding surface include cross-sectional analysis combined with optical and scanning electron microscopy, infrared analysis and X-ray techniques such as energy dispersive spectroscopy, diffraction and photoelectron spectroscopy. Chemical analysis of solutions collected from a corroding panel allows detection of the products leached from the corroding surface and these data can also be used to estimate the corrosion mechanism. For example, Elvins et al. [82] used inductively-coupled plasma mass spectroscopy to quantity the amount of zinc present in run-off solution collected from galvanized steel panels exposed at outdoor sites.

A mechanistic approach to corrosion resistance is of great use because it allows prediction of corrosion behaviour in environments and geometries other than those tested. Development of corrosion behaviour hypotheses allows efficient experimental design, avoiding redundant tests, reducing test variables and decreasing the overall test time. The disadvantages associated with corrosion product analysis are the expertise and specialised equipment required to conduct thorough analysis. Several analysis techniques may be required to perform robust mechanistic analysis and it is unlikely that a vehicle manufacturer would have all the necessary instruments in-house. In practice, research collaborations are often established to leverage the expertise of vehicle manufacturers, material suppliers and academic researchers. In the next section the approach adopted in this work is presented.

3.6. APPROACH ADOPTED IN THIS WORK

The prime objective of this work was to investigate the potential of zinc-magnesium coated steel (ZMG) as a next generation galvanized steel for the automotive industry. ZMG is a new material to the automotive industry and long-term data on its corrosion resistance is not yet available. Therefore, the approach adopted in this work was to compare corrosion behaviour of ZMG to that of conventional zinc-coated steel under accelerated corrosion test conditions and to offer corrosion mechanisms based on the observed effects and the current understanding of zinc

corrosion mechanisms. To this end, zinc corrosion mechanisms were reviewed and are presented in Chapter 4. It was important to select test parameters and test objects that could be related to realistic vehicle corrosion environments and to current vehicle manufacturing processes. The philosophies behind the methods selected are given in detail in the following sections and full details of the experimental methods are given in Chapter 5.

3.6.1. Corrosion Test Methods

The ZMG material used in this work was prototype material produced initially in the laboratory and later by pilot line in limited batches; therefore, it was important to make best use of the material supplied. Early reports of ZMG's corrosion resistance suggested greatly increased corrosion resistance versus conventional zinc coatings (24-fold [13] and 10-fold [14]); if ZMG exhibited such levels of corrosion resistance in natural weathering exposure then scant useful data would be generated by such an exposure programme within the project timeframe. Therefore, outdoor exposure testing of ZMG was not undertaken in this project.

Accelerated corrosion tests were required to generate data within the project time-frame. Wang et al. [64] observed that accelerated test methods can be conducted in one of two ways; by selecting conditions close to the field conditions (e.g. correlated cyclic corrosion test) or by increasing the severity of the corroding conditions to generate full-life corrosion effects within the test period (e.g. salt spray test). The first approach generates realistic corrosion mechanisms and modes but requires detailed knowledge of the expected mechanisms and the microenvironment that can trigger them. The second method gives greater corrosion acceleration and, provided the degree of corrosion expected in the field is known, gives clear pass or fail criteria to the automotive engineer. In this work, the corrosion mechanisms rather than the expected life-time of ZMG material was of prime interest, and therefore the former approach was adopted. No salt spray testing was conducted in this work, rather a cabinet cyclic corrosion test with relatively low sodium chloride concentration (1 wt.% NaCl) was selected to propose the mechanism of ZMG corrosion in a sodium chloride environment. Ström et al. [59,70] have demonstrated previously that the parameters used in this

test regime give reasonable correlation to actual vehicle body panel corrosion mechanisms in the field. Full details of the test methods and apparatus are given in Chapter 5.

Open circuit potential measurements and polarization tests were also conducted on ZMG. The purpose of these tests was to establish whether the ZMG material was significantly anodic to zinc in a sodium chloride solution. If a large potential difference existed, galvanic effects must be considered in the ZMG corrosion mechanism proposed. Hausbrand et al. [83-84] reported very similar electrochemical behaviour of ZMG and pure zinc, but with a corrosion potential (E_{corr}) approximately 10 mV more anodic [83] than zinc. The experimental set-up and the polarization test results are given in Chapter 5. Further electrochemical testing was not pursued in this work because constant immersion of the material in an electrolyte does not correspond well to the corrosion environment experienced by vehicle body panels in service and would not be useful in developing the corrosion mechanism.

3.6.2. Test Objects – Panels, Components or Vehicles?

It was tempting to construct vehicle components from ZMG and assemble the components to a vehicle for proving ground testing; but isolation of the different corrosion modes experienced by vehicle components was required to establish the corrosion mechanism of ZMG. Therefore simple panels were fabricated to test separately open corrosion, edge corrosion and crevice corrosion of ZMG in cabinet tests.

The cabinet corrosion testing was conducted in two phases; in the first phase the test duration required for initiation of red rust on open, unpainted panels of ZMG was established. Similar test panels of conventional galvanized steel were tested at the same time for comparison. The second phase incorporated painted panels with features to test the cut edge and crevice corrosion resistance of ZMG. No standard test panel exists for edge corrosion assessments and (as will be discussed in Chapter 4) relatively little published information is available on cut edge corrosion of automotive panels. A report by Suzuki et al. [71] is an exception and the edge

corrosion test panel design used here was based on their work. Many different crevice panel geometries have been suggested, including the SAE standard model shown in Fig. 3.14. The simpler crevice corrosion panel design suggested by Ström et al. [59] was selected in this work. The Ström sample includes a glass cover allowing visual assessment of corrosion evolution during the test, whereas the SAE panel uses a metal cover plate which itself must be fabricated and painted.

Once the corrosion mechanisms for ZMG in open, edge and crevice modes have been proposed it will be useful to conduct tests on panels or components incorporating two or more of these features to assess any interaction effects. Further tests must also be conducted on ZMG to ensure its compatibility with vehicle manufacturing processes such as forming, welding and joining. These tests are outside the scope of this project but are important for the overall assessment of the potential of ZMG to be the next generation galvanized steel for the automotive industry. Equally, compatibility tests must be conducted with satisfactory results before construction of vehicle components can be considered.

3.6.3. Paint Treatments

The automotive paint system comprises several layers, as shown in Fig. 3.11. The paint layers constitute a barrier to corrosive agents and therefore delay the onset of substrate corrosion. The painted panels used in this work were subject only to the pre-treatment processes (i.e. phosphate and e-coat) to ensure corrosion effects were observed during the test period and to avoid chemical interaction effects of topcoat and clearcoat constituents. These treatments were applied in the VCC paint facility at Gothenburg, Sweden by mounting test panels to the chassis rails of production vehicles. The effect of the paint treatments on corrosion resistance was accounted for by producing test panels of non-zinc coated steel. This comparison was especially important in the development of the edge corrosion mechanism because edge geometry affected paint coverage and ultimately edge corrosion.

3.6.4. Corrosion Resistance Assessments

An important result from this work was the comparison of ZMG corrosion resistance to that of conventional galvanized steel; if no corrosion benefit were

observed versus current construction materials there would be little interest in developing ZMG for automotive applications. The corrosion resistance of any material can be expressed in many ways. Appearance of red rust is of great concern to vehicle customers, therefore the evolution of red rust was used as an assessment criterion in this work. Image analysis was used to quantify the rusted area on the test panels in this work. Exposure time to red rust initiation has been suggested [56-57] but the initiation can occur between inspection periods, leading to errors in this result. Tsujimura et al. [17] used the time taken to cover 5% of the test panel surface with red rust as the assessment point. In this work, both initiation and propagation of red rust were tracked as far as possible.

Cross-sectional analysis of corroded test panels was carried out to aid development of the corrosion mechanisms at work. The morphology, thickness and composition of the corrosion products were assessed using a variety of techniques. Characterization of the corrosion products developed under different exposure conditions and on different panel configurations was required to propose reaction sequences and the overall corrosion processes. Thermodynamic and kinetic principles (introduced in Chapter 2 and discussed further in Chapter 4) were considered in the development of the corrosion mechanisms

3.7. SUMMARY

An extensive literature on the corrosion testing and analysis of automotive materials is available and this chapter examines only a small portion thereof. The large number of reports available and the variations in test procedures, objects and assessments reflect the complexity of vehicle corrosion. The prime objective of this work was to assess the potential of ZMG as a next generation galvanized steel for the automotive industry. Two requirements were adhered to in designing the experimental programme in this work; to develop corrosion mechanisms for ZMG based on the current understanding of zinc corrosion and to ensure that the corrosion data generated could be applied to automotive panels. Zinc corrosion mechanisms are discussed in detail in Chapter 4. Having reviewed zinc corrosion mechanisms, development of corrosion mechanisms for ZMG required a step-wise test plan, beginning with open corrosion modes on unpainted ZMG panels prior to

assessment of panels incorporating geometric features and paint treatments. Testing of conventional galvanized steel and uncoated steel panels at the same time allowed reliable comparison of the corrosion benefit of ZMG versus current materials. Testing galvanized steel at the same time also served as a quality check on the test methods because the behaviour of the galvanized material under test conditions could be compared to the literature. The use of cyclic corrosion tests developed specifically for the automotive industry and fabrication and painting of test panels in line with real automotive production processes ensured realistic corrosion resistance assessments. Full details of the experimental methods used are presented in Chapter 5.

Chapter 4

ZINC CORROSION MECHANISMS

4.1. INTRODUCTION

Zinc-coated or galvanized steel continues to be the prime construction material for mass-produced vehicle bodies. Guzman et al. [8] estimated in 2003 that 95% of the vehicle body was constructed from galvanized steel. There is a desire within the automotive industry to move to alternative zinc coatings offering improved corrosion resistance without increasing coating thickness. Thinner (less than 7 microns) metallic coatings are attractive as they may alleviate processing difficulties such as spalling of the coating during forming and brass formation on spot welder electrodes. Coatings with superior corrosion resistance compared to galvanized steel may eliminate the need for additional protection measures in corrosion-sensitive areas such as cut edges, enclosed sections and crevices between panels. Magnesium-containing zinc coatings have been highlighted as a potential next generation of galvanized steel, offering enhanced corrosion resistance without increased coating thickness. In this chapter, the literature concerning corrosion behaviour of conventional zinc-coated and zinc-magnesium coated steel relevant to the automotive industry is reviewed.

4.2. ZINC COATINGS FOR STEEL

The structure of a zinc coating depends upon its application method. Specific properties are associated with the different zinc coating structures and these are discussed in the following sections.

4.2.1. Application of Zinc Coatings

High production rates coupled with good surface quality are key criteria for the suitability of galvanized steel to automotive applications. Electroplating and hot-dipping are the most common zinc application methods for automotive sheet steel and these are discussed in turn in the following paragraphs. Vapour deposition is

emerging as a potential application method for tailored or multi-layer coatings and this coating method is also described.

Electrodeposition of coatings onto a conducting substrate is known as electroplating. The steel is immersed in a conducting solution containing a salt of the coating metal and is made the cathode by applying an electromotive force from an external source [85], as illustrated in Fig. 4.1 [86].
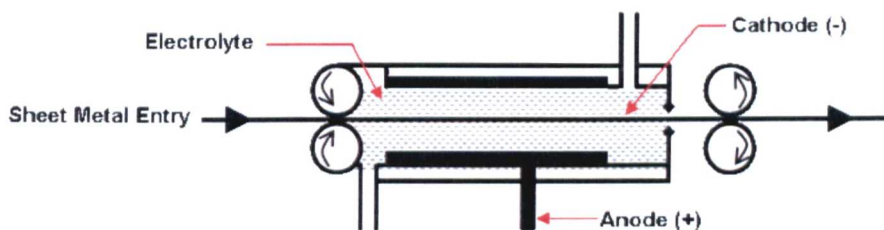
Fig. 4.1: Electrodeposition process for automotive steel sheet [86].

Coating deposition initiates through nucleation at defects in the crystal lattice of the substrate metal, such as dislocations at the surface, with subsequent crystal growth of the deposited metal from the nucleated sites. By this mode of growth, an adherent crystalline metal coating is built up on the substrate, bonded to the substrate by atomic linkages, which ensures complete adhesion without growth of alloy layers between coatings and substrate [85]. Modern electroplating cells operate at high current densities, up to about 100 A/dm^2 [1] and typically apply zinc to thicknesses of 4-13 μm (20-90 g/m^2) [21]. Line speed is limited only by mechanical factors for thinner coatings and may be as high as several hundred m/min although electroplating lines are generally less productive when thicker coatings are required. Electrodeposition does have the advantage of flexibility to produce single-side coated sheet or sheet with different coating weights each side.

Hot-dip coating lines operate on continuous strip processing achieving line speeds of up to 200 m/min. The steel is pickled in hydrochloric acid and fluxed in ammonium chloride to ensure a clean surface prior to immersion in a bath of molten zinc, as shown in Fig. 4.2 [87].
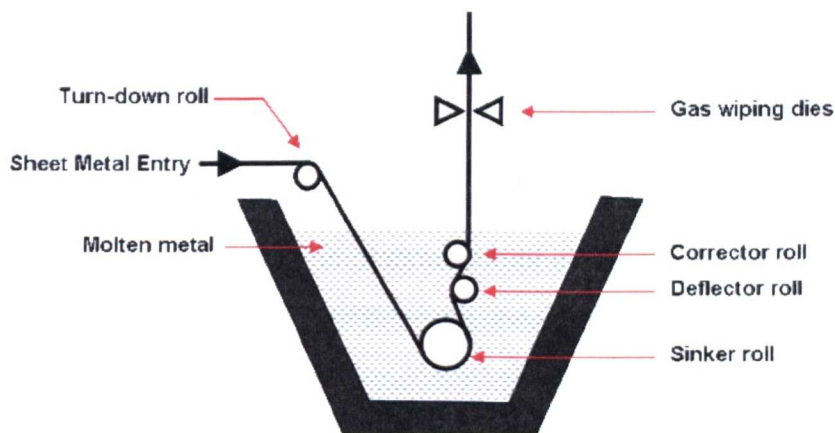
Fig. 4.2: Zinc bath in a typical continuous hot-dip galvanizing line [87].

The bath operates at a temperature of approximately 450°C ±5°C and usually contains 0.15% ±0.05% aluminium in order to prevent excessive growth of iron-zinc intermetallics at the steel-coating interface and thus ensure good adhesion of the zinc coating to the steel substrate [85]. Typical hot-dip zinc coatings are between 7-20 μm (40-140 g/m^2) and the coating thickness or weight is controlled by a low-pressure (typically 348 kPa or less) gas wiping system situated at the exit of the molten bath. The dipping process dictates that this coating method is unsuitable for production of single-side coated sheets, although different coating thicknesses can be developed on either side of the sheet using the gas wiping dies.

Physical vapour deposition (PVD) of metals is achieved by processing material in an evacuated chamber containing the vapourized coating metal and the article to be coated. The degree of vacuum required for the successful operation of the process is moderately high, being of the order of 10^{-2} to 10^{-3} N/m^2 [85]. When the coating metal enclosed in the vacuum chamber is heated, it passes into the vapour phase at a temperature considerably lower than its normal boiling point and the vapour that fills the chamber condenses to form an even, solid coating on all cooler surfaces – the work to be coated as well as the chamber walls.

Maeda et al. [88] described the installation of a continuous zinc vapour deposition line at a Japanese steel works. The line consisted of three main sections: the pre-treatment furnace, the vacuum system and the deposition chambers. The pre-treatment furnace was required to clean and activate the steel strip prior to coating

deposition. The vacuum section was a multi-stage vacuum chamber complete with vacuum sealing apparatus to generate a pressure differential from the atmosphere to the deposition chamber pressure. The deposition chamber comprised an evaporation vessel, a duct feeding the zinc vapour to the steel strip and a heated deflector roll. Electrical resistance heaters located above the vessel vapourized the molten zinc and the zinc vapour passed through a duct to deposit on one side of the steel strip that was wound around the heated deflector roll. Coating weight was controlled by the temperature of the electrical heaters and the movement of a shutter. The continuous vapour deposition line operated at line speed up to 200 m/min, with the deposition chamber achieving evaporation rates of up to 40 g/m^{2}s [88].

Both electrodeposition and hot-dipping lend themselves to high-volume, continuous production suitable for the automotive industry and are capable of producing zinc coatings of suitable thickness (7-10 μm) for vehicle body applications. Generally, hot-dip galvanized steel is the preferred material as it is produced via the cheaper process. According to Maeda et al. [88], PVD was more cost-effective than electrodeposition of zinc for production of single-sided coatings of 10–150 g/m^2 weight in Japan. Metzner et al. [89] described their high-deposition rate (up to several μm/s) PVD process in 2000 and suggested that the estimated deposition costs were "reasonable". The process descriptions given [85,88-89] indicate that PVD is a more expensive process than hot-dip galvanizing due to the multi-stage surface cleaning, the high-vacuum requirement and the significant energy inputs required to achieve high deposition rates. In addition, investment is required to develop full industrial scale continuous PVD coating lines. These factors mean that a PVD coating in the short term is likely to be significantly more expensive than conventional hot-dip galvanized coating. However, Guzman et al. [8] maintained that PVD of alloy coatings (Zn-Ti was suggested) of reduced thickness (i.e. <7 μm) could become a viable, economical alternative to hot-dip galvanized steel in the future. The authors [8] also observed that PVD is a more environmentally-friendly deposition process than conventional galvanizing because it does not generate effluent.

4.2.2. Structure of Zinc Coatings

The structure of a zinc coating depends on its application method and whether any secondary processing is undertaken. The microstructure of electrogalvanized steel (hereafter denoted EG) is single phase zinc in cross-section. The surface of the coating is characterized by crystallographic facets of the hexagonal zinc crystals and EG is somewhat more porous and rougher than automotive grade hot-dip galvanized steel.

The microstructure of hot-dip zinc coatings depends on the conditions in the bath and is also affected by the composition of the steel substrate [87]. The hot-dip galvanized steel used in this work was produced with low additions (approximately 0.15 wt.%) of aluminium to the zinc galvanizing bath to suppress the formation of iron-zinc intermetallic phases. The resultant coating, termed HDG hereafter, is largely continuous, ductile zinc but with iron-aluminium inhibition phase ($Fe_2Al_5Zn_x$) at the substrate to coating interface. Grain boundaries at the surface of the HDG coating may be enriched with aluminium, which oxidizes upon exposure to the atmosphere because aluminium in liquid zinc is not miscible with solid zinc. Zinc-iron intermetallics, described in Table 4.1, may develop in the galvanized coating if the aluminium content is not controlled precisely enough.

Table 4.1: Description of iron-zinc intermetallic phases [87,90].

Phase	Iron conc. (wt.%)	Formula	Structure	Vickers hardness
α-Fe	100	Fe(Zn)	Base centre cubic	104
Γ	25-31.5	Fe_3Zn_{10}	Hexagonal close packed	326
Γ¹	17.0-19.5	Fe_5Zn_{21}	Face centre cubic	505
δ	7.0-11.5	$FeZn_{10}$	Hexagonal close packed	358
ζ	5.0-6.0	$FeZn_{13}$	Monoclinic	208
η	<0.03	Zn(Fe)	Hexagonal close packed	52

The increased hardness of the intermetallic phases versus η-Zn and α-Fe means zinc coatings with significant levels of intermetallics are brittle and may "powder" or spall during forming operations, particularly deep-drawing. Marder [87] noted that it can be difficult to exert precise control over the aluminium content in the hot-dip bath because the aluminium exists both as a solute in the liquid zinc phase and as

intermetallic particles entrapped in the bath. It is the aluminium in solution that inhibits the zinc-iron intermetallic growth. Automotive-grade HDG is also produced from lead-free zinc and the absence of lead (and antimony) suppresses dendritic growth of zinc crystals, generating a smooth, spangle-free surface. The galvanized sheet may be temper rolled to flatten surface irregularities such as dross and grain boundaries, providing a very smooth surface for painting.

HDG may be heat-treated to generate a specific zinc-iron alloy coating, known as galvannealed steel. The exact microstructure of the galvannealed coating depends on the hot-dipping conditions and on the heat treatment parameters, but in general it comprises intermetallic zinc-iron phases with decreasing iron content from the substrate to the outer surface of the coated panel. Galvannealed steel is not suitable for deep-drawing applications due to the brittleness of the intermetallic phases, but it does offer some advantages which are discussed briefly in section 4.2.3. Zinc-aluminium alloys containing 5 wt.% or 55 wt.% aluminium are also produced by hot-dipping and these products have found widespread application in the architectural and household appliance industries. However, these materials have not to date been applied to vehicle body panels due to their unacceptable surface appearance and the hardness and brittleness of the intermetallic phases and are not considered in this work.

PVD of zinc onto a steel substrate generates a similar coating microstructure to that of EG [92], comprising a uniform hexagonal crystal structure with a well-defined zinc to substrate boundary. Alloy coatings can also be produced by PVD, either by co-deposition of two metal vapours from separate crucibles [13] or adding a PVD step to the end of a galvanizing line [93]. Alloys that have been investigated include zinc-iron, zinc-nickel, zinc-aluminium, zinc-magnesium (ZMG), zinc-titanium and zinc-manganese. However, it is ZMG that has been selected for commercialization for the automotive industry by steel producers due to reports of ZMG's corrosion benefits and compatibility with existing production processes and therefore ZMG is investigated in this work.

4.2.3. Properties of Zinc Coatings

Pure zinc coatings produced by electrogalvanizing, PVD or hot-dip galvanizing with aluminium additions, offer corrosion protection, good formability and class 1 (highest quality) surface appearance to the steel substrate. The corrosion resistance of zinc coatings is discussed in detail in Section 4.3 and other properties of the zinc coated versus non-coated steel that must be considered in vehicle assembly (forming, joining and painting characteristics) are discussed in the following paragraphs.

When iron-zinc intermetallics are present in a galvanized steel, (e.g. galvannealed steel), the material has a harder coating compared to pure zinc coatings, limiting the drawability. Powdering occurs when hard particles from the coating are abraded from the sheet surface. The rough surface of galvannealed coatings also tend to absorb the lubricating oil, leading to dry patches on the sheet surface and reduced control of the stamping operation and possibly splitting of the formed panel. Conversely, the presence of hard intermetallics may offer some advantage in clinched flange strength. Mataigne [91] reported that clinched flanges constructed from galvannealed steel exhibited increased mechanical strength under shear loading because coating particles were detached during deformation and were trapped between the assembled sheets, anchoring the flowing steel under shear stress. Furthermore, galvannealed coatings offer greater abrasion resistance to the assembled vehicle compared to soft zinc coatings [94] offering an advantage in stone chip resistance versus soft zinc coatings. Mataigne [91] cautioned that the weakest interface in the galvannealed coating was between the substrate and the coating; if the galvannealed coating was chipped from the surface, bare steel would be exposed directly to the environment.

Zinc-coated steel interferes with the spot welding process because some of the zinc melted by the spot welder electrode alloys with the electrode copper tip to form brass. The brass is brittle and breaks when the spot welder tip is withdrawn, causing an increase in the active surface of the electrode. This increased surface requires increased current to ensure consistent current density during body assembly. This challenge is overcome by dressing the weld tips at regular intervals

during spot welding of galvanized steel panels. Brass formation is less problematic when welding galvannealed steel compared to EG and HDG because the zinc is already alloyed to iron within the coating, therefore the zinc is less active for brass formation.

EG and HDG are not optimized for paint adhesion because their surfaces are smooth. A galvannealed steel surface has a natural micro-roughness that allows excellent paint adhesion. Rough surfaces are induced on EG and HDG in the phosphate stage of the paint treatment. Aluminium oxides on the surface of HDG must be removed as far as possible prior to phosphating and this is achieved by an alkaline rinse. Hydrofluoric acid added to the phosphate bath removes any remaining aluminium. The phosphated surface allows good adhesion of the electrodeposited paint.

Pin-holing or cratering during e-coat deposition is a problem associated with galvannealed steel, but not with EG or HDG. Hydrogen is evolved during electrolytic paint deposition and under normal circumstances it escapes through the uncured paint layer. If hydrogen evolution occurs suddenly and rapidly at some locations on the vehicle surface compared to others, a pocket of hydrogen may become trapped in the paint layer, impeding additional paint deposition. The gas pockets burst during e-coat curing leading to holes in the cured paint layer known as pin-holes or craters. Increased hydrogen evolution at discrete points on the surface can occur in galvannealed steel due to coupling of different zinc-iron intermetallic phases in contact with the paint. The homogeneous zinc coatings produced by EG or HDG have uniform electrochemical properties at the surface and do not suffer from pin-holing.

Zinc coating type is selected by considering its overall suitability in terms of its properties for the specific application in mind and the cost of the material. Generally, and as reported by [91], HDG is the most popular choice, giving a range of properties that are either inherently compatible with current manufacturing processes or that have resulted in changes to manufacturing processes to ensure compatibility, whilst retaining a low material cost. Cost should not only be

considered in terms of the coated material cost, but should also consider the overall cost to the vehicle due to use of one particular material versus another. For example, although ZMG is likely to cost more than HDG, it may offer the opportunity to reduce or eliminate secondary corrosion measures such as sealer or wax applications. Metzner et al. [94] and Schuhmacher et al. [93,95] maintained that in future, greater flexibility, a wider range of alloys and reduced thickness of coatings will be demanded and PVD coatings will increasingly find application.

4.3. ZINC CORROSION

A wealth of zinc corrosion rate data is available in the literature, as discussed in Chapter 3. The corrosion rate of zinc depends on the corrosion environment, as shown in Fig. 4.3 [89].
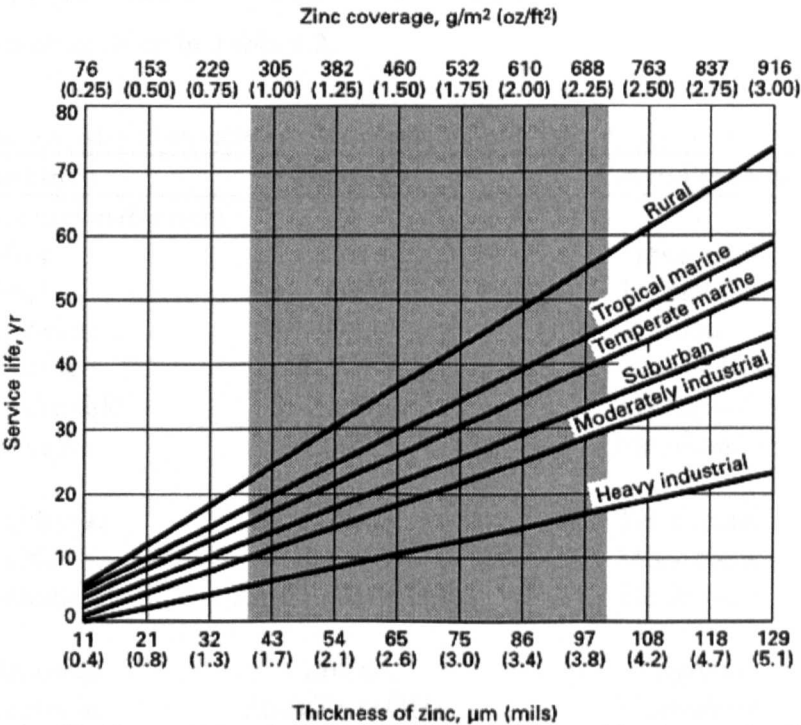
Fig. 4.3: Service life (time to 5% rusting of steel) versus thickness of the zinc coating for various atmospheres [89].

Fig. 4.3 also shows that the corrosion resistance of zinc increases linearly with the thickness of the zinc coating. A similar relationship was reported by Ström et al. [70] on scribed zinc-coated test panels exposed to the atmosphere and this observation was attributed to the constant rate of anodic consumption of exposed

zinc. The corrosion products formed in a given environment may be protective or non-protective in nature. Protective corrosion products serve to extend the service life of the zinc coating, and thus the service life of the coated product. Determination of the corrosion products formed in different environments therefore gives information about the expected service life. Analysis of the corrosion products also allows speculation of the corrosion mechanisms at work. Such an approach has been adopted by many researchers on zinc and other metals, and is used in this work for ZMG corrosion resistance. Development of the ZMG corrosion mechanism requires an understanding of the corrosion mechanism of zinc in various environments, which is discussed in the following sections.

4.3.1. Corrosion Products Formed on Zinc

Graedel [96] published a list of minerals that may be relevant to zinc corrosion, an extract of which is given in Table 4.2.

Table 4.2: Zinc minerals and crystalline substance possibly relevant to the corrosion of zinc [96].

Substance	Formula	Crystal system
Metal, oxides and hydroxides		
Zinc	Zn	Hexagonal
Zincite	ZnO	Hexagonal
Zinc oxide	ZnO	Cubic
Sweetite	$Zn(OH)_2$	Tetrahedral
Zinc hydroxide	$\beta\text{-}Zn(OH)_2$	Hexagonal
Wulfingite	$\varepsilon\text{-}Zn(OH)_2$	Orthorhombic
Chlorides		
Zinc chloride	$\alpha\text{-}ZnCl_2$	Tetrahedral
Zinc chloride	$\beta\text{-}ZnCl_2$	Monoclinic
Simonkolleite	$Zn_5Cl_2(OH)_8.H_2O$	Hexagonal
Carbonates		
Smithsonite	$ZnCO_3$	Trigonal
Hydrozincite	$Zn_5(CO_3)_2(OH)_6$	Monoclinic
Sulfates, sulfites and nitrates		
Zinkosite	$ZnSO_4$	Orthorhombic
Gunningite	$ZnSO_4.H_2O$	Monoclinic
Bianchite	$ZnSO_4.6H_2O$	Monoclinic
Basic zinc sulfate	$Zn_4SO_4(OH)_6$	
Zinc sulfite	$ZnSO_3$	
Zinc sulfite hydrate	$ZnSO_3.2H_2O$	Monoclinic
Zinc nitrate	$Zn(NO_3)_2$	

Naturally-occurring substances may be thermodynamically favoured in zinc corrosion in certain environments. Odnevall and Leygraf [97] compiled a table of detected zinc corrosion products reported in the literature up to 1994. Further studies have been conducted since that time and Table 4.3 is an updated list of corrosion products detected on zinc exposed in the atmosphere and in laboratory tests. The corrosion reactions and mechanisms involved are discussed in the following sections.

Table 4.3: Corrosion products detected on zinc following outdoor and laboratory exposures [32,97-115].

Corrosion product	Type of atmosphere			laboratory
	rural	urban	marine	
ZnO	[103,104,107]	[107,113]	[103-106, 108,113]	[98-100, 114,115]
ε-Zn(OH)$_2$	[97]	[97]	[97]	
Zn(OH)$_2$.nH$_2$O		[106]		
ZnCO$_3$			[105]	
Zn$_5$(CO$_3$)$_2$ (OH)$_6$	[32,103,104, 107,110, 111]	[32,106, 107,111]	[103,104, 106,108]	[98-100,102]
Zn$_4$CO$_3$(OH)$_6$.H$_2$O		[107]	[105,108]	[98,99,102, 112]
Zn$_5$Cl$_2$(OH)$_8$.H$_2$O		[113]	[103-106, 108,111,113]	[99,100,102, 112, 114,115]
ZnSO$_4$.nH$_2$O			[105]	
Zn$_4$(OH)$_6$SO$_4$.nH$_2$O	[110,111]	[106,111]	[103,104,106]	[98,102,114, 115]
Zn$_3$O(SO$_4$)$_2$			[103,104]	
NaZn$_4$Cl(OH)$_6$SO$_4$.6H$_2$O		[106,113]	[101,103,104, 106,109,111,113]	[115]
Zn$_4$Cl$_2$(OH)$_4$SO$_4$.5H$_2$O	[109]	[109]	[101,106]	
Zn(OH)$_8$(NO$_3$)$_2$				[102]
Zn$_5$(OH)$_8$NO$_3$.2H$_2$O				[102]

4.3.2. Aqueous Zinc Corrosion

Corrosion of zinc begins with the oxidation of zinc at anodic sites (4.1).

$$Zn(s) \rightarrow Zn^{2+}(aq) + 2e^- \qquad (4.1)$$

Zinc oxidation is balanced by a reduction reaction at cathodic sites; in aqueous corrosion environments, this is typically the reduction of dissolved oxygen (4.2).

$$\tfrac{1}{2}O_2(aq) + H_2O(aq) + 2e^- \rightarrow 2OH^-(aq) \qquad (4.2)$$
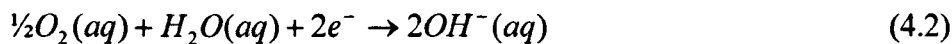
It can be expected that the zinc cation and hydroxide anion react to produce zinc hydroxide or zinc oxide. The overall reaction is given by (4.3).

$$Zn(s) + \tfrac{1}{2}O_2(aq) + H_2O(aq) \rightarrow Zn(OH)_2(am) \rightarrow ZnO(s) + H_2O(aq) \qquad (4.3)$$

Feitknecht [116] expanded upon the transformation of zinc to the hydroxide or oxides species and reported that the initial zinc hydroxide formed was amorphous and it changed on ageing either to an active form of oxide (as shown in (4.3)) or to a crystalline form of zinc hydroxide. Several authors have reported the presence of zinc oxide on corroded zinc (see Table 4.3) but, of the hydroxides, only wulfingite (ε-Zn(OH)$_2$), the only known naturally-occurring form of zinc hydroxide, has been reported [96-97]. Both zinc hydroxide and zinc oxide can precipitate from slightly acidic to alkaline conditions ($pH \approx 7-9$ [115]) and they may co-exist on the corroding zinc.

If very alkaline conditions developed ($pH > 14$ [118-119]) due to very active cathodic activity, zincate ions, $Zn(OH)_4^{2-}$, may form according to (4.4).

$$ZnO(s) + 2OH^-(aq) + H_2O(aq) \leftrightarrow Zn(OH)_4^{2-}(aq) \qquad (4.4)$$
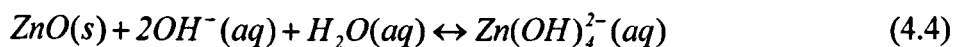
If such alkaline conditions developed, zincate may play some role in keeping the zinc surface accessible for further oxygen reduction, thereby perpetuating corrosion. Zinc oxide is crystalline and therefore could be expected to passivate the corroding surface where it forms, but it is also a semi-conducting oxide [96] and may itself be

sufficient catalyst for oxygen reduction by allowing electron conductivity [99,106,113]. In reality, a mixture of amorphous and crystalline zinc oxides and hydroxides is likely to co-exist on the corroding surface.

4.3.3. Zinc Corrosion in a Sodium Chloride Environment

In the presence of sodium chloride, chloride ions (Cl^-) migrate to anodic sites [98] where simonkolleite is formed according to (4.5), as described by Falk et al. [120].

$$5ZnO(s) + 2Cl^-(aq) + 6H_2O(aq) \leftrightarrow Zn_5(OH)_8Cl_2.H_2O(s) + 2OH^-(aq) \quad (4.5)$$
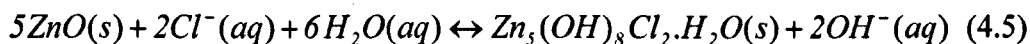
Reaction (4.5) shows that formation of simonkolleite releases hydroxide ions. The pH over the corroding surface may therefore be rather alkaline due to the formation of OH^- and the presence of Na^+, which react at cathodic sites to form sodium carbonate or sodium bicarbonate. Simonkolleite is not stable under alkaline conditions (requires pH range 6–8) [114,116]; the alkalinity associated with simonkolleite formation must be either neutralized or produced remotely from the simonkolleite. For example, alkalinity produced by simonkolleite formation at anodes can be neutralized by cathodic activity according to (4.4).

Increased alkalinity promotes cathodic activity. If the surface environment becomes too alkaline, simonkolleite breaks down and reaction (4.5) is displaced to the left. Released chloride ions would increase electrolyte conductivity and promote further corrosion. This hypothesis is illustrated by the stability diagram based on the report by Feitknecht [116] shown in Fig. 4.4.
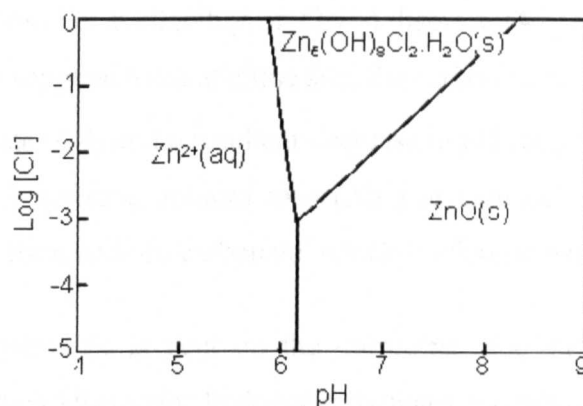
Fig. 4.4: Stability diagram of simonkolleite in aerated aqueous solutions with varying pH values and with concentration of zinc ionic species ($[Zn^{2+}]$) of 0.1M at 25°C [99,114,116,120].

Air-borne or sprayed sodium chloride particles deposit randomly on a zinc surface and their deliquescent nature enables rapid formation of a surface electrolyte and corrosion initiation. Corrosion does not progress uniformly over the zinc surface, but countless electrochemical cells are established on the corroding surface [114,115]. Formation of both simonkolleite and zinc oxide on a single test panel indicates separation of anodes and cathodes and significant variation in surface electrolyte pH [121]. Variation of pH level from 5.5 to 11.5 on the surface of a corroding steel-zinc couple was reported by Tada et al. [122]. This finding points to the heterogeneous nature of the corrosion mechanism on zinc in a sodium chloride-containing atmosphere. As corrosion progresses, zinc dissolution continues at the anode, leading to localized pitting attack.

4.3.4. The Role of Carbon Dioxide

The term "carbonatization" is used to describe the absorption of atmospheric carbon dioxide into the surface electrolyte, which progresses according to (4.6)-(4.8) [98,123].

$$CO_2(g) \leftrightarrow CO_2(aq) \tag{4.6}$$

$$CO_2(aq) + 2OH^-(aq) \leftrightarrow CO_3^{2-}(aq) + H_2O(aq) \tag{4.7}$$

$$CO_2(aq) + CO_3^{2-}(aq) + OH^-(aq) \leftrightarrow 2HCO_3^-(aq) \tag{4.8}$$
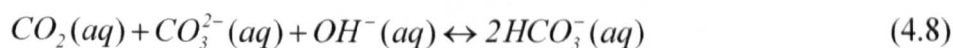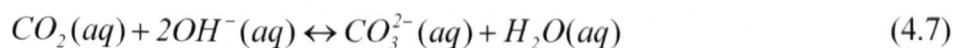
Alkaline conditions (i.e. availability of OH^-) displace (4.7) to the right. As more carbon dioxide is supplied to an alkaline site, the carbonate reacts further to produce hydrogen carbonate (4.8) and a resultant decrease in pH (consumption of OH^-). If sodium chloride is present, sodium ions (Na^+) at cathodic areas also react with carbonate ions to form sodium carbonate, which is alkaline but not hygroscopic.

Zinc oxide or hydroxide present on the corroding zinc surface may react with hydrogen carbonate to form zinc hydroxy carbonates according to (4.9)–(4.10).

$$4ZnO(s) + 2HCO_3^-(aq) + 3H_2O \leftrightarrow Zn_4CO_3(OH)_6.H_2O(s) + CO_3^{2-}(aq) \quad (4.9)$$

$$5ZnO(s) + 4HCO_3^{2-}(aq) + H_2O \leftrightarrow Zn_5(CO_3)_2(OH)_6(s) + 2CO_3^{2-}(aq) \quad (4.10)$$
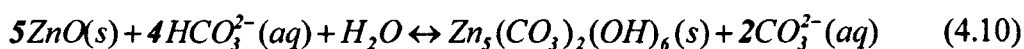
The resultant carbonate ions may react further with atmospheric carbon dioxide according to (4.8). The key action of (4.6)–(4.10) is the reduction of alkalinity at cathodes by carbonatization. Reduced pH levels allow the formation of the stable zinc carbonates and simonkolleite, thereby retarding the overall corrosion mechanism. In effect, the formation of zinc hydroxy carbonate and of hydrozincite may be considered an intermediate and necessary step for the formation of stable simonkolleite. Diminution of zinc corrosion by a factor of three to five in the presence of carbon dioxide was reported by Falk et al. [120]. Tests using constant spraying or immersion (high time of wetness, TOW) prevent effective carbonatization on the corroding surface and result in more rapid zinc corrosion. Fig. 4.5 shows the stability domain of simonkolleite and hydrozincite [123].
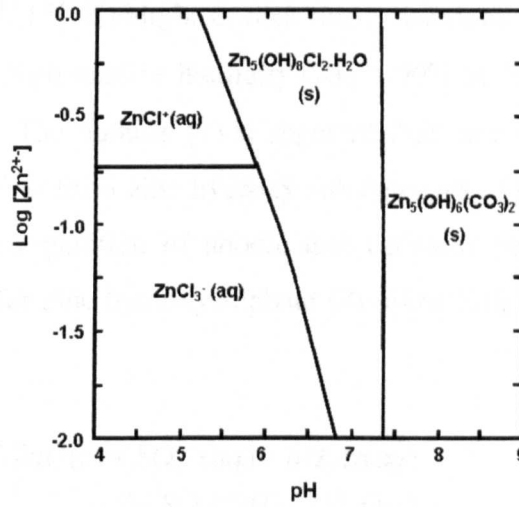
Fig. 4.5: Stability diagram for 1.3M Cl^- at 25°C and atmospheric concentration of CO_2 (g) (log P_{CO_2} = -3.5) [123].

Simonkolleite and hydrozincite are sparingly soluble corrosion products and therefore form a protective barrier against corrosion. Accordingly, formation of these corrosion products over a large portion of the corroding surface implies enhanced service life of a product compared to one where formation of large quantities of zinc oxide is favoured.

4.3.5. Effects of Sulphates and Nitrates on Zinc Corrosion

The effects of sulphates and nitrates on the corrosion of zinc have been studied in the literature [102,111,114,115,122]. Corrosive attack of zinc in humid air in the presence of sulphur dioxide (SO_2) progresses according to (4.11)-(4.14) [115].

$$SO_2(g) \leftrightarrow SO_2(aq) \tag{4.11}$$

$$SO_2(aq) + H_2O(aq) \leftrightarrow HSO_3^-(aq) + H^+(aq) \tag{4.12}$$

$$HSO_3^-(aq) + \frac{1}{2}O_2(g) \rightarrow SO_4^{2-}(aq) + H^+(aq) \tag{4.13}$$

$$SO_4^{2-}(aq) + ZnO(s) + 2H^+ \rightarrow ZnSO_4(aq) + H_2O(aq) \tag{4.14}$$
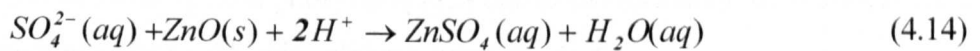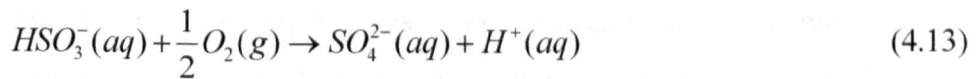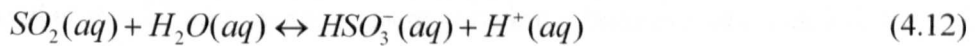
Svensson et al. [115] highlighted that these reactions can only take place in atmospheres with high relative humidity (RH > 90% at 20°C), when $ZnSO_4$ forms aqueous species. The authors [115] reported that zinc ions (Zn^{2+}) migrating to cathodic sites tend to form zinc hydroxy sulphates, (4.15), impeding the evolution of a macroscopic separation of anodic and cathodic sites. Fig. 4.6 shows the stability diagram for zinc hydroxysulphate ($Zn_4SO_4(OH)_6$, abbreviated ZHS) taken from [123].

$$Zn^{2+}(aq) + 3ZnO(s) + SO_4^{2-}(aq) + 6H_2O(aq)$$
$$\rightarrow Zn_4SO_4(OH)_6.3H_2O(s)$$

(4.15)
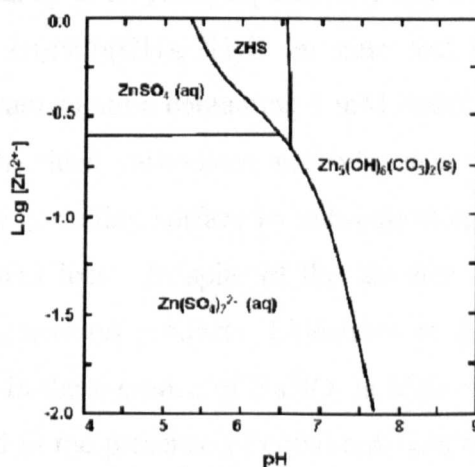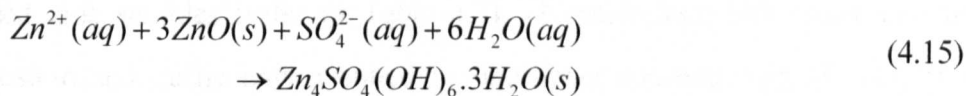
Fig. 4.6: Stability diagram with 0.5M SO_4^{2-} at 25°C and atmospheric concentration of $CO_2(g)$ (log P_{CO2} = -3.5) (ZHS = $Zn_4(OH)_6SO_4.H_2O$) [123].

If NaCl as well as SO_2 were present, however, the acidification of the electrolyte by sulphur dioxide dissolution (reaction (4.12)) may lead to instability of the protective corrosion product simonkolleite. Qu et al. [114] reported increased initial corrosion rate of zinc in a laboratory atmosphere containing both SO_2 and NaCl compared to the corrosion rate of zinc in NaCl or SO_2 alone. In the longer term and in environments with relatively low SO_2 concentration compared to NaCl concentration, (as likely to be found in natural environments), reduced corrosion rate was observed by both [114] and [115] due to the formation of sparingly soluble sodium zinc hydroxychloride sulphate, reaction (4.16).

$$3ZnO(s) + Zn^{2+}(aq) + SO_4^{2-}(aq) + Na^+(aq) + Cl^-(aq) + 9H_2O(aq)$$
$$\rightarrow ZnSO_4 3Zn(OH)_2 NaCl.6H_2O(s)$$
$$(4.16)$$
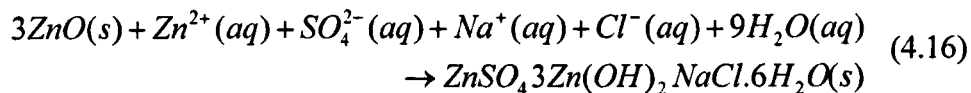
The solid product formed by (4.16) also requires precipitation of both Na^+ and Cl^-, the two main current-carrying ions in the system, thereby reducing the overall conductivity of the electrolyte.

Nitrate-containing zinc corrosion products have not been reported for naturally-exposed zinc samples (refer to Table 4.3). Nevertheless, NO_x emissions from combustion and traffic have resulted in significant concentration of NO_3^- in the atmosphere [112]. Mahdy et al. [102] reported the formation of basic zinc nitrates $Zn(NO_3)_2(OH)_8$ and $Zn_5NO_3(OH)_8.2H_2O$ on zinc test samples exposed in the laboratory to an acid rain solution containing 1 mM NaNO$_3$. Unlike the equivalent basic zinc hydroxy chlorides, carbonates and sulphates, the zinc hydroxy nitrates were washed from the corroding surface by subsequent spraying intervals, leading to continuous zinc mass loss. In spite of the absence of barrier protection via precipitation of sold corrosion products, Lindström et al. [112] showed that the corrosion rate of zinc in the presence of NaNO$_3$ at high relative humidity was one third of that registered in the presence of equal amounts of NaCl or Na$_2$SO$_4$. The authors [112] suggested that reduction of zinc corrosion was achieved by the reduction of nitrate by zinc, which led to increased pH in the surface electrolyte, as shown by (4.17)-(4.18).

$$Zn(s) + NO_3^-(aq) + H_2O(aq) \rightarrow Zn(OH)_2(s) + NO_2^-(aq) \qquad (4.17)$$

$$Zn(s) + 2NO_2^-(aq) + 2H_2O(aq)$$
$$\rightarrow Zn(OH)_2(s) + NO_2(g) + 2OH^-(aq) \qquad (4.18)$$
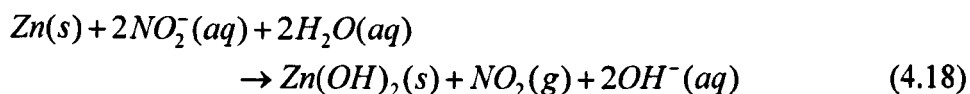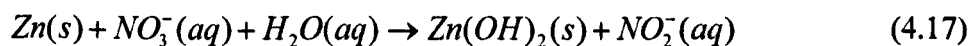
Stabilization of the pH at neutral to slightly alkaline levels allowed the precipitation of protective hydrozincite according to (4.9)-(4.10) and a resultant passivation of the zinc surface, as illustrated by Fig. 4.7 [112].
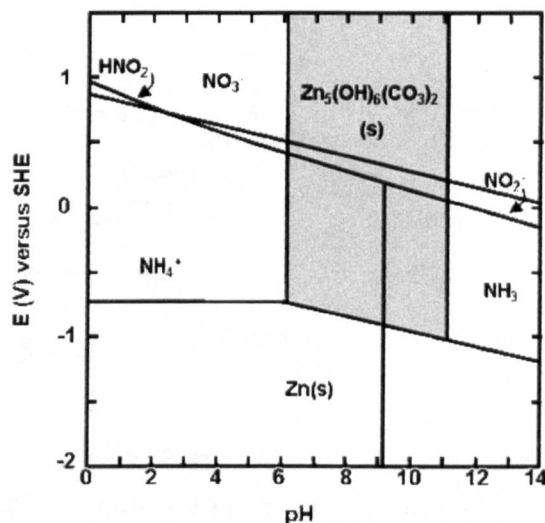
Fig. 4.7: Stability diagram for nitrate at 25°C and concentration of NO_3^- = 100 mM and for zinc metal (Zn(s)) and hydrozincite at atmospheric CO_2 pressure (concentration Zn^{2+} = 100 mM) [112].

In their previous study, Lindstrom et al. [123] reported the dependence of zinc corrosion on the concentration of Na^+ cations rather than on Cl^- or SO_4^{2-} anions and demonstrated an approximately linear relationship between sodium ion concentration and zinc corrosion rates in both NaCl and Na_2SO_4 environments. This relationship did not hold however for NaNO$_3$ tests [112]. It is clear then that the zinc corrosion products formed and the zinc corrosion rate depend on all the chemical species available during the corrosion reactions and the corrosion mechanism must incorporate these interactions. Fig. 4.8 illustrates the atmospheric corrosion sequences on zinc panels in different environments [97].

$$Zn(OH)_2$$

$$\downarrow$$

Cl⁻ > SO₄²⁻ $Cl^- > SO_4^{2-}$ Cl⁻ < SO₄²⁻ $Cl^- < SO_4^{2-}$

$$Zn_5(OH)_6(CO_3)_2$$

Marine / Urban / Industrial   Rural / Urban / Industrial

$$Zn_5(OH)_8Cl_2 \cdot H_2O \qquad\qquad Zn_4SO_4(OH)_6 \cdot nH_2O$$

Marine   Urban Industrial   Urban Industrial

$$NaZn_4Cl(OH)_6SO_4 \cdot 6H_2O \qquad Zn_4Cl_2(OH)_4SO_4 \cdot 5H_2O$$
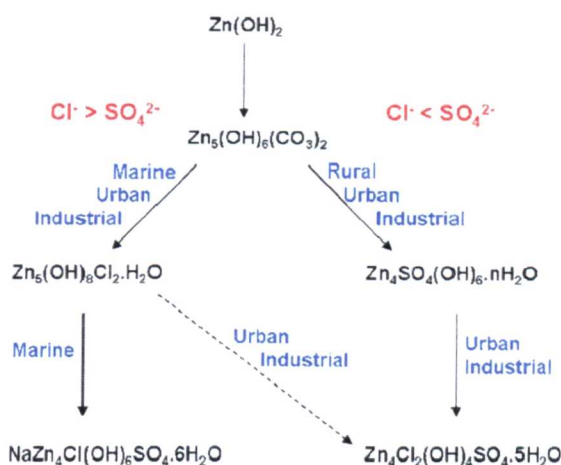
Fig. 4.8: Atmospheric corrosion of zinc in environments with *left* relatively high chloride concentration and *right* relatively high sulphate concentration [97].

4.3.6. Influences of Temperature and pH

Generally, increased temperature is assumed to increase reaction rates. For this reason many accelerated corrosion tests are performed at temperatures greater than 25°C even for simulated atmospheric regimes, (e.g. Ford APG test is performed at 50°C). However, Svensson et al. [124] showed that the corrosion rate of zinc in a SO_2-based environment increased as the temperature reduced. This was due to both increased deposition rates of SO_2 and the reduced rate of the reaction that formed protective zinc hydroxy sulphate (reaction (4.15)) at 4°C compared to 22°C and 30°C. Lindström et al. [99] reported increased zinc corrosion rate with increased temperature in a NaCl-based environment, but only in the absence of carbon dioxide. The increased corrosion rate was due to increased rate of zinc dissolution at anodic sites leading to greater pitting at higher temperatures (38°C and 22°C versus 4°C). Mahdy et al. [102] also reported increased zinc dissolution rates at higher temperature (approximately 40°C versus 20°C).

The corrosion rate of zinc was no longer dependent on temperature in the presence of CO_2 [99]. This was due to the compensation of increased NaCl-induced corrosion rate by the increased rate of zinc hydroxy carbonate formation (reactions (4.9)-(4.10)), the stabilization of pH by carbonatization and increased precipitation of simonkolleite at higher temperatures. The net effect was that the atmospheric corrosion of zinc in the presence of both NaCl and CO_2 was approximately independent of temperature. Mahdy et al. [102] cautioned that the morphology of

the corrosion product formed depends on the drying rate; increased electrolyte evaporation rates may be expected at higher test temperatures, potentially leading to cracking and porosity of the corrosion products, reducing their protective power. He et al. [111] also noted this effect and reported that longer dry periods and increased drying intervals allow increased dry deposition of corrodents in the corrosion product layer, increasing the solubility and reducing the adherence of the corrosion products.

Most corrosion studies described in the preceding sections were carried out in approximately neutral solutions. Magaino et al. [125] reported a step increase in zinc corrosion rate as the electrolyte (artificial acid rain solution) pH decreased to 3. He et al. [111] also reported increased zinc metal loss as pH of the acid rain solution decreased from 4.8 to 3.8, although their experiments were not conducted at *pH < 3.8*.

The literature reports show that the corrosion rate or dissolution rate of zinc depends on the nature of the corrosion products formed; i.e. long-term corrosion protection offered by zinc to the steel substrate is achieved via precipitation of solid corrosion products. The type and nature of the corrosion products precipitated on the corroding zinc surface depend on the chemical species available and their relative concentration. Thermodynamic stability diagrams presented in the literature allow speculation of the likely corrosion products in a given environment. Published reports of the production, structure and corrosion resistance of zinc-magnesium alloy coated steel (ZMG) are reviewed in the following section.

4.4. ZINC-MAGNESIUM COATED STEEL (ZMG)

ZMG is an emerging material for the automotive industry, not available at the time of writing as a commercial material from any steel supplier. Nevertheless, ZMG in some form or another has been considered for architectural and automotive applications, pioneered apparently by Japanese steel suppliers in the early 1990s, and reports of its production, structure and corrosion resistance do exist in the literature.

4.4.1. Production and Structure of ZMG

The coating structure of ZMG depends on the coating process used and the term ZMG may be applied to a rather broad family of magnesium-containing zinc coatings. One common property unites the ZMG variants described in the literature, namely enhanced corrosion resistance due to the presence of magnesium [13,93,14-17,83]. Kawafuku et al. [13] prepared ZMG by electron beam assisted physical vapour deposition (PVD) of zinc and magnesium on to a steel substrate. Co-deposition of zinc and magnesium generated a 90 wt.% zinc-10 wt.% magnesium alloy coating and no further processing steps were performed following deposition. X-ray diffraction (XRD) analysis showed that the coating consisted of intermetallic phases Zn_2Mg and $Zn_{11}Mg_2$ as well as η-Zn.

Morishita et al. [14-16] adopted a two-step coating process to produce ZMG; electrogalvanized steel was produced as a first step, then magnesium was electrodeposited onto the electrogalvanized steel. Thermal treatment (10 hours at 300°C) was required to achieve diffusion of magnesium into the zinc coating. Intermetallic phases Zn_2Mg and $Zn_{11}Mg_2$ were detected by XRD analysis of the heat-treated coating. Analysis of the coating cross-section revealed three diffusion zones within the coating: 7-13 wt.% magnesium at the outer layer of the coating corresponding to the Zn_2Mg phase; 2-7 wt.% magnesium at the inner layer corresponding to the $Zn_{11}Mg_2$ phase and a zinc-iron intermetallic phase Γ' (Fe_5Zn_{21} [87]) at the interface between the steel substrate and the coating.

Combining conventional galvanizing with PVD to produce ZMG was described by Schuhmacher et al. [93]. Use of electron beam evaporation or thermal jet vapour deposition enabled deposition rates up to several microns per second. Details of a pilot line to over-coat galvanized steel with thin PVD coatings achieving line speeds up to 60 m/min were presented. Short-term thermal alloying (in the temperature range 250°C-400°C) of the coating post-PVD was suggested to allow inter-diffusion of the zinc and the vapour-deposited metal. Although this production method did not achieve the high line speed (up to 200 m/min. [87]) of modern continuous hot-dip coating lines, the potential of PVD as a future production method for the next generation of metallic coatings was demonstrated. Production of ZMG by hot-

dipping can be achieved via the addition of aluminium to the molten metal pot to avoid dross formation [17,83]. Tsujimura et al. [17] produced hot-dipped coatings with varying aluminium and magnesium content. Zinc-6 wt.% aluminium-3 wt.% magnesium coating was analysed in detail and was proposed as the optimized coating structure for corrosion resistance.

4.4.2. Corrosion Testing of ZMG

Spray testing using 5 wt.% sodium chloride solution has been used to compare corrosion resistance of ZMG to conventional galvanized steel [13,14-16]. Kawafuku et al. [13] reported approximately 960 hours to red rust initiation on ZMG compared to 40 hours to red rust initiation on EG. The 24-fold improvement in corrosion resistance is even more remarkable because the coating weight of the ZMG coating was 20 g/m^2 whilst that of the EG coating was 40 g/m^2. Morishita et al. [14-16] reported a 10-fold increase in the time to red rust initiation for ZMG versus similar EG in a 5 wt.% salt spray test at 35°C. Immersion of ZMG in a 5 wt.% salt solution at room temperature produced rust after 41 days whereas a similar EG material produced red rust after 10 days [14]. Even after initiation of red rust on ZMG, corrosion progressed rather slowly; the area of red rust did not expand for a further 21 days of immersion in the salt solution.

Schuhmacher et al. [93] again reported superior corrosion resistance of ZMG versus pure zinc coatings in an automotive cyclic corrosion test. Similarly, Tsujimura et al. [17] reported increased corrosion resistance of zinc-aluminium coated steel with addition of magnesium in a cyclic corrosion test. Each test cycle consisted of 2 hours of spraying with 5 wt.% salt solution followed by 4 hours of drying and finally 2 hours of humidity. Corrosion resistance was quantified by recording the number of test cycles to cover 5% of the test panel area with red rust. Addition of 3 wt.% magnesium to the coating resulted in approximately a 10-fold increase in the number of test cycles to significant red rust.

A range of electrochemical tests on samples of pure zinc, iron and Zn_2Mg (the intermetallic usually present in ZMG) was performed by Hausbrand et al. [83]. Similar electrochemical behaviour was observed for the zinc and the zinc-

magnesium intermetallic when samples were immersed in a chloride-containing electrolyte. Immersion of the materials in buffer solution at pH 7.7 allowed measurement of the free corrosion potential. The free corrosion potential for the zinc-magnesium intermetallic was about 10 mV more negative than that of zinc and the corrosion current calculated by the Tafel method was found to be approximately 3×10^{-6} A/cm^2 for both zinc and Zn$_2$Mg. The similar electrochemical behaviour observed for the two materials suggests that the enhanced corrosion resistance of ZMG is not related to galvanic effects.

Several researchers have demonstrated enhanced corrosion resistance of zinc in an electrolyte containing magnesium chloride, MgCl$_2$ [83,123,126]. Hausbrand et al. [83] added magnesium chloride to a salt solution in the proportion 0.1 mol/litre MgCl$_2$ in 0.3 mol/litre NaCl and immersion of galvanized steel sheet in the magnesium-containing salt solution at 40°C generated almost no corrosion on the material surface after 4 days. Immersion of galvanized steel in 0.5 mol/litre NaCl solution without magnesium under the same conditions resulted in "severe" corrosive attack. This implies that corrosion of zinc was retarded due to the presence of magnesium in the sodium chloride-based environment. Lindström et al. [123] and Prosek et al. [126] assessed the corrosion resistance of zinc treated with magnesium chloride alone (i.e. without NaCl) and both reported increased corrosion resistance in MgCl$_2$ compared to NaCl-treated samples; Prosek et al. [126] quantified the increased corrosion resistance at 9-times that of zinc treated with NaCl.

4.4.3. Role of Magnesium in Corrosion Resistance of Zinc Alloy Coatings

Although there is general consensus that ZMG exhibits increased corrosion resistance compared to pure zinc coatings in a sodium chloride-based environment and that zinc corrosion by sodium chloride solutions is reduced when magnesium ions are also present, it is not clear how this improved corrosion resistance is achieved. Kawafuku et al. [13] proposed that the superior corrosion resistance of ZMG may be due to two factors: the formation of a dense, adherent layer of simonkolleite (Zn$_5$(OH)$_8$Cl$_2$.H$_2$O, see Table 4.3) on the surface of the test panel and the persistence of galvanic protection by the ZMG coating during corrosion.

Simonkolleite was detected in the corroded EG samples in conjunction with zinc oxide (ZnO) and the authors [13] suggested that the superior corrosion resistance of ZMG was due to the formation of simonkolleite alone, i.e. without zinc oxide. This observation is significant because the absence of zinc oxide suggests that magnesium ions altered the normal course of zinc corrosion in a sodium chloride-based environment. Further exploration is required to account for this observation.

Measurements of corrosion potential before and during the salt spray test showed that the ZMG coating maintained its initial corrosion potential (approximately -1.1 V versus saturated calomel electrode (SCE)) even after 500 hours of salt spray, whereas the corrosion potential of EG increased rapidly from the initial value of -1.1 V versus SCE to approximately -0.8 V versus SCE. Endurance of its initial corrosion potential shows that the ZMG substrate was protected against corrosion up to 500 hours of salt spraying.

XRD analysis of ZMG samples dipped in 5 wt.% NaCl aqueous solution showed rapid formation of magnesium oxide, MgO, on the test panel surface [16]. Zinc oxide, zinc hydroxide and simonkolleite were also observed on these test panels. Immersion testing was also performed on a sample of magnesium that had been machined from a billet. After 5 days of immersion, magnesium hydroxide ($Mg(OH)_2$) was detected on the magnesium surface. The authors reported that the magnesium hydroxide was non-protective, being powder-like in form, and proposed that the corrosion resistance of ZMG was related to the formation of the oxide rather than hydroxide of magnesium. In this case it was the morphology rather than the species of the corrosion product that was highlighted as the key corrosion protection mechanism because magnesium hydroxide in crystalline form would be expected to offer protection to the corroding surface.

Tsujimura et al. [17] used XRD to identify corrosion products on samples after 20 test cycles (as described in Section 4.4.2) and reported simonkolleite as the only corrosion product on Zn-6 wt.% Al -3 wt.% Mg coated steel. Zinc oxide and zinc hydroxy carbonate ($Zn_4CO_3(OH)_6.H_2O$) as well as simonkolleite were detected on steel test panels coated with Zn-4.5 wt.% Al-0.1 wt.% Mg after 20 test cycles,

although simonkolleite alone was detected at 10 cycles. The authors proposed that magnesium enhanced the corrosion resistance by the formation of magnesium-containing simonkolleite. Prosek et al. [126] also suggested the formation of magnesium-containing simonkolleite, with chemical formula $Zn_4Mg(OH)_8Cl_2.H_2O$, i.e. substitution of one Zn^{2+} for one Mg^{2+}, but this product has not yet been characterized. A synergistic effect between zinc and aluminium corrosion was realised in the zinc-aluminium-magnesium coating by the formation of stable zinc aluminium carbonate hydroxide [17]. This implies that the incorporation of either magnesium or aluminium ions into the corrosion product structure makes the compound less soluble or more efficient as a barrier to further corrosion. However, there are no insoluble or sparingly soluble forms of aluminium or magnesium hydroxy chlorides reported in the literature as detected corrosion products.

The observation of enhanced corrosion resistance of zinc in the presence of $MgCl_2$ (effectively the presence of Mg^{2+} in a chloride-environment) may also be relevant to the ZMG corrosion mechanism. Lindström et al. [123] and Prosek et al. [126] related this enhanced corrosion resistance to the formation of simonkolleite (or a magnesium-modified version thereof) rather than zinc hydroxycarbonates. Lindström et al. [123] suggested that amorphous magnesium hydroxide from the electrolyte precipitated directly onto cathodic sites of the corroding zinc surface and inhibited further oxygen reduction, but magnesium hydroxide was not detected on the corroded samples. Prosek et al. [126] suggested that the principal protective effect of $MgCl_2$ was the hydrolysis of $MgCl_2$ according to (4.19), resulting in a decrease in the surface electrolyte pH and consequently preferential precipitation of simonkolleite (or magnesium-modified simonkolleite) according to (4.5) [126].

$$MgCl_2(aq) + 2H_2O(aq) \rightarrow Mg(OH)_2(am) + 2Cl^-(aq) + 2H^+(aq) \qquad (4.19)$$
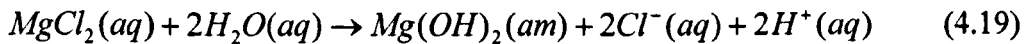
Prosek et al. [126] detected relatively small amounts zinc oxide on the corroded surface but no magnesium oxide or hydroxide species.

The findings point to reduced corrosion rates of magnesium-containing zinc coatings due to the precipitation of one or more solid corrosion products, although the protective compounds formed have not yet been characterized. A key question is how these protective corrosion products form on ZMG. Endurance of galvanic action cited by Kawafuku et al. [13] may be an effect of the increased general corrosion resistance rather than its cause. Most of the testing carried out on ZMG to date involves rather high levels of salt (5 wt.% NaCl in aqueous solution) and unrealistic environmental exposures such as constant salt spray or constant immersion. Although these test methods accelerate corrosion, the corrosion mechanism may be altered by the test method. Continuously wet test methods such as immersion or salt spray do not correlate well to actual field performance. A major reason for the discrepancy is that constant macro-wetness does not allow establishment of the local, separated anode and cathode surface chemistry that is found under real atmospheric conditions. For example, too great a salt load or too high a time of wetness (TOW) on the panel will reduce the amount of carbon dioxide that can be absorbed onto alkaline sites of the corroding surface. In this case, corrosion is accelerated unnaturally, as carbonates have been shown to retard the corrosion of zinc [120].

Cyclic corrosion testing incorporating wet and dry cycles such as that used by Tsujimura et al. [17] has been shown to generate corrosion behaviour that corresponds better to real-world environments [70]. All corrosion testing of ZMG to date has been conducted in a NaCl-based environment; the effects of sulphates, nitrates and acidic electrolytes on ZMG corrosion resistance have not been assessed. Field exposure data is not available for ZMG; therefore development of a robust corrosion mechanism for ZMG requires exploration of its behaviour in the variety of environments it may encounter in service.

4.5. PAINTED PANEL CORROSION

Typically, several paint layers are applied to automotive panels (as described in Section 3.4.2), providing a protective barrier against corrosion of the steel panel. The corrosion properties of these layers and weak points generated by vehicle body geometries are discussed briefly in the following sections.

4.5.1. Corrosion Protection by Paint

The properties of a paint layer that contribute to corrosion protection are its ability to act as a barrier to ion diffusion, adhesion to the metal, blocking of ionic paths between local anodes and cathodes on the metal to paint interface and its inhibitor content [30,127]. However, no paint is impermeable to water and oxygen [30] and these species may diffuse through pores within the paint layer [127]. Stratmann [128] proposed a model for the metal to paint system as shown in Fig. 4.9.
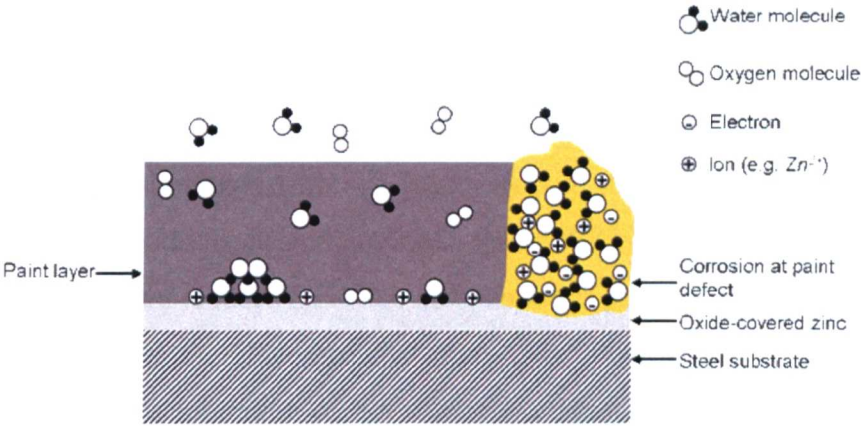
Fig. 4.9: Schematic of delaminating galvanized steel to paint interface with permeating O_2 and H_2O molecules, clusters at the interface and ions migrating along the interface from a defect site [128].

The paint layer is separated from the underlying metallic substrate by a thin but dense oxide layer. Water and oxygen molecules diffusing through the paint layer may enrich at the interface in the form of clusters [128]. In the presence of defects, (such as scratches or chips in the paint), ions diffuse along the interface, resulting in the build-up of an electrified interface between the oxide and the paint. The subsequent rate of corrosive attack, (i.e. paint delamination), depends on the rate of the electron transfer reaction (ETR) at this electrified interface, the redox properties of the oxide and the chemical stability of the interface relative to the species formed during the ETR, (e.g. stability of oxide layer in alkaline pH caused by reduction of molecular oxygen to OH^-) [127,128].

Fürbeth and Stratmann [47-49] showed that atmospheric carbon dioxide diffused through an amine-modified epoxy ester film (i.e. paint layer similar to e-coat) of 40-60 µm thickness and reacted with zinc oxide to precipitate protecting carbonates. A

3.5-fold reduction in paint delamination rate was observed on samples with CO_2 exposure compared to those without CO_2 exposure. The authors [49] proposed that the reduced delamination rate was due to a reduction in ETR rate at the oxide-paint interface, leading to inhibition of the oxygen reduction reaction. If ZMG can precipitate protecting corrosion products underneath the paint layer, it may offer increased resistance to paint delamination compared to conventional zinc coatings. In fact, Stratmann [128] highlighted ZMG as a next generation in protective coatings due to the formation of a specific oxide at the ZMG surface. X-ray photoelectron spectroscopy (XPS) sputter analysis of the material revealed the presence of an oxide film, approximately 4 nm thick, enriched in Mg^{2+} but also in significant amounts of Zn^{2+}. It was proposed [128] that the ZMG surface was covered by magnesium-oxyhydroxide highly doped with zinc. Analysis of the behaviour of this oxide by Scanning Kelvin Probe (SKP) showed that it exhibited enhanced stability and reduced ETR rate compared to a galvanized steel surface (i.e. conventional zinc oxide). Therefore ZMG may offer inhibition of oxygen reduction rate even without the migration of, for example, carbon dioxide through the paint film because the doped oxide itself inherently reduces ETR rates and consequently inhibits corrosion reactions at the metal to paint interface.

4.5.2. Panel Cut Edges

Cut edge corrosion is a form of localized corrosion that occurs at the edges of galvanized steel panels. Cut edge corrosion has been identified as failure mode of concern in the architectural industry [129,130] due to the manifestation of red rust, unsightly peel-back and blistering of the paint layers. Architectural panels are similar to automotive panels, but with relatively thicker zinc or zinc-alloy coatings (reflecting the longer service life expected of buildings compared to automobiles), guillotined rather than stamped edges and importantly, cutting of the panels post paint application rather than pre-paint application. This last difference means that the steel substrate is directly exposed to the atmosphere at the cut edges of architectural sheets, but automotive cut edges are covered by the paint layers.

The initiation of cut edge corrosion at cut edges of architectural galvanized panels is reported to be due to galvanic coupling of the steel and zinc (zinc anode and steel

cathode) [129-133]. Walter [131] reported that the initial rate of paint undercutting was determined by the cathode to anode area ratio, equivalent to the area ratio of steel to metallic coating exposed at the cut edge. A large cathode (i.e. thick steel panel) galvanically coupled to a small anode (i.e. thin zinc coating) resulted in increased corrosion rates. Theoretically, the zinc coating should offer galvanic protection to the steel substrate until all the zinc is anodically dissolved; use of thick zinc coatings would therefore avoid cut edge corrosion for a long service life. In practice, rusting of the substrate at the cut edge occurs earlier. Howard et al. [129,130] proposed that the galvanic protection offered by the zinc coating is lost as the corroding zinc recedes from the cut edge and the resistance of the electrical path between them becomes too great. An increase in electrical resistance may occur by drying of the electrolyte connecting the zinc to the steel. Walter [131] proposed that a crevice corrosion mechanism developed as the zinc anode dissolves and recedes from the cut edge, forming a crevice between the steel substrate and the paint film, as illustrated by Fig. 4.10.
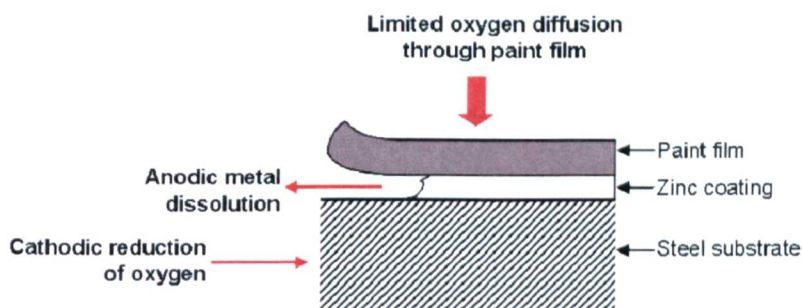
Fig. 4.10: Walter's model for crevice development at the cut edge of architectural panels [131].

Crevice conditions lead to increased rates of zinc dissolution and thereby earlier attack of the steel substrate. Further studies from the architectural industry have shown that cut edge corrosion effects were greater when the panel suffered from asymmetric coatings with paint films of effectively greater oxygen permeability on one side of the panel versus the other. This asymmetry was developed by applying thinner paint film [134], by inducing different degree of cure [44] and by photo-degradation [133] of the paint film on one side of the panel versus the other. All reported the establishment of a differential aeration concentration cell, with oxygen reduction (i.e. cathodic activity) occurring at the cut edge proximal to the paint with

increased oxygen permeability. An increase in pH due to oxygen reduction occurred underneath the paint film, degrading the paint film further by alkaline dissolution and allowing further oxygen reduction and increased corrosion progression [133].

Ogle et al. [46] observed that cut edge corrosion may be mitigated by the precipitation of protecting corrosion products onto the exposed steel (cathode) site. Precipitation of protective corrosion products may also occur at cathodic sites in the differential aeration cells described by [133]. Ogle et al. [46] described the protective effect as a self-healing function and noted that the formation of such films depends on the local chemical and electrochemical environment. The enhanced corrosion resistance of ZMG compared to conventional zinc coatings seems to be related to the formation of protective corrosion products; if this is the case, ZMG may also offer increased cut edge corrosion resistance. Indeed, enhanced cut edge corrosion resistance is listed as a benefit of hot-dip zinc-aluminium-magnesium alloy coated steel in the product information of Nisshin Steel's website [135] and precipitation of protective films were noted.

Rather less attention has been given to cut edge corrosion of automotive edges compared to architectural edges. This is likely due to the common practice of applying organic sealer to automotive edges, effectively isolating the metal edges from the corrosive environment and preventing corrosion during the vehicle service life. A report by Suzuki et al. [71] is an exception, in which the authors investigated the effects of zinc coating and cut edge shape (burred, squared and rounded edges) on cut edge corrosion. It was shown that the burr shape affected the thickness of the e-coat paint layer; no e-coat film thickness developed on the tip of the burrs and on the 90-degree corners of the cut edges. Increased e-coat paint thickness deposited on rounded edges resulting in reduced red rust compared to burred and squared edges on non-zinc coated steel. However, this relationship was not reported for e-coated panels constructed from galvanized steel because these panels did not exhibit significant rusting during the test period. The authors [71] concluded that cut edge geometry effects were negligible compared to the effects of zinc coatings. Currently, use of zinc-coated steel for automotive panels is standard

practice [8] and so it is worth investigating the effects of cut edge geometry on edge corrosion of automotive panels constructed from galvanized steel. Given the observance of increased cut edge corrosion associated with asymmetry on architectural sheets, it is expected that the asymmetric geometry and uneven e-coat coverage of automotive cut edges result in similar effects that have not been fully explored.

4.5.3. Crevices

The classical crevice corrosion mechanism described by Fontana [19] and in Section 2.3.3 is usually associated with de-passivation of metals (such as stainless steel). In this work, the term crevice corrosion is used to describe the accelerated corrosive attack observed within creviced areas on vehicles. E-coat may not be able to penetrate creviced areas generated during vehicle body construction due to the narrow opening and a resultant Faraday cage effect [79]. The absence of e-coat makes the creviced areas susceptible to accelerated corrosion attack compared to adjacent painted panels. Perpetuation of corrosion via concentration of corrosive electrolyte within the creviced area may develop subsequently if there is inadequate drainage from the crevice.

Increased corrosive attack of the material within the creviced area has been reported on vehicles in service [39], on test vehicles [79] and on laboratory test panels [59]. The corrosion rate inside the crevice depends on the microclimate developed within the creviced area, which in turn depends on the diffusion of ions into and out of the creviced area. Salt spray testing of creviced panels may result in obstruction of the crevice opening by voluminous corrosion products [72] and observations from such tests cannot be used to develop reliable mechanisms [79]. Zhu et al. [136] observed that the conditions developed within the crevice during a cyclic corrosion test depended on the drying time, with greater corrosive attack associated with shorter drying times. The shorter drying times were associated with faster dissolution rates of the zinc coating, leading to sites where the steel substrate was exposed. The exposed steel areas established as cathodic sites where oxygen reduction increased, leading to increased pH in the confined space, zinc oxide formation and continued oxygen reduction and perpetuation of the corrosion reactions within the crevice. If

this mechanism remains operative for automotive crevices, use of ZMG may again offer increased crevice corrosion resistance due to the precipitation of protective corrosion products.

4.6. SUMMARY

The importance of zinc-coated steel as a construction material is signified by the wealth of published reports on its corrosion properties. The literature gives an understanding of the corrosion mechanism of zinc and zinc-coated steel in various environments and explains why different corrosion rates are measured in different environments. Given the advanced understanding of zinc corrosion, it is not surprising that there is inertia to embrace newly-developed zinc-alloy coatings. At the same time, there is a desire within the automotive industry to move to alternative zinc coatings to alleviate processing issues and/or to reduce secondary corrosion protection measures. A relatively small number of reports on the corrosion resistance of zinc-magnesium coated steel (ZMG) exists, but each one reported a significant (at least 4-fold) improvement in corrosion resistance compared to that of approximately equivalent conventional galvanized steel. One objective of this work was to propose the corrosion mechanism of ZMG in different environments using the current understanding of zinc corrosion mechanisms as the baseline. Predictions of the applicability of ZMG to vehicle body construction and of the long-term corrosion resistance of ZMG in service may be made based on the understanding of the corrosion mechanism. If a corrosion benefit is realised by use of ZMG at cut edges and in creviced areas of automotive panels and the corrosion protection mechanism is proven to be robust, ZMG may offer the opportunity to reduce or delete secondary corrosion measures. This incentive provides motivation to explore ZMG's corrosion mechanisms in the open and localized corrosion modes.

Chapter 5

EXPERIMENTAL METHODS

5.1. INTRODUCTION

Two objectives of this study were to elucidate the mechanisms of edge corrosion and crevice corrosion of automotive panels and to assess the suitability of zinc-magnesium coated steel (ZMG) as a next generation galvanized steel for the automotive industry. Details of the experimental methods used are presented in this chapter. The test materials are described in Section 5.2 and test panel fabrication is discussed in Section 5.3. The corrosion test methods used are detailed in Section 5.4 and the corrosion resistance assessment methods are given in Section 5.5. The analysis techniques used to characterize corrosion products are described in Section 5.6. The results of these experiments are presented in Chapter 6 – Chapter 8.

5.2. MATERIALS

ArcelorMittal Ltd. supplied the sheet steel materials used in this work. The substrate, metallic coatings and paint treatments are described in turn in the following sections.

5.2.1. Substrate Material

The substrate was cold rolled low carbon steel type DC06 according to EN10130 [137] of 0.75 mm ±0.5 mm thickness. The mechanical properties and chemical composition of this steel are given in Tables 5.1 and 5.2 respectively.

Table 5.1: Typical Mechanical Properties of the Steel Substrate [137]

0.2% Proof Strength (N/mm^2)	Tensile Strength (N/mm^2)	Elongation A80 (% min.)
180	310 ±40	38

Table 5.2: Typical Chemical Composition of the Steel Substrate (ladle analysis wt.% max.) [137]

Carbon	Phosphorous	Sulphur	Manganese	Titanium
0.02	0.02	0.02	0.25	0.3

5.2.2. Metallic Coatings

Three different types of metallic coating were investigated in this work; conventional galvanized steel produced by electroplating (EG) or by hot-dipping (HDG) processes and zinc-magnesium alloy coating (ZMG). Fig 5.1 shows scanning electron microscope (SEM) images of each material surface. The HDG material had a surface texture, as shown in Fig. 5.1b.

(a)

(b)

(c)
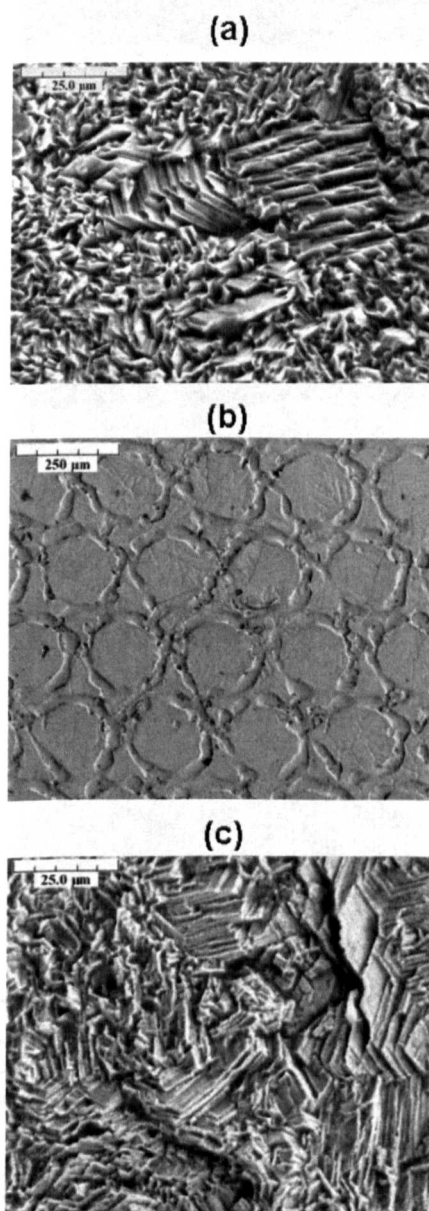
Fig. 5.1: SEM images of (a) EG (b) HDG and (c) ZMG surfaces. *Note reduced magnification for (b).*

ZMG was produced at a pilot line facility by over-coating EG with a layer of magnesium applied by physical vapour deposition. The coated sheet was

subsequently thermally treated to alloy the zinc and magnesium such that a layer of the phase Zn_2Mg was generated at the surface, with a layer of unalloyed zinc underneath. Fig. 5.2 shows SEM images in the back-scattered electron (BSE) mode of each coating type in cross-section. The thickness of each metallic coating layer was measured using image analysis and is given in Table 5.3.
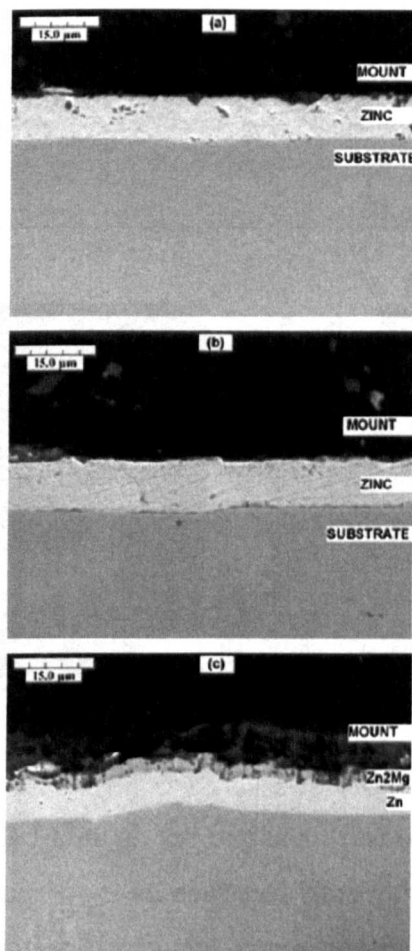
Fig. 5.2: SEM images (BSE mode) of (a) EG (b) HDG and (c) ZMG cross-sections.

Table 5.3: Coating layer thicknesses (average values of 20 measurements)

Coating	Thickness (μm)
Electrogalvanized (EG)	8.1 ±0.6
Hot-dip galvanized (HDG)	9.0 ±0.5
Zinc-magnesium (ZMG)	Zn_2Mg Layer: 2.2 ±0.6 Zn Layer: 6.0 ±1.0

5.2.3. Paint Treatments

Paint treatments described in Table 5.4 were applied at the Volvo Car Corporation (VCC) paint facility in Gothenburg, Sweden. The test panels were mounted on a rack, which in turn was bolted to either the front chassis rails or the lower back

panel of a production vehicle body, as shown in Fig. 5.3. This arrangement ensured that the test panels were treated in the same way as production vehicles. Spacers (metal clips) were inserted between the test panel and the mounting nut and bolt to create a gap, allowing paint deposition in this area.

Table 5.4: Paint Treatments

Description	Conditions
Alkaline degreasing	Dip and Rinse, 55°C
Phosphating	Gardobond 2600 (Chemetall)
Passivation	Gardolene 6800/6 (Chemetall)
E-coat	Cathoguard 350 (BASF)
Curing	20 minutes at 180°C
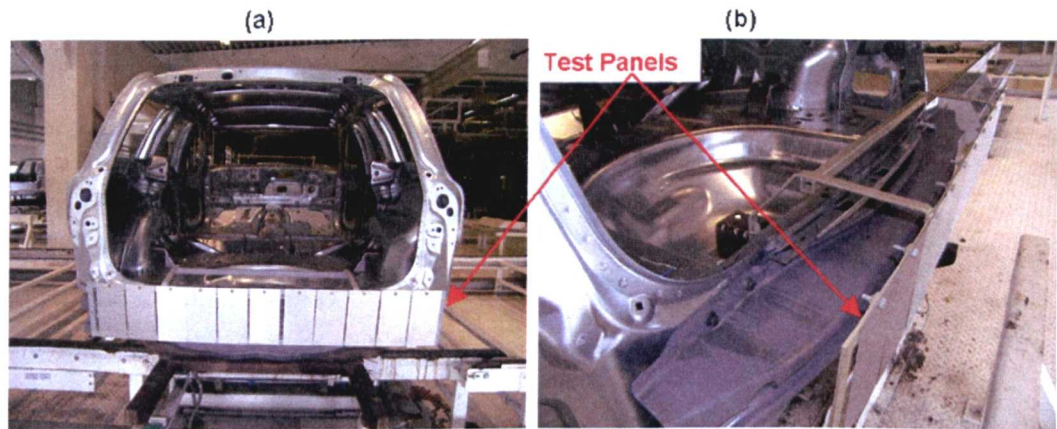
Fig. 5.3: Test panels mounted to a vehicle body for paint treatments. *Photos courtesy of VCC.*

The vehicle bodies travelled through the treatment line on skids (as shown in Fig. 5.3 *left*) and were suspended from an overhead carrier for full immersion into the treatment tanks. Alkaline degreasing was conducted in several steps of spraying and immersion to remove oil and other contamination from the panel surfaces. Once clean, the vehicle bodies were phosphated and passivated by dipping into chemical baths. These processes generated a textured crystalline surface on the body panels that is optimized for paint deposition. The vehicle bodies then progressed to the e-coat tank, shown in Fig. 5.4, where paint was deposited electrolytically.

Fig. 5.4: Immersion of a vehicle body in the e-coat tank. *Photos courtesy of VCC.*

The vehicle bodies travelled through ovens at line speeds such that each body was exposed to a temperature of 180°C for 20 minutes, as noted in Table 5.4, to cure the e-coat. The racks of test panels were removed from the vehicle bodies following e-coat curing, whilst the vehicle bodies continued to the paint post-treatment phases (paint primer, topcoat and clearcoat applications). Some damage to the paint was caused when removing the spacer clips but this was confined to the upper edge of the test panel only. Scribe lines were cut into one set of painted test panels. The scribes were cut using the scribe tool recommended by VCC and shown in Fig. 3.13. The handheld tool comprised a high speed steel (SKF 305 HSCo) parting tool with blade width of 0.50 mm ±0.02 mm. A guide was incorporated into the tool design to aid consistent scribing. The tool was applied to the panel such that the tool was 80° ±5° from the panel in the scribed line direction and the side of the blade made approximately a right angle with the plane of the test panel, see Fig. 5.5.
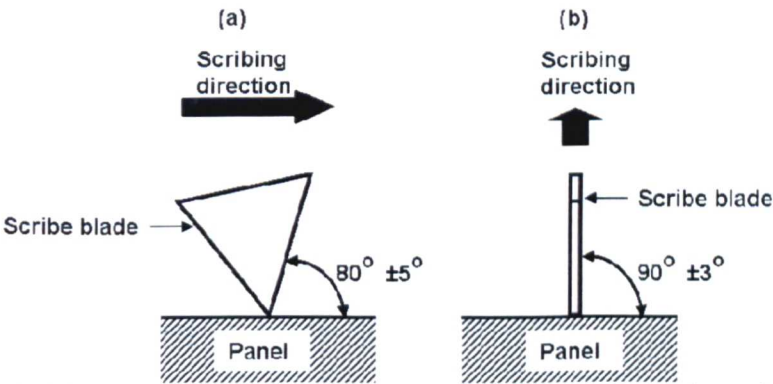
Fig. 5.5: Scribing process [69]. *Note* scribing direction in (b) is into the plane of the paper.

The scribe lines were approximately 70 mm in length (as recommended by [69]) and were cut parallel to the lower edge of the panel (i.e. with horizontal orientation). Each line was scribed until metal shavings were formed to ensure penetration to the

steel substrate. Scribed panels were subject to the Volvo cabinet corrosion test and scribe line creep measurements were made as described in Section 5.4.2. and Section 5.5.3 respectively.

5.3. TEST PANEL FABRICATION

Test panels were fabricated to develop different corrosion modes in the materials under investigation. Details of the processes used to fabricate the panels are given in the following sections.

5.3.1. Electrochemical Test Panels

A working electrode (W.E.) was constructed from the test material by cutting a rectangular panel measuring approximately 35 mm x 65 mm. The panel was degreased and dried prior to application of tape (type 851 PCB electroplater's tape supplied by 3M) to mask all but the test area and a connection area at the panel upper edge as shown in Fig. 5.6.
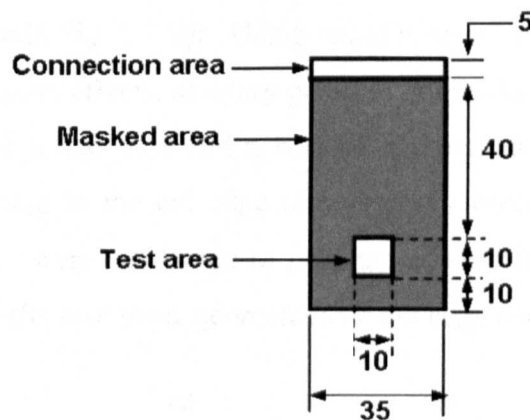
Fig. 5.6: Electrochemical test panel configuration. *Dimensions in mm, position tolerance ±1 mm.*

5.3.2. Open Corrosion Test Panels

Square test panels measuring approximately 100 mm x 100 mm were cut using a guillotine. No paint treatments were applied to panels in the open corrosion mode. Identification codes were punched into the lower left hand corner of each test panel. Masking tape was applied to the panel sides and upper edge to minimise edge corrosion effects on test panels in phase 1 of the corrosion testing plan. Tape was

not applied to the lower cut edge because it would interfere with the panel seating in the test racks.

Open corrosion test panels as described above were also fabricated for acid rain testing (described in Chapter 7). Undercutting of the masking tape used as edge protection in phase 1 testing was observed, therefore a blue tint stop-off lacquer (PL81/R3 supplied by Indestructible Paint Ltd., Birmingham, UK) rather than tape was applied to the edges for this phase 2 corrosion testing. Three coats of lacquer were applied with a 24-hour drying period at room temperature between each application. A round hole of 4 mm diameter was punched into the top of each test panel as an attachment point. The panels were suspended from an overhead rail in the corrosion cabinet by a plastic cable tie.

5.3.3. Edge Corrosion Test Panels: Panel Design

Suzuki et al. [71] produced panels for cut edge corrosion resistance by cutting a round hole of 40 mm diameter into a rectangular panel of 0.8 mm thick cold rolled steel sheet, as shown in Fig. 5.7 *left*. Using round holes as the test edges minimized errors due to orientation effects, as every possible orientation is included. A punch was used to cut the round hole and a burr of approximately 20 μm height was produced [71], leading to the cut edge cross-section illustrated in Fig. 5.7b *top*. Secondary processes were conducted to generate edges with square and rounded edges to assess the effects of these geometries on cut edge corrosion.
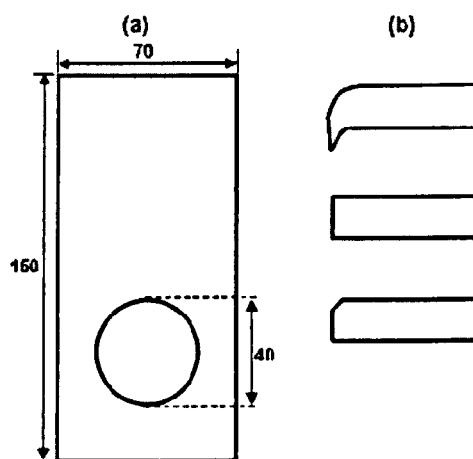
Fig. 5.7: Cut edge (a) test panel and (b) cross-sections *from top* as cut, square and rounded used by Suzuki et al. [71].

In this work, the geometries associated with stamped and laser cut edges were of interest because these are the processes used to cut automotive panels to size. Three cutting methods were selected to represent these geometries: punched hole with large punch-to-die clearance; punched hole with small punch-to-die clearance and laser cut hole. One of each edge type was cut into a square test panel (100 mm x 100 mm, as before) to ensure efficient use of material and to account for variations in corrosion due to panel location within the test cabinet. Round holes of 20 mm diameter were selected as a good fit for the test panel, allowing corrosion of the edges without overlapping of affected areas within the test period. The position of each edge type was rotated to mitigate orientation effects, such that three test panel types were generated, as shown in Fig. 5.8. An identifying code was punched into the lower left-hand corner of each panel and a 4 mm diameter fixing hole was punched at the upper edge of each panel.
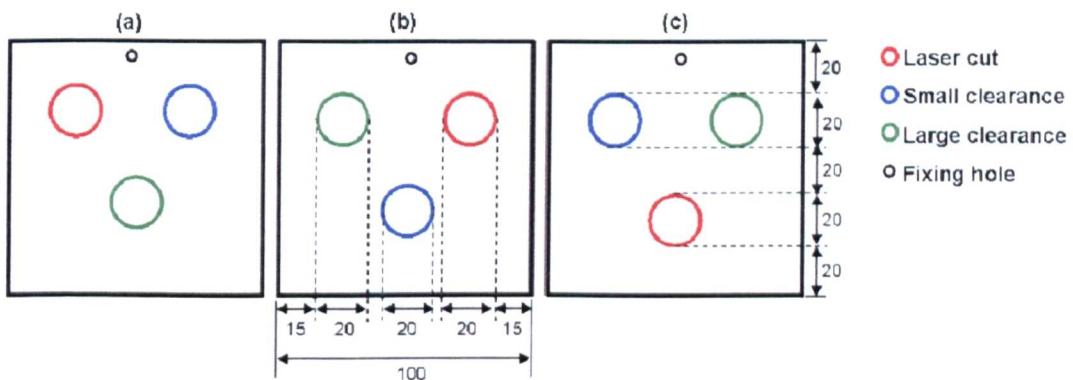
Fig. 5.8: Design of edge corrosion test panels used in this work. The position of each edge type was rotated, as illustrated in (a) – (c). *Dimensions in mm, position tolerance ±1 mm.*

5.3.4. Edge Corrosion Test Panels: Edge Production

Punched edges share a characteristic geometry with stamped edges [138], comprising distinct zones, known as rollover, shear or burnish, fracture and burr zones. The relative size of these zones varies with the punching conditions. A set of experiments was conducted to select the punching conditions and this is discussed in the following paragraphs.

Two criteria were adhered to in selecting the punching conditions; to keep the conditions close to real stamping conditions and to minimise variations in punched

edge geometry from panel to panel. Two kinds of punching tool were available for this work, one having a single piercing edge and the other having two piercing edges, as shown in Fig. 5.9a. The punch and die set (as supplied) was mounted in a universal testing machine, (Schenk Hydropuls equipped with a 100 kN load cell and hydraulic jaws), as shown in Fig. 5.9b. Two cross-head displacement rates were investigate, slow rate at 20 mm/min and fast rate at 1200 mm/min.

(a)   **(b)**
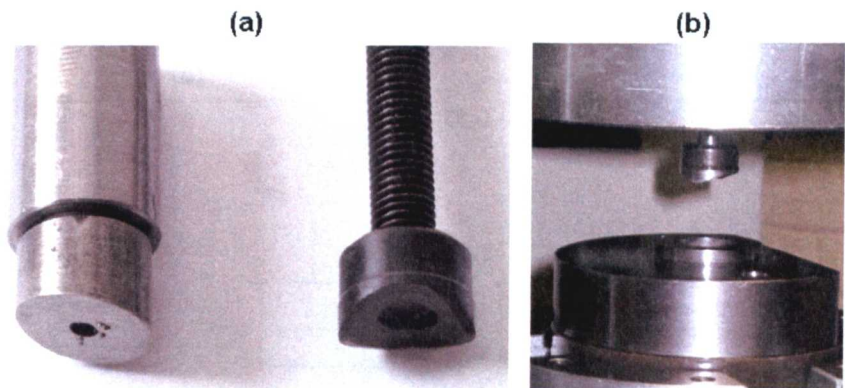
Fig. 5.9: Photographs of (a) punches investigated and (b) punch and die.

The effect of punch type on the average burr height was assessed under different punching conditions. The burr height was measured using a dial gauge and the average of four readings from different points on the round edge was calculated. It was found that the burr height varied at different points on the cut edge due to variations in the punch-to-die clearance at discrete points around the cutting plane. Every effort was made to align the punch and die to generate consistent punch-to-die clearance but a consistent gap could not be maintained. In addition to the alignment difficulties, it was also observed that the punches were not perfectly round, for example the double-pierce punch diameter varied from 20.18 mm to 20.23 mm. The average burr heights generated by the single and double-pierce punches under different punching conditions were measured and are shown in Fig. 5.10. Each boxplot represents the average data measured from 4 punched edges.

Punching Conditions:
(a) 1200 mm/min displacement rate, with lubricant
(b) 20 mm/min displacement rate, with lubricant
(c) 20 mm/min displacement rate, without lubricant
(d) 1200 mm/min displacement rate, without lubricant
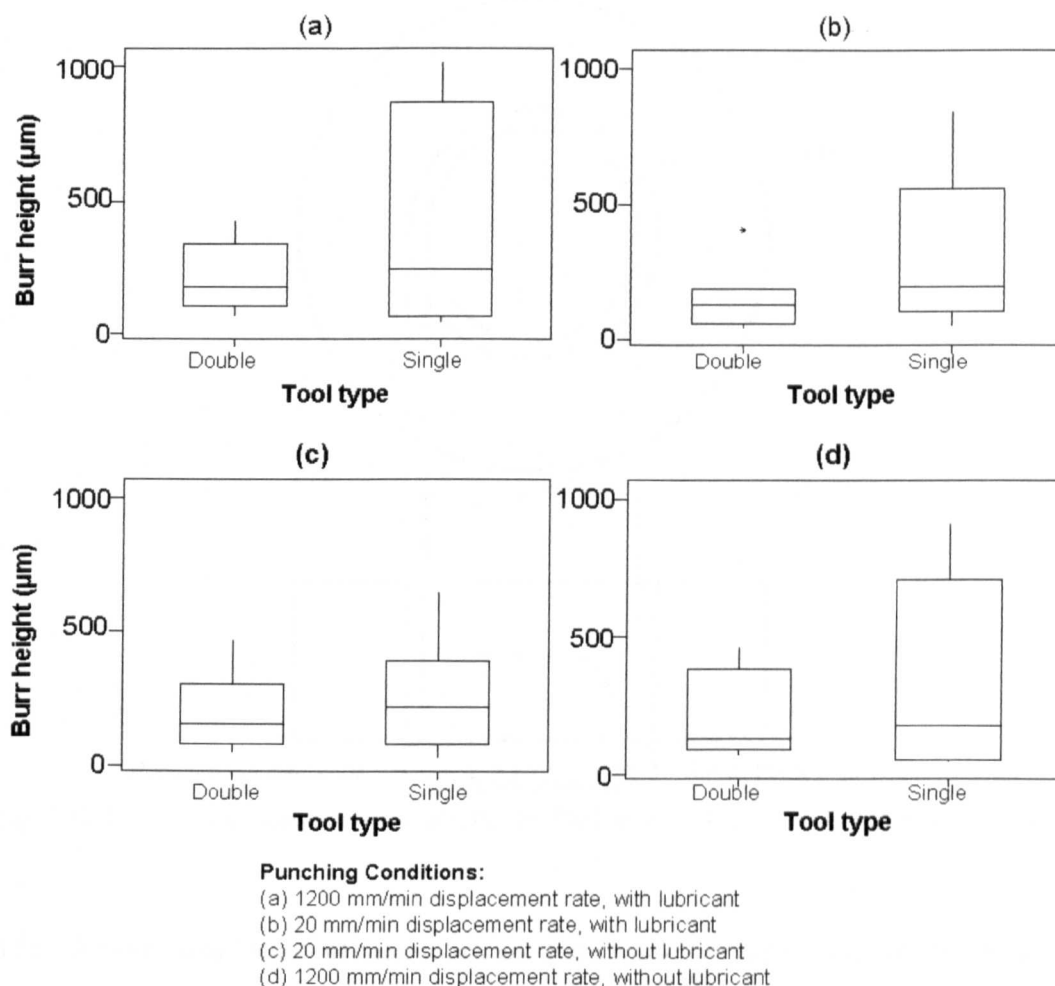
Fig. 5.10: Effect of tool type (double- or single-piercing) on average burr height under various punching conditions.

The double-pierce tool (RS stock number 543-579) shown in Fig. 5.9a *right* was selected for fabricating the test panels because it exhibited less variation in the average burr height of the cut edges. Having selected the punching tool, the following punching conditions were examined; punch-to-die clearance, cross-head displacement rate and use of stamping lubricant (lubricant type Fuchs 4107S). The clearance was varied by fabricating dies with different inner diameters, giving clearances of approximately 0.02 mm, 0.10 mm and 0.25 mm. The clearance was defined as the difference between the punch radius and the die radius, as illustrated by Fig. 5.11.
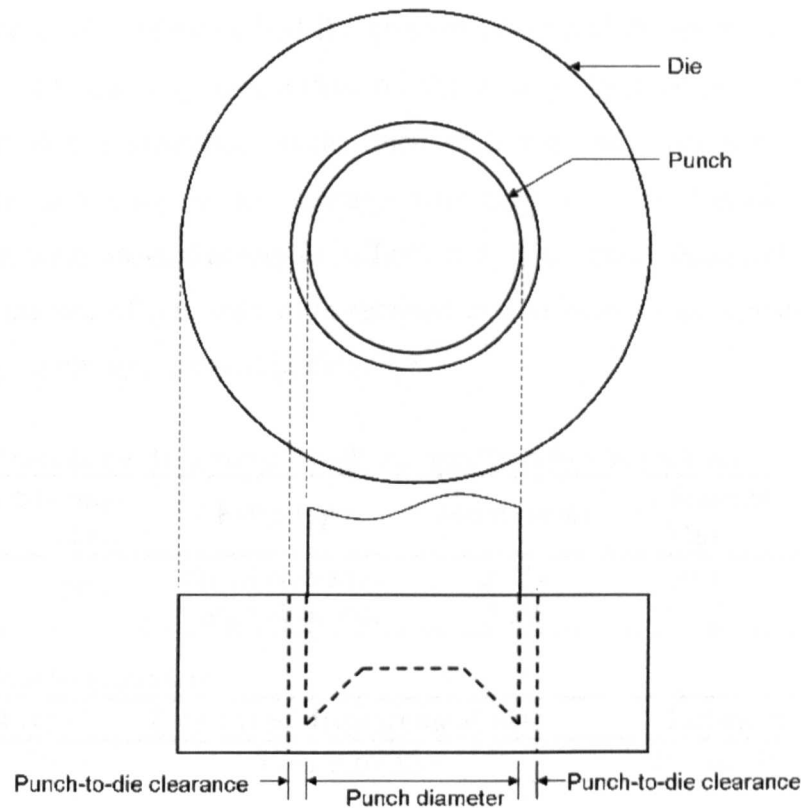
Fig. 5.11: Punch-to-die clearance was controlled by fabrication of dies with different inner diameters.

The effects of displacement rate, lubricant and clearance on the average burr heights of holes punched into non-zinc coated CRS are shown in Fig. 5.12.
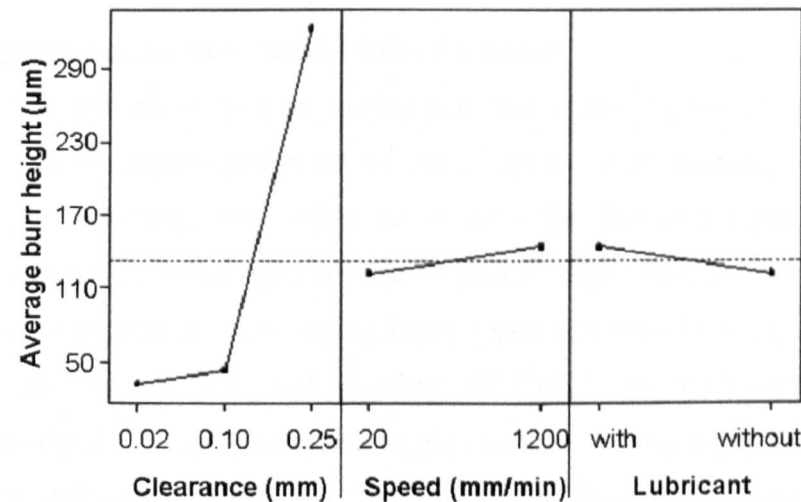
Fig. 5.12: Effects plot of punch-to-die clearance, cross-head displacement rate and lubricant on the average burr height of 4 holes punched in CRS.

The punch-to-die clearance had the greatest effect and the displacement rate and lubricant had relatively little effect on the average burr height. The data also suggested that a clearance greater than 0.10 mm was required to generate a significant difference in the average burr heights. The "small" and "large" clearances were selected as shown in Table 5.5. The faster cross-head displacement rate and the use of lubricant were selected to give better representation of actual stamping conditions, as noted in Table 5.6.

Table 5.5: Dies fabricated to generate "small" and "large" punch-to-die clearances.

Punch ∅ (mm)		Edge type	Die ∅ (mm)	Clearance (mm)	
Min.	Max.			Min.	Max.
20.18	20.23	Small clearance	20.24	0.01	0.03
		Large clearance	20.66	0.22	0.24

Table 5.6: Punching conditions.

Punch type	Crosshead displacement rate	Lubricant
Double Pierce	1200 mm/min	Fuchs 4107S

All laser cutting was conducted by a specialist local firm, Essex Laser Limited using a 4 kW Bystar 4020 equipped with a CO_2 laser. The characteristics of all three cut edge types (laser cut and punched with small and with large clearances) are presented in Chapter 8.

5.3.5. Edge Corrosion Test Panels: Edge Finishing

The effect of deburring, lacquer application and sealer application on cut edge corrosion was of interest and a set of cut edges for each material was finished accordingly. Deburring was performed on cut edges before the paint treatment, whereas lacquer and sealer were applied to painted edges (in-line with automotive manufacturing sequences). Deburring was performed manually using a hand-held Dremel multi-tool kit (RS stock number 312-0422) and solid lubricant. The objective of the deburring process was to remove burrs from the punched edges and to round the sharp corners (including those on the laser cut edges). Initial trials with the Dremel tool and a buffing fob on straight, guillotined edges gave favourable results; the sharp burr was removed, a rounded corner was generated and the zinc

coating was smeared onto the underside of the cut edge, (i.e. the lower edge mirrored the rollover zone), see Fig. 5.13.
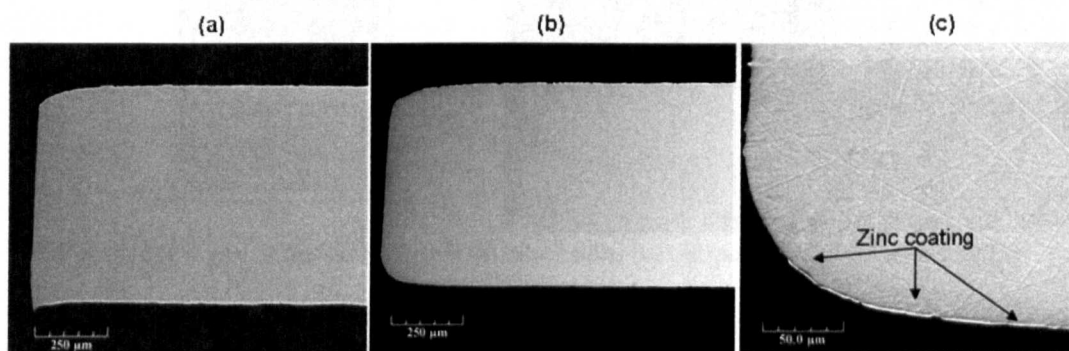
Fig. 5.13: (a) as-cut guillotined edge (b) deburred edge (c) high magnification view of deburred edge showing smearing of zinc.

Unfortunately it was more difficult to achieve the desired shape on the punched test edges used in this work due to their round shape and because a grinding wheel was required to remove the thick burrs. The final deburring process involved grinding to remove burrs and polishing and buffing to develop a rounded edge in place of the burr.

Clear lacquer conforming to FMC specification WSK-M1J208-A2 was sprayed onto both sides of one set of as-cut edges after the paint treatment process. The lacquer was allowed to dry at ambient conditions for 24 hours before moving the test panels. Organic sealer (Eftec Duplex sealer conforming to WSS-M4G334) was pumped onto one set of painted test edges and the sealed panels were cured at 170°C for 20 minutes.

5.3.6. Crevice Corrosion Test Panels

The crevice corrosion test panel designed by Ström et al. [59] and shown in Fig. 5.14 was adopted in this work.
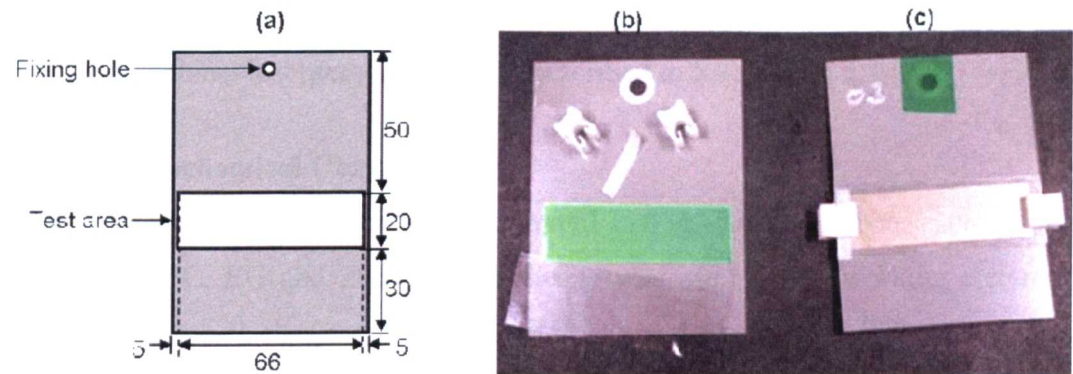
Fig. 5.14: Crevice corrosion test panel (a) dimensions (b) components and (c) assembly [5].

The test panels were laser cut to size (100 mm x 76 mm) to ensure flatness and the identifying code was punched into the lower left hand corner. The panels were degreased and a 20 mm x 66 mm strip of heat-resistant polyester tape (Shercon PC21) was applied to the panel 50 mm from the top edge to create the test area. A hole of 4 mm diameter was punched at the upper edge to fix the panel to the painting rack. Following processing through the paint pre-treatment line (described in Section 5.2.3), the tape was removed, exposing the unpainted test area. The strip of tape was applied to the fixing hole to prevent corrosion interference with the crevice area. The crevice was created by clipping two stacked standard glass microscope slides (measuring 76 mm x 26 mm and centred over the test area) onto the test area, as shown in Fig. 4.11b-c. A PTFE spacer of 0.25 mm thickness was inserted at one side (left hand side in Fig. 5.14c) to generate a wedge-shaped opening, with a 0.25 mm + e-coat thickness (approximately 0.03 mm) opening at one end and just the e-coat thickness opening at the other end of the crevice. Ström et al. [59] reported that such a wedge-shaped opening promoted full wetting of the test area during corrosion testing. Crevice panels were constructed for UC, EG and ZMG for testing in the Volvo cabinet corrosion test method and the results are presented and discussed in Chapter 8.

5.4. CORROSION TEST METHODS

Accelerated corrosion testing was selected in this work, as discussed in Chapter 3. An electrochemical test was conducted to assess any potential galvanic effects

between ZMG and conventional zinc coatings and the results are given in section 5.4.1. The cabinet test methods used are described in 5.4.2 and 5.4.3

5.4.1. Electrochemical Characterization

Three electrochemical test panels (illustrated in Fig. 5.6) were constructed from samples of UC, EG and ZMG and each one was used as the working electrode (WE) of a three-electrode cell. A saturated calomel electrode (SCE) was used as the reference electrode (RE) and a platinum electrode was used as the auxiliary electrode (AE). Electrical leads with a crocodile clip at one end were used to connect the electrodes to the corresponding inputs of a Gill 8 AC potentiostat. Each electrode was immersed in a beaker containing approximately 0.5 litres of electrolyte. The beaker was open to the atmosphere and the solution was not de-aerated. Insulation tape was wrapped around the electrical connections to ensure isolation of the conducting leads from the electrolyte. The experimental set-up is illustrated in Fig. 5.15.
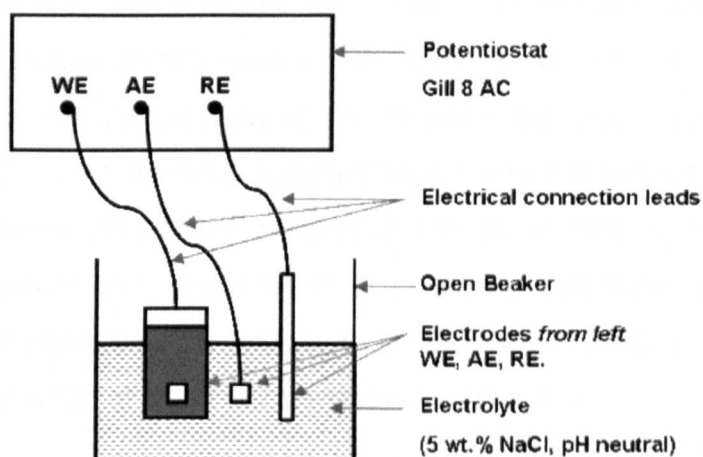
Fig. 5.15: Electrochemical test set-up.

A solution of 5 wt.% NaCl adjusted to neutral pH via the addition of sodium hydroxide (NaOH) was selected as the electrolyte, as it has excellent conducting properties and has been used in previous work by Suzuki et al. [71]. The beaker itself was seated in a heated water bath set at 30°C to maintain a consistent temperature for each experiment. Fresh electrolyte was used for each experiment and the AE was cleaned between polarization scans by rinsing it in concentrated

nitric acid, deionised water and drying. The open circuit potential (E_{corr}) of each material was measured after 5 and 30 minutes in the salt solution and the results are given in Table 5.7.

Table 5.7: Open circuit potential (E_{corr}) of UC, EG and ZMG in pH neutral 5 wt.% NaCl solution.

Material	Sample	E_{corr} versus SCE (mV)	
		5 min.	30 min.
UC	1	-656	-690
	2	-597	-617
	3	-666	-694
EG	1	-1027	-1034
	2	-1033	-1039
	3	-1041	-1052
ZMG	1	-1050	-1055
	2	-1022	-1042
	3	-1018	-1040

The results showed rather similar E_{corr} values for EG and ZMG with ZMG exhibiting on average slightly more anodic potentials than EG. The differences in potential measurements after 5 and 30 minutes showed that the materials did require a settling time. Variations in the measured results were due to scratches on the WE surface and undercutting of the masking tape by the electrolyte, which generated secondary corrosion reactions. Further E_{corr} measurements were taken on EG and ZMG after 50 minutes in the electrolyte giving average ZMG E_{corr} value 6 mV more anodic than that of EG, as summarized in Table 5.8.

Table 5.8: Open circuit potential (E_{corr}) measurements after 50 minutes immersion in 5 wt.%NaCl.

Material	Sample	50 min. E_{corr} versus SCE (mV)	Average E_{corr}
EG	1	-1042	-1050
	2	-1050	
	3	-1057	
ZMG	1	-1069	-1056
	2	-1049	
	3	-1051	

The E_{corr} values measured were 40-60 mV more anodic than the results published by Suzuki et al. [71] and this difference may be due to differences in the test materials and methods. For example, the measured results in Table 5.8 may have been affected by the presence of oxide layers, whereas [71] used NaOH to remove oxide species from the test material prior to testing in a de-aerated electrolyte. However the difference in open circuit potential value of EG and ZMG is of greater significance than the absolute value in estimation of galvanic effects. Hausbrand et al. [83] reported that ZMG was approximately 10 mV anodic to EG. These findings suggest that the corrosion resistance benefit offered by ZMG compared to conventional zinc coatings, such as EG, was not due to a significant galvanic effect between zinc and ZMG but other corrosion test methods are required to develop the corrosion mechanism of ZMG.

5.4.2. Volvo Cabinet Test Method

The Volvo cabinet test method comprised cycles of humidity, drying and intermittent spraying with 1 wt.% NaCl solution, acidulated to pH 4.2 via the addition of sulphuric acid [139]. The test cycles were relatively complex, (see figure 5.17 a-b), with two twelve-hour sub-cycles combined and repeated every week. Sub-cycle 2, incorporating salt spraying, was performed on Mondays and Fridays and sub-cycle 1 on the other days of the week. Salt solution was sprayed for a period of 15 minutes (step 2.1). The chamber was then kept at constant conditions with temperature (T) set to 35°C ±0.6°C and 97% ±2% relative humidity (RH) for 1 hour 45 minutes (step 2.2). The humidity was controlled such that the test panels remained wet (i.e. a liquid electrolyte was present on the panels' surfaces) during this phase. Steps 2.1 and 2.2 were repeated in sequence twice more to give a total time of wetness (TOW) of 6 hours per sub-cycle. An automated corrosion chamber constructed by the Volvo Car Corporation (VCC) test laboratory and shown in Fig. 5.18 was used to control the temperature and humidity. The spraying device comprised a number of nozzles mounted in series onto a rail (termed the precipitation rail), which was oscillated whilst spraying to ensure even coverage of the test panels, as illustrated by Fig. 5.19. Test panels were seated in racks and stood at an angle of 15° to vertical. The total test duration was 12 weeks, comprising a total of 168 12-hour humidity cycles.
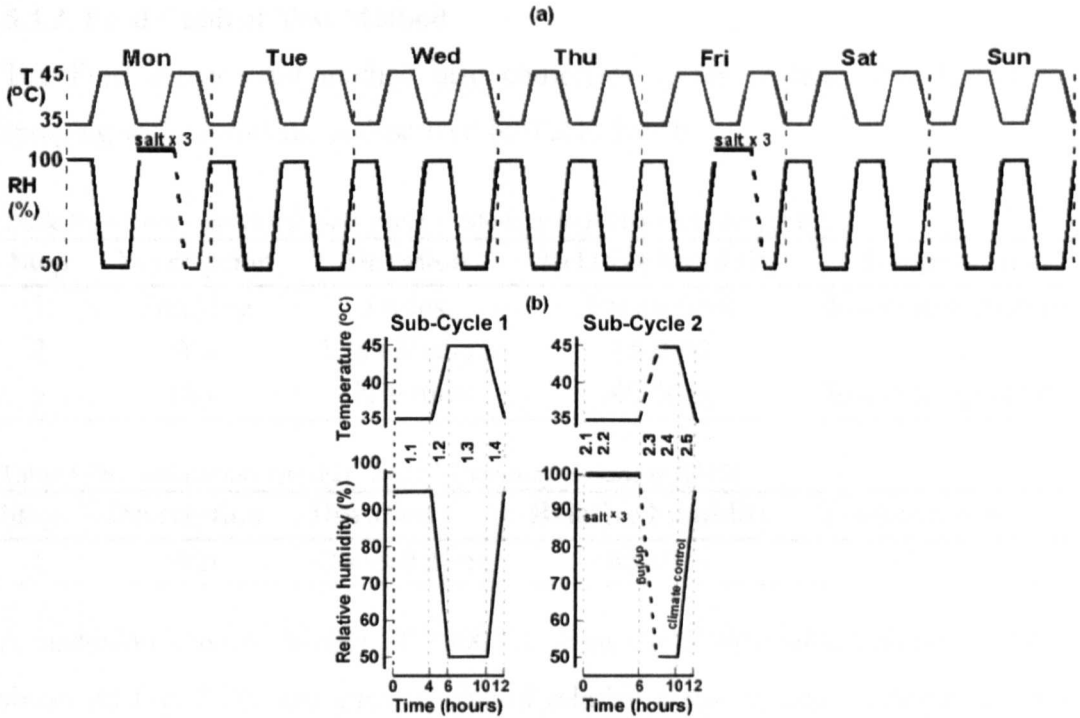
Fig. 5.17: Climate chamber conditions (a) weekly and (b) sub-cycles (*left*) without and (*right*) with salt spray [139]
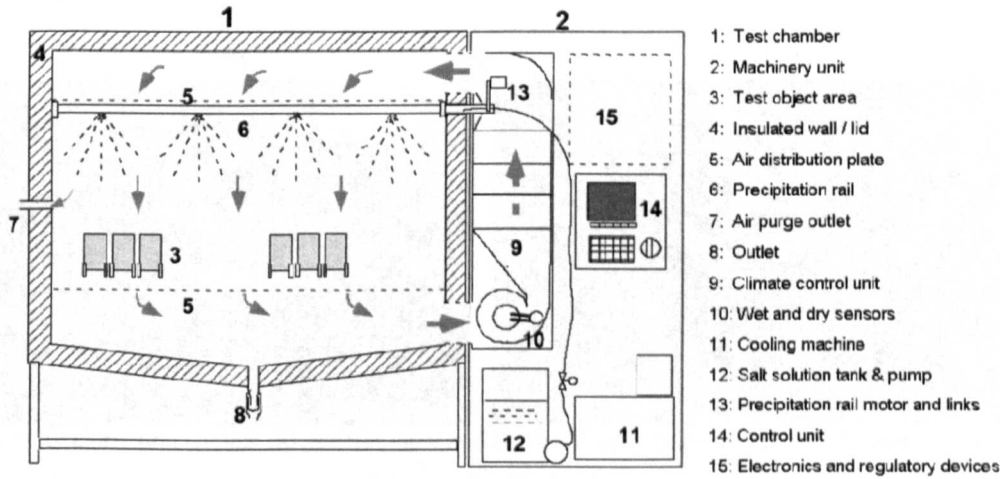
Fig. 5.18: Volvo corrosion cabinet [139].
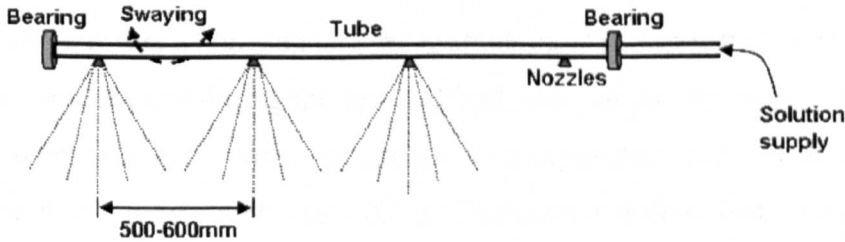
Fig. 5.19: Precipitation rail [139].

5.4.3. Ford Cabinet Test Method

The Ford cabinet test method also comprises cycles of humidity, drying and spraying with corrodent, as described by Table 5.9a-b.

Table 5.9a: Ford cabinet test daily cycle 1 (Monday to Friday inclusive) [140].

Step	Description	Duration	Relative humidity	Temperature
1	Spraying	5 mins.	Atmospheric	Room temperature
2	Wet	22hrs 55 mins	85-95%	50° ±2°C
3	Dry	1hr 0 mins	40-50%	Room temperature

Table 5.9b: Ford cabinet test daily cycle 2 (Saturday to Sunday) [140].

Step	Description	Duration	Relative humidity	Temperature
1	Wet	24hrs 0 mins	85-95%	50° ±2°C

A corrosion cabinet (Model SF/2000/CT from C&W Specialist Equipment Ltd.), shown in Fig. 5.20, was used to control relative humidity and temperature. The cabinet was equipped with spraying nozzles which were used to spray a salt solution (typically 5 wt.% NaCl pH 5.5 – 6.5) on to the test objects.

(a)   (b)

Fig.5.20: Corrosion cabinet (a) general view and (b) detail view of control panel. *Photos courtesy of FMC.*

In this work a special acid rain solution was used and it was applied manually to the test panels as it was a non-standard spray solution. The test panels were suspended from an overhead rail during the test and both sides of the test panel were sprayed evenly such that each panel comprised two equivalent test surfaces. It was estimated that approximately 0.6 – 0.7 g of solution was deposited on each panel at every spraying interval. The acid rain solution composition (given in Table 5.10)

was taken from the work of Howard et al. [129-130,141] and was described as being 10-times the strength of natural acid rain.

Table 5.10: Acid rain solution composition [129-130,141]

Constituent	Concentration (ppm)
Sulphuric acid (1.84 s.g.)	31.85
Ammonium sulphate	46.20
Sodium sulphate	31.95
Nitric acid (1.42 s.g.)	15.75
Sodium chloride	84.85
(pH adjusted to 3.5)	

5.5. CORROSION RESISTANCE ASSESSMENTS

Comparison of the corrosion resistance of ZMG to conventional zinc coated steel required an assessment that characterized each material's corrosion resistance. Assessment methods used in this work are described in the following sections.

5.5.1. Red Rust Area

The percentage of red rusted area on the test panel surface was used to express the corrosion resistance (more specifically the red rust resistance) of the unpainted test panels. High resolution photographs of each test panel were taken using a digital SLR camera fitted with a macro-lens. The photographs were analysed using an image analysis software package (Scentis from Struers Ltd.) with a multi-phase percent area module. The photographs were converted to gray scale images and were optimized for phase identification as required. Grey scale levels were assigned to each phase of interest on the panel surface (red rust, metallic surface, white corrosion products) and the percentage of the panel surface covered by red rust was calculated automatically.

The accuracy of the phase analysis depended upon the segregation of the phases in terms of grey-values. Reasonable separation of phases was observed on UC, EG and HDG samples, however corroded ZMG samples developed dark patches that were similar in grey-value to the red rust phase. Two measurements were taken on such ZMG samples, the first taking a low estimate and the second a high estimate of the red rust area and the mean of these measurements was selected as an estimate of

the red rust area. The error associated with red rust area on such ZMG samples was estimated from these measurements as approximately ±2%. A minimum of 2 samples of each material were assessed to generate average red rust percentage areas. The red rust area developed during corrosion testing varied between panels and these variations were generally greater than the errors estimated due to phase analysis.

5.5.2. Delaminated Paint Area

Edge corrosion test panels fabricated from zinc-coated steel suffered undercutting of the paint, evidenced by paint blistering adjacent to the cut edges. Blistered paint areas were considered corroded and the extent of the affected paint area indicated the corrosion associated with each edge. Blistered and delaminated paint was removed from the test panel using a clear polypropylene backed tape reinforced with glass yarn filaments and with synthetic rubber adhesive (Type 898 from 3M Ltd.). A strip of tape was applied firmly to the affected area leaving one end unfixed. The free end was grasped and pulled firmly such that close to a 180° angle was formed between the panel and the removed tape, as illustrated in Fig. 5.21.
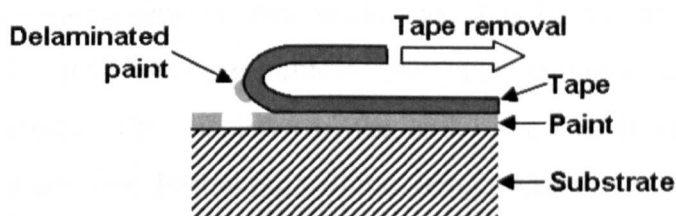
Fig. 5.21: Removing delaminated paint using tape.

A photograph of the area surrounding each test edge was taken following removal of the delaminated paint. Each photograph was taken at fixed position and magnification by mounting the camera in a tripod. A photograph of a rule was taken at the same time for use as a calibration for each set of photographs. Image phase analysis was used, as before, to calculate the area of the delaminated paint associated with each edge. Clear separation was observed between the grey values associated with intact paint and exposed substrate. Two of the three samples of each edge type tested were analysed in this way and the average of the two results was recorded. The paint on the third sample of each edge type was not removed to

allow examination of the paint layer distribution in cross-sectional analysis (discussed in the section 5.6).

Edge corrosion panels fabricated from UC did not exhibit paint delamination but extensive red rust was observed. Photographs of the corroded edges were processed in the same way as described above to calculate the total rusted area associated with each edge. All three samples of each UC edge type were assessed in this way prior to cross-sectional analysis of one of each type. The average red rust area associated with UC edges therefore represents the average of 3 measurements. UC panels exposed to the full 12-week corrosion test period did, in some instances, suffer increased rust areas due to corrosion of the fixing hole located at the top of each panel. The rust due to the fixing hole was blacked out in the photographs to avoid overestimation of the rusted area due to the test edges, but the edges themselves may have experienced increased corrosive attack due to rusting of the adjacent fixing hole. The position of each test edge was rotated so that this effect was mitigated in taking the average rust area.

5.5.3. Scribe Line Creep

Scribe line creep measurements were made according to the standard procedure developed by VCC [69]. No measurements were taken within 10 mm of either end to avoid edge effects. The remainder of the scribe line was divided into 5 equal segments (each measuring 10 mm on a 70 mm length scribe line), as shown in Fig. 5.22.
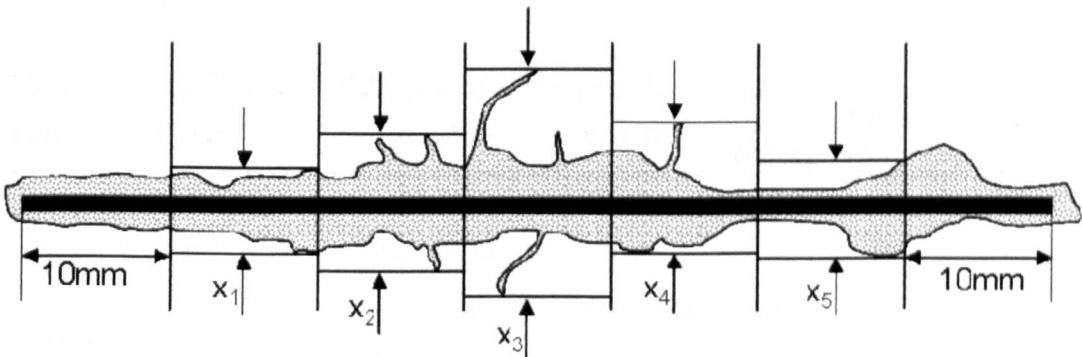
Fig. 5.22: Scribe line creep measurement [69].

The maximum creep width in both directions within each segment (x_1 to x_5 in Fig. 5.22) was measured using Vernier calipers. The scribe line creep measurement was calculated by taking the average of x_1 to x_5 and subtracting the original scribe width (0.5 mm).

5.6. CORROSION PRODUCT CHARACTERIZATION

Characterization of the corrosion products formed on each material during the corrosion tests allowed estimation of the corrosion mechanisms involved, as discussed in Chapter 4.

5.6.1. Cross-sectional Analysis: Sample Preparation

Samples were cut from test panels to analyse the coating appearance before and after corrosion treatments, and to examine the morphology and composition of any corrosion products. Thin samples were cut using a hand-guillotine and degreased using industrial methylated spirits (IMS). Acetone cannot be used to clean painted panels because it softens and attacks the e-coat layer. A metal clip was used to support the section such that the cross-section of interest was parallel to the face of the sample. The degreased sections were mounted in Struers Polyfast, a conductive resin with low shrinkage designed to give good edge retention. The resin was cured under 30kN pressure with 7 minutes heating and 4 minutes of cooling in a Struers Labopress-3. The grinding and polishing cycle was taken from the Struers website application notes [142] and is given in Table 5.11. A Struers Rotopol-22 polishing wheel equipped with a RotoForce-4 specimen holder was used to control the preparation parameters and up to 3 specimens were prepared at once.

Table 5.11: Mounted cross-section preparation method [142]

Type	Cloth	Suspension	Lubricant	Speed (rpm)	Force (N)	Time (min.)
Grinding	SiC #320	None	Water	300	30	as req'd
	MD Largo	DiaPro AL	None	150	30	4
Polishing	MD Dac	DP A 3μm	DP yellow	150	25	4 - 6
	MD Dur	DP A 1μm	DP yellow	150	20	4 – 6

The silicon-carbide grinding step was performed in 2-minute intervals with fresh grinding paper and rinsing of the sample between each interval. The total silicon-carbide grinding time varied between panels, (depending on the sample size and type), but at least 2 mm of resin material (approximately 5 repetitions of 2-minute grinding intervals) was removed from each sample. Non-aqueous polishing suspension and non-aqueous lubricant (Struers' DP type "A" suspension and yellow lubricant) were required to generate zinc-coated material microsections of acceptable quality because aqueous solutions etched the zinc coating. Only freshly-polished samples of corroded test panels could be used in SEM analysis because the appearance of the corroded samples degraded within a short time, even when stored in a desiccator.

5.6.2 Cross-sectional Analysis: Microscopy

Scanning electron microscopy (SEM) was used to view and analyse cross-sections of the materials and geometries of interest. Two different instruments were used in this work, a CamScan and a JEOL 6400. The samples were viewed in back-scattered electron (BSE) mode to highlight different material phases (e.g. zinc coating versus steel substrate) as seen in Fig. 5.2. The beam voltage was set to 20 kV to ensure excitation of the metallic iron and zinc phases, which have characteristic Kα energies as shown in Table 5.12 [143].

Table 5.12: Characteristic energies of elements of interest in this work [143]

Characteristic Line	C	O	Mg	Cl	Fe	Zn
Kα (keV)	0.277	0.525	1.253	2.621	6.398	8.628
Kβ (keV)	-	-	1.295	2.815	7.056	9.569
L1 (keV)	-	-	-	0.183	0.615	0.884

Unfortunately the appearance of the paint layer was similar to that of the mounting resin in BSE mode, making it difficult to distinguish the paint from the resin. Secondary electron (SE) images were also collected, but the paint layer charged even at 5 kV accelerating voltage, giving unsatisfactory images. Optical micrographs of the samples were collected to show the paint layers and together with the BSE SEM micrographs generated full pictures of the painted samples

condition as corrosion progressed. The microscope used was a Univar-MET from Reichert-Jung equipped with a Q-Imaging Micropublisher digital camera and connected to Struers' Scentis image analysis software.

Characteristic X-rays of the elements present are also generated by exciting a sample with an electron beam. Both SEM instruments used in this work were equipped with an energy dispersive X-ray (EDS) analysis system and EDS was used to show the distribution of the elements of interest, e.g. zinc, iron, magnesium, oxygen, in corroded cross-sections. EDS analysis was carried out in both line-scan and spot analysis modes, with the line scan showing the transition of elemental distribution through corrosion product and coating layers, and spot analysis showing elemental characterization at a specific point.

The SEM/EDS cross-sectional analysis was used to assess each material's corrosion resistance. For example, corrosion product morphology (whether dense, adherent and protective or cracked, porous and non-protective) could be assessed using BSE images. EDS analysis was used to check for the presence of iron in corrosion products; its presence indicated corrosive attack of the substrate, implying break-down of the corrosion protection system. One shortcoming of the SEM/EDS analysis was the inability to resolve very light elements, including carbon. The presence of carbon (in the form of carbonates) within the corrosion products was of interest in this work and therefore additional analysis techniques were required.

5.6.3. X-Ray Diffraction (XRD)

X-ray diffraction (XRD) allows characterization of the crystalline phases present on a sample surface by measuring the intensity of the scattered X-ray beam at different incident and scattered angles. A Siemens D500 powder diffractometer with copper $K\alpha$ target and theta-2 theta goniometer was used in this work. The goniometer gives accurate positioning of the sample and the detector as they are rotated through a range of angles. A sample measuring approximately 100 mm^2 was cut from each unpainted test panel. Where required, the samples were compressed in a universal testing machine to ensure flatness. The sample was mounted in the fixing clamp

and the diffraction scan was input to the EVA control software. A step-wise scan
was selected and the settings are given in Table 5.13.

Table 5.13: XRD scan settings

Input X-ray	2θ Start	2θ Finish	2θ Step	Step Dwell
Cu Kα 40kV 25mA	10°	80°	0.02°	2 seconds

The resultant diffractograms of X-ray intensity versus diffraction angle (2θ) were
compared to reference standards from the joint committee on powder diffraction
standards (JCPDS) database linked to the Diffrac-AT analysis software. Crystalline
corrosion products (such as zinc oxide (ZnO) and magnesium hydroxide $Mg(OH)_2$)
as well as the metallic material phases (Fe from the substrate and Zn from the
metallic coating) were identified in this way. Correction factors were applied to the
2θ values in the measured data by comparison of the metallic Fe and Zn peaks to
the reference diffractograms. Further details of the XRD analysis steps are given in
Appendix I.

5.6.4. X-ray Photoelectron Spectroscopy (XPS)

X-ray photoelectron spectroscopy (XPS) is more surface-sensitive than XRD
because the detected signal comes from photoelectrons that have escaped the solid
surface (top 5-10 nm of the surface) without experiencing scattering events. XPS
was carried out using a Kratos Axis Ultra instrument. Analysis samples of 10 mm
diameter were cut from the test panels using wire erosion cutting to ensure flatness
of the samples and to avoid disturbance of the sample surface. The samples were
stored in aluminium foil or polystyrene Petri dishes rather than plastic bags to avoid
contamination of the surface by silicone release agents.

The X-ray source was mono-chromated Al-Kα (1486.6 eV) operated at 15 mA
emission current and 10 kV anode potential. The area of analysis was defined by
the largest slot aperture of 300 μm x 700 μm. Survey scans of the samples were
conducted at 80 eV pass energy and high resolution scans at 20 eV pass energy
were performed over a narrow range of energies characteristic of the elements of
interest, (carbon, oxygen, zinc and magnesium). Data analysis was carried out

using CasaXPS software with Kratos sensitivity factors to determine atomic percentage (at.%) values from the peak areas. Components were fitted under the high-resolution scan peaks to give chemical information about the elements of interest. The components' energy values were compared to literature data (e.g. [144,145]). Three scans were run on each sample and charge correction was applied using the adventitious carbon peak at 285 eV. XPS was used primarily for analysis of thin oxide layers on the materials' surfaces. XPS operates under high vacuum (chamber pressure typically 10^{-9} Torr) and therefore heavily corroded samples could not be analysed by XPS due to out-gassing by the corrosion products. Further details of the XPS data analysis procedure are given in Appendix II.

5.6.5. Glow Discharge Optical Emission Spectroscopy (GDOES)

Thicker corrosion products could be analysed using glow discharge optical emission spectroscopy (GDOES), which produces a profile of elemental concentration versus depth. The GDOES instrument operates by producing a stream of argon ions that mill material from the analysis sample surface. The sputtered material is excited in a low pressure (typically 5-10 Torr) plasma discharge and the resulting light emission is used to characterize the sample's composition. The principle is illustrated in Fig. 5.23.
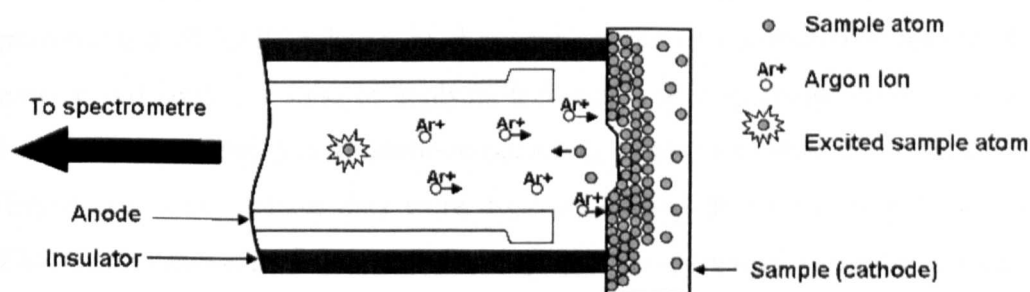

Fig. 5.23: GDOES analysis principle [146].

A LECO GDS-750 equipped with a 4 mm diameter anode and operated at -700 V and 20 mA in an argon atmosphere was used to analyse corroded and uncorroded unpainted test panels. Analysis samples measuring approximately 100 mm^2 were cut from the test panels using a guillotine and mounted in the sample holder. The

rear surface of the heavily corroded samples was ground to remove corrosion products and ensure conductivity of the sample. The atomic concentration of the elements of interest (carbon, oxygen, zinc, magnesium and iron) was evaluated using the standard Leco quantitative depth profile (QDP) analysis. The instrument was calibrated using standards of known composition, although a full range of calibration standards was not available for magnesium. A Mitutoya Surftest profilometer was used to measure the depth of the analysed (sputtered) areas and the depth profiles produced by the GDOES instrument were corrected to match the measured depths.

5.7. SUMMARY

The materials and panel geometries used in this work were selected to generate data that could be related to automotive body panels. Accelerated corrosion tests were required to give corrosion resistance data within the timeframe of the project. Electrochemical testing suggested that ZMG was slightly anodic to conventional zinc coatings in a neutral 5 wt.% NaCl solution, but both ZMG and EG exhibited similar behaviour in a potentiodynamic polarization scan. Accelerated cabinet testing comprising cycles of humidity, salt spray and drying was conducted to test the materials in a corrosion environment more similar to that experienced by vehicles in service than the full immersion condition required for electrochemical tests. Test panels of UC, HDG and EG were fabricated to assess the corrosion performance of ZMG relative to the performance of conventional uncoated and zinc-coated steel. A suite of analysis techniques was employed to determine the bulk and superficial transformations occurring within the protective zinc coatings during corrosion. These data were used to develop the corrosion mechanism of ZMG and to assess its potential as a next generation galvanized steel for automotive vehicle bodies.

Chapter 6

SODIUM CHLORIDE ENVIRONMENT

6.1. INTRODUCTION

The corrosion resistance of zinc-magnesium coated steel (ZMG) and the behaviour of electrogalvanized steel (EG) and hot dip galvanized steel (HDG) in a sodium chloride (NaCl)-based environment are investigated in this chapter. The materials and experimental methods used are given in Section 6.2. The corrosion resistance assessments are given in Section 6.3 and the corrosion products are characterized in Section 6.4. The results are discussed in Section 6.5 and a corrosion mechanism for ZMG in a NaCl-based environment is proposed.

6.2. MATERIALS AND EXPERIMENTAL METHODS

6.2.1. Cabinet Testing

Open corrosion test panels (described in Section 5.3.2) were fabricated from EG, HDG and ZMG materials. The test panels were subject to the Volvo cabinet test method (see Section 5.4.2) for a total of 12 weeks. Three samples of each material were removed from the test cabinet after 4, 8 and 12 weeks of testing. Surface corrosion behaviour was of prime interest in this test phase and edge corrosion effects were not considered. Each panel was designated V4, V8 or V12, meaning Volvo test method with 4, 8 and 12 weeks of exposure respectively (see Table 6.1).

6.2.2. Oxide Growth

A further set of test samples, (one of each coating type), was treated in the Ford corrosion cabinet (described in Section 5.4.3) at 50°C ±2°C and 87% ±3% relative humidity for analysis of the initial stages of oxide growth by X-ray photoelectron spectroscopy. The samples were discs of 10 mm diameter cut to size using wire erosion. A micro-pipette was used to deposit a thin layer of sodium chloride solution (1 wt.% NaCl acidified to pH 4.2, similar to the Volvo cabinet test solution) on to one sample type (O8NaCl) before exposure in the climate chamber.

Each sample was labelled O4, O8 or O8NaCl representing oxide growth samples with 4 hours, 8 hours in the climate chamber without contaminant and 8 hours in the climate chamber with sodium chloride dosing, respectively (see Table 6.1). The samples were supported in a horizontal position in the climate chamber so that the test disc upper surface was wet for the entire exposure period. The lower surface was marked to ensure that analysis was performed on the upper surface only. Table 6.1 lists the test panel types investigated in this chapter.

Table 6.1: Test panel designations and exposure conditions.

Exposure type	Test panel designation	Exposure period	Solution
Volvo cabinet test method	V4	4 weeks	1 wt.% NaCl at pH 4.2
	V8	8 weeks	
	V12	12 weeks	
Oxide growth	O4	4 hours	None
	O8	8 hours	None
	O8NaCl	8 hours	1 wt.% NaCl at pH 4.2

6.2.3. Corrosion Product Characterization

Evolution of red rust was observed during each test and image analysis phase identification was used to express the percentage of panel surface covered in red rust. XRD was used to analyse each material surface before corrosion and after 4, 8 and 12 weeks of corrosion (uncorroded and V4, V8, V12 samples). The corroded samples were taken from within the test panels, i.e. away from the panel edges, and the front surface of the panel was analysed in each case. Further details of the XRD data analysis steps are given in Appendix I. XPS was carried out to establish the surface condition of the materials before and in the earliest stages of corrosion. Three scans were run on each analysis sample (before corrosion treatment and O4, O8 and O8NaCl). XPS analysis was also conducted on samples of each material following 4 weeks of testing according to the Volvo cabinet test method (sample V4). Following initial data collection, a further 5 scans were run on the ZMG sample subjected to 4 weeks of corrosion testing (sample V4). Reference XPS data was generated for ZnO, $ZnCO_3$, $Mg(OH)_2$, $MgCO_3$ and $Mg_5(OH)_2(CO_3)_4.4H_2O$ using analysis grade chemicals. Further details of the XPS data analysis steps are

given in Appendix II. The CamScan scanning electron microscope with energy dispersive X-ray spectrometry (SEM/EDS) was used to view and analyse cross-sections of the corroded samples. EDS line scans were taken from within the resin mount to the steel substrate to track the dispersion of zinc and iron within the corrosion products.

6.3. GENERAL CORROSION RESISTANCE

General corrosion resistance of each coated material was quantified by measurement of the percentage of red rust present on the untreated panel faces during the automated corrosion test as shown in Table 6.2.

Table 6.2: Percentage of panel surface covered by red rust (median of 3 measurements).

Coating	4 weeks	8 weeks	12 weeks
Front surface of test panels			
EG	48% ±12%	61% ±10%	79% ±4%
HDG	31% ±23%	49% ±12%	74% ± 4%
ZMG	0%	<1%	10% ±3%
Rear surface of test panels			
EG	6% ±1%	35% ±10%	53% ±26%
HDG	6% ±1%	28% ±11%	61% ±13%
ZMG	0%	0%	4% ±2%

Significant rust was defined as at least 5% of the panel surface visibly rusted, in accordance with the work of Tsujimura et al. [17]. The number of cycles to significant rusting of each material and each panel surface was also measured and the results are shown in Fig. 6.1.
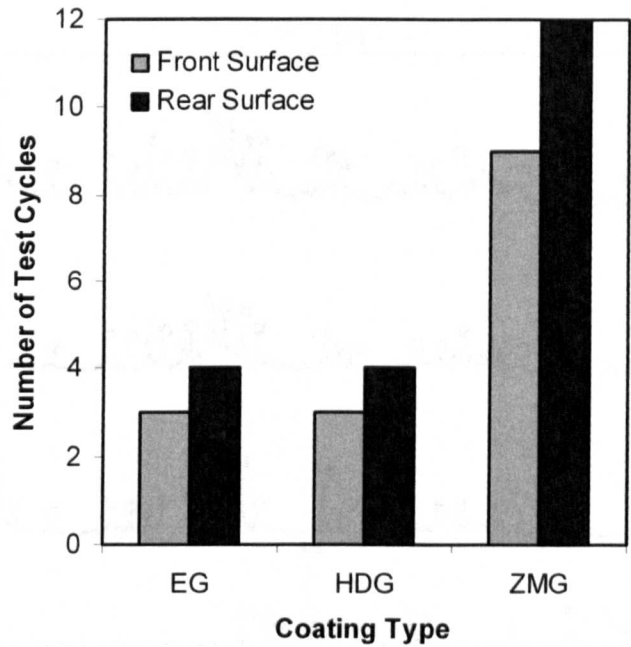
Fig. 6.1: Number of test cycles to significant (at least 5% of total panel surface) red rust.

6.4. CORROSION PRODUCT CHARACTERIZATION

6.4.1. Corrosion Product Characterization by XRD

Fig. 6.2 shows the X-ray diffractograms obtained on EG and ZMG after 4, 8 and 12 weeks of corrosion. The diffractogram obtained from each sample before corrosion testing is also shown for comparison. Peaks at $2\theta \approx 45°$ and $2\theta \approx 66°$ are attributable to diffraction from the steel substrate. As expected, the galvanized steels (EG and HDG) gave similar results and only the EG diffractogram is shown in Fig. 6.2. Metallic zinc peaks were seen on EG and HDG only in the non-corroded samples. Simonkolleite and zinc oxide peaks were detected after 4 weeks of corrosion. A broader peak at $2\theta \approx 13°$ indicated the presence of zinc hydroxy carbonate. As corrosion progressed, the relative intensity of the zinc corrosion products peaks decreased whilst iron-containing corrosion products peaks increased in intensity. The diffractograms for the ZMG samples (Fig. 6.2b) illustrate the material's greater resistance to corrosion. A single crystalline corrosion product, simonkolleite, was detected after 4 weeks of corrosion testing. No zinc oxide was detected by XRD during the 12 weeks of testing.
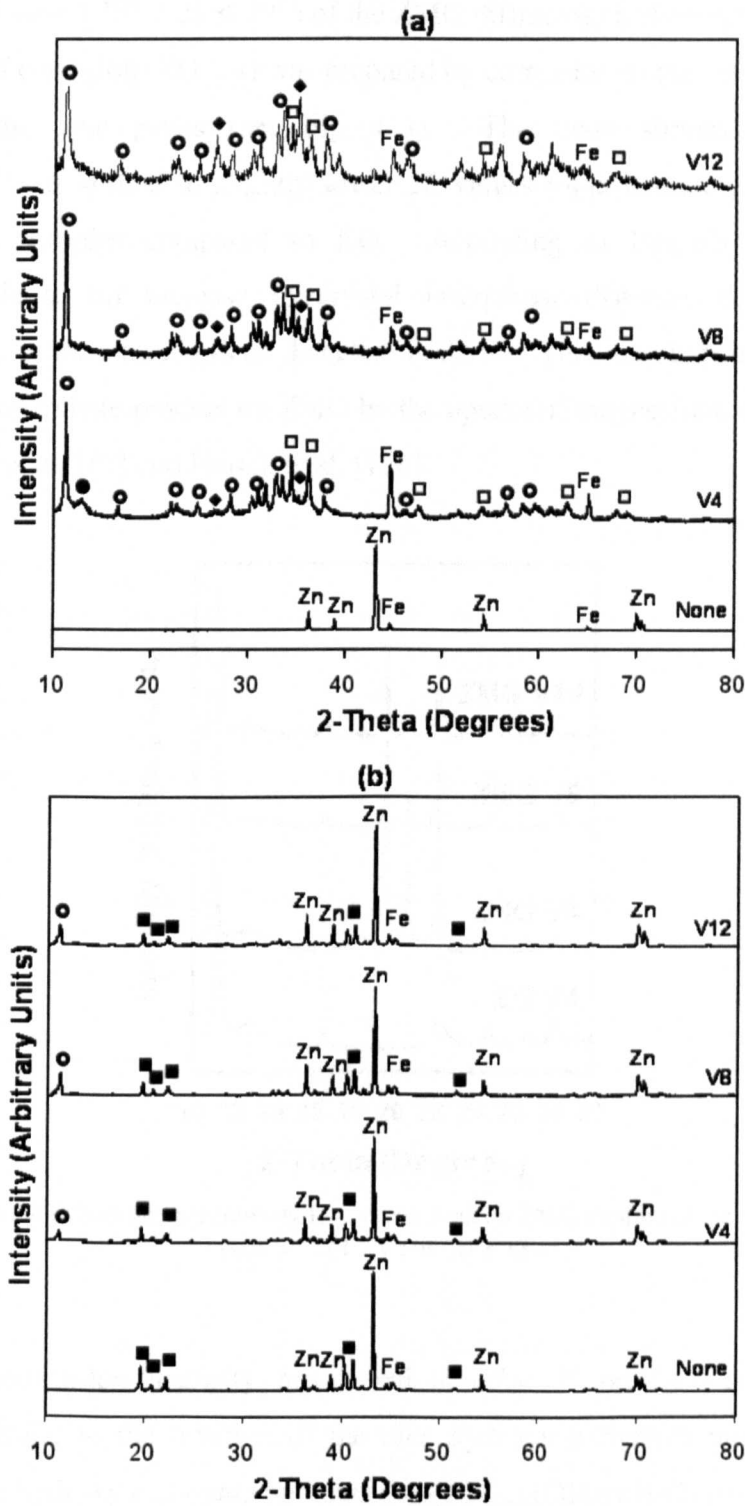
Fig. 6.2: XRD diffractograms of (a) EG and (b) ZMG without corrosion treatment and after 4, 8 and 12 weeks of corrosion testing (none, V4, V8 and V12, respectively).

Notes:
Open circle = simonkolleite $Zn_5(OH)_8Cl_2.H_2O$
Closed circle = zinc hydroxy carbonate $Zn_4(OH)_6CO_3.H_2O$
Open square = zinc oxide ZnO
Closed diamond = iron oxides and hydroxides
Closed square = zinc magnesium Zn_2Mg

A detailed view ($10° \leq 2\theta \leq 30°$) of the ZMG diffractograms compared to EG after 4 weeks of corrosion (EG V4) was prepared by correction of the 2θ scale relative to the metallic zinc peaks (see Fig. 6.3). The main simonkolleite peak at $2\theta \approx 11.2°$ was shifted to slightly lower 2θ values (approximately $2\theta - 0.04°$) for the ZMG samples compared to EG. According to Bragg's law, the shift corresponds to an increase in crystal interplanar distance, d, of 0.02–0.03 Ångstroms in the simonkolleite detected on ZMG. This may indicate modification of the simonkolleite product on ZMG by the uptake of magnesium, as suggested by Tsujimura et al. [17] and Prosek et al. [126].
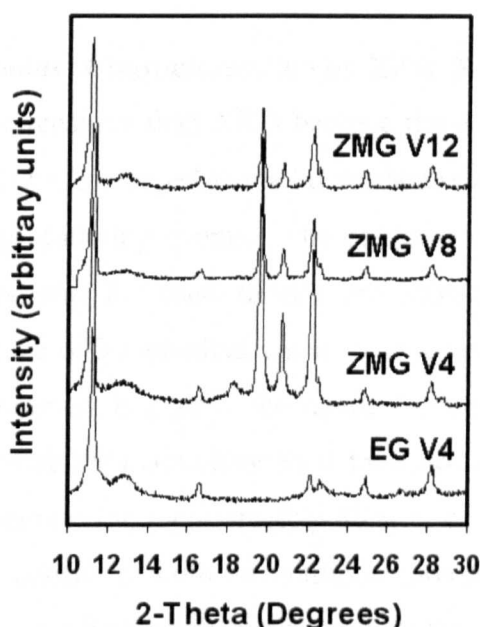
Fig. 6.3: Detail diffractograms showing low, broad peak on ZMG samples at $2\theta \approx 13°$ and extra peak on ZMG V4 at $2\theta \approx 18.4°$.

Fig. 6.3 shows a low intensity, broad peak at $2\theta \approx 13°$ on ZMG at each analysis interval, similar to the position of the zinc hydroxy carbonate peak on EG V4. Magnesium hydroxy carbonate hydrates ($Mg_5(CO_3)_4(OH)_2 \cdot nH_2O$) (n=4,5) also have a main diffraction peak close to $2\theta \approx 13°$ although they also have a stronger peak at $2\theta \approx 15°$. Crystalline species that have been subjected to shear stress, nano-crystalline species and amorphous species may exhibit broad diffraction peaks. It is possible that the hydroxy carbonate species detected on ZMG was not fully crystallized. The hydroxy carbonate peak was less pronounced after 8 weeks of

corrosion (V8) compared to the samples after 4 weeks (V4) and after 12 weeks (V12) of corrosion. No simonkolleite or hydroxy carbonate peaks were detected by XRD on a second sample of ZMG V4. These observations indicate that the carbonate product on ZMG was formed locally on the sample surface and was not a continuous layer. Due to the low intensity of the hydroxy carbonate signal on ZMG, it was not possible to diagnose the exact product present using XRD. A small peak at $2\theta \approx 18.4°$, which may be attributed to magnesium hydroxide, was also observed on ZMG V4 but not on the samples corroded for a longer period. This indicates that magnesium hydroxide may have transformed to other products (e.g. hydroxy carbonate or modified simonkolleite) as corrosion progressed.

6.4.2. Corrosion Product Characterization by XPS: Survey Scans

XPS is more surface sensitive than XRD because the detected signal comes from photoelectrons which have escaped the solid surface (top 5-10 nm of the surface) without experiencing scattering events. The atomic concentrations (at.%) of the detected elements present for each sample are shown in Fig. 6.4. The value presented is the average of 3 individual scans. Some variation in elemental atomic concentration was observed; in general the standard deviation was less than 3 at.%. Carbon and oxygen were the main elements detected on EG and HDG samples for each treatment, accounting for approximately 80 at.% of the surface material. The carbon content may consist of both adventitious carbon (i.e. contamination) and carbonate products. Contributions from zinc and, in the case of ZMG, magnesium were recorded. The presence of magnesium resulted in relatively lower concentrations of carbon and oxygen on ZMG samples without corrosion treatment (none) and following the oxide growth exposures (O4, O8 and O8NaCl). Following the longer exposure period (4 weeks) of V4, large amounts of carbon and oxygen were recorded on the ZMG surface. Magnesium concentration was lower on the NaCl-treated samples (treatments O8NaCl and V4) than on the samples without NaCl treatment, indicating dissolution of magnesium and/or zinc enrichment of the surface layers in the sodium chloride environment.

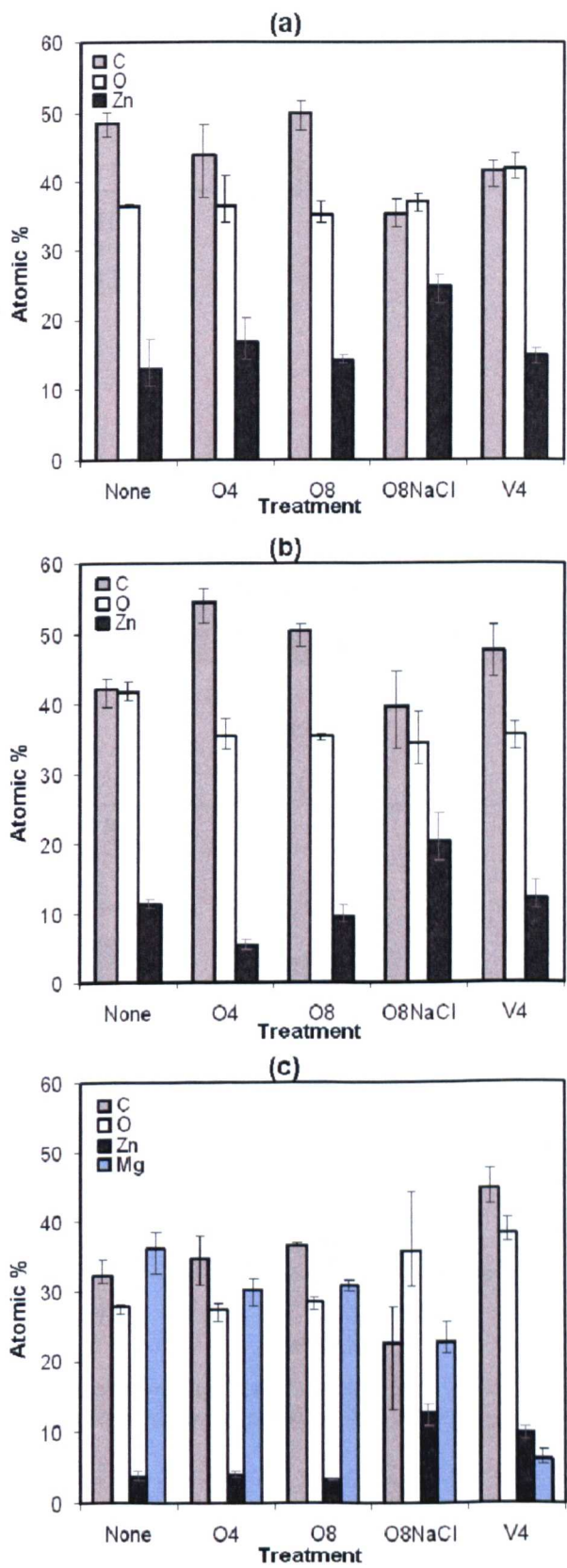Fig. 6.4: XPS survey scan showing atomic percentages (at.%) of main elements for (a) EG (b) HDG and (c) ZMG sample surfaces.

Measured ratios of oxygen to zinc and magnesium are shown in Fig. 6.5 and calculated ratios of possible corrosion compounds are shown in Table 6.3.
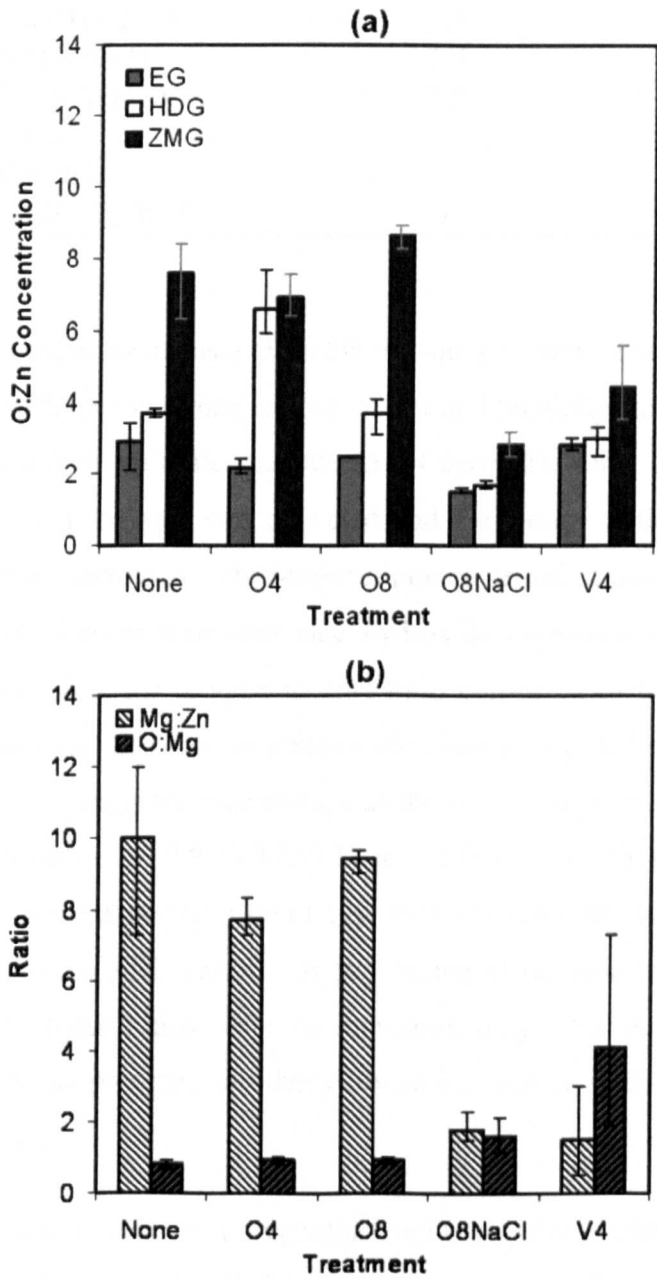

Fig. 6.5: XPS survey scan quantifications. Ratios of (a) oxygen to zinc and (b) magnesium to zinc and oxygen to magnesium (ZMG sample only).

Table 6.3: Calculated ratios of possible corrosion compounds.

Compound	O:Zn	O:Mg
ZnO	1.0	-
Zn(OH)$_2$	2.0	-
Zn$_4$CO$_3$(OH)$_6$.H$_2$O	2.5	-
Zn$_5$(CO$_3$)$_2$(OH)$_6$	2.4	-
Zn$_5$Cl$_2$(OH)$_8$.H$_2$O	1.8	-
MgO	-	1.0
Mg(OH)$_2$	-	2.0
Mg$_5$(CO$_3$)$_4$(OH)$_2$.4H$_2$O	-	3.6

The zinc to oxygen ratios measured on the test samples show that the zinc surfaces were enriched with oxygen when exposed to air and humidity (high oxygen to zinc ratio without treatment and after treatments O4 and O8). Once NaCl was applied (treatment O8NaCl) the zinc was activated and the values of the zinc to oxygen ratios at the surface increased. The longer exposure period of treatment V4 allowed the formation of simonkolleite and zinc hydroxide carbonate, reducing the zinc activity and increasing the oxygen to zinc ratio compared to treatment O8NaCl. Formation of sodium carbonate or sodium bicarbonate also led to reduced zinc to oxygen ratio as the oxygen concentration at the surface increased. EG and HDG zinc to oxygen ratios of 2.8 (+0.2,-0.1) and 3.0 (+0.3,-0.5) respectively were relatively close to the expected ratio of zinc hydroxy carbonate after treatment V4, in agreement with the XRD results. A percentage of the zinc was in the form of simonkolleite, so these ratios serve as indicators only. Excess oxygen may be accounted for by the presence of other carbonates, such as sodium carbonates, on the sample surface.

Calculation of carbon to zinc and magnesium ratios was not possible due to the high levels of carbon contamination on the sample surfaces (see Fig. 6.4). Magnesium to zinc and oxygen to magnesium ratios for ZMG samples are shown in Fig. 6.5b. The magnesium to zinc ratios measured after the short-term exposures (O4, O8 and O8NaCl) were greater than the ratio of Zn$_2$Mg, indicating magnesium-enrichment of the surface layers in the early stages of corrosion. After treatment V4, the measured ratio was 1.5 (+1.5,-1.0), closer to the ratio of Zn$_2$Mg, but on average with excess magnesium. Oxygen to magnesium ratios for non-NaCl treated

samples (None, O4 and O8) were close to unity, indicating the presence of MgO. Once salt was applied, an excess of oxygen was observed, indicating hydroxide and possibly carbonate formation. After treatment V4, the ratio of oxygen to magnesium was 4.1 (+3.2,-2.2), indicating the presence of significant levels of oxidized species other than MgO. The large variations in elemental concentrations on ZMG after treatment V4 indicate a mixture of corrosion products on the sample surface.

6.4.3. Corrosion Product Characterization by XPS: Detail Scans

Examination of the elemental peak positions and shapes gives more information about the compounds present on the samples' surfaces. Charge correction of the high resolution scans to the main carbon 1s peak at 285 electron Volts (eV) on the energy scale enabled measurement of peak positions. Differential charging of some samples (for example EG after treatments O8NaCl and V4 and HDG after treatment O8NaCl) caused the detected photoelectron peaks to broaden, making the data difficult to interpret. In these cases, charge correction was estimated by cross-referencing the metallic peak positions. In the following sections, peak analysis and component fitting of each of the elements of interest is discussed in turn.

Zinc peak analysis

Analysis of the binding energy (BE) and kinetic energy (KE) of the zinc and oxygen XPS signals gives information about the state of the zinc on the corroded test samples. Reference data [145, 147-148] for metallic zinc and zinc oxide Zn 2p BE are similar but they can be differentiated by measurement of the zinc Auger peak, Zn LMM, positions, as shown in Table 6.4. Analysis grade samples of ZnO and $ZnCO_3$ were also analysed and the measured signals are given in Table 6.4 (marked with [a]). The measured energy values for zinc, oxygen and carbon main peaks for EG, HDG and ZMG following each treatment are given in Table 6.5.

Table 6.4: Reference energy values for zinc and zinc compounds main peaks from the literature [145,147-149] or measured in this work using analysis grade chemicals.

Signal	Zn	ZnO	Zn(OH)$_2$	ZnCO$_3$	Zn$_5$(CO$_3$)(OH)$_6$
Zn 2p BE	1021.7 [145]	1022.1 [145,147] 1021.6[a]	1022.7 [147]	1022.0[a]	1021.7 [149]
Zn LMM KE	992.1 [145]	988.1 [147] 988.4[a]	986.5 [147]	987.4[a]	988.0 [149]
O 1s BE	-	530.2 [148] 530.5[a]	Not available	531.7[a]	Not available
C 1s BE	-	-	-	289.6[a]	289.1 [149]

[a] Measured in this work.

Table 6.5: Measured energy values of zinc, oxygen and carbon main peaks on EG, HDG & ZMG for each treatment.

| Material | Signal | Treatment | | | | |
		None	O4	O8	O8NaCl	V4
EG	Zn 2p BE	1021.9	1021.3	1021.9	1021.3	1021.8
	Zn LMM KE	987.6	986.9	987.3	987.5	987.9
	O 1s BE	531.8	531.7	532.0	531.9	531.7
	C 1s BE	289.0	289.2	288.7	charged	charged
HDG	Zn 2p BE	1022.0	1021.9	1021.5	1021.7	1021.7
	Zn LMM KE	987.5	987.2	987.8	987.8	987.4
	O 1s BE	531.7	531.7	531.4	532.0	531.7
	C 1s BE	288.9	288.4	288.7	charged	289.0
ZMG	Zn 2p BE	1022.0	1022.5	1022.0	1021.6	1022.0
	Zn LMM KE	987.6	989.3	987.7	987.8	987.3
	O 1s BE	531.7	531.8	531.6	531.8	532.0
	C 1s BE	289.2	289.3	288.9	charged	289.7

The measured results for zinc 2p and Auger peaks on EG and HDG show reasonable agreement with reference data for zinc oxide and for hydrozincite (Zn$_5$(CO$_3$)$_2$(OH)$_6$). The oxygen energy values measured did not show close agreement with the literature data for zinc oxide, but were close to the measured BE of zinc carbonate (ZnCO$_3$). This product was recently reported on zinc exposed to a marine environment by Natesan et al. [105] but has not been detected by other workers (see Table 4.3), nor was it indicated here by the XRD analysis. Considering the oxygen to zinc ratios shown in Fig. 6.5a, the data suggest the presence of a mixture of zinc oxide and a zinc carbonate corrosion product on the EG and HDG samples. It is likely that the carbonate product was zinc hydroxy carbonate, (Zn$_4$(OH)$_6$CO$_3$.H$_2$O), as identified by XRD. No XPS reference data

were found for zinc hydroxy carbonate. Simonkolleite reference data were not available but the XRD results showed that this product was present after treatment V4, hosting a significant percentage of the corroded zinc.

Unfortunately, no reference data for Zn_2Mg were found so measurements on ZMG must be treated with caution. ZMG showed similar zinc, oxygen and carbon energy values to EG and HDG samples, indicating a possible mixture of zinc oxide and a carbonate species on the corroding surface. The carbonate on ZMG may be bound to zinc or magnesium.

Magnesium Peak Analysis

Magnesium enrichment in the surface layers of ZMG without treatment and after treatments O4 and O8 was indicated by the zinc to magnesium ratios (Fig. 6.5b) and the oxygen to magnesium ratios were close to the atomic ratio of magnesium oxide. Reference data for magnesium compounds from the literature and measured in this work are given in Table 6.6. The measured magnesium 2p, 1s and Auger peak positions for ZMG samples following each corrosion treatment are given in Table 6.7.

Table 6.6: Reference [145] energy values of magnesium and magnesium compounds main peaks.

Signal	Mg [145]	MgO [145]	Mg(OH)$_2$	MgCO$_3$[a]	Mg$_5$(OH)$_2$(CO$_3$)$_4$.4H$_2$O[a]
Mg 2p BE	49.6	50.4	49.5 [145] 49.6[a]	50.6	50.1
Mg KLL KE	1185.6	1180.4	1180.2[a]	1179.9	1180.5 & 1178.0
Mg 1s BE	1303.2	1304.0	1302.7 [145] 1303.3[a]	1304.6	1303.8 & 1305.5
O 1s BE	-	532.1	531.3[a]	532.1	531.8 & 533.9
C 1s BE	-	-	-	290.1	286.0 & 289.8

[a] Measured in this work.

Table 6.7: Measured energy values of magnesium main peaks on ZMG for each treatment.

Signal	Treatment				
	None	O4	O8	O8NaCl	V4
Mg 2p BE	50.3	49.9	50.0	50.0	-
Mg KLL KE	1180.9	1180.1	1180.6	1180.7	1180.0
Mg 1s BE	1303.9	1303.6	1303.2	1303.0	-

The measured values in Table 6.7 indicate the presence of magnesium oxide before corrosion treatment. The reduction in magnesium 1s BE values points to the transformation of magnesium oxide to magnesium hydroxide as the corrosion exposures increased. No reference data were found for Zn_2Mg so it was not possible to assess the samples for its presence. The oxygen 1s values were dominated by the carbonate species ($BE \approx 532eV$). Unfortunately no magnesium 2p or 1s signal was detected after treatment V4 and the reference data show little separation of magnesium Auger peak positions for the oxide, hydroxide and carbonate species. These limitations prevented estimation by XPS of the magnesium condition after treatment V4.

Carbonate on ZMG

The adventitious carbon peak occurs at $BE = 285eV$ and oxidized carbon was displaced to a higher $BE \approx 289eV$. Analysis of the C 1s XPS scan confirmed the presence of a carbonate corrosion product on EG and HDG, in agreement with the XRD results. The presence of a carbonate species on ZMG after treatment V4 was also shown by the XPS scans (Fig. 6.6). Reference scans of $Mg_5(OH)_2(CO_3)_4.4H_2O$, $MgCO_3$ and $ZnCO_3$ were compared to the ZMG O 1s and C 1s scans. The ZMG C 1s peak was closer to the zinc carbonate than to the magnesium carbonate or magnesium hydroxy carbonate peaks but the O 1s peak was rather broad and generally shifted to lower energy values compared to the zinc carbonate peak and showed closer alignment to the magnesium hydroxy carbonate scan. Full width half maximum (FWHM) measurements of the peak components showed a broadening of the oxygen 1s peak on ZMG V4, indicating a mixture of carbonate and oxide species. The carbonate component was not discernible on every ZMG sample; only 2 of 5 samples analysed showed distinct carbonate peaks, indicating heterogeneous distribution of the carbonate product. The detection of carbonate by XPS indicates that the carbonate product was present within the top 5–10 nm of the material's surface.

(a)

(b)
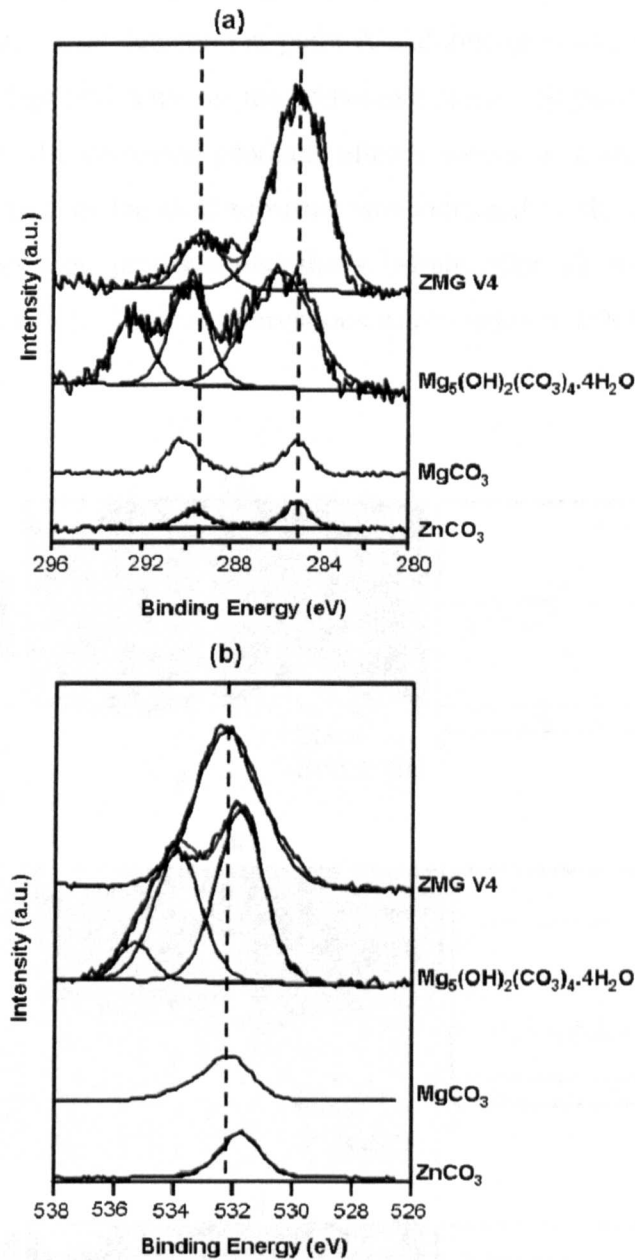
Fig. 6.6: Comparison of ZMG V4 to reference carbonate peaks for (a) C 1s peaks and (b) O 1s peaks.

6.4.4. Corrosion Product Characterization by SEM/EDS

SEM analysis of the corroded panel cross-sections revealed the corrosion product morphologies; EDS analysis was used to check for the presence of iron in the corrosion products. Heterogeneous corrosion was observed in all cases.

Fig. 6.7a-c shows SEM micrographs and corresponding EDS line scans for EG samples after 4, 8 and 12 weeks of the Volvo cabinet test. Line scans were taken

from point A on the mounting resin (and outside the sample area) to point B within the steel substrate. Iron detection at point A and zinc response at point B indicate the level of background noise in the respective scans. Significant levels of iron were detected in the corrosion products after 8 weeks of corrosion testing (Fig. 6.7b). Pitting attack of the steel substrate was indicated by the u-shaped interface between the corrosion products and the substrate after 12 weeks of corrosion testing, (see Fig. 6.7c). Similar observations were made on HDG samples analysed in the same way.
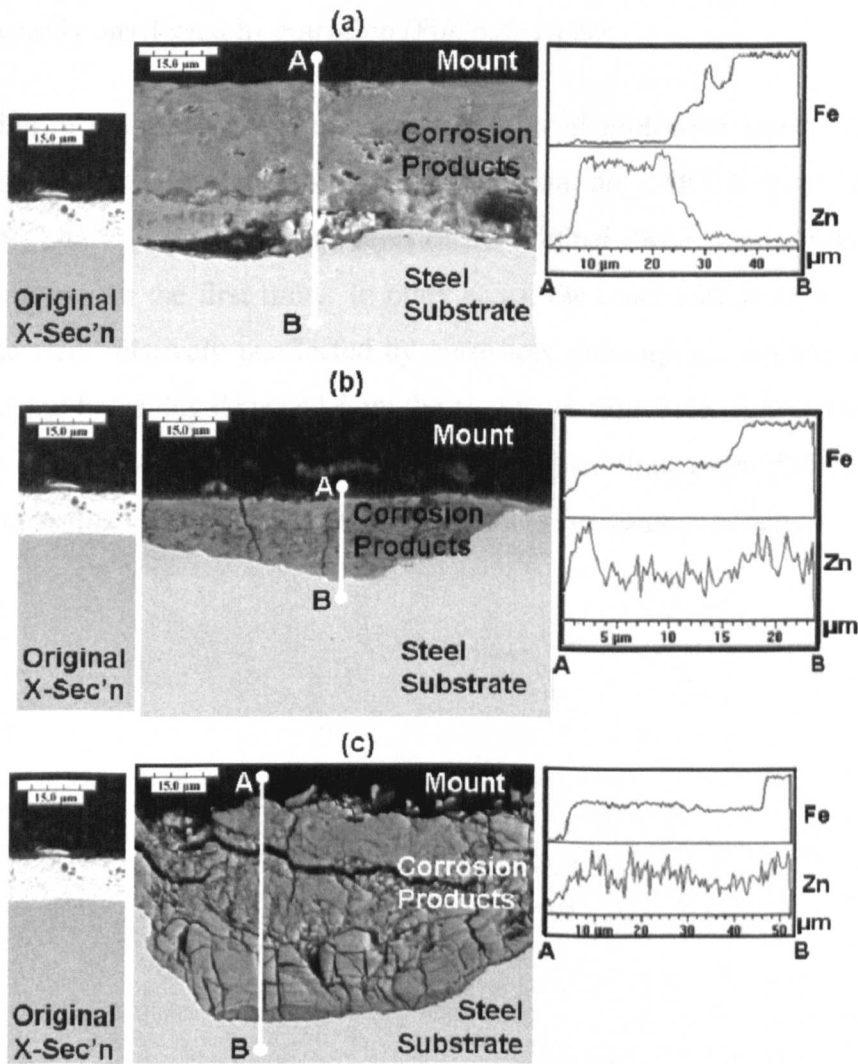

Fig. 6.7: Cross-sections of EG sample after (a) 4 (b) 8 and (c) 12 weeks of Volvo cabinet test. EDS line scans show iron and zinc presence along line AB.

SEM images of ZMG cross-sections after 4, 8 and 12 weeks of corrosion testing (test panels V4, V8 and V12) are shown in Fig. 6.8a-d. EDS analysis showed that

no iron was present in the corrosion products even after 12 weeks of corrosion testing. ZMG V4 appeared relatively unaffected in some areas (cathodes) and at other areas (anodes) exhibited significant corrosive attack (see 6.8a *centre* and *right*). A corrosion product offering barrier protection was observed on ZMG after 8 weeks of corrosion testing (see Fig. 6.8b *centre* and 6.8c). The dense layer of approximately 8 µm thickness extended over 400 µm of the sample surface. EDS analysis indicated the presence of zinc, magnesium, chlorine, carbon and oxygen within the layer. Cracked and porous corrosion products were observed at other areas of the ZMG V8 sample but the underlying zinc layer of the original coating was generally unaffected by corrosion (Fig. 6.8b *right*).

Protection of the steel substrate via precipitation of protective corrosion products was also observed after 12 weeks of corrosion on ZMG (Fig. 6.8d *centre*). Corrosive attack of the inner zinc layer of the original ZMG coating was observed in some areas for the first time. In other areas, the inner zinc layer and the steel substrate were relatively unaffected by corrosion, although the Zn_2Mg phase was depleted and becoming detached from the zinc layer (Fig. 6.8d *right*). These cross-sections show that ZMG coating protected the steel substrate even after 12 weeks of corrosion testing via the precipitation of protective corrosion products.

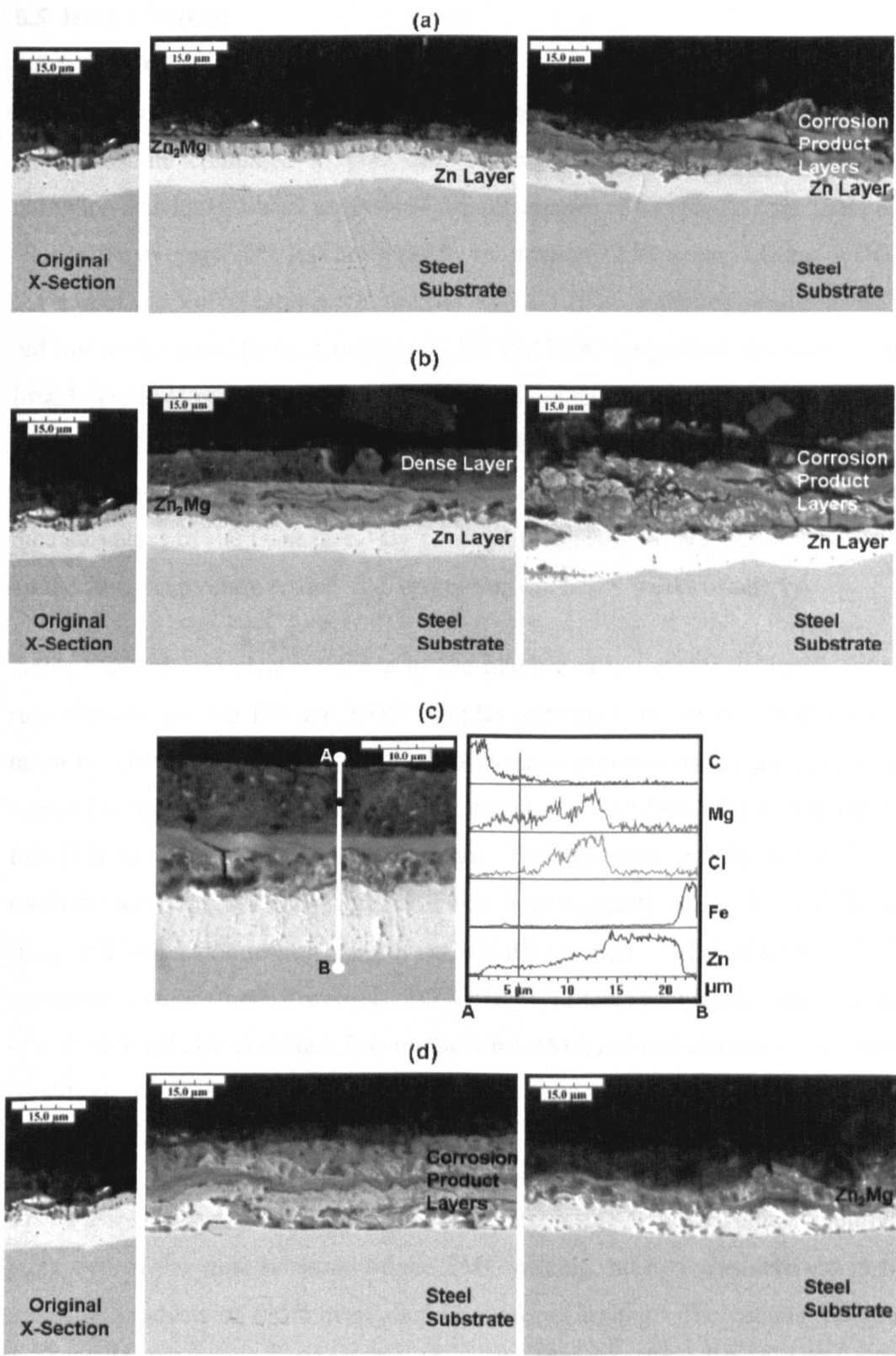**(a)**

(b)

(c)

(d)

Fig. 6.8: Cross-sections of ZMG sample after (a) 4, (b) 8 and (d) 12 weeks of Volvo cabinet test; (c) detail view and EDS line scan of corrosion products on ZMG V8 *centre*.

6.5. DISCUSSION

6.5.1. General Corrosion Resistance

The results confirm that the ZMG coating offers superior corrosion protection to the steel substrate compared to pure zinc coatings when tested to an automotive corrosion standard. Visual analysis of the appearance of test panels (see Table 6.2) showed on average 70% less coverage by red rust on ZMG versus EG and HDG at the end of the Volvo cabinet test period. EG and HDG exhibited similar levels of red rust on the panel faces. Corrosion of EG and HDG progressed far enough in the first 4 weeks of corrosion testing to produce significant rusting on the front faces. The more sheltered rear faces suffered less rusting at first but by the end of the test, the rear face rust percentage upper values were approximately the same as the median values of the front face. By contrast, practically no red rust was observed on the zinc-magnesium coated steel samples in the first 8 weeks of test.

Assessment of corrosion resistance by the number of test cycles to significant red rust showed that the EG and HDG samples generated rust in one-third the time taken by ZMG (see figure 6.1). A 3-fold increase in corrosion resistance of ZMG versus EG and HDG is rather modest compared to the 10-fold [17,14-160] and 24-fold [13] increases reported in the literature. The difference may be due to the test methods used; greater corrosion resistance improvements were observed in salt spray and immersion testing using 5 wt.% NaCl solution. Constant wetting of the corroding surface (time of wetness, TOW=100% of test time) leads to rapid attack of conventional zinc coatings. It is implied that ZMG resisted corrosion even under conditions of high TOW. The mechanisms involved will be explored in the following sections.

Visual assessment as well as SEM-EDS and XRD results indicated almost complete protection of the steel substrate by the ZMG coating: no iron was detected in the corrosion products of ZMG even after 12 weeks of testing. The contrast between the EG and ZMG cross-section after 12 weeks of testing (Fig. 6.7c and Fig. 6.8d) highlights the improvement in corrosion resistance achieved by ZMG. These findings suggest that time to surface rusting should not be taken as the single quantification of a material's resistance to corrosion. This point was highlighted by

the work of Morishita et al. [14], which reported a long incubation period after initiation of red rust on ZMG. A recent investigation by Ström et al. [59] suggests a similar, although less effective, phenomenon on zinc coatings; even after consumption of the zinc coating, the material did not immediately exhibit the corrosion rate of uncoated steel.

Combination of XRD and XPS analysis gives information about superficial and bulk transformations within the metallic coating. Corrosion products formed on the zinc coatings in this work correspond well to those reported in the literature (refer to Table 4.3). The XRD, XPS and cross-sectional analysis of ZMG suggests that a modified protection mechanism is at work when the zinc coating contains magnesium. Using the mechanisms of zinc corrosion in a NaCl-based environment discussed in Chapter 4 as a baseline, a mechanism was proposed for the corrosion of ZMG in a sodium chloride-based atmosphere. The possible reactions taking place before and during the corrosion treatments are developed in the following sections.

6.5.2. ZMG Corrosion in a NaCl-based Atmosphere: Initial Condition

XPS analysis in this work confirmed the presence of MgO on the surface of ZMG before and during the early stages of corrosion. Magnesium oxide, unlike zinc oxide, is an insulator and may act to hinder oxygen reduction, suppressing the overall corrosion reaction. Inhibition of zinc corrosion in magnesium-containing sea water, attributed to the formation of protective, insoluble magnesium-hydroxide, has been reported in the literature [23,150]. The oxygen to magnesium ratios detected by XPS on the ZMG samples in this work before corrosion treatment and after treatments O4 and O8 (0.8 ($\pm$0.1), 0.9 ($\pm$0.1) and 0.9 ($\pm$0.1) respectively) were closer to the stoichiometric composition value of MgO (1.0). If the magnesium oxide layer was very thin (less than 5-10 nm), some magnesium from the Zn_2Mg phase of coating may have been detected by XPS, increasing the magnesium peak intensity and reducing the calculated O:Mg ratio. The measured component peak positions were close to the reference data for MgO (see Table 6.6 and Table 6.7), indicating that the surface of ZMG was passivated by MgO formation before any corrosion testing took place. Therefore the first step in the

corrosion mechanism of ZMG is the formation of a passivating layer of MgO when ZMG is exposed to air. This is in agreement with Stratmann [128], who reported a magnesium oxide layer of 4 nm thickness on ZMG.

### 6.5.3. ZMG Corrosion in a NaCl-based Atmosphere: Humid Conditions

Magnesium hydroxide is thermodynamically more stable than magnesium oxide in the presence of water [25,151] and $Mg(OH)_2$ formation may be expected on samples exposed to wetter conditions, according to (6.1).

$$MgO(s) + H_2O(aq) \rightarrow Mg(OH)_2(s) \qquad (6.1)$$
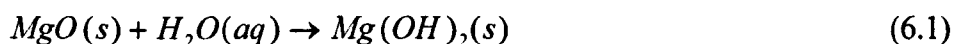
When ZMG corrodes in an aqueous sodium-chloride environment, such as treatments O8NaCl and V4, magnesium may be expected to oxidize electrochemically to form hydrolysed ions in solution (6.2).

$$Mg(s) \rightarrow Mg^{2+}(aq) + 2e^- \qquad (6.2)$$

The anodic reaction (6.2) is balanced by the reduction of dissolved oxygen according to (6.3).

$$\tfrac{1}{2}O_2(aq) + H_2O(aq) + 2e^- \rightarrow 2OH^-(aq) \qquad (6.3)$$
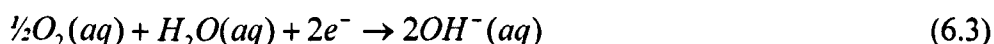
The magnesium ions produced by (6.2) precipitate as magnesium hydroxide, $Mg(OH)_2$, on cathodic areas of the surface where reaction (6.3) has led to increased pH (6.4).

$$Mg^{2+}(aq) + 2OH^-(aq) \rightarrow Mg(OH)_2(s) \qquad (6.4)$$
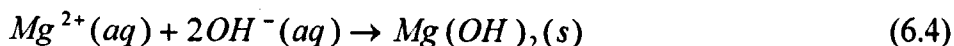
The oxygen to magnesium ratio, 1.6 (+0.5,-0.4), calculated from XPS measurements on ZMG after treatment O8NaCl was in the range of $Mg(OH)_2$. Variations in the measured values may be explained by the heterogeneous corrosion products as shown by the cross sections in Fig. 6.8. $Mg(OH)_2$ is thermodynamically stable in alkaline conditions and electrochemically inert [25]. Cathodic activity can be reduced as high pH sites are covered by a magnesium
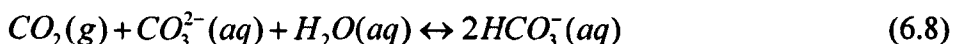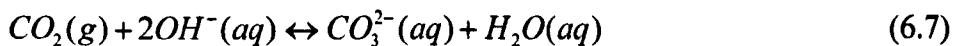
hydroxide precipitate. Depending on the nature of the formed film, it may offer further protection to the underlying material.

6.5.4. ZMG Corrosion in a NaCl-based Atmosphere: CO_2 Influence

Lindström et al. [152] reported that magnesium hydroxide is converted to magnesium hydroxy carbonate in the presence of carbon dioxide. The test conditions in this work allowed access of carbon dioxide to the corroding surface and the precipitated hydroxide layer may convert to hydroxy carbonates according to reactions (6.5-6.6).

$$2Mg(OH)_2(s) + CO_3^{2-}(aq) + 3H_2O(aq) \tag{6.5}$$
$$\leftrightarrow Mg_2CO_3(OH)_2 \cdot 3H_2O(s) + 2OH^-(aq)$$

$$5Mg_2CO_3(OH)_2 \cdot 3H_2O(s) + 3CO_3^{2-}(aq) + H_2O(aq) \tag{6.6}$$
$$\leftrightarrow 2Mg_5(CO_3)_4(OH)_2 \cdot 4H_2O(s) + 6OH^-(aq)$$
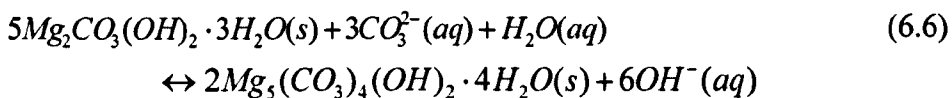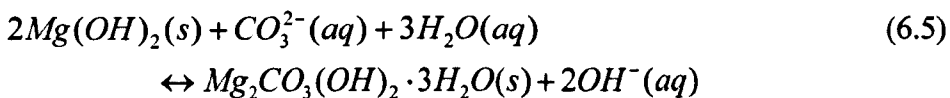
The released hydroxide ions will react with supplied carbon dioxide, reactions (6.7)-(6.8). The presence of hydroxy carbonate on corroding ZMG was suggested by the presence of a low intensity, broad peak at $2\theta \approx 13°$ on the diffractograms (Fig. 6.2-6.3).

$$CO_2(g) + 2OH^-(aq) \leftrightarrow CO_3^{2-}(aq) + H_2O(aq) \tag{6.7}$$

$$CO_2(g) + CO_3^{2-}(aq) + H_2O(aq) \leftrightarrow 2HCO_3^-(aq) \tag{6.8}$$

A recent study of magnesium corrosion in a sodium chloride environment by Jönsson et al. [153] suggested that direct transformation of magnesium hydroxide to magnesium carbonate occurs rather rapidly under atmospheric conditions (6.9):

$$Mg(OH)_2(s) + CO_2(g) \rightarrow Mg(CO)_3(s) + H_2O(s) \tag{6.9}$$
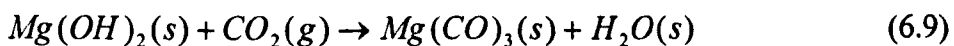
Hydration of magnesium carbonate leads to nesquehonite ($MgCO_3.3H_2O$) and subsequently hydromagnesite formation ($Mg_5(OH)_2(CO_3)_4.4H_2O$). The MgO-CO_2-H_2O stability diagram devised by White [154] (see Fig. 6.9) shows likely formation

of magnesium carbonate under atmospheric conditions and magnesium hydroxy carbonate stability under conditions of high humidity.
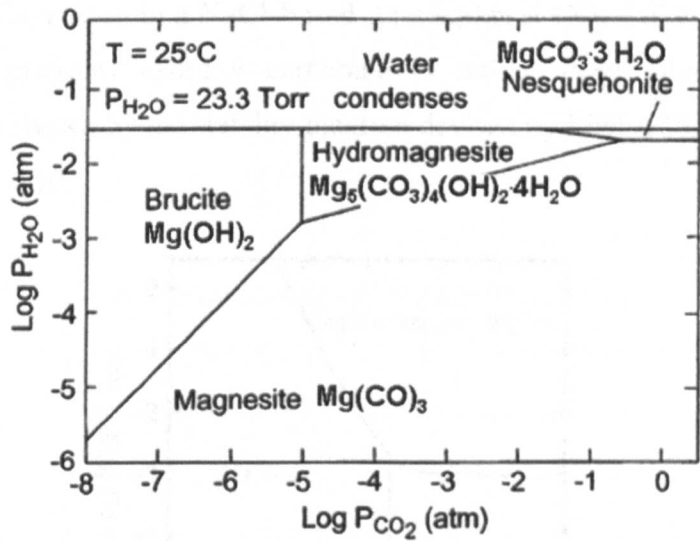

Fig. 6.9: Stability diagram for the $MgO-CO_2-H_2O$ system in the solid vapour region [154].

The oxygen to magnesium ratios of the hydrated magnesium hydroxy carbonates in reactions (6.5), (6.6) and (6.9) are 4.0, 3.6 and 3.0 respectively. The oxygen to magnesium ratio calculated from XPS measurements for ZMG V4 was 4.1 (+3.2,2.2). A large variation in calculated ratio can be expected in heterogeneous corrosion; some areas may be rich in hydroxy carbonate corrosion products, other areas may be rich in magnesium hydroxide (O:Mg=2:1). Some of the oxygen was also bound to zinc in the form of simonkolleite. Taking the ratio of magnesium to zinc to oxygen as 1:1.5:4.1 (from Fig. 6.5a-b), and assuming all detected magnesium was bound to $Mg_5(OH)_2(CO_3)_4.4H_2O$ and all detected zinc was bound to simonkolleite, a theoretical magnesium to oxygen ratio can be calculated as 6.3. Taking magnesium hydroxide as the magnesium compound and taking zinc oxide as the zinc compound gives a theoretical magnesium to oxygen of 3.5. These values are within the range of magnesium to oxygen ratios (4.1 (+3.2,-2.2)) calculated from XPS scans on ZMG V4.

It is proposed that magnesium hydroxy carbonate was likely formed on the corroding ZMG surface in this work, although full and direct evidence of its

presence was not generated. Possible effects of the presence of magnesium hydroxy carbonate on the corroding surface are explored in the following section.

6.5.5. ZMG Corrosion in a NaCl-based Atmosphere: CO_3 Effect

Hydrated magnesium hydroxy carbonate is stable under alkaline to neutral conditions, as shown by the stability diagram devised by Lindström et al. [155] and shown in Fig. 6.10.
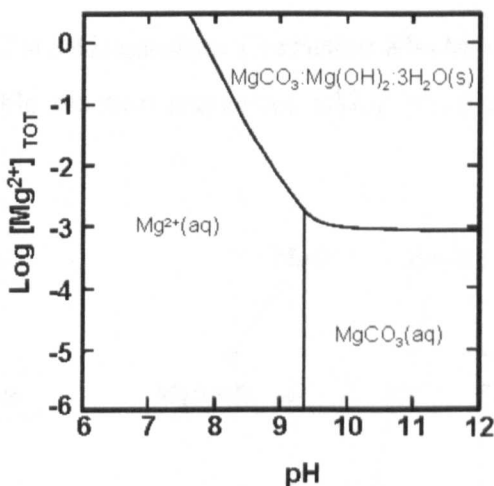
Fig. 6.10: Thermodynamic stability diagram for artenite ($Mg_2(OH)_2CO_3.3H_2O$) formed in the presence of 350 ppm CO_2 [155].

The presence of hydrated magnesium hydroxy carbonate effectively extends the passive region of the zinc coating into more alkaline conditions. Hydroxy carbonates of magnesium may be subject to dissolution during wetting cycles of the corrosion exposure, particularly if the applied solution is acidic, as used in this work (salt solution acidified to pH 4.2). This point explains why the hydroxy carbonate on ZMG was difficult to detect. If the applied solution were not acidified, the magnesium corrosion products may have endured for a longer time, extending the corrosion resistance of ZMG. This may have been the case in previous work [13-17] and the reason for the more dramatic corrosion resistance improvements reported.

6.5.6. ZMG Corrosion in a NaCl-based Atmosphere: Simonkolleite Formation

XRD analysis showed a diminution of Zn_2Mg peak intensity as corrosion progressed and XPS measurements showed a decrease in magnesium to zinc ratios

for ZMG from a value of 10 (+2.0,-2.7) without corrosion treatment to a value of 1.5 (+1.5,-1.0) after 4 weeks of corrosion (see Fig.6.5b). These results support the hypothesis that the magnesium-containing compounds were washed off the samples during the longer term testing, exposing zinc from the underlying zinc layer of the ZMG coating. The environment we have arrived at is conducive to the formation of simonkolleite (reaction 4.5), having intermediate pH values, high chloride concentration and the availability of zinc.

6.5.7. Summary of Zinc-Magnesium Corrosion Mechanism Proposed

The proposed possible reaction sequences taking place on the ZMG surface are illustrated by Fig. 6.11.
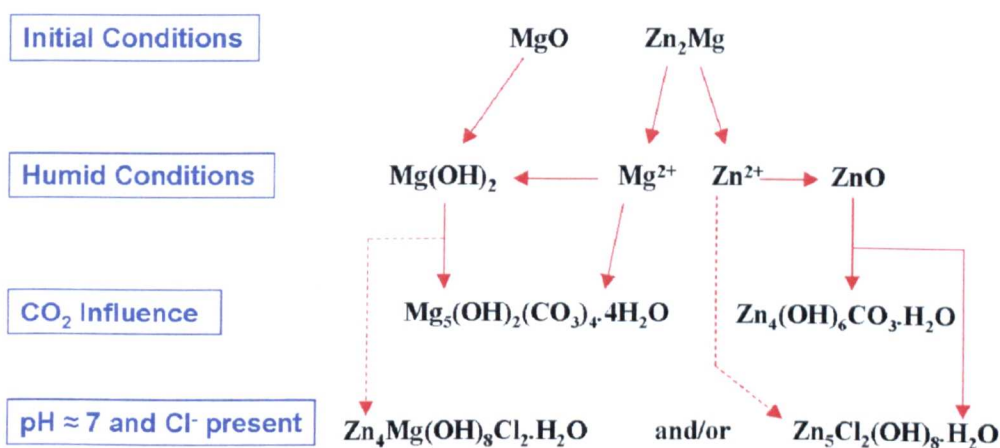
Fig. 6.11: Proposed reactions for corroding ZMG in a NaCl-based environment and with access to atmospheric carbon dioxide.

Both Mg^{2+} and Zn^{2+} ions from the Zn_2Mg phase of the ZMG coating go into solution when the material is subject to electrochemical attack (humid conditions in Fig. 6.11). The more zinc-enriched regions will act as cathodes, and oxygen reduction (reaction (6.3)) progresses. The magnesium ions form stable precipitates of magnesium hydroxide on the cathodes, reducing the general activity and facilitating simonkolleite formation from the corroding zinc. Simonkolleite may be formed directly from chloride complexes at the anodes or via the transformation of zinc oxide. The release of hydroxide associated with simonkolleite formation can be neutralized by carbon dioxide uptake and carbonatization at the cathodes (reactions (4.6)-(4.8)).

The magnesium hydroxide at the cathodes slowly transforms into more carbonate-containing hydroxides (6.5)-(6.6). Continued suppression of oxygen reduction at the cathodes allows the corroding zinc to form further protective simonkolleite. The overall corrosion activity is reduced compared to zinc corrosion and eventually large portions of the surface are protected by simonkolleite. This mechanism of protection also extends to the zinc phase of the original ZMG coating, as long as a supply of magnesium ions is available.

Existing magnesium-containing corrosion products as well as particles of Zn_2Mg constitute a source and a buffer for further protection; if cathodic activity and pH levels increase, reactions (6.5) and (6.6) are displaced to the left, reforming magnesium hydroxide. Flushing the corrosion products with acidified solution may cause the magnesium hydroxy carbonates to dissolve and leach out of the corrosion products to some extent, as they are not as stable or insoluble as simonkolleite at intermediate pH values [155]. Even if carbonatization of the magnesium hydroxide is a key phenomenon for allowing simonkolleite to form and passivate the ZMG surface, little of this compound may actually remain within the corrosion products. A source of magnesium was created by adding magnesium to the electrolytic solution in the work of Hausbrand et al. [83] and Prosek et al [126] and enhanced corrosion resistance of zinc was observed. This implies that it is unlikely that the mechanism of protection of ZMG relates to the formation of a special form of magnesium-containing simonkolleite: rather it is the continuous ability of the magnesium corrosion products to neutralize hydroxide ions at the cathodes that creates the conditions for insoluble simonkolleite to extend over the corroding surface.

6.6. CONCLUSIONS

Zinc-magnesium coated steel, (ZMG), has greater corrosion resistance in a sodium chloride-containing atmosphere than conventional zinc-coated steel of similar coating thickness. A 3-fold increase in time to significant red rust was recorded on ZMG versus conventional zinc-coated steel in an automotive cyclic corrosion test. The mechanism proposed for corrosion of ZMG in this work comprises the following steps:

- Retarding oxygen reduction reactions at cathodes by the formation of protective magnesium hydroxide.

- Decreased oxygen reduction facilitates the formation of stable simonkolleite.

- Hydroxides associated with simonkolleite formation are neutralized by carbonatization at the cathodes.

- Magnesium hydroxide at the cathodes is transformed into carbonate-containing hydroxides, which in turn facilitate further formation of protective simonkolleite.

Chapter 7

ACID RAIN ENVIRONMENT

7.1. INTRODUCTION

The results presented in Chapter 6 suggested a 3-fold improvement in corrosion resistance of zinc-magnesium alloy coated steel (ZMG) compared to conventional zinc coated steels tested according to the Volvo cabinet method. According to the corrosion mechanism proposed, the efficacy of ZMG's corrosion resistance depends upon the formation of protective corrosion products; crucially the precipitation of magnesium hydroxide at cathodic sites, blocking oxygen reduction. The effectiveness of ZMG's corrosion resistance may be diminished if it is exposed to an environment unfavourable to the retention of magnesium-containing phases or to the formation of magnesium-containing corrosion products. For example, exposing the corroding surface to acidified solution may remove alkaline magnesium hydroxide and if this occurred in the early stages of corrosion, the overall corrosion resistance of ZMG would be reduced and may approach the corrosion resistance of conventional zinc coatings. The corrosion resistance of galvanized steel and ZMG in an acid rain environment is investigated in this chapter. The materials and experimental methods are described in Section 7.2 and the corrosion assessments and corrosion product characterizations are given in Sections 7.3-7.4. The results and the corrosion mechanisms involved are discussed in Section 7.5.

7.2. MATERIALS AND EXPERIMENTAL METHODS

7.2.1. Cabinet Testing

Four open corrosion test panels with lacquered edges (described in Section 5.3.2) were fabricated from each of the materials, (EG, HDG and ZMG). The test panels were subject to the Ford cabinet test with manual spraying by acid rain solution, as described in Section 5.4.3. The test procedure was repeated using a sodium chloride solution (1 wt.% NaCl acidified to pH 4.2) for comparison with the acid rain test. Four sets of test panels were produced; two sets were tested using the

sodium chloride solution and two sets were tested with the acid rain solution. One sample of each material was removed after 6 weeks of corrosion testing for corrosion product characterization. The samples were suspended from an overhead rail in the cabinet and both sides of the test panel were sprayed evenly such that each panel comprised two equivalent test surfaces.

7.2.2. Corrosion Product Characterization

Development of red rust was observed during each test and image analysis was used to quantify the percentage of the surface covered by red rust. Square samples, measuring approximately 100 mm^2, were cut from test panels of EG and ZMG after 6 weeks of corrosion testing for analysis by XRD. Depth profile analysis was carried out on the same corroded and uncorroded samples by Glow Discharge Optical Emission Spectrometry (GDOES) using a Leco GDS-750 QDP spectrometer, as described in Section 5.6.5. A profilometer (Mitutoya Surftest analyser) was used to measure the depths of the analysed areas and the results from the spectrometer were corrected to match the measured sputter depths. Additional samples were cut from the EG and ZMG panels following 6 weeks exposure for XPS analysis. Cross-sections of EG and ZMG exposed to each environment were also analysed by SEM/EDS.

7.3. GENERAL CORROSION RESISTANCE

The percentage of red rust present on each corroding surface in sodium chloride and acid rain environments was measured and the results are presented in Fig. 7.1. The percentages shown up to 6 weeks of exposure represent the averages of 4 samples (2 panels with 2 surfaces each) and thereafter the values presented are the averages of 2 samples (1 panel with 2 surfaces). A source of error in the ZMG samples was due to the darkening of the ZMG samples' surfaces during corrosion treatment. The image analysis software required greyscale images; conversion of the corroded ZMG image led to overlapping of red rust and darkened areas in the image analysis. To minimise the error introduced, the final value reported for red rust proportion was the average of the results recorded from low-end and high-end estimates. These final measurements obtained were relatively consistent, with average and maximum deviations of (±1%) and (+4%,-3%) respectively.
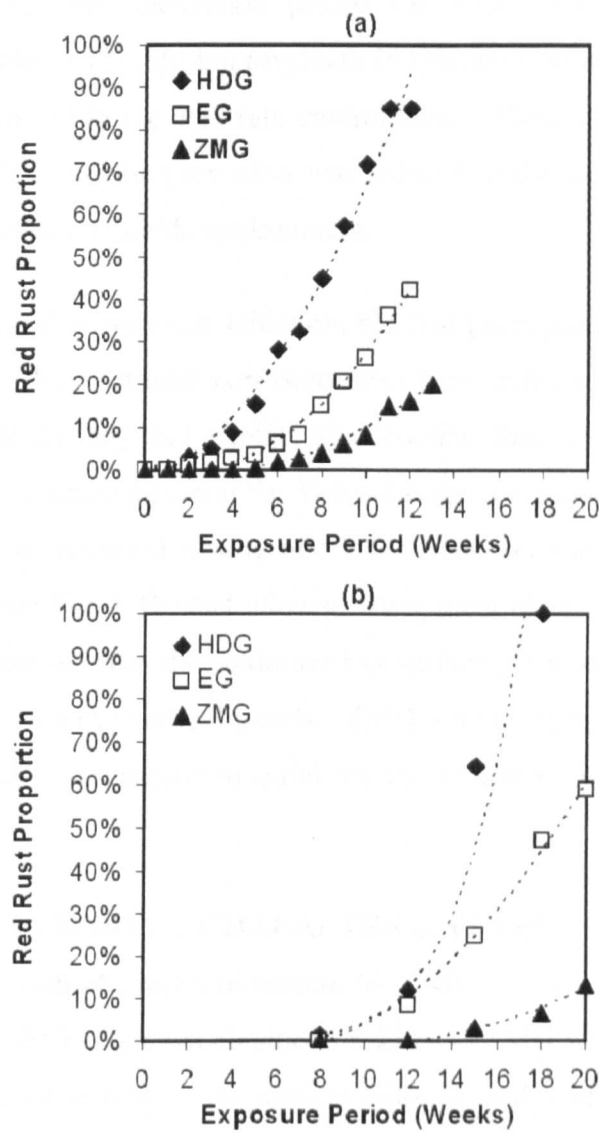
Fig. 7.1: Percentage red rust on EG, HDG and ZMG in (a) sodium chloride and (b) acid rain environments.

Fig. 7.1 shows that in general, ZMG exhibited superior resistance to red rust initiation and propagation compared to EG and HDG. Fig. 7.1a shows that EG and HDG developed red rust within 2 weeks of exposure to the sodium chloride environment, whereas ZMG suppressed red rust formation until 6 weeks of exposure. This observation indicates a 3-fold increase in resistance to initiation of red rust for ZMG compared to HDG and EG in the sodium chloride environment, in agreement with the findings of Chapter 6. An incubation period of 8 weeks to red rust initiation was observed for EG and HDG in the acid rain environment,

compared to a 12-week incubation period for ZMG (see Fig. 7.1b). This observation indicates a 1.5-fold improvement in resistance to red rust initiation for ZMG compared to EG in the acid rain environment. These data indicate that the efficacy of ZMG's corrosion protection was reduced in the acid rain environment compared to the sodium chloride environment.

Fig. 7.1 also shows that after rust initiation, red rust propagated at a faster rate on HDG compared to EG. Similar corrosion rates were expected for EG and HDG used in this work as they had similar zinc coating thicknesses and equivalent corrosion rates were observed using the Volvo cabinet test method in Chapter 6. It is proposed that the increased rusting of HDG versus EG was due to the surface texture of HDG (see Fig. 5.1b) that allowed entrapment of the electrolyte onto the test panels' surfaces whereas the smoother EG surface allowed increased draining of the electrolyte from the vertical panels. ZMG is more similar to EG, therefore EG was used as the comparison material for the remainder of this experimental phase.

7.4. CORROSION PRODUCT CHARACTERIZATION

7.4.1. Corrosion Product Characterization by XRD

Fig. 7.2 shows the diffractograms obtained for EG and ZMG without corrosion and following 6 weeks of testing in the sodium chloride and acid rain environments respectively. Peaks observed at $2\theta \approx 45°$ and $2\theta \approx 66°$ are attributable to diffraction from the steel substrate. The presence of metallic zinc and Zn_2Mg phases in corroded samples indicates preservation of the original metallic coatings, or at least portions thereof. Simonkolleite ($Zn_5Cl_2(OH)_8.H_2O$), with its main diffraction peak at $2\theta \approx 11.2°$, was the prime corrosion product detected on both EG and ZMG in the sodium chloride environment, (see Fig. 7.2b). The main simonkolleite peak on ZMG was broader than the reference diffractogram, possibly indicating uptake of magnesium into the simonkolleite, as suggested by Tsujimura et al. [17] and Prosek et al. [126] and as observed in Chapter 6.

Notes:
Open circle = Simonkolleite $Zn_5(OH)_8Cl_2.H_2O$
Open diamond = Zinc hydroxy carbonate
$\qquad Zn_5(OH)_6(CO_3)_2$ or $Zn_4(OH)_6CO_3.H_2O$
Open square = Zinc oxide ZnO
Closed triangle = Magnesium hydroxide $Mg(OH)_2$
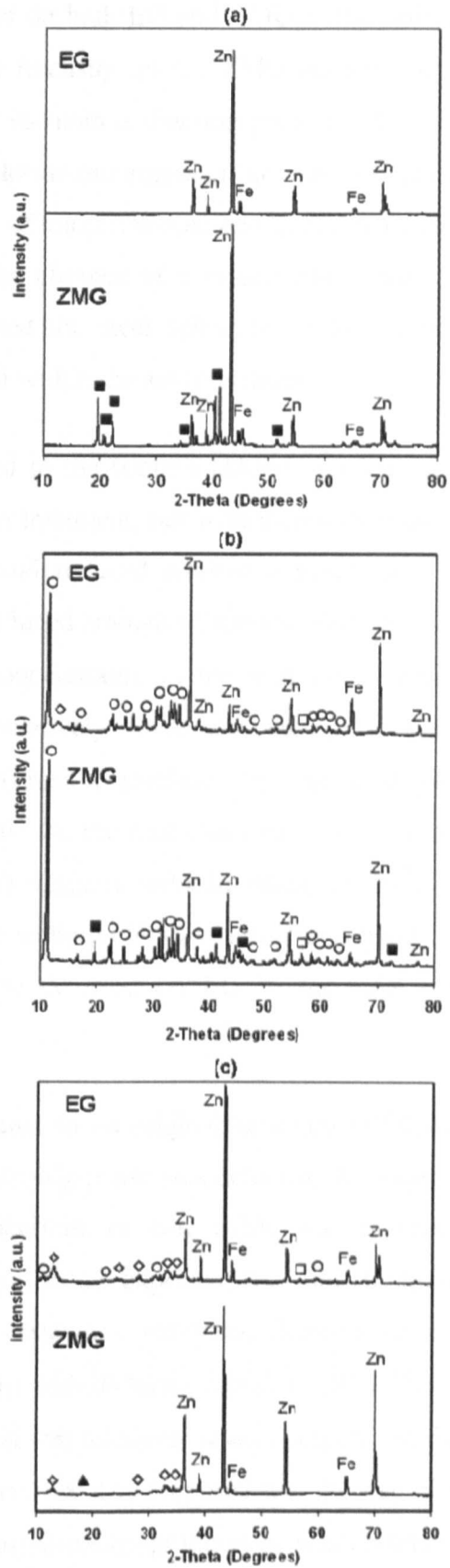Closed square = Zinc-magnesium Zn_2Mg

Fig. 7.2: Diffractograms for EG and ZMG (a) before corrosion and after 6 weeks exposure to (b) sodium chloride and (c) acid rain environments.

A zinc oxide peak at $2\theta \approx 57°$ was detected on both EG and ZMG in the sodium chloride environment, with greater relative intensity on the ZMG sample. Zinc hydroxy carbonate ($Zn_5(OH)_6(CO_3)_2$), with its main diffraction peak at $2\theta \approx 13°$, was also observed on EG in the sodium chloride environment but was not clearly detected on the ZMG sample. The presence of unreacted zinc on EG and unreacted zinc and Zn_2Mg on ZMG, coupled with the absence of iron corrosion products, indicates that the metallic coatings protected the steel substrate up to 6 weeks exposure in the sodium chloride environment within the analysis areas.

Similar corrosion products to those detected in the sodium chloride environment were detected on EG following the acid rain treatment, but with increased relative concentration of zinc hydroxy carbonate and reduced relative concentration of simonkolleite, as shown in Fig. 7.2c. The reduced amount of simonkolleite may be due to several factors; reduced chloride concentration in the acid rain solution compared to the sodium chloride solution, relatively slower corrosion progression and the proton-induced dissolution of corrosion products by the acid rain precipitation. The similarity of the zinc peaks on the acid rain treated EG sample and the uncorroded EG samples (Fig. 7.2a) suggests reduced attack of the zinc coating in the acid rain test compared to the sodium chloride test. No sulphur- or nitrogen-containing corrosion products were detected on EG in the acid rain environment.

ZMG exhibited significant alteration compared to its original structure following the acid rain treatment; none of the original Zn_2Mg phase was detected. In contrast to the EG sample, no evidence of simonkolleite or zinc oxide was detected, although small diffraction peaks similar to those expected for zinc hydroxy carbonate were detected. The only other crystalline substance detected on the sample was magnesium hydroxide ($Mg(OH)_2$) with diffraction peak at $2\theta \approx 18.4°$. The amount of magnesium hydroxide detected was relatively small compared to the amount of Zn_2Mg in the original coating; therefore it is proposed that the majority of the Zn_2Mg phase either formed amorphous corrosion products or was dissolved from the corroding surface by the attack of the acid rain solution. Similar to EG, no sulphur- or nitrogen-containing corrosion products were detected by XRD.

Detailed views of the ZMG diffractograms over the range $10° \leq 2\theta \leq 34°$ are shown in Fig. 7.3. Arrows in Fig. 7.3a (NaCl environment) indicate peaks that are unique to the ZMG sample (i.e. were not present on EG following the same treatment). These peaks correspond partially to the reference diffractogram of magnesium hydroxy carbonate, $Mg_5(CO_3)_4(OH)_2.nH_2O$ (n=4,5), and did not correspond to any other expected corrosion product. The diffractogram indicates that magnesium remained on ZMG following the sodium chloride treatment, either as Zn_2Mg or as magnesium-containing corrosion products.

Notes:
Open circle = Simonkolleite ($Zn_5Cl_2(OH)_8.H_2O$)
Open diamond = Zinc Hydroxy Carbonate
($Zn_5(OH)_6(CO_3)_2$ or $Zn_4(OH)_6CO_3.H_2O$)
Open square = Zinc Oxide (ZnO)
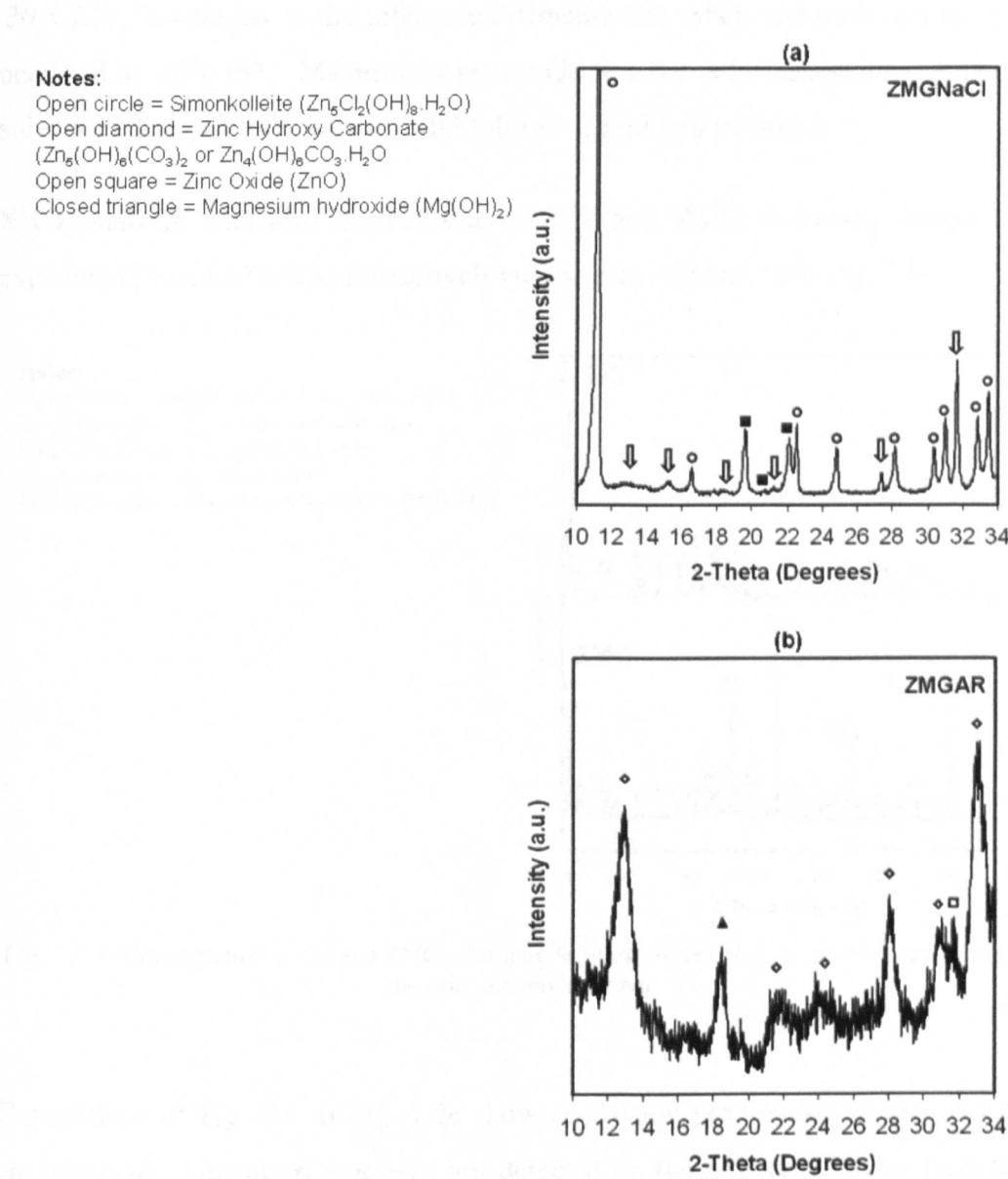Closed triangle = Magnesium hydroxide ($Mg(OH)_2$)

Fig. 7.3: Detail diffractograms for ZMG in (a) sodium chloride and (b) acid rain environments. Arrows show new peaks in the sodium chloride environment.

The detail diffractogram of ZMG following acid rain treatment (Fig. 7.3b) shows a relatively noisy diffractogram, possibly indicating the presence of non-crystalline corrosion products on the corroded sample. This diffractogram confirms that simonkolleite did not form on ZMG following acid rain treatment, as no indication of the main simonkolleite peak at $2\theta \approx 11.2°$ was detected. The possible presence of zinc oxide was indicated by a small peak at $2\theta \approx 31.8°$. The peaks assigned to zinc hydroxy carbonate were rather broad compared to the reference diffractogram, and the peak at $2\theta \approx 33°$ had greater relative intensity compared to the peak at $2\theta \approx 13°$, in contrast to the reference diffractogram, where the more intense peak occurred at $2\theta \approx 13°$. Magnesium hydroxide was the only magnesium-containing substance detected by XRD on ZMG following acid rain treatment.

XRD analysis was also carried out on EG and ZMG following longer-term exposure (21 and 27 weeks respectively) to the acid rain test, (see Fig. 7.4).

Notes:
Open circle = Simonkolleite ($Zn_5Cl_2(OH)_8.H_2O$)
Open diamond = Zinc Hydroxy Carbonate
($Zn_6(OH)_6(CO_3)_2$ or $Zn_4(OH)_6CO_3.H_2O$
Open square = Zinc Oxide (ZnO)
Closed triangle = Magnesium hydroxide ($Mg(OH)_2$)
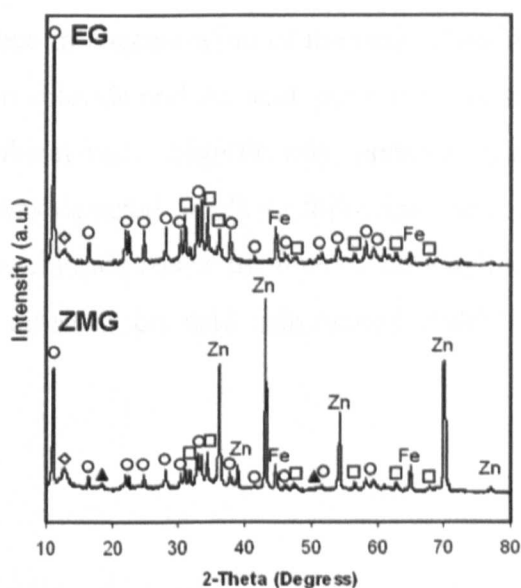
Fig. 7.4: Diffractograms for EG and ZMG after long-term exposure (21 & 27 weeks respectively) to the acid rain environment.

Comparison of Fig. 7.4 to Fig. 7.2c shows corrosion progression in the acid rain environment. Unreacted zinc was not detected on the EG sample after long term exposure and the intensities of the simonkolleite and zinc oxide peaks increased versus 6 weeks of exposure. Detailed analysis of the EG diffractogram following

longer-term exposure showed small peaks attributable to sulphate-containing corrosion products, such as $Zn_4(OH)_6SO_4.H_2O$ and $NaZn_4Cl(OH)_6SO_4.6H_2O$, which have been reported in both natural and laboratory exposure (see Table 4.3). The ZMG sample exhibited metallic zinc peaks, as well as simonkolleite, zinc oxide, zinc hydroxy carbonate and magnesium hydroxide corrosion products. The presence of protective corrosion products (simonkolleite and zinc hydroxy carbonate) as well as unreacted zinc, suggests that the barrier protection mechanism due to precipitation of solid corrosion products observed on ZMG in NaCl-based testing was established in the longer term in the acid rain environment.

7.4.2. Corrosion Product Characterization by XPS: Survey Scans

The atomic concentrations (at.%) of the elements detected for EG and ZMG following 6 weeks exposure to the sodium chloride and acid rain environments by XPS survey scans are shown in Fig. 7.5. The results for each material before corrosion treatment and after 4 weeks of the Volvo cabinet test (V4) are shown for comparison. Fig. 7.5 shows little difference in concentration of the main elements following 6 weeks exposure to the sodium chloride and the acid rain environments and following 4 weeks of the Volvo cabinet test. Significantly, approximately equivalent concentration of magnesium was detected on ZMG following the acid rain treatment and following the sodium chloride-based treatments, although no magnesium-containing substances were detected on acid rain-treated ZMG by XRD.
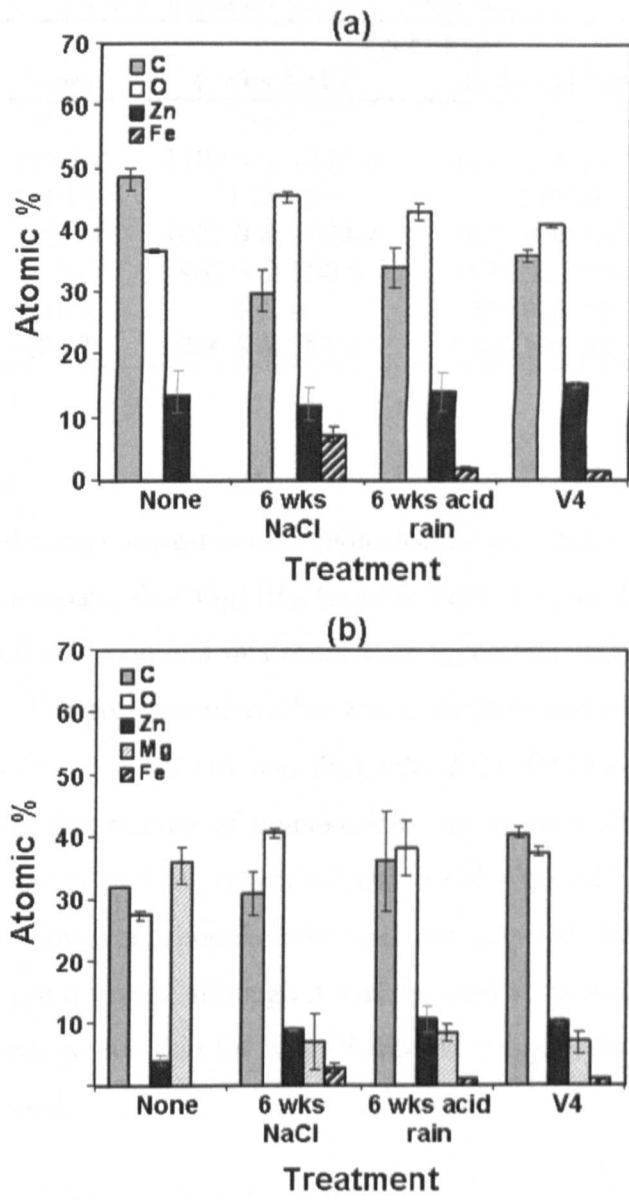
Fig. 7.5: XPS survey scans showing relative atomic percentages (at.%) of main elements detected for (a) EG and (b) ZMG following different corrosion treatments.

7.4.3. Corrosion Product Characterization by XPS: Detail Scans

The main peak positions of the elements of interest for ZMG were measured and the results are presented in Table 7.1. The values measured on ZMG without corrosion treatment and after treatment V4 are included in the table for comparison. The results show rather similar measurements for ZMG following 6 weeks exposure to sodium chloride (6wks NaCl) and acid rain (6wks acid rain).

Table 7.1: Measured energy values (eV) of main peaks on ZMG following the corrosion treatments.

Signal	Treatment			
	None	6 wks NaCl	6wks acid rain	V4
Mg 2p BE	50.3	50.3	50.1	-
Mg KLL KE	1180.9	1180.6 & 1175.0	1180.7 & 1175.7	1180.0
Mg 1s BE	1303.9	1303.8	1303.4	-
Zn 2p BE	1022.0	1022.0 & 1024.4	1021.8 & 1024.0	1022.0
Zn LMM KE	987.6	987.9 & 990.5	987.5 & 990.3	987.3
O 1s BE	531.7	531.6	531.6 & 533.4	532.0
C 1s BE	289.2	286.3 & 289.1	286.2 & 289.3	289.7

Zinc peak analysis

The XPS chemical energy measurements indicated the presence of zinc oxide, ZnO or zinc hydroxy carbonate, $Zn_5CO_3(OH)_6$ (refer to Table 6.4) for ZMG exposed to 6 weeks of NaCl and acid rain and this result is in agreement with the XRD results shown in Fig. 7.2. The presence of another zinc corrosion product was indicated by small peaks at Zn 2p $BE \approx 1024\,eV$ and Zn LMM $KE \approx 990.4\,eV$. Boshkov et al. [156] suggested that the presence of simonkolleite may be indicated by Zn 2p peaks at 1021.9, 1023.1 and 1024.9 eV, which coincide relatively well with the additional peaks measured. However, simonkolleite was not detected on acid-rain treated ZMG by XRD at just 6 weeks, although it was detected at 27 weeks. It is possible that some simonkolleite, too thin for XRD detection, was present on the acid rain-treated ZMG at 6 weeks.

Magnesium peak analysis

Comparison of the measured magnesium peaks to the reference peaks in Table 6.6 indicates the presence of magnesium hydroxide, $Mg(OH)_2$ and magnesium hydroxy carbonate $Mg_5(OH)_2(CO_3)_2.4H_2O$ for ZMG samples following 6 weeks of NaCl and acid rain treatments. C 1s peaks at $BE \approx 286\,eV$ and O 1s peak at higher binding energy ($BE \approx 533-534\,eV$) further indicate the presence of magnesium hydroxy carbonate for the corroded ZMG. Unfortunately reference XPS data for magnesium hydroxy carbonate with n=5 ($Mg_5(OH)_2(CO_3)_2.5H_2O$), were not available. However, it is likely that both magnesium hydroxy carbonate compounds exhibit rather similar XPS profiles. Either way, the XPS results are in agreement with the XRD data for ZMG tested in the NaCl environment, i.e. zinc oxide, zinc hydroxy

carbonate and possibly simonkolleite and magnesium hydroxy carbonate were formed on the corroded surface. However, the XPS results also suggest similar corrosion products and significant concentration of magnesium for ZMG exposed to the acid rain environment, which were not indicated by the XRD results. Absence of these compounds from the diffractogram indicates that they were either too thin to be detected by XRD at the settings used or that they were amorphous. Further analysis of the ZMG corrosion products was required to gain information about the differences in the acid rain and NaCl-treated ZMG.

7.4.4. Corrosion Product Characterization by GDOES

Distribution of carbon, oxygen, zinc, magnesium and iron in ZMG following the sodium chloride and acid rain corrosion treatments was assessed using GDOES. Fig. 7.6 shows the distribution of these elements in the top 26 μm of ZMG samples before corrosion treatment, after 6 weeks of the sodium chloride test and after 6 weeks of the acid rain test, (curves A, B and C respectively). Incorporation of carbon and oxygen into the samples' surface layers indicates corrosion activity and the depth to which these elements occur indicates the thickness of corrosion products. The dissolution of metallic elements can be discerned by comparing concentration and distribution of these elements in corroded and uncorroded samples. The presence of carbon and oxygen on ZMG without corrosion treatment (curve A) is shown to a depth of approximately 3-4 μm. Following corrosion treatments, ZMG samples showed carbon to depths of approximately 15 μm in the NaCl environment (curve B) and up to 19 μm in the acid rain environment (curve C). Oxygen was detected to a depth of 12 μm in the NaCl environment and to a depth of 14 μm in the acid rain environment. These data indicate on average thicker corrosion product mass for acid rain treated ZMG than for the sodium chloride treated ZMG.

Distribution of the metallic elements zinc, magnesium and iron is shown in Fig. 7.6c to Fig.7.6e respectively. Quantification of zinc and magnesium in the top 3 μm of the uncorroded sample should have corresponded to the phase Zn_2Mg; curve A of Fig. 7.6c and Fig. 7.6d shows that the magnesium quantity was overestimated and that the zinc quantity was underestimated. The zinc and magnesium traces for

the corroded samples were flattened compared to the original material, showing re-distribution of these elements over a greater depth as corrosion products formed within the analysis areas. The distribution of zinc in the acid rain environment was displaced by approximately 5 μm, indicating formation of corrosion products on top of a zinc-rich layer.
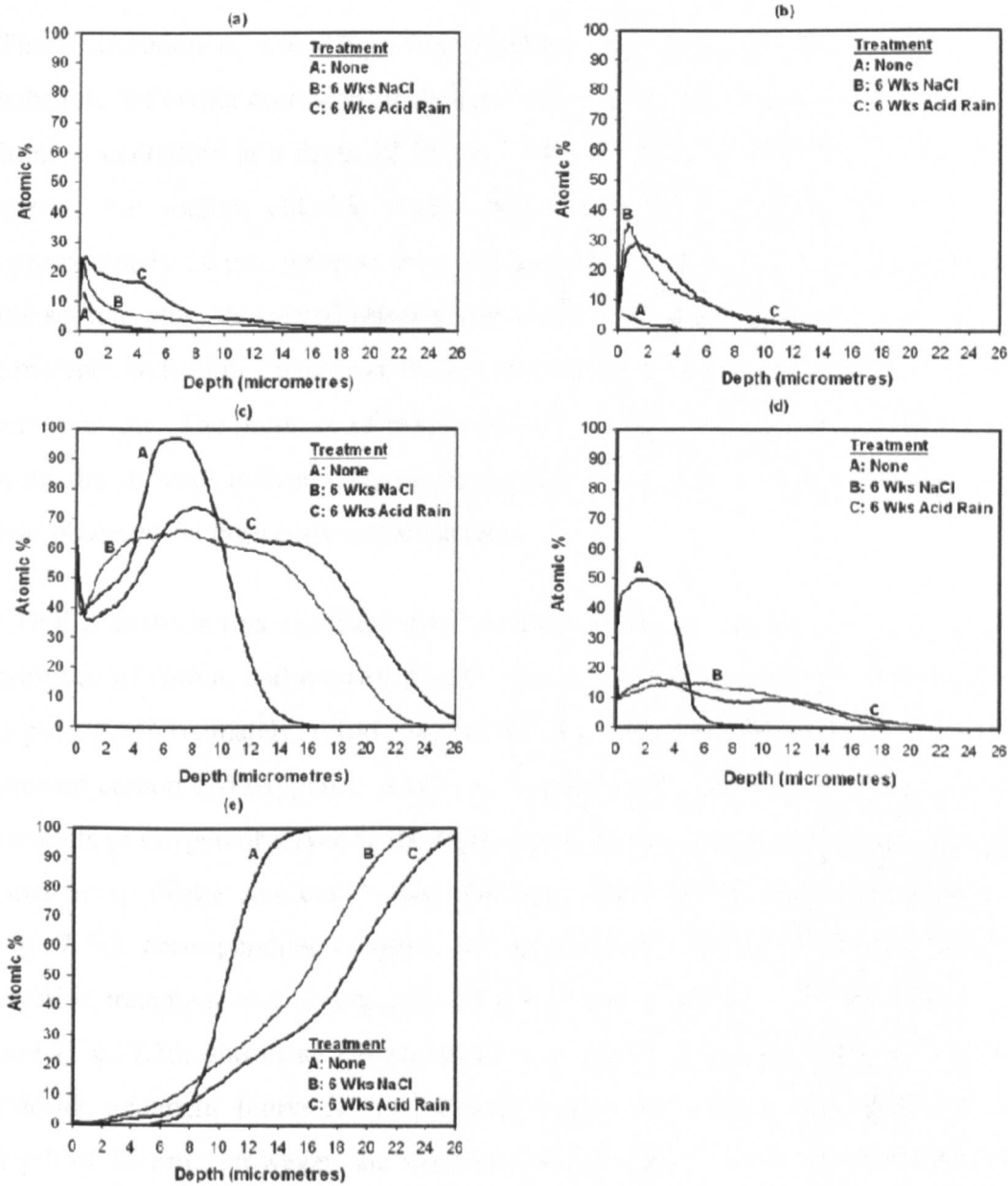

Fig. 7.6: GDOES analysis showing distribution of (a) carbon, (b) oxygen, (c) zinc, (d) magnesium and (e) iron in ZMG before and after corrosion treatments.

The presence of oxygen and carbon within the top 5 μm of the acid rain sample suggests the presence of magnesium hydroxide and possibly carbonate (refer to Fig.

7.6a-b). It is worth noting that the zinc trace did not achieve 100% concentration for ZMG in either sodium chloride or acid rain environments. Nevertheless, unreacted zinc may be present on these samples (as shown by XRD analysis) because the GDOES analysis gives an average signal over a relatively large area (disc of 4 mm diameter).

The distribution of iron (Fig. 7.6e) indicates the degree of attack of the steel substrate following corrosion treatments. The uncorroded sample achieved 100% iron concentration at a depth of 16 μm. The corroded samples produced broader curves; the sodium chloride treated achieved 100% iron level at a depth of approximately 24 μm, whereas the acid rain treated sample curve was broader than the sodium chloride treated sample, with 100% iron detected at approximately 28 μm depth, indicating on average thicker corrosion products on ZMG in the acid rain environment. The presence of iron close to the sample surface (i.e. less than 6 μm from the surface) indicates incorporation of iron into the corrosion products, and was observed for both corrosion treatments.

GDOES analysis was also performed on EG samples, as shown in Fig. 7.7. The presence of carbon and oxygen on EG without corrosion treatment is shown to a depth of approximately 1 μm, (see curve A on Fig. 7.7a-b). Corroded samples showed carbon and oxygen to depths of approximately 10-12 μm, with significant amounts of oxygen observed in the top 8 μm of the sodium chloride treated sample. Broadening of the zinc curves was observed following corrosion treatments (see Fig. 7.7c), corresponding to depths of approximately 16 μm following sodium chloride treatment and 12 μm following acid rain treatment. The distribution of iron (Fig. 7.7d) shows an off-set in the x-axis of the sample following sodium chloride treatment, (curve B), with similar slope compared to uncorroded EG to a depth of 16 μm. However, the material did not achieve 100% iron concentration (i.e. uncorroded substrate) even at a depth of 26 μm. This change of slope may indicate corrosion effects at the coating to substrate interface or heterogeneous corrosion of the material. The acid rain treated sample achieved 100% iron at a depth of approximately 23 μm, indicating on average thinner corrosion products on this sample than on the sodium chloride treated sample.
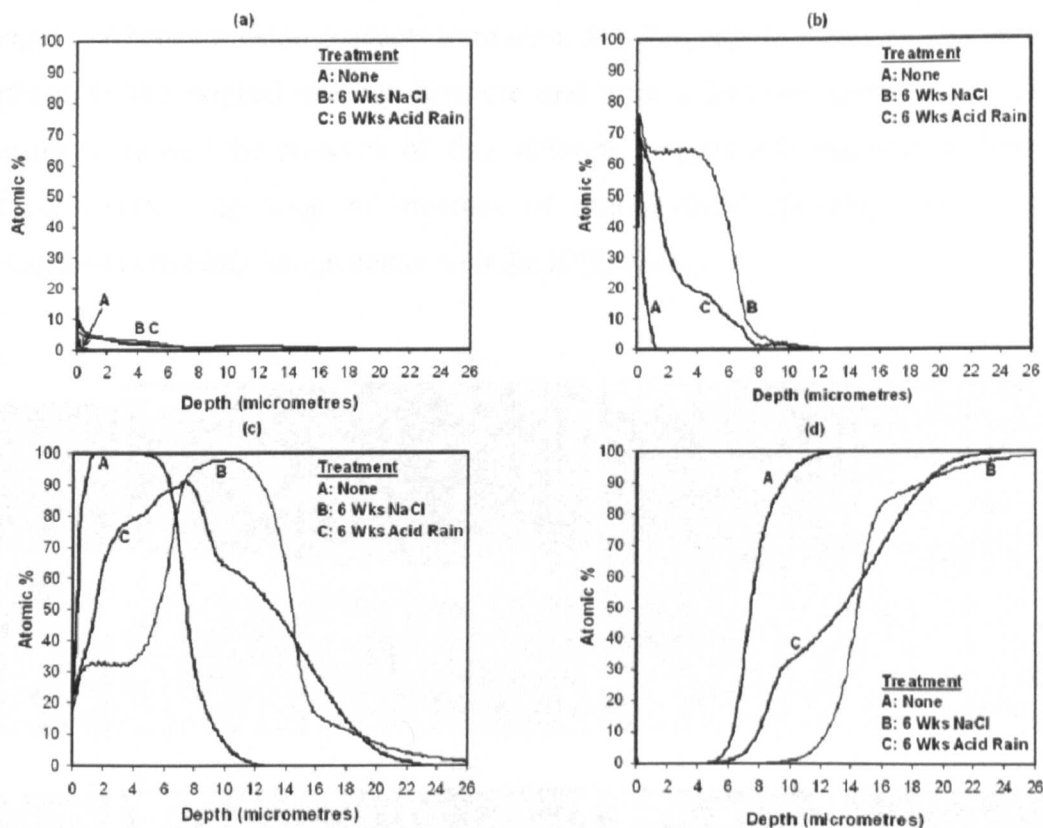
Fig. 7.7: GDOES analysis showing distribution of (a) carbon, (b) oxygen, (c) zinc and (d) iron in EG before and after corrosion treatments.

These profiles show a reversal of behaviour between ZMG and EG; ZMG developed thicker corrosion products in the acid rain environment whereas EG developed thicker corrosion products in the sodium chloride environment. Depending on the nature of the corrosion products formed, thicker layers of corrosion products may serve to offer greater or lesser protection to the steel substrate. Cross-sectional analysis of the corroded samples gives further information about the corrosion products.

7.4.5. Corrosion Product Characterization by SEM/EDS

SEM analysis of ZMG and EG cross-sections after 6 weeks of corrosion in the sodium chloride and acid rain environments revealed the corrosion product morphologies (see Fig. 7.8-7.10). Heterogeneous corrosion of ZMG in the sodium chloride environment was evident. Large areas of the sample appeared relatively unaffected by corrosion (see Fig. 7.8a *centre*) whilst significant amounts of corrosion products (up to 20 μm thick) were observed in some areas (Fig. 7.8a

right). Where corrosion products were seen, they had largely consumed the Zn$_2$Mg phase of the original coating structure and bore a lamellar appearance. EDS analysis showed the presence of zinc, chlorine, oxygen and magnesium through these layers, suggesting the presence of simonkolleite, (possibly modified by magnesium uptake), in agreement with the XRD results.
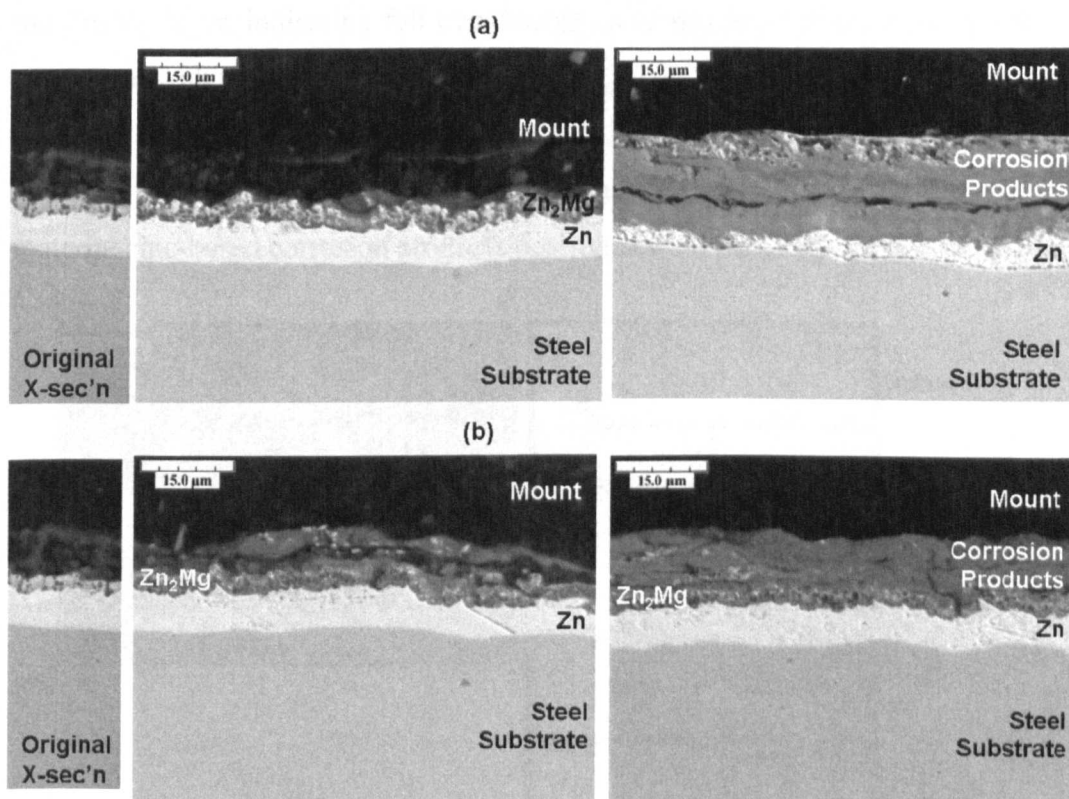
Fig. 7.8: SEM micrographs of ZMG cross-sections showing corrosion products after 6 weeks of testing in (a) sodium chloride and (b) acid rain environments. Images show *from left* original cross-section, relatively unaffected and affected areas of the corroded samples.

Unaffected areas were difficult to find on the ZMG sample tested in the acid rain environment. Differences in the thickness of corrosion products were observed with less affected zones having up to 8 μm (see Fig. 7.8b *centre*) and more affected zones having up to 15 μm of corrosion products, with the thickness measured from the upper surface of the original Zn$_2$Mg phase. The cross-section shown in Fig. 7.8b *right* was most representative of the sample generally, where 10–12 μm of corrosion products situated on top of the Zn$_2$Mg phase. The corrosion products appeared to be lamellar and dense. The appearance of the Zn$_2$Mg phase was

affected by the acid rain treatment and in some areas was difficult to differentiate from the corrosion products.

EDS analysis of ZMG following 6 weeks of acid rain treatment (see Fig. 7.9) showed the presence of magnesium, concentrated over a 5 µm depth, in line with the Zn_2Mg phase of the original coating. Oxygen also penetrated the full depth of the Zn_2Mg layer, indicating full transformation of this layer to oxidized species, in agreement with the diffractogram shown in Fig. 7.2c. Some leaching of magnesium into the upper layer of corrosion products may be indicated by the left-hand shoulder in the magnesium line scan but generally at this area of the corroded material zinc-based corrosion products precipitated on top of the Zn_2Mg phase site.
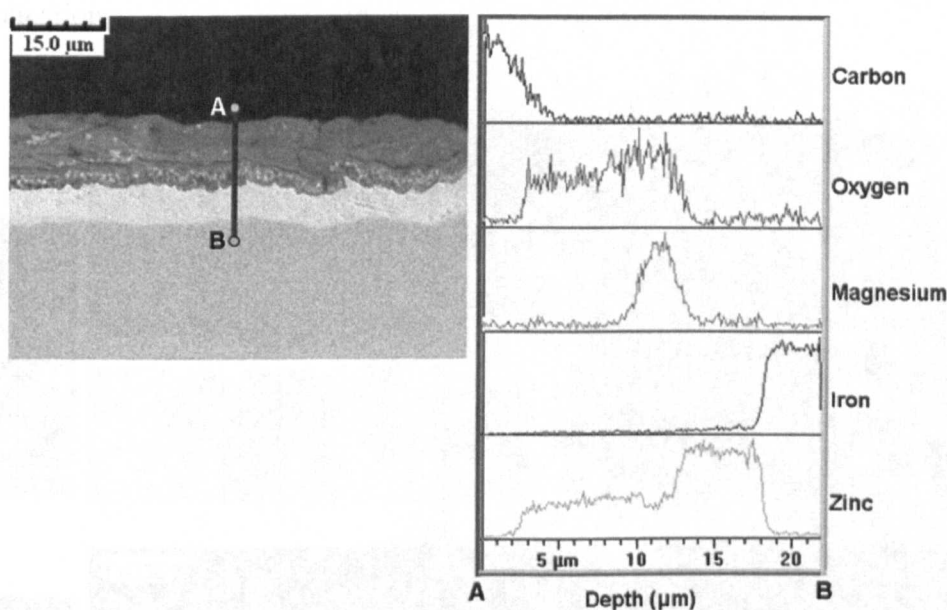
Fig. 7.9: EDS line scan on ZMG following 6 weeks of acid rain treatment showing concentration of magnesium in the region originally occupied by the phase Zn_2Mg.

Fig. 7.10a shows cross-sections of EG following 6 weeks of sodium chloride treatment. No unaffected areas were observed, and those areas least affected exhibited approximately 20 µm of corrosion products on top of the original zinc coating (see Fig. 7.10a *centre*). In some areas the original zinc coating transformed into corrosion products of up to 50 µm thickness (see Fig. 7.10a *right*). The corrosion products appeared lamellar and were probably protective in the early stages of the corrosion test. However, by 6 weeks of exposure, cracking of the

corrosion products was observed, giving access to the substrate and allowing red rust development. Fig. 7.10b *centre* and *right* show cross-sections of EG following 6 weeks of acid rain treatment. Compared to the sodium chloride treatment, relatively little corrosion products were formed after 6 weeks by the acid rain treatment and some areas were relatively unaffected by the treatment (Fig. 7.10b *centre*). In other areas, localized attack of the zinc coating and formation of up to 28 µm of corrosion products was observed (Fig. 7.10b *right*). EDS analysis of these corrosion products showed the presence of zinc, oxygen and small amounts of chlorine, sulphur and iron. The corrosion products did not appear to be dense or protective in nature, but were rather voluminous and disordered, possibly due to the repeated dissolution of alkaline corrosion products by the acid rain solution applications.
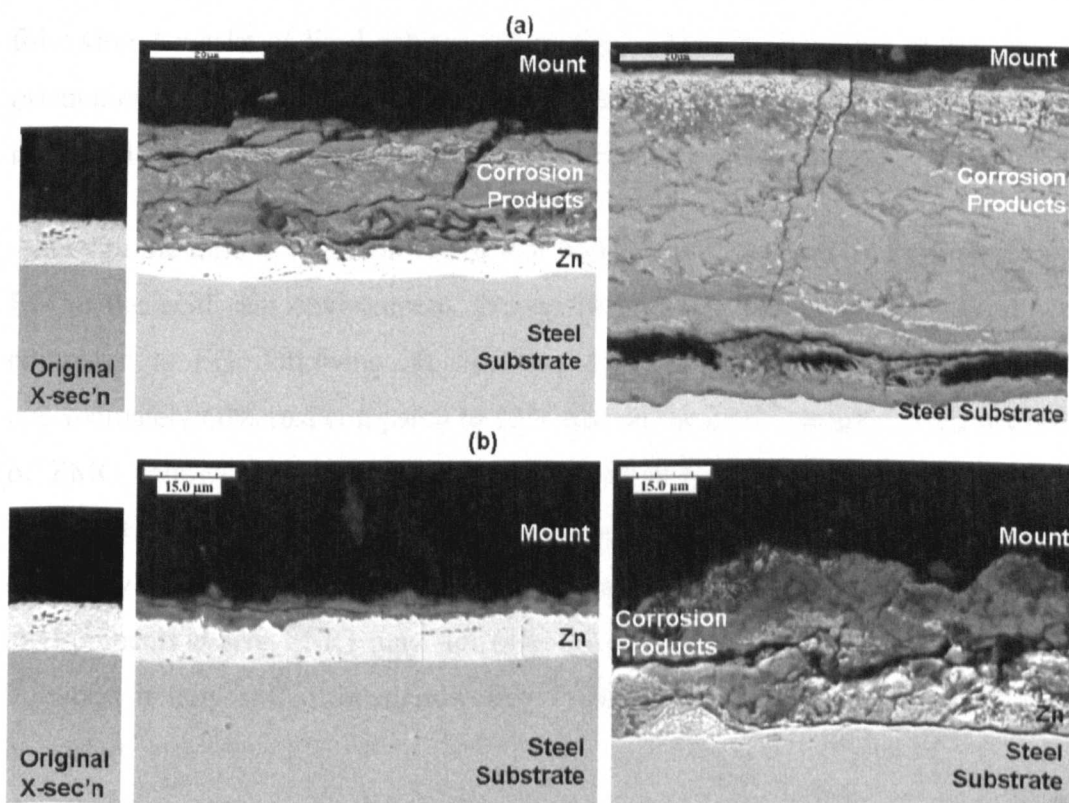

Fig. 7.10: SEM micrographs of EG cross-sections showing corrosion products after 6 weeks of testing in (a) sodium chloride and (b) acid rain environments. Images show *from left* original cross-section, relatively unaffected and affected areas of the corroded samples. Note scale bar lengths in (a) are 20 µm and in (b) are 15 µm.

7.5. DISCUSSION

7.5.1. General Corrosion Resistance

The assessment of general corrosion resistance by time to red rust initiation showed that the acid rain test was less severe than the sodium chloride test and that the improvement in resistance to red rust initiation of ZMG versus EG was halved in the acid rain environment compared to the sodium chloride environment. The 1.5-fold improvement in resistance to red rust initiation of ZMG versus EG in the acid rain environment represents a significant reduction compared to the literature values of 10 and 24-fold improvements of ZMG in salt spray testing and the 3-fold improvement reported in Chapter 6. It is also worth noting that the Ford cabinet test method with manual spraying was less aggressive in terms of red rust development than the Volvo cabinet test method. For example, 48% red rust was measured for EG following 4 weeks of Volvo test (see Table 6.2) compared to 3% rust for EG following 4 weeks of Ford cabinet test method. This is likely due to the vertical orientation of the test panels and the reduced spraying times in the latter, leading to more rapid draining of the electrolyte from the surface.

Although the time to initiation of red rust was relatively similar for both ZMG and EG in the acid rain environment, propagation of red rust on ZMG was slower compared to EG; following 20 weeks of testing, the EG sample surface bore approximately 60% rust compared to 15% rust on the ZMG sample. XRD analysis of ZMG following 27 weeks of the acid rain test showed the presence of the protective corrosion product simonkolleite, supporting the idea of a self-healing capability on ZMG suggested by Morishita et al. [14-16]. This implies that even in environments where ZMG may not offer greatly enhanced resistance to red rust initiation it may still offer significantly improved protection against perforation corrosion.

Use of red rust evolution on the corroding surface to assess corrosion resistance in severe corrosion environments over the longer term is not accurate. The rusted area on the EG sample treated to the sodium chloride environment did not propagate uniformly over the entire corroding surface but concentrated in the lower half of the panel. Thus, the EG sample was removed from test after 12 weeks of corrosion

because the lower half was close to perforation, even though the upper half of the test panel was relatively free from red rust (overall red rust proportion ≈ *42%*). This shows that the vertical panel orientation led to increased corrosion effects at the lower edges of the panels compared to the upper areas.

7.5.2. Corrosion Product Analysis: Sodium Chloride Environment

XRD and XPS analysis showed that simonkolleite, zinc oxide and zinc hydroxy carbonate formed on both EG and ZMG in the sodium chloride environment. These same corrosion products were found following the Volvo cabinet test in Chapter 6 (see Fig. 6.2). The presence of zinc hydroxy carbonate shows that atmospheric carbon dioxide was incorporated into the corrosion products. The detail diffractogram shown in Fig. 7.3a indicated additional corrosion product(s) on ZMG after 6 weeks of NaCl corrosion treatment. These peaks may be due to magnesium hydroxy carbonate, $Mg_5(CO_3)_4(OH)_2.nH_2O$, (n=4,5). Although the alignment with the reference scan was not perfect, close alignment was seen for the unique peaks at $2\theta \approx 15.1°,22.5°,27.3°$, which could not be assigned to any other expected zinc-containing corrosion products. In addition, the XPS data suggest the presence of magnesium hydroxy carbonate (see Table 7.1 and Table 6.6.) for ZMG following both NaCl and acid rain treatments.

GDOES analysis was also used to assess the corrosion products formed on EG and ZMG in the sodium chloride environment. It is important to note that the GDOES profiles represent an average signal from the analysed area of approximately 12.6 mm^2 and not absolute values at a single point. This is particularly important in the interpretation of profiles from samples that have suffered heterogeneous corrosion, as is the case here (see Fig. 7.8 and Fig. 7.10). For example, at uncorroded areas, the steel substrate may be just 9 µm (coating thickness) distant from the surface, whereas the steel substrate may be at a much greater distance from the surface when corrosion products precipitated. This explains the low, broad profiles generated on the corroded samples.

The GDOES profiles generated by analysis of EG in the sodium chloride environment showed a layer of oxygen-rich zinc corrosion products (approximately

30 wt.% Zn and 65 wt.% O) of approximately 5 µm thickness. The measured zinc to oxygen proportion (0.46) of this layer lies between the calculated zinc to oxygen proportions of simonkolleite (0.56) and zinc hydroxy carbonate (0.42). Zinc hydroxy carbonate has zinc to carbon ratio of 2.5 and relatively small amounts of carbon were registered by the analysis. Some carbon due to sodium carbonate or bicarbonate may also reside close to the corroding surface. These observations show that GDOES analysis on EG complemented the XRD analysis of corrosion products and that the corrosion products formed over a relatively large area on EG in the sodium chloride environment.

The quantification of zinc and magnesium for ZMG by GDOES did not correspond well to the expected values (see Section 7.4.4). Weiss [157] noted that zinc-based multi-matrix materials may be prone to greater variations in sputter factors than other materials. It is clear that the presence of magnesium in ZMG affected the accuracy of the quantifications in this work. Further calibration samples are required to generate accurate quantifications of the ZMG components by GDOES. It was confirmed that the GDOES analysis did not give magnesium readings where no magnesium was present: the same calibration was used on EG and ZMG samples and no magnesium was registered on the former.

It is not clear how the inaccuracy in zinc and magnesium quantifications affected the accuracy of oxygen, carbon and iron quantifications. A correction factor to generate the expected zinc to magnesium ratios was considered but was not applied because no single correction could satisfy the entire profile. Assuming that the calibration affected the corroded samples in a similar way to the uncorroded sample means that some portion of the magnesium profiles shown in Fig. 7.6c belongs to zinc. The carbon and oxygen profiles also seem out of alignment; the carbon profiles persist to a greater depth than the oxygen profiles on ZMG, yet carbon without oxygen would not be expected within the corrosion products or coating layer. It is likely that the inaccuracy of the calibration increased at low concentrations. This was observed by Peláez et al. [158] when investigating the accuracy of GDOES analysis of low-concentration additions to various zinc coatings. The inaccuracies in elemental quantifications on ZMG mean it was not

possible to confirm precise corrosion products on ZMG by GDOES. However, the shapes of the profiles generated and comparisons between ZMG behaviour in the two environments give useful information and will be discussed in the next section.

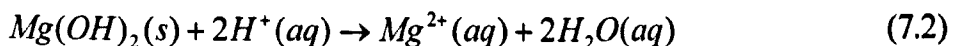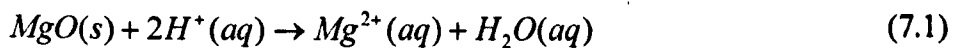### 7.5.3. Corrosion Product Analysis: Acid Rain Environment

The acid rain test resulted in significant changes in the ZMG coating structure even over a short period, in spite of being a less aggressive test than the sodium chloride test. No evidence of the Zn_2Mg phase of the ZMG coating was detected by XRD following 6 weeks of the acid rain treatment and the only magnesium-containing substance detected was magnesium hydroxide. The relatively small peak of magnesium hydroxide detected by XRD could not account for all the magnesium originally present in ZMG. It can be seen from Fig. 7.2c that the zinc diffraction peaks on ZMG following acid rain treatment were very similar to the zinc peaks on EG following the same treatment; that is to say, ZMG following acid rain treatment appears similar to EG following the same treatment. The question to be answered is what happened to the Zn_2Mg phase of ZMG following the acid rain treatment?

XPS analysis showed equivalent concentration of magnesium on the acid rain-treated and sodium chloride-treated samples, although XPS concentration may represent only a thin layer and at a discrete point on the sample surface. Chemical analysis by XPS suggested the presence of magnesium hydroxy carbonate at the corroding surface of ZMG in the acid rain environment. GDOES analysis gives elemental concentration through the corrosion product layers and over a greater surface area and the average amount of magnesium on ZMG is indicated by the area under the GDOES profiles in Fig. 7.6d. The area for the uncorroded sample was estimated at approximately 200–225 units and areas for sodium chloride and acid rain treated samples were estimated at 175 units each. Although these figures can be taken as indicators only, it seems likely that a significant portion of the magnesium was retained on the ZMG surface. Therefore it does not seem likely that all or most of the magnesium was dissolved and washed from the corroding surface during the acid rain test.

The zinc hydroxy carbonate detected by XRD may have hosted some magnesium substituted for zinc, in the same way that previous work [83,126] suggested modification of simonkolleite by magnesium uptake. This would explain the misalignment of the diffractograms observed in Section 7.4.1. The shape of the magnesium profile generated by GDOES analysis indicates that some magnesium was incorporated into the corrosion products. This can be seen from the double-n shaped curve, with two distinct peaks. These separate peaks represent the areas with little corrosion product (see Fig. 7.8b *centre*) with magnesium-enrichment close to the surface and the areas with thicker layers of corrosion product (Fig. 7.8b *right*) where the magnesium-rich layer lies underneath the corrosion products. The peak representing a depth of approximately 3 μm reached a value of 16 at.% magnesium whereas the peak representing a depth of approximately 12 μm reached a maximum magnesium concentration of 12 at.%. This suggests that the possibility that the magnesium concentration at a depth of 3 μm may have been boosted by additional magnesium, i.e. some magnesium from the Zn_2Mg layer was incorporated into the corrosion products. In the next section a mechanism is proposed for ZMG corrosion in the acid rain solution.

7.5.4. Corrosion Mechanism Proposed for ZMG in the Acid Rain Environment

Prior to corrosion exposures, a thin air-formed film of magnesium oxide is present on the surface of ZMG. This layer is too thin to be detected by XRD but was detected by XPS in Chapter 6 and reported by Hausbrand et al. [84] and Stratmann [128]. Some magnesium hydroxide may also be present at the surface in humid atmospheres. The initial spraying of ZMG test panels leads to proton-induced dissolution of the magnesium oxide and hydroxide films according to reactions (7.1) and (7.2).

$$MgO(s) + 2H^+(aq) \rightarrow Mg^{2+}(aq) + H_2O(aq) \qquad (7.1)$$

$$Mg(OH)_2(s) + 2H^+(aq) \rightarrow Mg^{2+}(aq) + 2H_2O(aq) \qquad (7.2)$$

As the surface layer is dissolved by (7.1) and (7.2), electrochemical attack of the Zn_2Mg phase is initiated. When the acidity of the sprayed electrolyte dose is

consumed by reactions (7.1) and (7.2), then oxygen reduction according to (7.3) becomes the dominant cathode reaction.

$$\tfrac{1}{2}O_2(aq) + H_2O(aq) + 2e^- \rightarrow 2OH^-(aq) \tag{7.3}$$
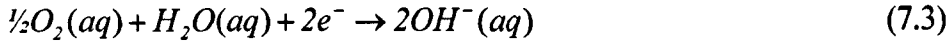
Mg^{2+} ions formed by reactions (7.1) and (7.2) that remained on the corroding surface react with the hydroxide anion to re-precipitate as magnesium hydroxide according to (7.4):

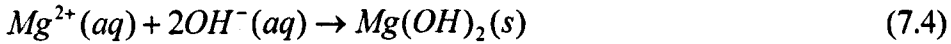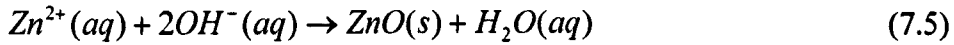$$Mg^{2+}(aq) + 2OH^-(aq) \rightarrow Mg(OH)_2(s) \tag{7.4}$$

Meanwhile, electrochemical attack of the Zn_2Mg phase of the coating causes both Zn^{2+} and Mg^{2+} cations go into solution. Magnesium cations are consumed by reaction (7.4) and zinc cations follow a similar reaction to form zinc oxide (7.5).

$$Zn^{2+}(aq) + 2OH^-(aq) \rightarrow ZnO(s) + H_2O(aq) \tag{7.5}$$

The XRD data show that magnesium hydroxide was present but little or no zinc oxide was present on ZMG after 6 weeks of acid rain treatment (refer to Fig. 7.2c). At high pH sites, magnesium hydroxide formation (7.4) and zinc oxide formation (7.5) both occur. Magnesium hydroxide blocks the cathodic activity and retards the overall corrosion reaction more effectively than zinc oxide. However, zinc hydroxy carbonate was the dominant zinc corrosion product observed on ZMG after 6 weeks of acid rain treatment, showing that any zinc oxide then transformed to zinc hydroxy carbonate as atmospheric carbon dioxide was absorbed according to (7.6).

$$5ZnO(s) + 4HCO_3^-(aq) + H_2O(aq) \tag{7.6}$$
$$\leftrightarrow Zn_5(OH)_6(CO_3)_2(s) + 2CO_3^{2-}(aq)$$
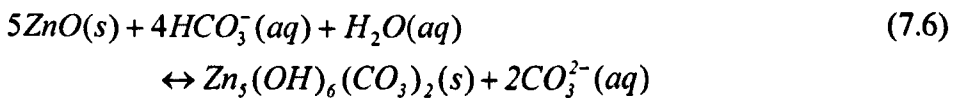
Magnesium hydroxy carbonate may also precipitate according to (7.7).

$$10Mg(OH)_2(s) + 8CO_3^{2-}(aq) + 5H_2O(aq) \tag{7.7}$$
$$\leftrightarrow 2Mg_5(CO_3)_4(OH)_2 \cdot 5H_2O(s) + 16OH^-(aq)$$
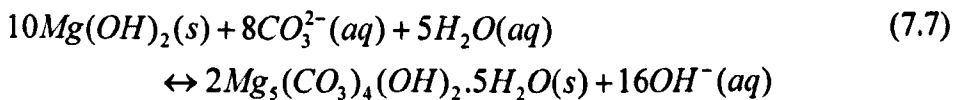
As chloride concentration increased over the longer term testing (refer to Fig. 7.4), formation of simonkolleite (possibly modified by magnesium uptake) progressed according to (7.8).

$$5ZnO(s) + 2Cl^-(aq) + 6H_2O(aq) \qquad (7.8)$$
$$\leftrightarrow Zn_5(OH)_8Cl_2 \cdot H_2O(s) + 2OH^-(aq)$$
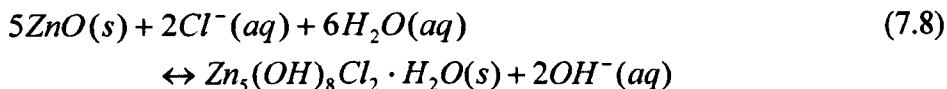
Hydroxide produced by (7.7)-(7.8) is consumed by magnesium cations according to (7.4). Thereby, enhanced protection of the steel substrate is offered by magnesium-containing zinc coatings due to formation of protective magnesium hydroxide at high pH cathodic sites and protective zinc- or magnesium-hydroxy carbonates and simonkolleite at intermediate pH anodic sites. Subsequent spraying with the acidified solution re-dissolves the corrosion products. Preferential dissolution of the alkaline magnesium hydroxide [156], reaction (7.2) rather than zinc oxide is likely (note the increase in zinc oxide concentration in Fig. 4 versus Fig. 2c). The cycle of re-precipitation of corrosion products begins as the acidity of the electrolyte is consumed by dissolution of the corrosion products and oxygen reduction dominates as the cathodic reaction.

However, this protective mechanism may be undermined at any spraying interval if the acid activity cannot be consumed by the corrosion products on the ZMG surface, preventing oxygen reduction and subsequent magnesium hydroxide precipitation at alkaline sites. He et al. [111] showed that a greater dwell time and increased acidity of corroding solution led to increased metal runoff rates on zinc. It was also shown that a sufficient rain volume is required to transport soluble corrosion species, such as aqueous Mg^{2+} and Zn^{2+} ions, from the corroding surface. The spray period used in this work was relatively short and the vertical panel orientation led to rather rapid draining of the acid rain solution from the corroding surface, with the exception of the panel lower edges. Initiation of red rust was observed at the lower edges of the test panels, which suffered increased dwell time and volume of solution compared to the rest of the panel due to the vertical orientation of the panel and surface tension effects. It is proposed that in these areas, magnesium ions produced by reactions (7.1) and (7.2) were washed from the

corroding surface. Electrochemical attack of the Zn_2Mg phase would ensue according to (7.9)

$$Zn_2Mg(s) \rightarrow 2Zn^{2+}(aq) + Mg^{2+}(aq) + 4e^- \qquad (7.9)$$
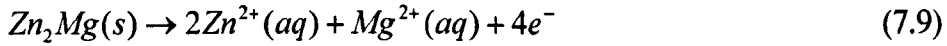
This anodic reaction may be balanced by either hydrogen evolution (7.10) or by direct dissolution of corrosion products according to (7.2) and (7.11)-(7.13).

$$2H^+(aq) + 2e^- \rightarrow H_2(g) \qquad (7.10)$$

$$8H^+(aq) + Zn_5Cl_2(OH)_8.H_2O(s) + 8e^- \qquad (7.11)$$
$$\rightarrow 5Zn^{2+}(aq) + 2Cl^-(aq) + 9H_2O(aq)$$

$$2H^+(aq) + ZnO(s) + 2e^- \rightarrow Zn^{2+}(aq) + H_2O(aq) \qquad (7.12)$$

$$2H^+(aq) + Mg_5(OH)_2(CO_3)_4.4H_2O(s) + 2e^- \qquad (7.13)$$
$$\rightarrow 5Mg^{2+}(aq) + 4CO_3^{2-}(aq) + 6H_2O(aq)$$
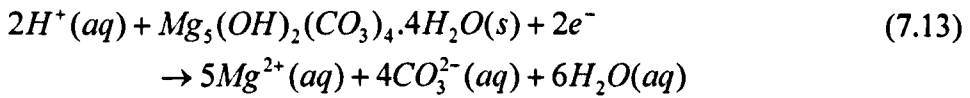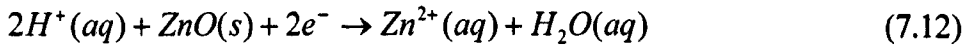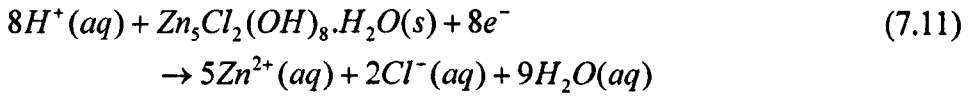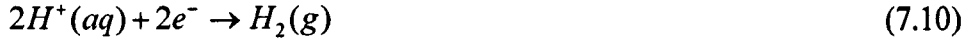
Hausbrand et al. [84] reported that Zn_2Mg is susceptible to dealloying with preferential magnesium dissolution because magnesium is less noble than zinc. Runoff of the magnesium and subsequently zinc cations from the Zn_2Mg phase of the corroding surface reduces the corrosion benefit afforded by ZMG compared to EG at the lower edges of the panels. A corrosion benefit was realised at the upper areas of the panel where oxygen reduction and reduced metallic runoff allow protective mechanisms to establish.

The reduced red rust resistance of ZMG compared to EG in acid rain reported in this work is due to the aggressive corrosion environment developed at the lower edge of the vertical test panels. Despite runoff of dissolved metallic species from the ZMG sample at this area, ZMG did still offer some overall advantage (1.5-times) in resistance to red rust initiation compared to EG, although this may be due in some part to the increased thickness of the ZMG coating compared to the EG coating. Panel areas subject to reduced dwell time and volume of acid rain spray

exhibited enhanced corrosion resistance compared to EG, as evidenced by the relatively slower propagation of rust over the panel surface (4-fold improvement in red rust resistance over a 20-week test period).

These observations show that the corrosion resistance of ZMG may be reduced when subject to copious acidic precipitation and high dwell times (e.g. drizzle type precipitation [111] and horizontal panel orientation). However, in environments where the magnesium is not drained from the corroding surface, the synergistic effects of co-corrosion of zinc and magnesium described in Chapter 6 can establish. The corrosion resistance advantages of using ZMG as a construction material therefore depend on the local environment that the component will experience and on the component geometry. Long-term corrosion rate data in natural weathering conditions are required to make reliable assessments of the corrosion benefit of magnesium-containing zinc coatings.

7.6. CONCLUSIONS

- The sodium chloride test regime (1 wt.% NaCl acidified to pH 4.2) was a more aggressive corrosion test of zinc-based coatings than the acid rain test (simulated acid rain solution acidified to pH 3.5).

- Although zinc-magnesium coated steel (ZMG) retained its improved resistance to red rust initiation versus electrogalvanized steel (EG), the magnitude of improvement was halved in the acid rain test (1.5-fold improvement) compared to its improvement in the sodium chloride test (3-fold improvement).

- Longer term data showed that even though ZMG exhibited reduced resistance to red rust initiation in acid rain relative to its resistance in sodium chloride, propagation of rust continued at a reduced rate compared to EG. Following 20 weeks of exposure to the acid rain environment, the proportion of the ZMG surface covered by red rust was 25% that of the EG surface.

- It is proposed that the corrosion resistance advantage of ZMG depends upon the formation and preservation of magnesium hydroxide at high-pH cathodes

and that the greatest corrosion improvement versus conventional zinc coatings is observed when magnesium hydroxide precipitates in the earliest stages of corrosion.

Chapter 8

PAINTED PANELS

8.1. INTRODUCTION

The corrosion mechanisms proposed in Chapters 6 and 7 suggest that ZMG offers enhanced corrosion resistance compared to conventional zinc coatings due to the precipitation of protective corrosion products. This protective action proved to be active over the full test period in both the sodium chloride and the acid rain environments used in this work. The nature of ZMG's corrosion protection mechanism implies that ZMG may offer increased corrosion protection at areas of reduced paint thickness or paint defects, such as scribe lines, cut edges and crevices (refer to Section 4.4.2). Use of galvanized steel alone does not provide adequate corrosion protection at the cut edges and creviced areas of the vehicle body and secondary protection materials such as sealer and lacquer are often applied. The corrosion resistance of painted panels of ZMG is investigated in this chapter and the influence of edge geometry, construction material, deburring, lacquer and sealer applications of edge corrosion resistance are explored. The materials and experimental methods used are given in Section 8.2. Assessments of scribe line, edge corrosion and crevice corrosion resistance of ZMG panels compared to conventional galvanized steel panels are given in Sections 8.3-8.5 respectively and the results are discussed in Section 8.6.

8.2. MATERIALS AND EXPERIMENTAL METHODS

8.2.1. Materials and Test Panels

Three different types of painted test panels were assessed. Square panels (measuring approximately 100 mm x 100 mm) were cut from uncoated steel (UC), electrogalvanized steel (EG), hot-dip galvanized steel (HDG) and zinc-magneisum coated steel (ZMG). The panels were processed in the pre-treatment line of Volvo Car Corporation's (VCC's) paint shop so that each panel was degreased, phosphated

and e-coated (painted). Scribe lines were cut into the painted panels as described in Section 5.2.3.

Edge corrosion test panels with three different cut edge types, as shown in Fig. 5.8, were fabricated from UC, HDG and ZMG. UC was included in this test phase to assess the effects of edge geometry in isolation from the effects of metallic coatings on cut edge corrosion resistance. HDG and EG exhibited similar corrosion rates in the open corrosion mode when tested according to the Volvo cabinet test (see Fig. 6.1 and Table 6.2); therefore only one of these materials was tested to reduce the total number of test panels. HDG was selected in preference to EG because HDG is more commonly used as a construction material for automotive vehicle bodies. One set of edge corrosion panels comprised three individual panels with the position of the test edges rotated, such that each edge type occupied each edge position (refer to Fig. 5.8). Three sets of panels were produced for each material with the edges in the as-cut condition. Three further sets of test panels were fabricated for each material with deburred edges. The panels were then processed in the paint pre-treatment line as described in Section 5.2.3, yielding phosphated and e-coated test panels. Two additional sets of panels for each material were fabricated with edges in the as-cut condition, but were covered by either lacquer or sealer after the paint treatment, as described in Section 5.3.3. The final data set included 3 materials, 3 edge cutting methods and 4 edge finishing methods, as described by Table 8.1.

Table 8.1: Edge corrosion test variables considered.

Metallic coating	Edge cutting method	Edge finishing
Uncoated (UC)	Laser cutting	None (as-cut) + paint
Hot-dip galvanized (HDG)	Small clearance punching	Deburred (before paint)
Zinc-magnesium (ZMG)	Large clearance punching	Lacquered (after paint)
		Sealed (after paint)

Crevice corrosion test panels (described in Section 5.3.4) were fabricated from UC, HDG and ZMG.

8.2.2. Corrosion Test Method

All the painted panels were tested according to the Volvo cabinet method (described in Section 5.4.2). The panels were seated in racks and stood at an angle of 15° to vertical. The panels were oriented such that the scribe line, the non-burred side of the punched edges and the crevices were on the upward facing surface (panel front). The test duration was 12 weeks and samples were removed from the test chamber at intervals during the test to assess corrosion propagation. The lacquered and sealed edge corrosion panels were assessed only after completion of the test (i.e. after 12 weeks) due to their reduced corrosion rates.

8.2.3. Corrosion Resistance Assessments

Scribe line creep was measured as described in Section 5.5.3. Edge corrosion was assessed by measuring the corrosion-affected area (e.g. red rust for UC and paint delamination for HDG and ZMG) associated with each edge type. Crevice corrosion resistance was assessed by measurement of the red rust area within each crevice. All area measurements were made using image analysis. Cross-sectional analysis was carried out using optical light microscopy and a Jeol 6400 scanning electron microscope (SEM) enabled with energy dispersive spectrometry (EDS). Optical micrographs showed the distribution of paint and the SEM micrographs in back-scattered electron (BSE) mode highlighted the distribution of metallic coating and corrosion products. X-ray diffraction (XRD) analysis was carried out on samples cut from the unpainted area (i.e. test area) of the crevice corrosion panels.

8.3. SCRIBE LINE CREEP

The scribe line creep was measured as described in Section 5.5.3 on one panel of each material after 4, 8 and 12 weeks of corrosion testing according to the Volvo cabinet test method (described in Section 5.4.2) and the results are shown in Fig 8.1.
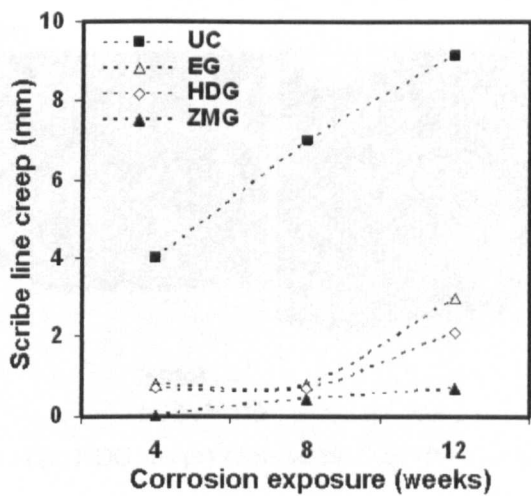
Fig. 8.1: Scribe line creep measurements.

Use of zinc-coated steel rather than UC resulted in at least a 3-fold reduction in scribe line creep after 12 weeks of corrosion testing. The slightly greater scribe creep resistance of HDG compared to EG may be due to the increased zinc coating thickness of the former. ZMG offered increased resistance to corrosion initiation at the scribe line versus the other materials as noted by the absence of creep for ZMG following 4 weeks of corrosion testing. A further 3-fold reduction in scribe line creep was observed for ZMG versus EG and HDG following 12 weeks of corrosion testing, although an improvement of this magnitude was not observed at the 8 week interval.

Fig. 8.2 shows cross-sections through the middle of the scribed areas on HDG and ZMG after 12 weeks of corrosion testing. The paint (e-coat) layer has been artificially highlighted by shading.

Fig. 8.2: Cross-sections of (a) HDG and (b) ZMG scribe lines after 12 weeks of corrosion testing.

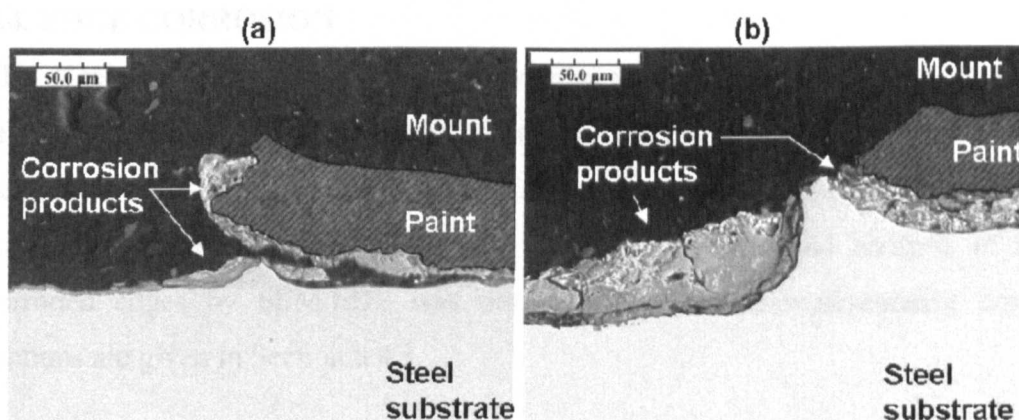Fig. 8.2a shows delamination of the paint layer from the HDG surface adjacent to the scribed area. Zinc-containing corrosion products were observed at the underside of the delaminating paint but the thin layer of corrosion products visible at the scribed area for HDG were iron-based. Relatively thicker corrosion products were observed on the scribed area of the ZMG sample, (see Fig. 8.2b). EDS analysis showed that these corrosion products contained zinc, oxygen, chlorine and iron, with increasing chlorine concentration towards the edge of the scribe (left to right in Fig. 8.2b). The corrosion products underneath the paint layer did not contain iron, but EDS analysis showed the presence of zinc, oxygen and chlorine. Negligible magnesium was detected by EDS. Paint delamination was not observed for the ZMG sample. Comparison of Fig. 8.2a and Fig. 8.2b shows a greater steel shoulder at the ZMG scribe line, indicating either a deeper scribe line or greater substrate attack than for HDG. Variations in the scribe line depth cannot be avoided because they were cut manually. Unfortunately there were not enough samples available to assess whether increased scribe line creep was associated with deeper cuts.

8.4. EDGE CORROSION

The edge corrosion resistance of each material was assessed and some geometric effects were also included in this test phase. The edges investigated are described in Section 8.4.1 and the corrosion-affected areas measured with each edge type for each material are presented in Section 8.4.2. Cross-sectional analysis of the corroded edges by SEM/EDS was performed and some representative cross-sections are given in Section 8.4.3.

8.4.1. Edge Characterization

Coverage of the edges by zinc coating (where present) and e-coat paint was assessed. Fig. 8.3 shows the cut edges developed by each cutting method. Zinc was not present along the laser cut edge and receded from the cut edge corners by 4-5µm due to vapourization of the zinc by the laser. The punched edges shared characteristic edges defined by a rollover, shear and burr zone, as described in Section 5.3.2. The zinc coating adhered to the rollover zone and traces of the zinc coating were observed at the junction of the shear and rollover zones, but generally the shear and burr zones were not covered by zinc.

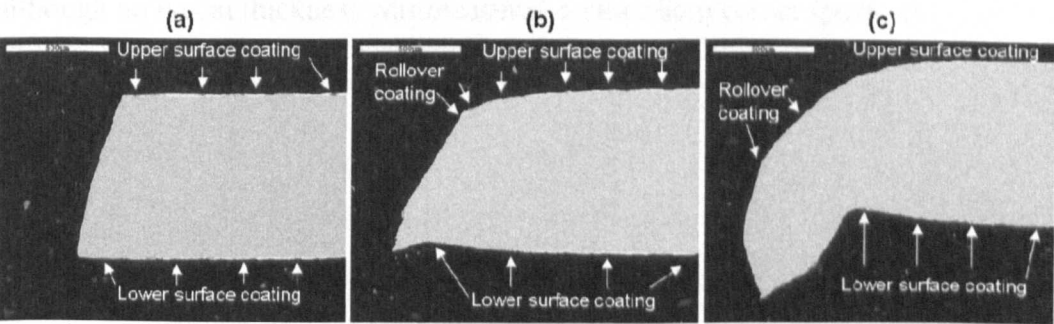Fig. 8.3: Edges as cut by (a) laser (b) small clearance punch and (c) large clearance punch.

Burrs were removed from the punched edges using a grinding wheel and the modified corner was then reshaped by polishing and buffing. No modifications were made to the rollover zones of the punched edges. The resultant cross-sections are shown in Fig. 8.4, with arrows indicating the maximum extent of the metallic coating coverage.

(a)   **(b)**
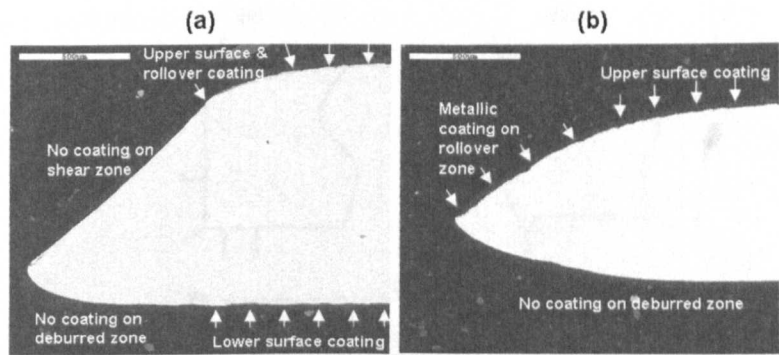
Fig. 8.4: Deburred edges cut by (a) small clearance punch and (b) large clearance punch for HDG. Arrows indicate extent of zinc coating coverage.

Unfortunately, some of the metallic coating was removed from the HDG and ZMG edges during the deburring process. Up to 1 mm was removed from the burr zone of the small clearance and up to 3 mm was removed from the burr zone of the large clearance punched edges (see Fig. 8.4b). The thickness of the e-coat paint layer for each edge was measured and the results are shown in Fig. 8.5 and Fig. 8.6. All sharp edges (measurement points b and e) suffered reduced e-coat thickness compared to the thickness at the lower surface (point g). Slightly greater e-coat thicknesses were measured on the deburred edges (compare Fig. 8.5 and Fig. 8.6) although no e-coat thickness was measured on the sharp corner (point e).

Fig. 8.5: E-coat thickness (a) measurement points on laser cut edges (b) measurement points on punched edges and (c) measurements.

Fig. 8.6: E-coat thickness (a) measurement points and (b) measurements for deburred punched edges.

8.4.2. Edge Corrosion Resistance

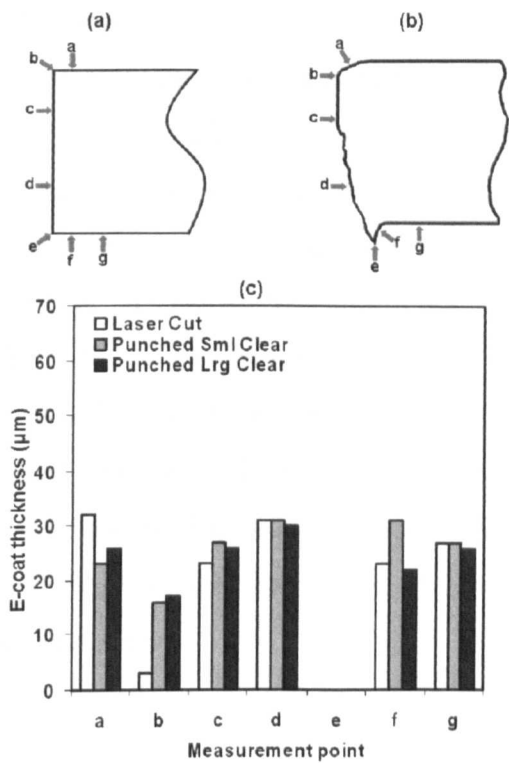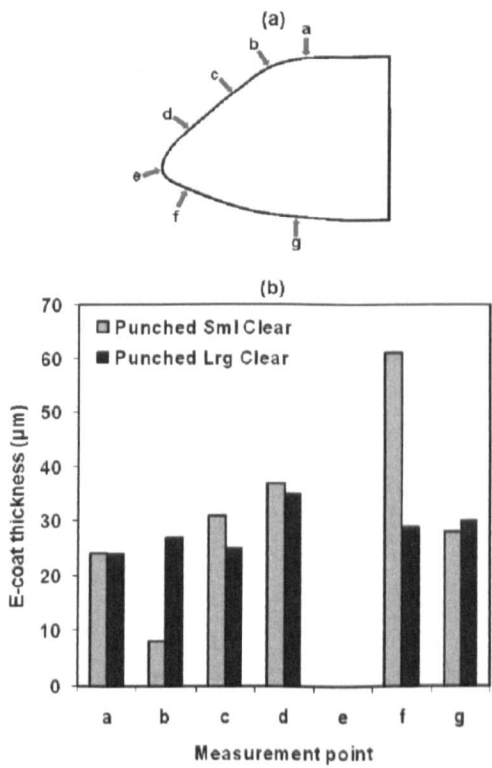The corrosion-affected area associated with each edge type and each material was measured as described in Sections 5.5.1-5.5.2. The total affected area was the sum of the affected areas on the front and rear surfaces of each edge type. Each result for UC at each interval and for HDG and ZMG after 8 weeks is the average of 3 measurements; each result for HDG and ZMG after 4 and 12 weeks is the average of 2 measurements. This is because paint was not removed from one sample each of HDG and ZMG after 4 and 12 weeks to allow cross-sectional analysis with the paint intact. The lacquered edges of each material were assessed in the same way following 12 weeks of corrosion testing. No corrosion-affected area was observed for sealed edges; the sealer offered complete inhibition of edge corrosion for the duration of the test for each material.

Effect of Material

The total corrosion-affected area for each material during the corrosion test is shown in Fig. 8.7. Painted UC panels suffered the greatest corrosion attack. Use of HDG resulted in a significant (approximately 6-fold after 12 weeks of testing) reduction in the affected area compared to UC. ZMG offered further reductions in affected area compared to UC and to HDG (approximately 25-fold and 4-fold respectively after 12 weeks of testing). It can also be seen from the figure that the rate of corrosion propagation over the test period increases in the order $ZMG < HDG << UC$.
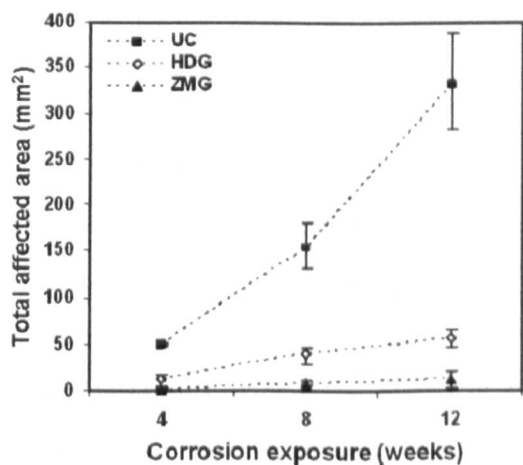

Fig. 8.7: Total affected area on cut edges for UC, HDG and ZMG during the corrosion test.

Effect of Cutting Method.

Little difference was observed in the total corrosion-affected areas due to punching with small or large clearances, as shown in Fig. 8.8. The ZMG trends for punched edges were similar to the HDG trends generally but were of much lower magnitude and are not shown in the figure for clarity. Slightly reduced affected areas were observed for the laser cut edges compared to the punched edges for HDG throughout the test and for UC after 4 and 8 weeks. A sharp increase in the average affected area of laser cut edges was observed on UC at 12 weeks. This observation may be due to the merging of corrosion fronts from two points (points b and e in Fig. 8.5) on the laser cut edges compared to the single-front attack expected on punched edges.
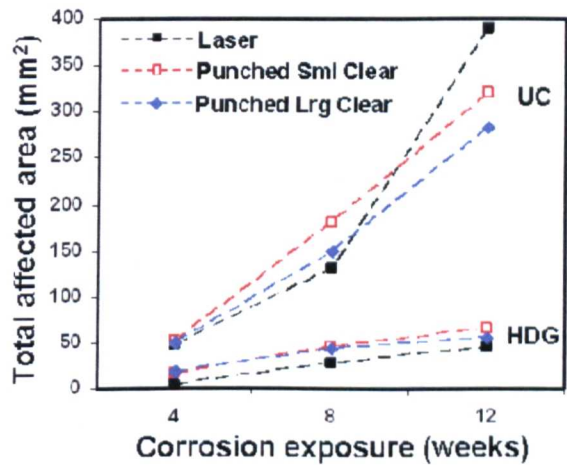
Fig. 8.8: Effect of cutting method on affected area for UC and HDG during the corrosion test.

Effect of Burr on Punched Edges.

The effect of the burr on punched edges was assessed by comparing the affected areas measured on the rollover side versus the burr side of each panel. Fig. 8.9 shows the ratio of these areas for each material at small and large clearances during the test. The affected area depended on the edge geometry, with greater corrosive attack measured on the burr side (*Rollover : Burr < 1*). Greater differences between rollover and burr side corrosion were observed for the large clearance punch and the ratio of rollover to burr side corrosion increased as the corrosion test progressed. These trends indicate corrosion initiation at the burr side of the punched edges for each material, even though the burr was situated at the rear side

of the panel, which was more sheltered from corrosion due to the panel orientation (see Fig. 6.1). The affected area rollover:burr ratios generally increased as corrosion progressed, indicating more uniform attack on both sides of the punched edges. However, preferential attack at the burr side continued throughout the test because the ratio did not reach unity.
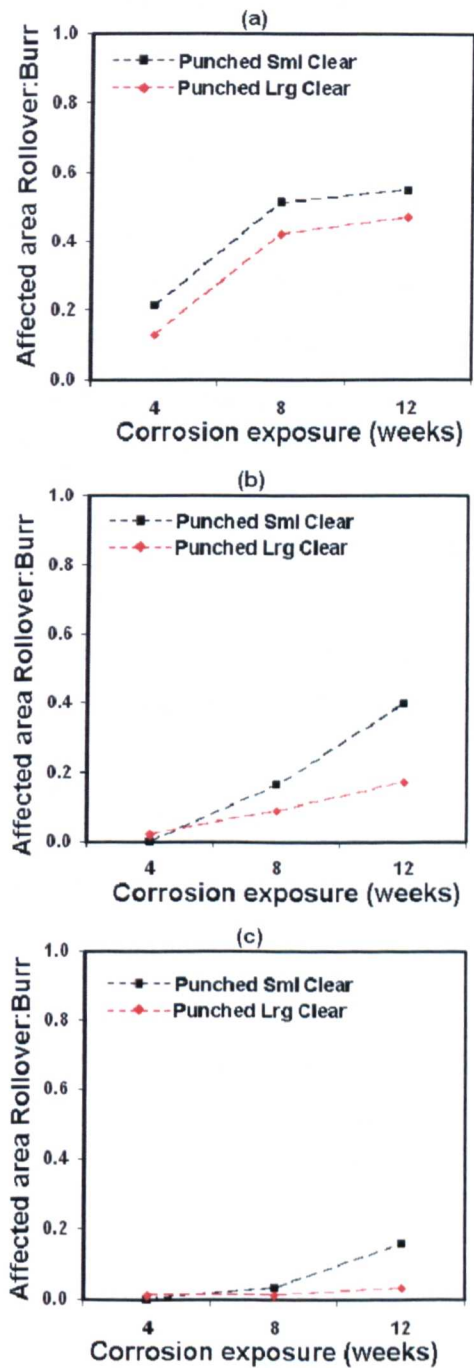
Fig. 8.9: Rollover to burr side affected areas for punched edges of (a) UC, (b) HDG and (c) ZMG.

Effect of De-Burring Process.

The effect of deburring on the total affected areas for each material during the corrosion test is shown in Fig. 8.10.
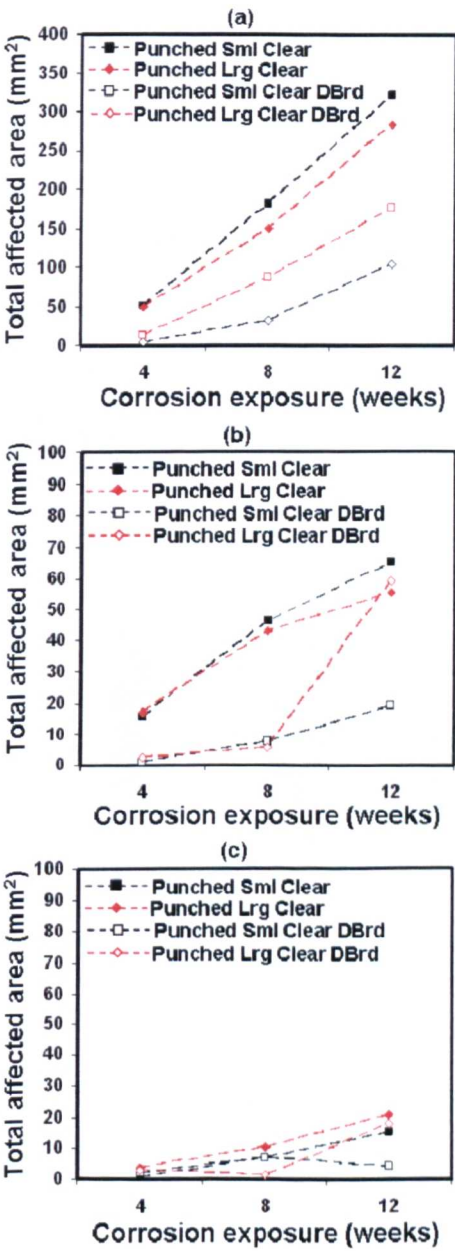
Fig. 8.10: Effect of deburring ("DBrd") on total affected areas for (a) UC, (b) HDG and (c) ZMG. *Note reduced y-scale on (b)-(c) compared to (a).*

The deburred edges on UC exhibited reduced corrosion attack compared to the as-cut edges. A similar trend was observed on HDG and ZMG up to 8 weeks of corrosion testing, however increased corrosion attack was observed on deburred edges originally formed by punching with large clearance after 12 weeks of

corrosion testing. These trends indicate that deburring or reshaping the cut edge delays corrosion initiation, but corrosion may propagate at increased rates compared to as cut edges if too much of the metallic coating is removed.

Effect of Lacquer Application.

The ratios of corrosion-affected areas for lacquered edges compared to as-painted edges for each material following 12 weeks of corrosion testing are shown in Fig. 8.11. Lacquer application resulted in reduced corrosion attack for each material and each edge type (*Lacquered:As painted < 1*).
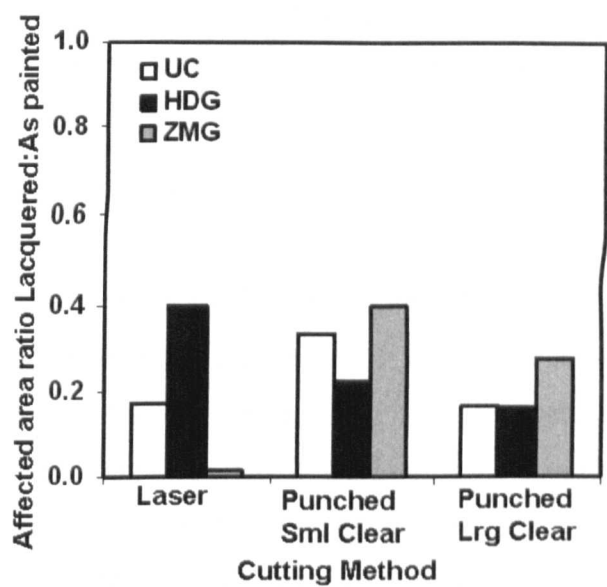
Fig. 8.11: Ratio of total affected areas for edges lacquered after painting to the as-painted edges after 12 weeks exposure to the Volvo cabinet test.

The relative effectiveness of deburring prior to paint and lacquering after paint was assessed by comparing the ratio of affected areas on lacquered edges to deburred edges, see Fig. 8.12. Lacquering after painting generally resulted in greater corrosion resistance than deburring before painting for edges punched with a large clearance (ratio < 1), but little difference was observed in the effects of each process for edges punched with a small clearance. Deburring before painting gave greater corrosion benefit than lacquering after painting for ZMG edges punched with small clearance (ratio > 1).
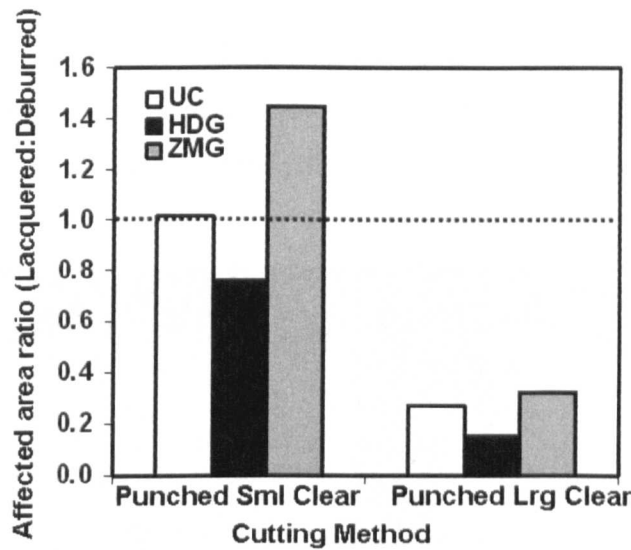
Fig. 8.12: Ratios of affected areas on (painted and lacquered) and (deburred and painted) punched edges after 12 weeks of corrosion testing.

8.4.3. Cross-sectional Analysis

Cross-sectional analysis was carried out using scanning electron and optical microscopy. The analysis confirmed corrosion initiation at areas with reduced paint thickness (measurement points b and e for laser cut edges and point e for punched edges in Fig. 8.5a-b). Figs. 8.13-8.15 show cross-sections of HDG and ZMG punched edges (small clearance) after 12 weeks of corrosion testing. Voluminous corrosion products extended from the burr zone underneath the paint layer along the lower surface of the HDG panel. The rollover zone of HDG was relatively unaffected at this particular cross-section with significant amounts of bright, uncorroded zinc apparent (see Fig. 8.15a), but the loss of paint from the shear and fracture zones indicates transport of corroding species along the metal to paint interface from the burr to rollover zones. Corrosive attack at the rollover side of the HDG panel may proceed and indeed was indicated by the increasing trend in Fig. 8.9b.

Corrosion products were also observed at the burr zone of the ZMG edge and the corrosion front extended along the lower surface for a distance of approximately 0.7 mm (compared to approximately 2.5 mm for HDG) before bright, unreacted zinc was observed. Corroded metallic coating at the rollover zone may have resulted from diffusion of corrodents through the paint layer (reduced in thickness at the

rollover to shear zones junction) or by the transport of corroding species from the burr zone along the fracture and shear zones to the rollover zone (see Fig. 8.15b) or from defects outside the plane of view. However, the corrosion products did not appear to affect the adherence of the paint layer to the ZMG edge.
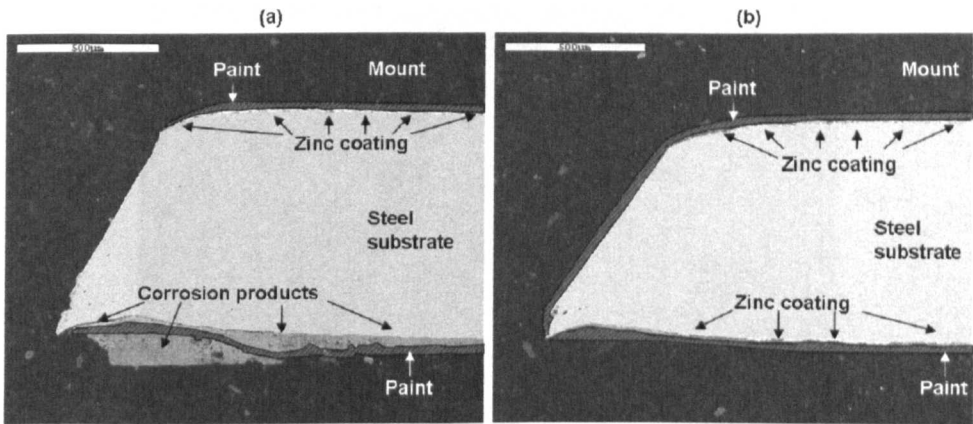
Fig. 8.13: Cross-sections of as-cut (punched with small clearance) edge for (a) HDG and (b) ZMG after 12 weeks of corrosion testing.
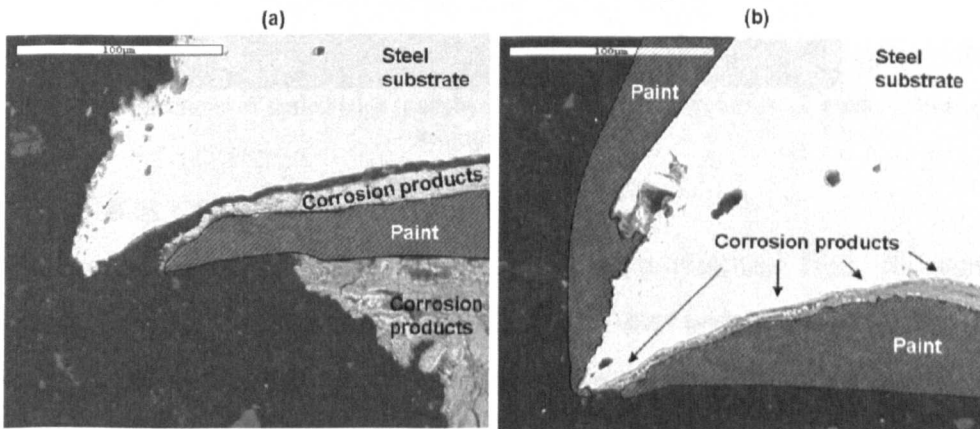
Fig. 8.14: Detailed views of burr zones of as-cut edges (punched with small clearance) for (a) HDG and (b) ZMG after 12 weeks of corrosion testing.
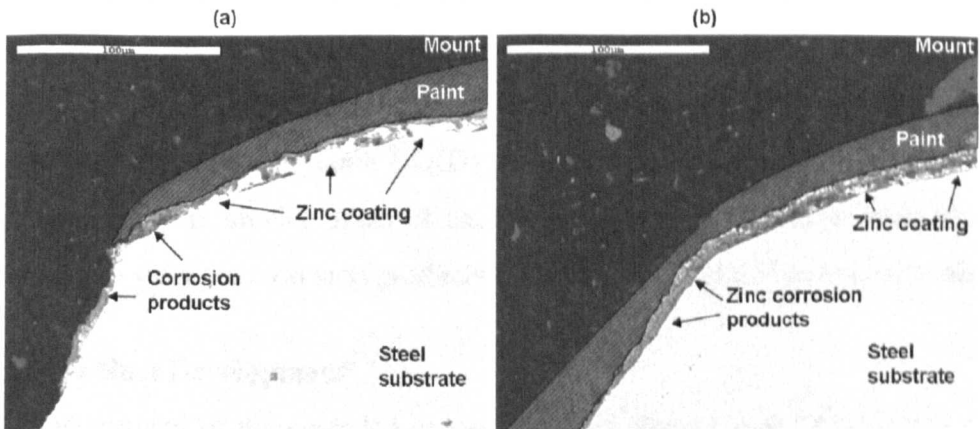
Fig. 8.15: Detailed views of rollover zones of as-cut edges (punched with small clearance) for (a) HDG and (b) ZMG after 12 weeks of corrosion testing.

The cross-section of a sealed edge for ZMG after 12 weeks of corrosion testing is shown in Fig. 8.16. The sealer acted as a barrier to corrosion and the edge showed no evidence of corrosion attack even at the end of the test period. Similar observations were made for HDG and UC.
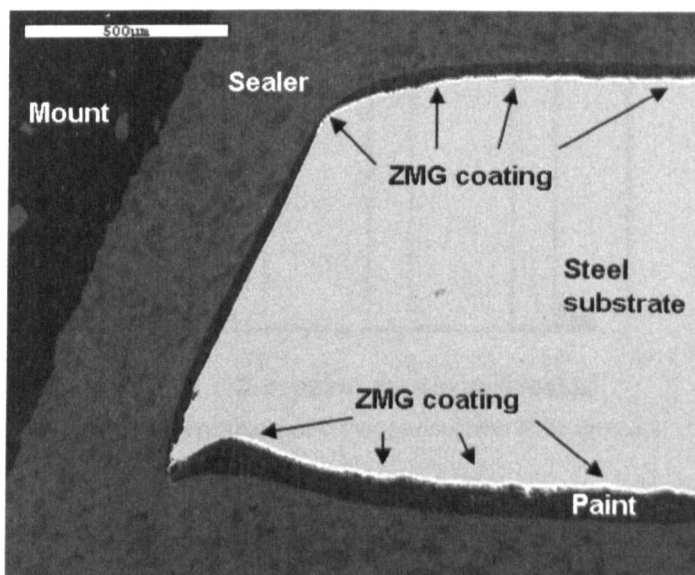
Fig. 8.16: Cross-sections of sealed edge (punched with small clearance) after 12 weeks of corrosion testing (ZMG).

8.5. CREVICE CORROSION

Crevice corrosion test panels (see Fig. 5.14) were removed from the cabinet following 6, 8 and 12 weeks of corrosion testing. Apart from a small overlap, paint was not present within the crevice area and corrosion products on the crevice area could be viewed through the glass covers. One UC test panel was removed after 2 weeks of testing when the proportion of the crevice surface that was covered by red rust approached 100%. General crevice corrosion resistance was assessed by visual analysis of the red rust that developed within the crevice area, as discussed in Section 8.5.1. X-ray diffraction (XRD) analysis was performed on the corrosion products within the crevice areas of each material. Cross-sectional analysis was carried out to view the corrosion products following 12 weeks of corrosion testing.

8.5.1. Red Rust Development

Visual assessment of the corroded crevice samples showed that UC suffered rapid red rust development, with 95% coverage following 2 weeks of corrosion testing and the HDG sample area was 93% red rust after 8 weeks of testing. ZMG offered

significantly improved red rust resistance compared to HDG, as indicated by the measurements shown in Fig. 8.17 and by the photographs in Fig. 8.18.
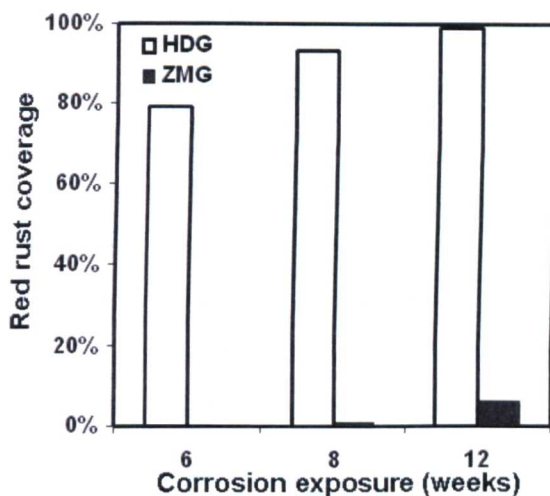
Fig. 8.17: Percentage of crevice area covered by red rust.

(a) (b)
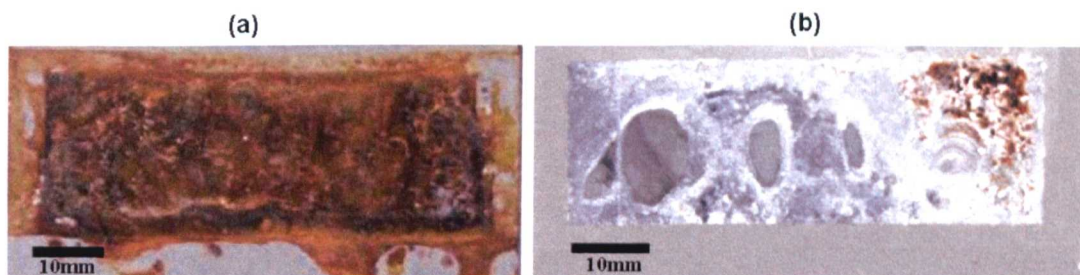
Fig. 8.18: Photographs of (a) HDG and (b) ZMG after 12 weeks of crevice corrosion testing.

8.5.2. Corrosion Product Characterization by XRD

XRD diffractograms for HDG and ZMG crevice panels after 6, 8 and 12 weeks of corrosion testing are shown in Fig. 8.19. The diffractograms obtained for uncorroded HDG and ZMG are shown for comparison. Peaks at $2\theta \approx 45°$ and $2\theta \approx 66°$ are due to diffraction from the steel substrate.

The diffractograms obtained for HDG (Fig. 8.19a) under crevice conditions show almost complete dissolution of the zinc coating after 6 weeks of corrosion testing; note the low unreacted zinc peaks present at $2\theta \approx 36°$, $2\theta \approx 39°$ and $2\theta \approx 43°$. Zinc corrosion products (simonkolleite, zinc hydroxy carbonate and zinc oxide) were also detected after 6 weeks but were not detected after 8 weeks. Iron corrosion products dominated by the end of the 12-week test period, (as also shown

in Fig. 8.18), although a peak at $2\theta \approx 63°$ indicated the endurance of zinc oxide on the corroding surface. However zinc oxide is unlikely to give corrosion protection to the corroding material; indeed the HDG 12 week diffractogram was very similar to the diffractogram collected from UC after 2 weeks of crevice corrosion testing, indicating almost complete loss of the zinc corrosion protection from HDG by the end of the test period.

The diffractograms for ZMG (Fig. 8.19b) show a more gradual transformation of zinc from both the Zn$_2$Mg and Zn phases of the coating to zinc corrosion products (simonkolleite, zinc oxide and eventually zinc hydroxy carbonate). Zn$_2$Mg was detected after 8 weeks of testing but not after 12 weeks and the unreacted zinc peaks ($2\theta \approx 43°$ and $2\theta \approx 54°$) diminished in intensity as the test progressed.
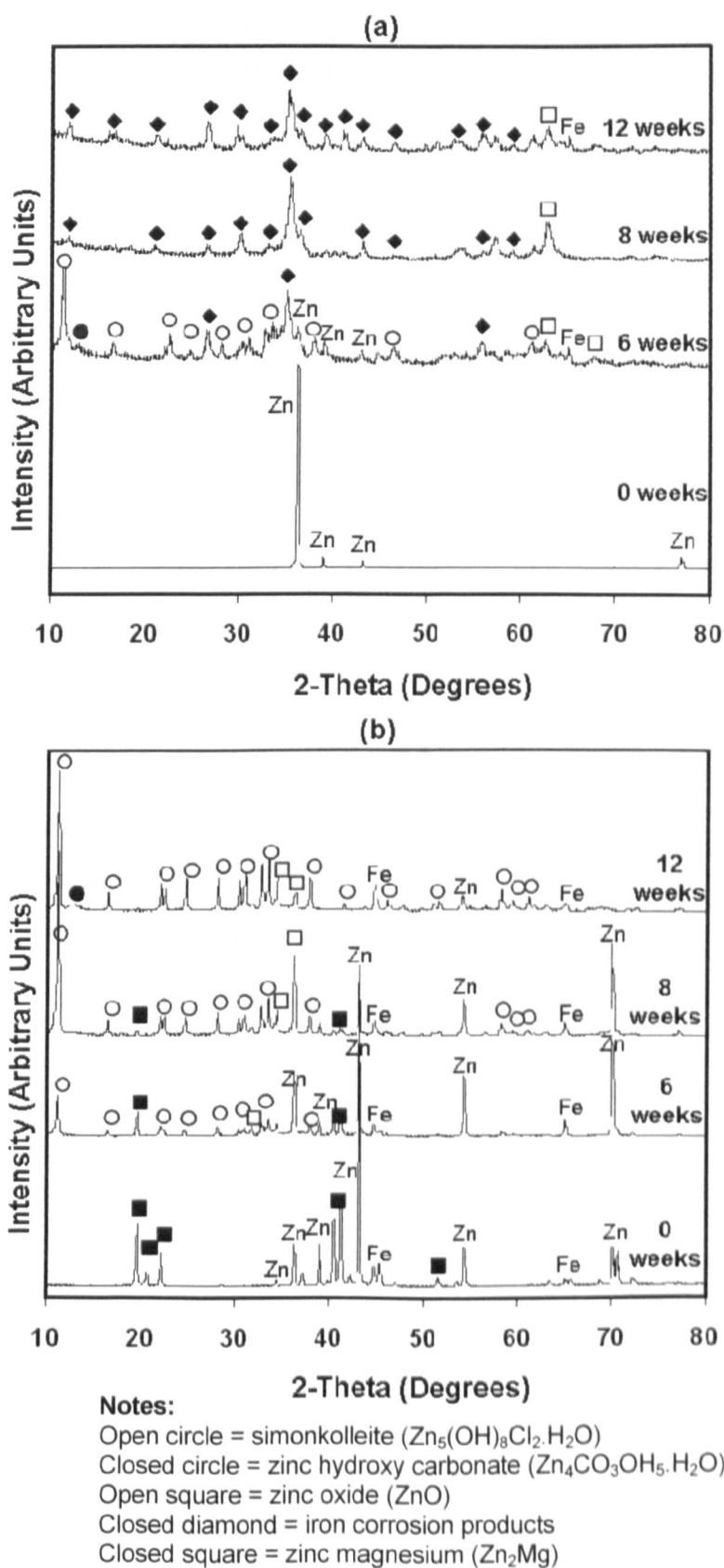
Fig. 8.19: XRD diffractograms for (a) HDG and (b) ZMG crevice areas after 0, 6, 8 and 12 weeks of corrosion testing.

Detail diffractograms ($10° \leq 2\theta \leq 30°$) for ZMG given in Fig. 8.20 show the transformation of the original metallic phases to corrosion products between 6 and 12 weeks of corrosion testing. Similar to the findings in Chapters 6 and 7, magnesium-containing corrosion products were not easily detected on the corroding surface. A small peak attributable to magnesium hydroxide was detected on ZMG after 6 weeks (closed triangle in Fig. 8.20a) but no other magnesium-containing corrosion products were detected by XRD during the test.

Notes:
Open circle = simonkolleite ($Zn_5(OH)_8Cl_2.H_2O$)
Closed circle = zinc hydroxy carbonate ($Zn_4CO_3(OH)_5.5H_2O$)
Closed square = zinc magnesium (Zn_2Mg)
Closed triangle = magnesium hydroxide ($Mg(OH)_2$)
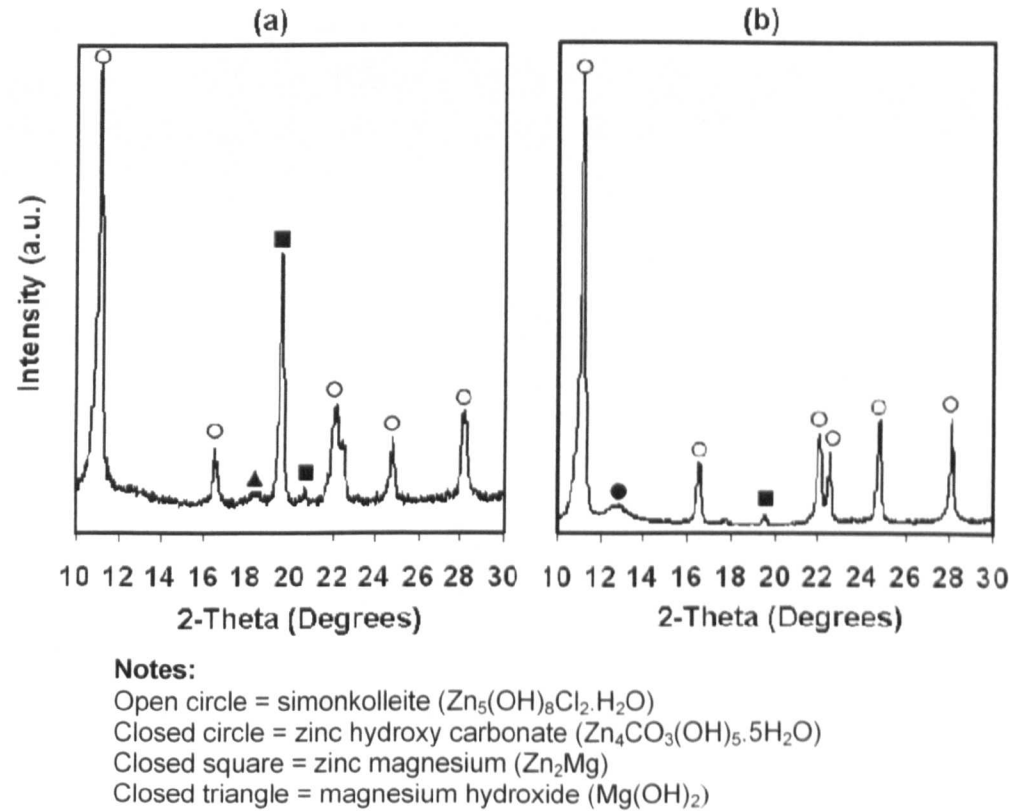
Fig. 8.20: Detail diffractograms for ZMG after (a) 6 and (b) 12 weeks of corrosion testing.

The main simonkolleite peak ($2\theta \approx 11.2°$) for ZMG was displaced to lower 2-theta values and was broader than the simonkolleite peaks detected for the HDG 6-week crevice sample and for the EG 4-week sample in Chapter 6, indicating possible uptake of magnesium into the simonkolleite structure. The magnitude of the 2θ shift for the simonkolleite peak on ZMG increased as the crevice corrosion test progressed, with shifts of $2\theta - 0.06°$, $2\theta - 0.10°$ and $2\theta - 0.12°$ measured after 6,

8 and 12 weeks respectively. This may indicate increased binding of magnesium into simonkolleite as Zn_2Mg went into solution.

8.5.3. Cross-sectional Analysis

Dense, lamellar corrosion products of up to 15 μm thickness were observed on the cross-section of the ZMG crevice area following 12 weeks of corrosion testing, as shown in Fig. 8.21.
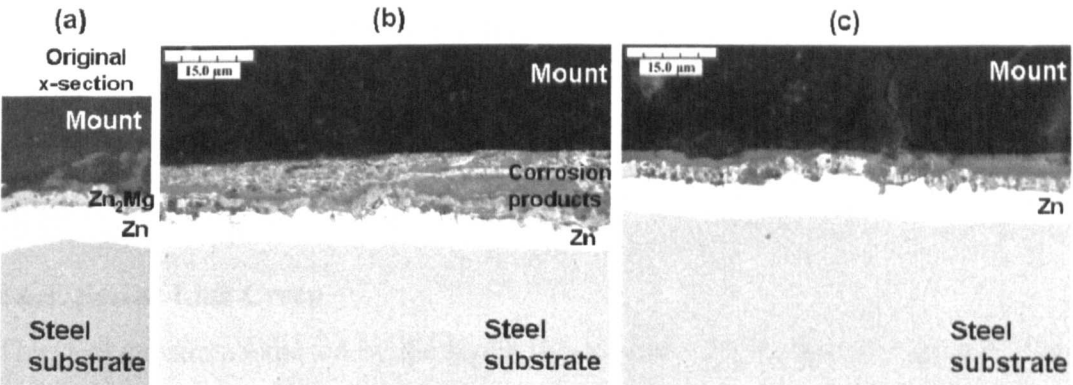
Fig. 8.21: Cross-sections of ZMG (a) before corrosion testing and (b) heavily corroded area after 12 weeks and (c) relatively unaffected area after 12 weeks of corrosion testing.

In some areas, the material was relatively unaffected by corrosion, compare Fig. 8.21a and Fig. 8.21c, and the Zn_2Mg phase of the original ZMG coating appeared unaffected by corrosion. The underlying zinc phase of the original ZMG coating appeared intact and unaffected at each point along the cross-section investigated. These observations were not in agreement with the XRD diffractograms (see Fig. 8.19), which indicated dissolution of the Zn_2Mg phase and diminution of the metallic zinc peaks after 12 weeks of corrosion testing. It is proposed that these differences are due to the location of the analysis samples; the XRD sample was cut from the right hand side of the crevice area shown in Fig. 8.19b whereas the cross-section was cut from the centre to the left hand side of the crevice area (parallel to the lower edge). Red rust initiation and significant white corrosion products were observed at the right hand side of the crevice area and these products were detected by XRD. The PTFE spacer (see Section 5.3.4) was situated at the right hand side of this ZMG sample; therefore increased corrosion for ZMG was associated with the

larger crevice opening (approximately 0.28 mm compared to approximately 0.03 mm). This observation is discussed in Section 8.6.3.

8.6. DISCUSSION

The results presented in this chapter demonstrate the corrosion benefit offered by coating of painted panels with ZMG versus HDG in areas of aggressive corrosion. Painted panels constructed from ZMG were 3-times more resistant to corrosion creep from the scribe line and were 4-times more resistant to corrosion from cut edges after 12 weeks of corrosion testing. ZMG also offered significant benefit in crevice corrosion resistance (approximately 15-times greater red rust resistance) compared to HDG (see Fig. 8.18). The mechanisms that may be involved in each case are discussed in turn in the following sections.

8.6.1. Scribe Line Creep

The steel substrate exposed by the scribe line acts as a site for the oxygen reduction (cathodic reaction) according to (8.1).

$$\tfrac{1}{2}O_2(aq) + H_2O(aq) + 2e^- \rightarrow 2OH^-(aq) \qquad (8.1)$$
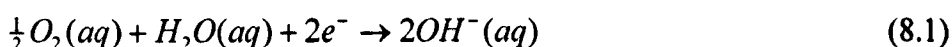
For galvanized steel, the adjacent zinc coating dissolves anodically according to (8.2).

$$Zn(s) \rightarrow Zn^{2+}(aq) + 2e^- \qquad (8.2)$$

Zinc ions react with hydroxide ions released by (8.1) to form zinc oxide, which may deposit onto the scribed area. Zinc oxide may allow the oxygen reduction reaction to continue because it is semi-conducting and anodic dissolution of the zinc coating along the metal to paint interface progresses. EDS analysis of the corrosion products underneath the paint layer and adjacent to the scribed area of the HDG panel indicated the presence of zinc, oxygen and chlorine. Transport of Cl^- ions from the defect confirms anodic activity underneath the paint layer, as proposed by Townsend et al. [159]. Ström et al. [70] reported an inverse relationship between paint undercutting from a scribe line on galvanized panels and the zinc coating thickness, indicating that the paint undercutting is determined by the progress of the

anodic dissolution front. The anodic front progress in turn, is limited by the rate of oxygen reduction at cathodic zones; in the early stages of corrosion, the cathode is at the exposed steel in the scribed area. As undercutting progresses, the cathodic zone tails the anodic dissolution front [70], leading to alkalinization of the paint to metal interface, dissolution of the phosphate layer and delamination of the paint, a phenomenon termed cathodic delamination [160]. Delamination of the paint allows greater access of corroding species (water, oxygen, Na^+, Cl^-) and the corrosion front continues. Rust develops at the scribed area when the zinc dissolution reaction (8.2) is no longer coupled to the oxygen reduction reaction (8.1) at the scribe, and oxygen reduction and iron dissolution occur at the scribed area, as described by reaction (8.3).

$$Fe(s) + \tfrac{1}{2}O_2(aq) + H_2O(aq) \rightarrow Fe(OH)_2(s) \qquad\qquad (8.3)$$

The overall mechanism is illustrated by Fig. 8.22.
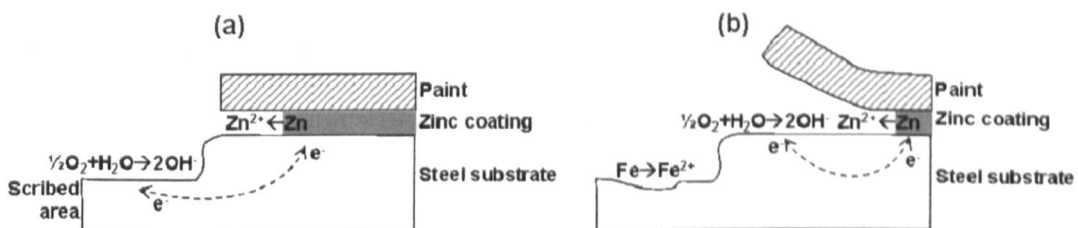
Fig. 8.22: Paint undercutting from a scribe line on galvanized steel at (a) early and (b) later stages.

Oxygen reduction may also occur at the paint-to-metal interface due to the diffusion of oxygen and water molecules through the paint layer, adding further to the anodic dissolution of the zinc coating [159].

Fürbeth et al. [47-49] demonstrated that corrosion propagation from a defect cut through to the steel substrate was greatly mitigated by exposure to carbon dioxide; i.e. precipitation of carbonates underneath the paint layer suppressed the oxygen reduction reaction, thereby limiting the overall corrosion progression. For ZMG, decreased oxygen reduction rates may occur at the early stages of scribe line corrosion due to the preferential formation of magnesium hydroxide (8.4) rather than zinc oxide adjacent to the cathode site.

$$Mg^{2+}(aq) + 2OH^-(aq) \leftrightarrow Mg(OH)_2(s) \qquad\qquad (8.4)$$
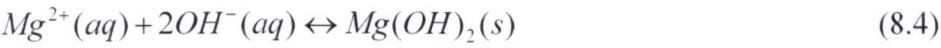
Magnesium hydroxide is a solid insulator, blocking oxygen reduction and avoiding the establishment and spreading of an alkaline active cathode. As the corrosion exposure continues, further corrodents are supplied to the defect area. EDS analysis of the corrosion products precipitated onto the scribed area of the ZMG sample after 12 weeks of corrosion indicated zinc-based corrosion products and the presence of chlorine. This is direct evidence of the inhibition of the cathodic reaction (8.1) at the scribed area of ZMG because Cl^- ions migrate to anodic sites. It is proposed that a pH gradient from alkaline to essentially neutral established at the scribed area, due to inhibition of the cathodic reaction, and the relatively slow progress of corrosion compared to the supply of Cl^- and CO_3^{2-} ions that may combine with Zn^{2+} to form protective corrosion compounds such as hydrozincite and simonkolleite, which further retard oxygen reduction.

Meanwhile, corroding species may be transported along the metal to paint interface at the edge of the scribe. Provided there is a supply of Mg^{2+} from Zn₂Mg, then oxygen reduction reaction will be retarded and alkalinity will be reduced compared to the non-magnesium zinc coated steel. The delay to oxygen reduction gives time for transformation of Zn^{2+} to protective corrosion products. The overall mechanism is described by Fig. 8.23.

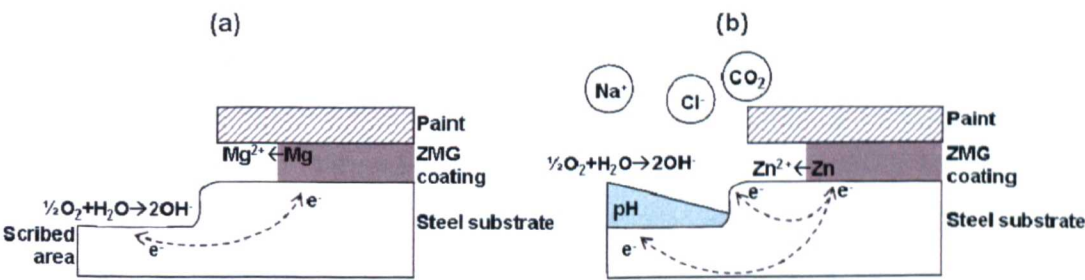Fig. 8.23: Paint undercutting from a scribe line on ZMG at (a) early and (b) later stages.

The presence of an insulating oxide layer between the paint and the metal surface that blocks the transfer of electrons has been reported by Hausbrand et al. [84] and Stratmann [128]. This oxide layer affords further corrosion protection because

oxygen reduction cannot occur easily via the diffusion mechanism described for zinc coatings by [159]. In summary, the scribe line corrosion resistance achieved by ZMG is greater than that of conventional zinc coatings due to the reduction of cathodic activity by precipitation of protective corrosion products and the insulating properties of the oxide layer present at the paint to metal interface.

8.6.2. Edge Corrosion Resistance

Whilst scribe lines penetrated to the steel substrate and developed a cathodic zone of a given area, the cathodic areas associated with cut edges depended upon the geometry of the cut edge, which, in turn, depended on the edge cutting method. The establishment of differential aeration corrosion cells with cathodic sites at zones of increased paint permeability (for example areas with reduced paint thickness) has been reported for cut edges of architectural panels [44,133,134]. Two sharp corners with little or no paint coverage were observed on laser cut edges and a single sharp corner (burr tip) developed on punched edges and these areas acted as cathodic sites for oxygen reduction, (reaction 8.1), similar to the scribed area described in the previous section. The reduction of solid iron to Fe^{2+} ions is the anodic reaction for UC panels (overall reaction (8.3)), leading to rapid rusting at the cut edges of UC compared to the general surface.

The alternative anodic reactions available to HDG and ZMG are dissolution of zinc and zinc and magnesium, respectively. Oxygen reduction at cathodic sites on the HDG cut edge is balanced by anodic dissolution of the adjacent zinc coating. As corrosion progresses, transport of alkaline species OH^- along the non-zinc coated cut edge may be expected and, coupled with diffusion of water and oxygen through the paint layer, results in dissolution of the phosphate layer and delamination of the paint (see Fig. 8.13a). The full cut edge length can act as a site for oxygen reduction once the paint has been removed and an increase in the corrosion rate results. Paint delamination from the laser cut edges may occur more quickly than for punched edges due to the spreading of cathodic activity from both the upper and lower corners, although this effect was not observed in the affected area measurements for HDG within the 12-week test period. The mechanism proposed for laser cut and punched edges is illustrated by Fig. 8.24 and Fig. 8.25 respectively.
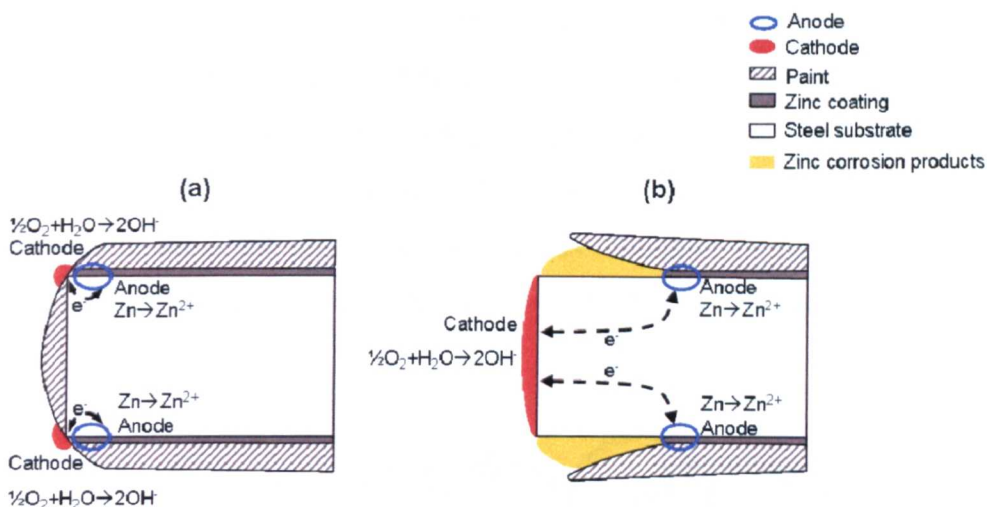
Fig. 8.24: Edge corrosion mechanism proposed for laser cut panels at (a) early and (b) later stages.
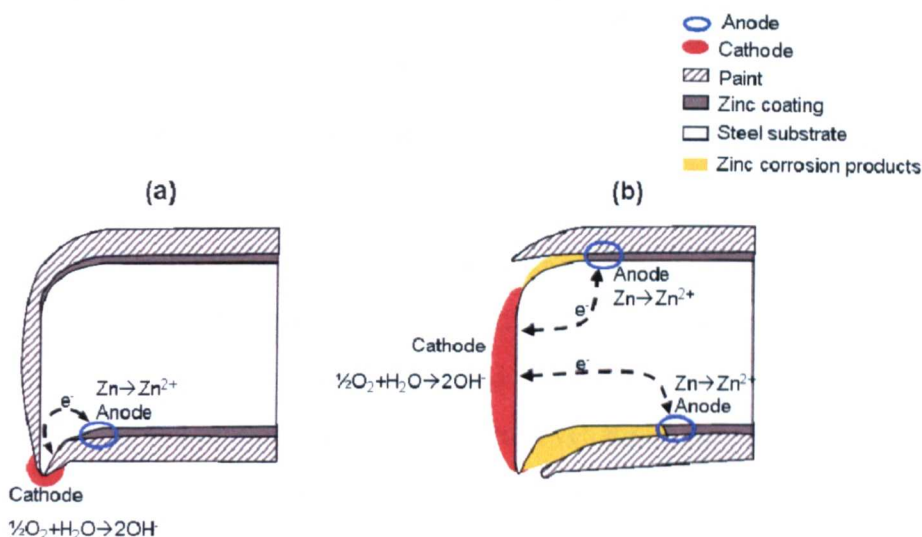
Fig. 8.25: Edge corrosion mechanism proposed for punched edges at (a) early and (b) later stages.

If the rate of oxygen reduction is slow, then the anodic reaction is also slow and the alkaline cathodic zone is limited, allowing precipitation of protective corrosion products, as observed by Ogle et al. [46]. It is clear from the experiments conducted in this work that ZMG offers greater inhibition of oxygen reduction than conventional zinc coatings and retards the overall corrosion progression by formation of $Mg(OH)_2$. Thereafter, solid zinc-based corrosion products further passivate the corroding surface. It is not surprising, then, that ZMG exhibited superior edge corrosion resistance than HDG.

There is one further aspect to consider for ZMG cut edges and that is the presence of an especially insulating interface between the ZMG surface and the paint layer, as proposed by Hausbrand et al. [84] and Stratmann [128]. This insulating oxide serves to inhibit reduction of oxygen molecules that have diffused through the paint layer and reside at the paint to metal interface; therefore its presence is significant for corrosion at the rollover zone of punched ZMG edges, as illustrated by Fig. 8.26.
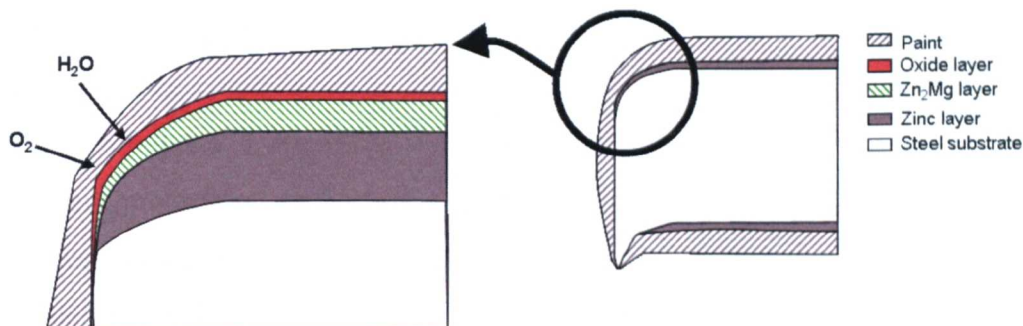
Fig. 8.26: Inhibition of oxygen reduction at rollover zone due to insulating oxide at the ZMG surface.

The ratios of affected areas associated with rollover versus burr zones are shown in Fig. 8.9 and it can be seen that ZMG had greater differences in affected area measurements for these two areas compared to HDG. Furthermore, the effect of greater corrosion at burr zones compared to rollover zones was more pronounced at the large clearance (i.e. larger rollover zone) compared to the small clearance. These observations imply a measurable effect in edge corrosion resistance due to the presence of an insulating, zinc-doped magnesium oxide species at the paint to metal interface at the rollover zone of punched ZMG edges.

The edge finishing methods investigated in this work had varied success in terms of increasing edge corrosion resistance. Deburring was most effective for UC because the increased overall paint thickness afforded extra protection to the cut edges. However, deburring had a negative effect on HDG and ZMG edges due to the removal of the metallic coating from the lower edges. This negative effect is apparent in Fig. 8.10b-c where a sharp increase in the corrosion-affected area was observed for deburred, large clearance edges of both materials. If the corrosion test was extended to a longer period, the deburred small clearance edges may also

exhibit a sharp increase in corrosion-affected area. The effect of removing the zinc coating is to extend the active cathode zone; therefore once the paint barrier is overcome by corrosion, greater rates of anodic dissolution establishes due to the increased cathodic reaction.

Lacquer and sealer constitute further barriers to the diffusion of corrodents. The lacquer appeared to be more effective on laser cut rather than punched edges; this may be due to the difficulty of adhesion of the sprayed lacquer to the sharp burrs compared to the paint-covered laser cut corners. Negligible edge corrosion was observed for the combination of lacquer with laser cutting and ZMG over the test period (see Fig. 8.11). Fig. 8.12 shows that lacquer application is a more effective additional protection method than deburring for punched edges with large clearance, although little difference was observed between the two finishing methods for small clearance edges. However, it is likely that the negative effects of metallic coating removal due to deburring would appear over a longer test period, making lacquer application the more robust method for enhanced edge protection compared to as-cut edges. Sealer application prevented cut edge corrosion for all the materials, including UC, over the 12-week test period.

8.6.3. Crevice Corrosion Resistance

The crevice corrosion test yielded the most dramatic enhancement of corrosion resistance of ZMG compared to HDG (see Fig. 8.18). The XRD diffractograms show that the zinc coating and zinc-containing corrosion products on HDG were almost completely consumed within 12 weeks of corrosion testing. ZMG proved more resilient, especially at the side of the crevice with reduced opening (left hand side of Fig. 8.18b), with some areas apparently unaffected by corrosion (see Fig. 8.21c).

A small diffraction peak due to magnesium hydroxide was observed on the surface of ZMG following 6 weeks of corrosion testing (see Fig. 8.20a). It is proposed that, as observed in the open corrosion mode in Chapter 6, formation of magnesium hydroxide in the early stages of corrosion led to a reduction of cathodic activity and consequent reduction of corrosion activity within the ZMG crevice compared to the

HDG crevice. It is interesting to note from the ZMG diffractograms in Fig. 8.19b that simonkolleite was formed by 6 weeks of corrosion testing, whereas zinc hydroxy carbonate was not detected until 12 weeks of testing. Similarly, a relatively large simonkolleite peak but a small zinc hydroxy carbonate peak was observed for HDG following 6 weeks of corrosion testing. These observations point to concentration of chloride ions within the crevice area compared to the bulk electrolyte, in accordance with the crevice model of Fontana [19] and to limited diffusion of CO_2 into the creviced areas, as noted by Zhu et al. [36]. It can also be observed that ZMG did not require the precipitation of hydroxy carbonates as an intermediate step to simonkolleite formation, indicating the inherent ability of ZMG to neutralize OH^- produced by simonkolleite formation.

The observation of reduced corrosion effects at the ZMG crevice area adjacent to the narrow opening is also interesting. The glass panel used to create the crevice overlapped the e-coat edge (see Fig. 5.14). Assuming effectively no opening between the glass panel and the top of the paint means oxygen must diffuse through the paint layer to reach the unpainted crevice area. The insulating oxide at the surface of ZMG inhibits electron transfer [128], thereby decreasing oxygen reduction as shown by Fig. 8.27.
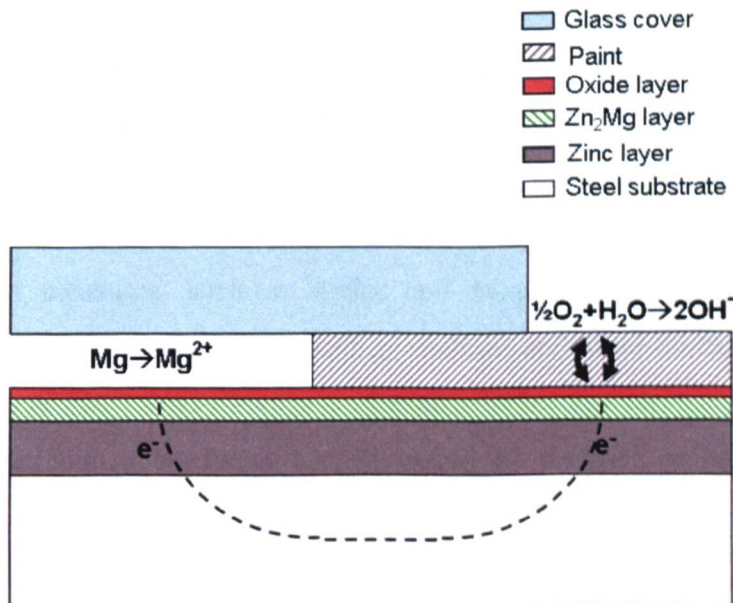
Fig. 8.27: Decreased oxygen reduction by ZMG surface oxide at crevice area without opening.

Ström et al. [59] reported that the wedge-shaped opening of the crevice panel used in this work promotes full wetting of the of the crevice area for conventional zinc-coated steel. Fig. 8.18b indicates presence of unaffected patches towards the left-hand side of the ZMG crevice but these were not located directly adjacent to the extreme left hand edge of the crevice where the minimal opening was located. It is also worth noting that the end of the test area with reduced crevice opening to corrodents also suffers reduced drainage of corrodents from the test area. Therefore it is suggested that the apparent enhanced corrosion resistance of ZMG compared to HDG in the crevice corrosion condition is a real effect but further testing with varied crevice opening width may be of interest.

The 15-fold improvement in red rust resistance of ZMG compared to HDG in the crevice mode is similar in magnitude to the improvements reported by Kawafuku et al. [13] and Morishita et al. [14] following salt spray testing (24-fold and 10-fold, respectively). Salt spray testing may share some similarity with crevice corrosion testing for conventional zinc-coated steels, where the electrolyte within the crevice contains relatively low carbon dioxide and high chloride concentrations. Salt spray and crevice corrosion testing may therefore represent the worst case scenario for conventional zinc-coated steels, but the corrosion resistance mechanisms available to ZMG make it less sensitive to these aggressive conditions.

8.6.4. Requirement for Secondary Corrosion Protection Materials

The enhanced resistance to cut edge and crevice corrosion achieved by ZMG-based panels compared to HDG-based panels suggests that the use of ZMG as a vehicle body construction material may enable the reduction of secondary corrosion protection measures, such as sealer and lacquer application. The protective mechanisms proposed in the preceding sections are based on the inherent material properties of ZMG (and ZMG in conjunction with paint treatments) and therefore it is expected that a corrosion benefit would be realised on vehicle components constructed from ZMG compared to components constructed from HDG. Test panels of ZMG offered especially enhanced (15-fold) resistance to crevice corrosion compared to HDG test panels and if such corrosion benefits translated to vehicle bodies then reduction of sealer application may be possible.

ZMG-based panels also offered increased resistance (4-fold) to cut edge corrosion compared to HDG-based panels. However, ZMG-based panels, even with additional protection from paint and (paint and lacquer), did not achieve the same level of corrosion resistance as painted and sealed edges constructed from UC, HDG and ZMG. Therefore, the question remains whether ZMG-based panels with paint but without sealer or lacquer can offer adequate resistance to cut edge corrosion. It is worth noting that sealer application under laboratory conditions and on simplified test panels guaranteed complete coverage of the cut edges by a thick layer of sealer material whereas under industrial conditions, tolerance stack-ups and access difficulties may lead to thinner or misplaced sealer application. Generally, inherent material resistance to corrosion rather than resistance depending on a multi-material system is more robust.

The relationships between cut edge geometries and cut edge corrosion mechanisms investigated in this chapter may have practical applications for stamping, burr height tolerance, edge finishing operations and panel orientation in vehicle assembly. Relatively little difference was observed in edge corrosion effects for laser cut and punched edges. Similarly, little difference was observed in the total cut edge corrosion effects for edges punched with small clearances and those punched with large clearances. It was the sharpness of the burr tip, and not the height of the burr, that results in reduced coverage by paint and consequently, initiation of corrosion at the burr zone of punched edges. The rollover zones of punched edges represented the best possible case for cut edge corrosion resistance, with full coverage by metallic coating and by paint. Edges punched with large clearances benefited from greater rollover zones, but the increased distance between the burr tip and the metallic coating may negate this benefit in terms of the total affected area over longer term corrosion exposures.

8.7. CONCLUSIONS

Painted panels of ZMG exhibited increased corrosion resistance compared to similar panels constructed from conventional galvanized steel. The enhanced corrosion resistance of ZMG was due to the precipitation of protective corrosion products, especially the precipitation of magnesium hydroxide in the early stages of

corrosion, limiting cathodic activity. When the cathodic reaction (oxygen reduction) occurred at the paint-to-metal interface, (e.g. crevice with negligible opening as shown in Fig. 8.27), ZMG offered a further protective mechanism due to the presence of an especially insulating oxide at the ZMG surface, as described by Hausbrand et al. [84] and Stratmann [128]. The effectiveness of the ZMG corrosion protection mechanisms was observed for scribe lines, cut edges and creviced area, with 3-fold, 4-fold and 15-fold increases in corrosion resistance measured respectively. These results and the mechanisms proposed suggest that ZMG may offer enhanced corrosion resistance to automotive body panels compared to conventional galvanized steel. The overall findings of this work are summarized and discussed in the next chapter.

Chapter 9

SUMMARY AND CONCLUSIONS

9.1. INTRODUCTION

This chapter summarizes the findings of this work with respect to the objectives and industrial context described in Chapter 1; that is, whether zinc-magnesium coated steel may find application as the next generation of galvanized steel for the automotive industry. An outlook is proposed in Section 9.3 and recommendations for future work are given in Section 9.4. The major conclusions arising from this work are listed in Section 9.5.

9.2. SUMMARY

The key aim of this work was to assess the potential of zinc-magnesium coated steel (ZMG) as a next generation galvanized steel for the automotive industry. A significant corrosion benefit of ZMG versus conventional galvanized steel, in addition to compatibility of ZMG with existing manufacturing processes, would be required to introduce ZMG to the automotive industry because it is likely to be more expensive than conventional zinc-coated steel (such as hot-dip galvanized steel (HDG)). The magnitude of the corrosion resistance benefit of ZMG versus conventional galvanized steel and the protective mechanisms involved are summarized in the following sections.

9.2.1. Corrosion Resistance Benefit Afforded by ZMG

There are many test procedures, test panels and assessment techniques available and recommended to assess a material's corrosion resistance (as discussed in Chapter 3). The approach adopted in assessing a new material's corrosion performance, even relative to an existing material tested at the same time, influences the corrosion resistance measurements obtained. Table 9.1 summarizes the corrosion benefit of ZMG versus conventional zinc coated steels (such as electrogalvanized steel (EG) and HDG) reported in the literature [13,14,17] and measured in this work. It may

be assumed that when the pH of the salt solution was not reported, it was not adjusted, implying a slightly acidic solution ($5.5 \le pH \le 6.5$).

Table 9.1a: Corrosion resistance benefit of ZMG versus conventional zinc coatings reported in the literature [13,14,17].

ZMG type	Test method	Assessment	Solution	Corrosion benefit
PVD Zn & Mg	Salt spray	Time to red rust initiation	5 wt.% NaCl pH not reported	24-fold vs. EG [13]
Electrodeposited Mg onto EG + alloyed	Immersion	Time to red rust initiation	5 wt.% NaCl pH not reported	4-fold vs. EG [14]
Electrodeposited Mg onto EG + alloyed	Salt spray	Time to red rust initiation	5 wt.% NaCl pH not reported	10-fold vs. EG [14]
Hot-dipped Zn-6wt.%Al-3wt.%Mg	Cyclic test	Time to 5% red rust coverage	5 wt.% NaCl pH not reported	10-fold vs. Zn-Al coated steel [17]

Table 9.1b: Corrosion resistance benefit of ZMG versus conventional zinc coatings assessed in this work.

ZMG type	Test method	Assessment	Solution	Corrosion benefit
PVD Mg onto EG + alloyed	Volvo cabinet test	Time to 5% red rust	1 wt.% NaCl pH 4.2	3-fold vs. EG & HDG
	Volvo cabinet test	% red rust after 12 weeks	1 wt.% NaCl pH 4.2	8-fold vs. EG and HDG
	Ford cabinet test	Time to red rust initiation	1 wt.% NaCl pH 4.2	3-fold vs. EG and HDG
	Ford cabinet test	Time to red rust initiation	Acid rain pH 3.5	1.5-fold vs. EG and HDG
	Ford cabinet test	% red rust after 20 weeks	Acid rain pH 3.5	4-fold vs. EG
Painted[a] PVD Mg onto EG + alloyed	Volvo cabinet test	Scribe line creep after 12 weeks	1 wt.% NaCl pH 4.2	3-fold vs. EG & HDG
		Edge corrosion affected area after 12 weeks	1 wt.% NaCl pH 4.2	4-fold vs. HDG
		Crevice corrosion % red rust after 12 weeks	1 wt.% NaCl pH 4.2	15-fold vs. HDG

[a] Pre-treatment phase (phosphate and e-coat) only.

Table 9.1 shows that the magnitude of ZMG's corrosion resistance benefit versus EG or HDG varied from 1.5 to 24, depending on the test method, assessment criterion and corroding solution used. The variations in the data highlight the potential dangers of selecting a corrosion protection system based on red rust resistance measurements from a single accelerated test. Even with all the data given in Table 9.1, it is difficult for the automotive engineer to decide whether use of ZMG would enable deletion of, for example, sealer at a cut edge of the vehicle.

However, it can be concluded from Table 9.1 that ZMG appears to offer a corrosion resistance benefit versus zinc-coated steel and that the protection mechanism involved was effective in a variety of test environments.

Establishing the corrosion mechanism gives a more reliable assessment of the corrosion protection afforded by a particular coating system to the steel substrate than quantification of red rust resistance because the mechanistic approach allows extrapolation of corrosion behaviour to environments and situations other than those tested. A mechanistic approach was adopted in this work and the combination of various analysis techniques with an understanding of the mechanisms of zinc corrosion were used to explain the observations of red rust resistance.

9.2.2. ZMG Corrosion Protection Mechanism in a NaCl Environment.

The presence of magnesium in ZMG afforded additional inhibitive protection to the steel substrate compared to zinc-coated steel. The mechanism proposed for the corrosion of ZMG in a sodium chloride environment is based on the findings of Chapter 6 and begins with the dissolution of Mg^{2+} and Zn^{2+} ions from the Zn_2Mg phase of the coating when the material is subject to electrochemical attack. The more zinc-enriched regions act as cathodes because magnesium is anodic to zinc, and oxygen reduction (reaction (4.2)) progresses. The magnesium ions form stable precipitates of magnesium hydroxide, $Mg(OH)_2$, at the cathodes, reducing the general activity and facilitating simonkolleite ($Zn_5(OH)_8Cl_2.H_2O$) formation (reaction 4.5) from the corroding zinc. The net hydroxide released by simonkolleite formation can be neutralized by carbon dioxide uptake and transformation of zinc oxide and magnesium hydroxide to hydroxy carbonates at the cathodes. Continued suppression of oxygen reduction at the cathodes allows the corroding zinc to form further protective simonkolleite. The overall corrosion activity is reduced compared to zinc corrosion and eventually large portions of the surface are protected by simonkolleite. The key difference compared to conventional galvanized steel corrosion is the formation of magnesium hydroxide, which is apparently more effective in blocking oxygen reduction than zinc oxide.

This corrosion protection mechanism was also effective under the same test conditions but with creviced test panels (see Chapter 8), where ZMG exhibited 15-times greater red rust resistance than HDG. The detection of simonkolleite without zinc hydroxy carbonate on the creviced area of ZMG indicates that ZMG itself inherently neutralizes both oxygen reduction at cathodes and hydroxide released from simonkolleite formation during the first 8 weeks of corrosion testing. This enhanced ability to neutralize hydroxides even with reduced access to carbon dioxide may explain the large corrosion resistance benefits reported for ZMG versus EG in salt spray testing.

Painted test panels of ZMG may benefit from a further protective action; the presence of a zinc-doped magnesium oxide layer of approximately 4 nm thickness on the surface of the material [128]. This special oxide layer has been shown to act as an effective insulator to electron transfer (see Section 4.5.1). This means that oxygen reduction cannot progress as easily on painted panels of ZMG compared to painted panels of HDG and EG. This property may have increased the corrosion benefit of ZMG observed at the rollover zone of cut edges and at crevices with small openings (see Sections 8.6.2-8.6.3).

9.2.3. ZMG Corrosion Protection Mechanism in an Acid Rain Environment.

ZMG exhibited reduced corrosion resistance benefit (in terms of relative resistance to red rust initiation compared to EG) in the acid rain environment, as described in Chapter 7. However, red rust propagation for ZMG continued at a reduced rate compared to EG and after 20 weeks of exposure the proportion of the ZMG test panel covered by red rust was one quarter that of EG. If the test panels had been oriented at an angle other than vertical (e.g. seated in racks at 15° to vertical as in the Volvo test method) then rust may not have concentrated in the lower half of the EG test panel, and greater differences in surface rust proportion between EG and ZMG may have been realised.

The mechanism proposed for ZMG corrosion in the acid rain environment suggests a possible limiting factor for ZMG corrosion resistance; its efficacy depends on the presence of alkaline MgO or $Mg(OH)_2$. If very acidic and voluminous precipitation

occurs, magnesium oxide/hydroxide may be flushed from the ZMG panel, effectively etching the surface, exposing the underlying zinc layer and eliminating the corrosion benefit of ZMG versus EG. The test conditions used in Chapter 7 did not lead to the elimination of ZMG's corrosion benefit over the entire panel but the increased dwell time and volume of acid rain solution at the lower edge of the test panels caused ZMG's corrosion behaviour to become more similar to that of EG. What is the significance of this finding? The scenario tested in Chapter 7 seems rather extreme compared to the natural service environment of a vehicle. However, if similar acidic solution stagnated in a creviced area of the vehicle body, it is possible that the corrosion benefit of ZMG versus EG would be reduced. A further question then is whether acidic solution is found in creviced joints of vehicles in service; but that is outside the scope of this work. What is of prime interest here is to establish the limits of ZMG's corrosion protection mechanism: interrogation of the likelihood of encountering those limits in service may be conducted according to each potential application of ZMG. Exposure of ZMG to natural weathering sites in industrial and heavily polluted areas may be required to make such a judgement.

9.3. OUTLOOK

The corrosion resistance benefit demonstrated by prototype versions of ZMG in laboratory testing to date warrants further investigation of its suitability for vehicle body construction. Most importantly, the corrosion mechanism of ZMG must be confirmed on fully-painted panels, sub-assemblies and vehicles. The efficacy of the corrosion protection mechanism offered by ZMG must be confirmed on actual vehicles. Essentially, the limits of ZMG's corrosion resistance should be established in the laboratory and at natural exposure sites prior to use as a construction material for saleable vehicles.

Further investigations required from the automotive manufacturer's perspective include confirmation of ZMG's compatibility with vehicle construction processes. Any incompatibilities found may limit the range of ZMG applications or indeed eliminate it as a candidate material for body construction at all. Corrosion and durability testing of vehicle bodies or sub-assemblies constructed from ZMG can be carried out at proving grounds once ZMG has proved its compatibility with

manufacturing processes. Corrosion rate measurements of ZMG exposed at outdoor weathering sites are required to confirm *the results obtained and* mechanisms proposed from laboratory and proving ground testing. Long-term exposure data are required to interpret and extrapolate accelerated test results with confidence.

These points highlight the significant amount of testing required to develop confidence in ZMG as a next generation of galvanized steel for the automotive industry. As more data on the properties of ZMG are established, the risk associated with its use is reduced. The automotive engineer must make a judgement on when the level of risk associated with ZMG is reduced to an acceptable level and the overall benefits of its use outweigh the potential disadvantages. It can be expected that a conservative and step-wise approach would be adopted by most manufacturers, with targeted application of ZMG to certain panels or features as a test-case for the material. Ultimately, ZMG must provide an economic (e.g. reduced overall cost) or business (e.g. marketing advantage) imperative in addition to functional benefits to become the next generation of galvanized steel for the automotive industry. In the following sections the relative advantages of and impediments to introduction of ZMG as a vehicle body construction material are discussed.

9.3.1. Advantages of Introducing ZMG for Vehicle Body Construction

The increased corrosion resistance of ZMG versus HDG and EG may be exploited in a number of ways. Substitution of ZMG for conventional galvanized steel, coupled with high levels of corrosion protection from paints, sealers, waxes and sympathetic body design may afford greater robustness to the existing corrosion protection system. The corrosion benefit of ZMG is inherent to the material and does not depend on processing parameters during vehicle construction, such as the accuracy of location, the volume of material applied and control of curing parameters, as may be the case for added materials such as sealers, waxes and lacquer. This additional robustness may allow some relief in the provision of e-coat access and air escape holes which are necessary at some areas of the vehicle body for full e-coat penetration. It is desirable to minimize such holes because they must

be plugged at a later stage of vehicle construction (i.e. after e-coat deposition) to ensure acceptable noise, vibration and harshness (NVH) properties of the vehicle body.

Alternatively, ZMG could be used to alleviate certain processing difficulties associated with the use of thicker zinc coatings, such as metallic coating spalling during forming and brass formation on welder electrodes. For example, ZMG of standard thickness could be used instead of EG or HDG of greater thickness to achieve the same level of corrosion resistance. Alternatively, standard thickness EG or HDG panels could be replaced by ZMG with reduced coating thickness. Thus, ZMG may be introduced to relieve process issues associated with particular panels or joint designs, or may be introduced to impart increased overall corrosion protection to the vehicle body.

The increased resistance of ZMG versus HDG to edge and crevice corrosion demonstrated in Chapter 8 highlights a second potential strategy for ZMG introduction. Use of ZMG may enable reduction or elimination of secondary corrosion protection processes such as lacquer, sealer and wax application at panel edges and creviced areas. This may result in reduced material and processing cost, reduced material complexity, enhanced recyclability and reduced overall vehicle body weight. The results presented in Chapter 8 are preliminary, based on rather small numbers (3 at each interval) of test panels with simplified geometry and only the pre-treatment stages of the paint process. However, the results are useful because they demonstrate a measurable corrosion resistance benefit of ZMG versus HDG. Furthermore, the corrosion protection mechanisms exhibited by the test panels should remain active for full vehicle panels because the mechanisms are *inherent* properties of the material and they have proved effective in the most challenging scenarios for the vehicle body; *i.e. at damaged paint* areas, at cut edges and in creviced areas without any paint coverage.

To date, the use of pre-painted panels in the automotive industry has been hindered by the persistent problem of edge corrosion. In the longer term, use of ZMG as a base material may be a step towards more widespread use of organically pre-treated

(i.e. painted prior to body assembly) panels for vehicle body construction and the reduction of the paint treatments performed by the vehicle manufacturer, as envisioned by Schuhmacher et al. [95].

9.3.2. Impediments to Introducing ZMG for Vehicle Body Construction

The greatest impediment to ZMG introduction is its increased cost versus current materials. Although not currently commercially available, it is expected that the unit cost of ZMG will be significantly greater than that of conventional galvanized steel because the ZMG producers must invest in new plant and purchase additional raw materials. The ZMG material used in this work was based on electrogalvanized steel and the magnesium was applied via the high-vacuum and multi-step PVD process, each of which is a more expensive process than hot-dipping. The cost of ZMG would be minimized if a single-step hot-dipping production process could be used. The hot-dipped version of ZMG described by Tsujimura et al. [17] had to include aluminium as a well as magnesium to avoid dross formation in the molten metal pot. The resultant zinc-aluminium-magnesium alloy coating may have a spangled surface appearance which would not be acceptable for visible vehicle body panels; however, such a material could be used for non-visible panels such as floor panels and door inner panels. ZMG based on PVD of magnesium onto HDG may also be cheaper in terms of production costs than the ZMG used in this work, where the magnesium was deposited onto EG although HDG may require additional surface treatments prior to deposition of the magnesium due to the presence of (for example) aluminium oxide on the HDG surface (see Section 4.2.2). The unit cost of commercial ZMG will depend on the production rates as well as the production method, which are currently unknown.

The cost of using ZMG as a vehicle construction material should be considered in terms of the overall vehicle cost; for example, an increased unit cost of ZMG could be partially offset by elimination of secondary corrosion protection measures, which constitute both a material cost and a processing cost to the manufacturer. Ultimately, use of ZMG must generate some economic or business advantage versus HDG and EG to be considered as a substitute for current materials.

A further impediment to ZMG introduction is the risk associated with using a new material in an existing product. Although a significant number of reports demonstrating the improved corrosion resistance of magnesium-containing zinc coatings exist, the capability of ZMG to offer increased corrosion resistance to a vehicle in service is unproven. Uncertainty persists when only accelerated test data on simplified laboratory test specimens are available. Further uncertainty is associated with using existing test methods on a new material because a test method that may be used with a certain confidence level on EG or HDG may not give such reliable results for ZMG.

Finally, a suitable construction material must also be compatible with the current forming, joining and painting processes and a comprehensive testing programme of ZMG is required prior to its introduction as a construction material. Such a testing programme constitutes a considerable expense to the automotive manufacturer but the evidence of ZMG's corrosion resistance benefit presented in this work may justify such a programme.

9.4. RECOMMENDATIONS FOR FUTURE WORK

The following investigations are recommended for further clarification of the corrosion protection mechanism of ZMG.

- Initiate a long-term exposure programme for ZMG panels, both on vehicles and at marine and industrial sites. Panels should be in both the painted and unpainted condition with scribe lines cut into painted panels. Measurements of scribe line creep for ZMG panels may be compared to literature data for EG and HDG. Analysis of the corrosion products precipitated onto unpainted panels of ZMG would allow confirmation of accelerated corrosion test methods and the corrosion protection mechanism of ZMG. ZMG panels incorporating a crevice and exposed at industrial or heavily-polluted sites may exhibit reduced corrosion protection compared to similar panels exposed at marine sites and should be included in the exposure programme.

- Laboratory testing of crevice corrosion test panels with an acid rain solution (pH 3.5) should be conducted. Similar testing with sodium chloride solution acidified to pH 3.5 should also be conducted to separate the influences of

sodium and chloride ions' concentrations and the solution pH. Both ZMG and conventional zinc-coated steel (EG and/or HDG) panels should be tested at the same time for comparison. Evolution of red rust within the crevice should be tracked to assess the corrosion resistance benefit of ZMG versus the conventional zinc coatings. Characterization of the precipitated corrosion products should be conducted to clarify the corrosion mechanism at work.

- Scanning electrochemical techniques such as the scanning Kelvin probe (SKP) and the scanning vibrating electrode technique (SVET) have been used to illustrate anodic and cathodic activity on corroding systems in real time. Usually, corrosion occurs by immersion of a sample in electrolyte but more realistic corrosion mechanisms occur for zinc-coated steel when the sample is subject to cyclic corrosion. It would be interesting to investigate the use of SKP or SVET on samples that have pre-corroded for a set interval in a cyclic corrosion test. Cross-sections of the corroded sample would have to be used to ensure a flat surface but it may be possible to track anodic and cathodic activity, (e.g. on a cut edge), with increasing exposure to a cyclic corrosion test.

- If ZMG is to be introduced to the automotive industry in a step-wise manner, the interaction of ZMG and HDG or EG must be investigated. A ZMG crevice corrosion panel with a HDG or EG cover instead of the glass cover shown in Fig. 5.14 could be constructed and its corrosion resistance compared to (for example) a HDG panel with a HDG cover. Alternatively, the SAE perforation test panel configuration shown in Fig. 3.14 could be used, with different base plate and cover plate materials.

- An interesting observation from the diffractograms obtained from the ZMG crevice area (Fig. 8.19b) was the presence of simonkolleite without zinc hydroxy carbonate. Corrosion of conventional zinc-coated steel in non-CO_2 containing atmosphere leads to greater corrosion rates compared to the corrosion rates observed under atmospheric conditions (approximately 350 ppm by volume of CO_2). It seems possible that the corrosion rate of ZMG is less sensitive to reduced CO_2 concentration, at least in the short term. It would be interesting to conduct corrosion tests of ZMG in non-CO_2

containing atmosphere and compare the results to ZMG exposed in a similar way to atmospheric levels of CO_2.

9.5. CONCLUSIONS

1. An extensive literature is available for corrosion test methods, corrosion rate data and corrosion mechanisms of galvanized steel. The corrosion rate depends on the test method used and a suite of corrosion exposures is required to develop reliable corrosion mechanisms. Corrosion test regimes that stimulate mechanisms that occur naturally are essential when long-term, unaccelerated data are not available.

2. Test conditions such as panel orientation, quantity and frequency of precipitation events, access to atmospheric CO_2 as well as thermal and humidity cycling and contaminant concentration influence the corrosion behaviour of zinc coatings. These parameters should be included in any corrosion test reports and prescribed for standard test methods.

3. The multi-analytical approach adopted in this work was required to account for bulk and superficial transformations of the ZMG coating phases; e.g. XPS without XRD or vice-versa did not yield adequate data to propose reliable corrosion mechanisms for ZMG.

4. ZMG offers enhanced corrosion protection compared to conventional zinc coatings in a sodium-chloride environment due to a barrier mechanism whereby magnesium-containing corrosion products block cathodic activity, retarding the overall corrosion activity. According to the literature [83,126], this protective mechanism extends to zinc dosed with magnesium-containing electrolytes; i.e. the presence of magnesium ions, whether they originate from the electrolyte or the corroding surface, retards zinc corrosion in a sodium chloride environment.

5. ZMG benefits from an additional corrosion protection mechanism that would not manifest on zinc dosed with magnesium-containing electrolytes; that is, the presence of a highly-insulating zinc-doped magnesium oxide layer at the

ZMG surface. A corrosion benefit, attributed to this insulating oxide, was observed at the rollover zone and within creviced areas of painted ZMG panels.

6.   The efficacy of ZMG's protection mechanism appeared to be attenuated in an acid-rain environment due to proton-induced dissolution of the alkaline magnesium hydroxide from the corroding surface.

7.   Edge corrosion is affected by the distribution of the metallic coating and the paint layers around the edge, which in turn are affected by the cutting method used. The rollover zone of punched edges represent the best case scenario for cut edges, with full metallic and e-coat coverage and a minimal corrosion-affected area compared to the burr zones.

8.   Deburring of punched edges prior to paint application results in an increased incubation period prior to corrosion initiation. However, the propagation of edge corrosion for deburred metallic-coated steel was greater than that of non-deburred metallic-coated steel.

9.   The presence of sealer on cut edges resulted in complete suppression of edge corrosion over the test period used and sealer application was the most effective method of retarding corrosion.

10.   The corrosion mechanisms proposed for ZMG and the corrosion benefits measured in this work show that ZMG has potential to be the next generation galvanized steel for the automotive industry. It is recommended that compatibility testing, further corrosion resistance investigations and economic studies are conducted to apply ZMG to vehicle body construction.

REFERENCES

1. H.E. Townsend: *Coated steel sheets for corrosion resistant automobiles,* (1991) Proc. of the corrosion/91 symposium, Texas, USA: NACE Int.

2. Y. Nagata, T. Hamanaka: *Status and Prospect of Japanese Automotive Anticorrosion Technology,* (1991) Proc. of the 5th automotive corrosion & prevention conference 21/10/91-23/10/91, Michigan,USA: SAE 912302

3. A.C. Tiburcio, M.J. Yergin: *U.S. Automotive Corrosion Trends 1998 SAE (ACAP) Automotive Body Corrosion Survey Results,* (2003) Proc. SAE 2003 world congress 03/03/03-06/03/03, Michigan, USA: SAE 2003-01-1244.

4. Anon.: *The federal/provincial anti-corrosion code and owners care guide for motor vehicles,* (1978) Canada: consumer and corporate affairs.

5. Hon.W. Allmand: *Development of the anti-corrosion code for motor vehicles,* (1978) Proc. of the design for the automotive corrosion prevention conference, Detroit, USA: SAE P-78.

6. M. Roennholm: *Corrosion protection of car bodies in Finland,* (1989) Proc. of the subzero engineering conditions conference 09/01/89-11/01/89, Finland: SAE 890008.

7. K. Kikuchi, M. Isobe, C. Kato, M. Uchida: *JSAE review,* v.22 (2001) 205-210.

8. L. Guzman, G.K. Wolf, G.M. Davies: *Surface coatings and technology,* v.174-175 (2003) 665-670.

9. T.C. Simpson, A.W. Bryant, G. Hook, R.A. Daley, R.J. Swinko: *US automotive corrosion trends over the past decade,* (1995) Proc. International congress and exposition 27/02/95-02/03/95, Michigan, USA: SAE 950375.

10. M. Uchida, S. Kurokawa, K. Mochizuki: *Corrosion behaviour of a vehicle submitted in service in subtropical marine environment of Okinawa island for eight years,* (1996) Proc. International congress and exposition 26/02/96-29/02/96, Michigan, USA: SAE 960021.

11. L. Bednar: *Automotive body component field corrosion behaviour in the deicing salt zone,* (1997) Proc. international congress and exposition 24/02/97-27/02/97, Detroit, USA: SAE 971002.

12. R. Dietz: *European automotive industry's design and materials philosophy for achieving corrosion protection today, and over the coming decade*, (1991) Proc. automotive corrosion and prevention conference and exposition 21/10/91-23/10/91, Michigan, USA: SAE 912301.

13. J. Kawafuku, J. Katoh, M. Toyama, K. Ikeda, H. Nishimoto, H. Satoh: *Properties of zinc alloy coated steel sheets obtained by continuous vapour deposition*, (1991) Proc. of the 5th automotive corrosion & prevention conference 21/10/91-23/10/91, Michigan,USA: SAE 912272.

14. M. Morishita, K. Koyama, M. Murase, Y. Mori, 1996: *ISIJ international*, v.36, n.6 (1996) pp. 714-719.

15. M. Morishita, K. Koyama, Y. Mori, 1997: *ISIJ international*, v.37, n.1 (1997) pp.55-58.

16. M. Morishita, K. Koyama, Y. Mori: *Materials transaction JIM*, V.38 n.8 (1997) 719-723.

17. T. Tsujimura, A. Komatsu, A. Andoh, 2001. *Proc. Galvatech June 2001*, Belgium: Stahleisen 2001, pp.145-152.

18. J.M. West: *Basic corrosion and oxidation*, (1986) 2nd Ed., Ellis Horwood Ltd., Chichester, UK.

19. M.G. Fontana: *Corrosion engineering*, (1986) 3rd Ed., McGraw-Hill International Editions, Singapore.

20. K. Tretheway, J. Chamberlain: *Corrosion for science and engineering*, (1995) 2nd Ed., Longman Group Ltd., Essex, UK.

21. R. Baboian, (ed.): *Corrosion tests and standards: application and interpretation*, (2005) 2nd Ed., ASTM Int.: Philadelphia, USA.

22. L.J. Korb, D.L. Olson, (ed.): *Metals handbook volume 13: Corrosion*, (1987) 9th Ed., ASM Int.: Ohio, USA. ISBN 0-87170-007-7.

23. C.J. Slunder, W.K. Boyd: *Zinc: its corrosion resistance*, (1971), Zinc development association: London, UK.

24. J.G. Stark, H.G. Wallace: *Chemistry data book*, (1984) 2nd Ed., John Murray (Publishers) Ltd., London, UK.

25. M. Pourbaix: *Atlas of electrochemical equilibria in aqueous solutions*, (1966) Pergamon Press Ltd., Oxford, UK.

26. W.M. Latimer: *The oxidation states of the elements and their potentials in aqueous solutions*, (1952) 2nd Ed., Prentice Hall Inc., New York, USA.

27. D.B. Freeman: *Phosphating and metal pre-treatment*, (1986) Woodhead-Faulkner: Cambridge, UK.

28. R.W. Zurilla, V. Hospadaruk: *Quantitative test for zinc phosphate coating quality*, (1978) Proc. Automotive engineering congress and exposition 27/02/78-03/03/78, Michigan, USA: SAE 780187.

29. K. Arlt: *Electrochimica acta*, v.39 n.8/9 (1994) 1189-1193.

30. A. Amirudin, C. Barreau, R. Hellouin, D. Thierry: *Progress in organic coatings*, v.25 (1995) 339-355.

31. ISO 9223-1992(E): *Corrosion of metals and alloys – corrosivity of atmospheres – classification*, (1992) ISO Geneva, Switzerland.

32. S. Cramer, J.P. Carter, P.J. Linstrom, D.R. Flinn: Environmental effects in the atmospheric corrosion of zinc. In: S.W. Dean, T.S. Lee, Eds.: *Degradation of metals in the atmosphere*, (1988) ASTM STP 965, Philadelphia USA, pp.229-247.

33. ASTM G50-76: *Standard practice for conducting atmospheric corrosion tests on metals*, (2003) ASTM Int. Philadelphia, USA.

34. D. Davidson, L. Thompson, F. Lutze, B. Tiburcio, K. Smith, C. Meade, T. Mackie, D. McCune, H. Townsend, R. Tuszynski: *Perforation corrosion performance of autobody steel sheet in on-vehicle and accelerated tests*, (2003) Proc. SAE world congress 03/03/03-06/03/03, Michigan, USA: SAE 2003-01-1238.

35. G. Gao, T. Wang, V. Makeyev: *Corrosion rates of steel, zinc and bi-metal couples in the field and in laboratory exposures*, (2002) Proc. SAE world congress 04/03/02-07/03/02, Michigan, USA: SAE 2002-01-0206.

36. F. Zhu, B. Rendahl, D. Thierry: *British corrosion journal*, v.35 n.3 (2000) 195-203.

37. J.B. Vrable: *Comparison of corrosion performance of zinc and iron-zinc alloy coatings in accelerated, atmospheric and highway automotive tests*, (1985) Proc. international congress and exposition 25/02/85-01/03/85, Michigan, USA: SAE 850002.

38. L. Bednar, L. Cockerham: *Proc. International body engineering conference*, (1995) 31/10/95-02/11/95, Michigan, USA: IBEC pp.125-135.

39. S. Kurokawa, M. Uchida, C. Kato, K. Mochizuki, T. Kato: *Evaluation of the corrosion rate of zinc coated steel sheets for automotive body use*, (1997) Proc. international congress and exposition 24/02/97-27/02/97, Michigan, USA: SAE 971003.

40. M.L. Stephens: *SAE ACAP division 3 project: evaluation of corrosion test methods*, (1989) Proc. automotive corrosion and prevention conference 04/12/89-06/12/89, Michigan, USA: SAE 892571.

41. J.R. Scully, D.W. Taylor: Laboratory testing. In: R. Baboian (Ed.), *Metals handbook* 9th ed., v.13 (1987) ASM Int., Ohio USA, pp.212-228.

42. ASTM G59-97: *Standard test method for conducting potentiodynamic polarization resistance measurements*, (2003) ASTM Int. Philadelphia, USA.

43. ASTM G71-81: *Standard guide for conducting and evaluating galvanic corrosion tests in electrolytes*, (2003) ASTM Int. Philadelphia, USA.

44. D.A. Worsley, D. Williams, J.S.G. Ling: *Corrosion science*, v.43 (2001) 2335-2348

45. J. Elvins, J.A. Spittle, D.A. Worsley: *Corrosion science*, v.47 (2005) 2740-2759.

46. K. Ogle, S. Morel, D. Jacquet: *Journal of the electrochemical society*, v.153 n.1 (2006) B1-B5.

47. W. Fürbeth, M. Stratmann, *Corrosion science*, v.43 (2001) 207-227.

48. W. Fürbeth, M. Stratmann, *Corrosion science*, v.43 (2001) 229-241.

49. W. Fürbeth, M. Stratmann, *Corrosion science*, v.43 (2001) 243-254.

50. P.L. Bonora, F. Deflorian, L. Fedrizzi, *Electrochimica acta*, v.41 n.7/8 (1996) 1073-1082.

51. F. Mansfeld, L.T. Han, C.C. Lee, C. Chen, G. Zhang, H. Xiao, *Corrosion science*, v.39 n.2 (1997) 255-279.

52. B. Rajagopalan: *Rapid corrosion performance evaluation of metallic alloys by electrochemical polarisation technique*, (2007) Proc. symposium on international automotive technology 17/01/07-20/01/07, Pune, India: SAE 2007-26-068.

53. ASTM B117-03: *Standard practice for operating salt spray (fog) apparatus*, (2003) ASTM Int. Philadelphia, USA.

54. ASTM G85-02: *Standard practice for modified salt spray (fog) testing*, (2002) ASTM Int. Philadelphia, USA.

55. SAE J2334: *Laboratory cyclic corrosion test*, (2003) SAE Int. Philadelphia, USA.

56. F.W. Lutze, K.A. Smith, R. Mason, D. Nymberg, L.S. Thompson, C. Meade, L. McQuiston, R. Singleton, C. Handsy: *Update on the developments of the SAE J2334 laboratory cyclic corrosion test*, (2003) Proc. SAE world congress 03/03/03-06/03/03, Michigan, USA: SAE 2003-01-1234.

57. T.K. Christman, J.T. Stropki, C.K. Schoff: *Evaluation of accelerated corrosion test procedures*, (1989) Proc. automotive corrosion and prevention conference and exposition 04/12/89-06/12/89, Michigan, USA: SAE 892583.

58. T.S. Doppke, A.W. Bryant: *The salt spray test – past, present and future*, (1983) Proc. automotive corrosion and prevention conference and display 05/12/83-07/12/83, Michigan, USA: SAE 831815.

59. M.A. Ström, G. Ström, G. Strannhage: *Making the best of corrosion testing*, (2006) Proc. EuroCorr conference 24/09/06-28/09/06, Maastricht, Netherlands: European Corrosion Federation.

60. H.E. Townsend, D.C. McCune: *Round-robin evaluation of a new standard laboratory test for cosmetic corrosion*, (1997) Proc. international congress and exposition 24/02/97-27/02/97, Michigan, USA: SAE 970734.

61. C.R. Shastry, L.S. Thompson, F.W. Lutze: *Performance of coatings for underbody structural components*, (2001) Proc. SAE world congress 05/03/01-08/03/01, Michigan, USA: SAE 2001-01-0363.

62. F. Bovard, J. Tardiff, T. Jafolla, D. McCune, G. Courval, K.A. Smith, F. Lee, J. Repp, S. Ramamurthy, R.J. Shaffer, F.M. Vartolas: *Development of am improved cosmetic corrosion test for finished aluminum autobody panels*, (2007) Proc. SAE world congress 16/04/07-19/04/07, Michigan, USA: SAE 2007-01-0417.

63. D. Thierry, N. Le Bozec, C. Lille, N. Arlt, A. Morizot, P.J. Cunat: *Basic considerations for the development of a corrosion test for stainless steels used for automotive applications*, (2004) Proc. SAE world congress 08/03/04-11/03/04, Michigan, USA: SAE 2004-01-0887.

64. T. Wang, D. Nymberg, M. Ström: *A comparative study of corrosion test environments at three proving grounds*, (2003) Proc. SAE world congress 03/03/03-06/03/03, Michigan, USA: SAE 2003-01-1240.

65. S. Oh, B. Min: *Development of accelerated corrosion test mode considering environmental condition*, (2002) Proc. SAE world congress 04/03/02-07/03-02, Michigan, USA: SAE 2002-01-1231.

66. T. Wang, G. Gao, J. Bomback, M. Ricketts: *A vehicle micro corrosion environmental study of field and proving ground tests*, (2001) Proc. SAE world congress 05/03/01-08/03/01, Michigan, USA: SAE 2001-01-0646.

67.　E. Calmona: *Corrosion protection - automotives*, (2005) Proc. SAE Brazil congress and exhibit 22/11/05-24/11/05, Sao Paulo, Brazil: SAE 2005-01-4176.

68.　ASTM D3170-03: *Standard test method for chipping resistance of coatings*, (2003) ASTM Int. Philadelphia, USA.

69.　VCS 1021,29: *Scribing of a surface coated test object and evaluation of the propagation from scribe when corrosion testing*, (2002) Volvo Car Corporation, internal company document.

70.　M. Ström, G. Ström: *A statistically designed study of atmospheric corrosion simulating automotive field conditions under laboratory conditions - Final Volvo report*, (1993) Proc. 6th automotive corrosion and prevention conference 04/10/93-06/10/93, Michigan, USA: SAE 932338.

71.　S. Suzuki, T. Kanamaru, A. Katsutoshi, J. Morita: *Proc. Corrosion/91 symposium*, (1992) Texas, USA NACE, pp.34.1– 34.19.

72.　E. Almeida, M. Morcillo: *Surface and coatings technology*, v.124 (2000) 169-189.

73.　E. Almeida, M. Morcillo: *Surface and coatings technology*, v.124 (2000) 44-52.

74.　S. Wakano, M. Nishihara: *Perforation corrosion resistance of several coated steels in two simulated model tests*, (1989) Proc. SAE international congress and exposition 27/02/89-03/03/89, Michigan, USA: SAE 890706.

75.　K. Miki, M. Iwai, H. Sakai, S. Nomura: *Weathering test of hem model set inside automotive door*, (1989) Proc. automotive corrosion and prevention conference and exposition 04/12/89-06/12/89, Michigan, USA: SAE 892568.

76.　W. Oldenburg, T. Dorsett, T. Masterson: *Perforation corrosion performance of various materials using mini-door test specimens correlated with vehicle road and laboratory test results*, (1989) Proc. automotive corrosion and prevention conference and exposition 04/12/89-06/12/89, Michigan, USA: SAE 892579.

77.　L.A. Roudabush, T.E. Dorsett: *A review of perforation corrosion testing – 1980 – 1990*, (1991) Proc. automotive corrosion and prevention conference and exposition 21/10/91-23/10/91, Michigan, USA: SAE 912285.

78.　J. Repp, S. Sampson, I.C. Handsy: *Corrosion evaluation of army and automotive materials in Hawaii*, (2006) Proc. SAE world congress 03/04/06-06/04/06, Michigan, USA: SAE 2006-01-1649.

79. J. Macciocco, T.E. Dorsett, T.D. Masterson, R.J. Kammerer: *Perforation corrosion evaluation of precoated steels by Ford APG cyclic test*, (1993) Proc. automotive corrosion and prevention conference and exposition 04/10/93-06/10/93, Michigan, USA: SAE 932364.

80. ASTM D610-01: *Standard test method for evaluating degree of rusting on painted steel surfaces*, (2001) ASTM Int., Philadelphia USA.

81. ASTM G1-03: *Standard practice for preparing, cleaning and evaluating corrosion test specimes*, (2003) ASTM Int., Philadelphia, USA.

82. J. Elvins, J.H. Sullivan, J.A. Spittle, D.A.Worsley: *Corrosion engineering, science and technology*, v.40 n.1 (2005) 43-50.

83. R. Hausbrand, M. Rohwerder, M. Stratmann, C. Schwerdt, B. Schuhmacher, G. Grundmeier: *Proc. Galvatech 2001*, Belgium:Stahleisen (2001) pp.161-167.

84. R. Hausbrand, M. Stratmann, M. Rohwerder: *Steel research*, v.74 n.7 (2003) 453-458.

85. V.E. Carter: *Metallic coatings for corrosion control*, (1977) London: Newnes-Butterworth, Chap.4, p.108.

86. C. Belleau, D.K. Kelley: *Effects of galvanized steel defects on painted appearance of exposed panels*, (1983) Proc. international congress and exposition 28/02/83-04/03/83, Michigan, USA: SAE 830491.

87. A.R. Marder: *Progress in materials science*, v.45 (2000) 191-271.

88. M. Maeda, T. Ito, T. Aiko, K. Hashimoto, H. Furukawa, K. Yanagi: *Installation of a continuous zinc vapour deposition line*, (1986) Proc. international congress and exposition 24/02/86-28/02/86, Michigan, USA: SAE 860272.

89. A.R. Marder: *Materials selection and design*, v.20 (1997) ASM handbook, p.470.

90. C. Belleau, D.K. Kelley: *Galvanized coating effects in outer body panels*, (1983) Proc. international congress and exposition 28/02/83-04/03/83, Michigan, USA: SAE 830516.

91. J.M. Mataigne: *Hot dip pure zinc galvanized and iron-zinc galvannealed coated steel sheets for external car body panels*, (2001) Proc. SAE world congress 05/03/01-08/03/01, Michigan, USA: SAE 2001-01-0077.

92. M. Maeda, S. Umeda, N. Tsukiji, K. Narikawa: The product made by a zinc vapour deposition line, (1986) Proc. international congress and exposition 24/02/86-28/02/86, Michigan, USA: SAE 860273.

93. B. Schuhmacher, C. Schwerdt, U. Seyfert, O. Zimmer: *Surface and coatings technology*, v.163-164 (2003) 703-709.

94. C. Metzner, B. Scheffel, F.H. Roegner: *New developments of PVD-layers onto metallic sheets and* strips, (2000) Proc. 43rd annual technical conference, 15/04/00-20/04/00, Denver,USA: Society of vacuum coaters.

95. B. Schuhmacher, W. Müschenborn, M. Stratmann, B. Schultrich, C.P. Klages, M. Kretscmer, U. Seyfert, F. Förster, H.J. Tiller: *Advanced engineering materials*, v.3 n.9 (2001) 681-689.

96. T.E. Graedel: *Journal of the electrochemical society*, v.136 n.4 (1989) 193C-203C.

97. I. Odnevall, C. Leygraf: Reaction sequences in atmospheric corrosion of zinc. In: W.W. Kirk, H.H. Lawson, (Eds.): *Atmospheric corrosion*, (1994) ASTM STP 1239 Philadelphia USA, pp.VI.1-VI.15.

98. T. Falk, J.E. Svensson, L.G. Johansson: *Journal of the electrochemical society*, v.145 n.1 (1998) 39-44.

99. R. Lindström, J.E. Svensson, L.G. Johansson: *Journal of the electrochemical society*, v.147 n.5 (2000) 1751-1757.

100. Y.Y. Chen, S.C. Chung, H.C. Shih: *Corrosion science*, v.48 n.11 (2006) 3547-3564.

101. R.S. Jayasree, V.P. Mahadevan Pillai, V.U. Nayar, I. Odnevall, G. Keresztury: *Materials chemistry and physics*, v.99 (2006) 474-478.

102. G.A. El-Mahdy, K.B. Kim: *Corrosion*, v.61 n.5 (2005) 420-427.

103. J. Morales, F. Díaz, J, Hernández-Borges, S. González: *Corrosion science*, v.48 (2006) 361-371.

104. J. Morales, F. Díaz, J, Hernández-Borges, S. González: *Corrosion science*, v.49 (2007) 526-541.

105. M. Natesan, G. Venkatachari, N. Palaniswamy: *Corrosion science*, v.48 n.11 (2006) 3584-3608.

106. R. Ramanauskas, P. Quintana, P. Bartolo-Pérez, L. Díaz-Ballote: *Corrosion*, v.56 n.6 (2000) 588-597.

107. E. Almeida, M. Morcillo, B. Rosales: *British corrosion journal*, v.35 n.4 (2000) 284-288.

108. E. Almeida, M. Morcillo, B. Rosales: *British corrosion journal*, v.35 n.4 (2000) 289-296.

109. I. Odnevall, M. Westdahl: *Corrosion science*, v.34 n.8 (1993) 1231-1242.

110. I. Odnevall, C. Leygraf: *Corrosion science*, v.36 n.6 (1994) 1077-1087.

111. W. He, I. Odnevall Wallinder, C. Leygraf: *Corrosion science*, v.43 (2001) 127-146.

112. R. Lindström, L.G. Johansson, J.E. Svensson: *Journal of the electrochemical society*, v.150 n.12 (2003) B583-B588.

113. R. Ramanauskas: *Applied surface science*, v.153 (1999) 53-64.

114. Q. Qu, C. Yan, Y. Wan, C. Cao: *Corrosion science*, v.44 (2002) 2789-2803.

115. J.E. Svensson, L.G. Johansson: *Corrosion science*, v.34 n.5 (1993) 721-740.

116. W. Feitknecht: *Chemistry and industry*, v.5 (1959) 1102-1109.

117. R. Lindström, J.E. Svensson, L.G. Johansson: *Journal of the electrochemical society*, v.149 n.4 (2002) B103-B107.

118. D.C.W. Kannangara, B.E. Conway: *Journal of the electrochemical society*, v.134 n.4 (1987) 894-906.

119. B.E. Conway, D.C.W. Kannangara: *Journal of the electrochemical society*, v.134 n.4 (1987) 906-918.

120. T. Falk, J.E. Svensson, L.G. Johansson: *Journal of the electrochemical society*, v.145 n.9 (1998) 2993-2999.

121. M.C. Bernard, A. Hugot-Le Goff, D. Massinon, N. Phillips: *Corrosion science*, v.35 n.5-8 (1993) 1339-1349.

122. E. Tada, K. Sugawara, H. Kaneko: *Electrochimica acta*, v.49 (2004) 1019-1026.

123. R. Lindström, J.E. Svensson, L.G. Johansson: *Journal of the electrochemical society*, v.149 n.2 (2002) B57-B64.

124. J.E. Svensson, L.G. Johansson: *Corrosion science*, v.38 n.12 (1996) 2225-2233.

125. S. Magaino, M. Soga, K. Sobue, A, Kawaguchi, N. Ishida, H. Imai: *Electrochimica acta*, v.44 (1999) 4307-4312.

126. T. Prosek, D. Thierry, C. Taxén, J. Maixner: *Corrosion science*, v.49 (2007) 2676-2693.

127. G. Grundmeier, W. Schmidt, M. Stratmann: *Electrochimica acta*, v.45 (2000) 2515-2533.

128. M. Stratmann: *Corrosion*, v.61 n.12 (2005) 1115-1126.

129. R.L. Howard, S.B. Lyon, J.D. Scantlebury: *Progress in organic coatings*, v.37 (1999) 91-98.

130. R.L. Howard, S.B. Lyon, J.D. Scantlebury: *Progress in organic coatings*, v.37 (1999) 99-105.

131. G.W. Walter: *Corrosion science*, *v.35 n.5-8 (1993) 1391-1404.*

132. I. Dehri, R.L. Howard, S.B. Lyon: *Corrosion science*, v.41 (1999) 141-154.

133. S. Böhm, H.N. McMurray, S.M. Powell, D.A. Worsley: *Electrochimica acta*, v.45 (2000) 2165-2174.

134. M. Challis, D.A. Worsley: *British corrosion journal*, v.36 n.4 (2001) 297-303.

135. Anon.: *ZAM catalogue* [on-line]. Available at: http://www.nisshin-steel.co.jp/nisshin-steel/english/product/ecatalog/htm/R-15/index.htm [Accessed 30th July 2007].

136. F. Zhu, D. Persson, D. Thierry: *Corrosion*, v.57 n.7 (2001) 582-590.

137. BS EN 10130:1999+A1: *Cold-rolled low-carbon steel flat products for cold forming – technical delivery conditions*, (1999) British Standards Institution.

138. ASM Int.: *Metals handbook*, 9th ed. v.14 ASM International: Ohio, USA (1988), pp.459-471.

139. VCS 1027,149: *Accelerated corrosion test*, (2002) Volvo car corporation, internal company document.

140. FLTM BI-123: *Painted sheet metal corrosion test (laboratory-simulated Arizona proving ground test*, (2001) Ford global technologies Inc., internal company document.

141. R.L. Howard, I.M. Zin, J.D. Scantlebury, S.B. Lyon: *Progress in organic coatings*, v. 37 (1999) 83-90.

142. E. Weidmann: *Metallographic preparation of zinc coatings*, [on-line] available at: http://www.struers.com/resources/elements/12/64526/AppZincEnglish.pdf [Accessed 11th July 2007]

143. Anon.: *Periodic table of the elements*, [on-line] available at: http://www.edax.com/service/periodic.cfm [Accessed 18th July 2007].

144. D. Briggs, M.P. Seah: *Practical surface analysis, Auger and X-ray photoelectron spectroscopy*, (1990) v.1 2nd ed., Wiley & Sons, Chichester, UK pp.599-609.

145. C.D Wagner, A.V. Naumkin, A. Kraut-Vass, J.W. Allison, C.J. Powell, J.R. Rumble Jr. : *NIST X-ray photoelectron spectroscopy database*, [on-line] available at: http://srdata.nist.gov/xps/ [Accessed 18th July 2007].

146. Anon.: *Utilizing glow discharge in optical emission spectroscopy*, [on-line] available at: http://www.leco.com/products/inorganic/gds/pdf/203-989.pdf [Accessed 18th July 2007].

147. L.S. Dake, D.R. Baer, J.M. Zachara, 1989: *Surface and interface analysis*, v. 14 (1989) 71-75.

148. V.I. Nefedov, M.N. Firsov, I.S. Shaplygin, 1982: *Journal of electron spectroscopy related phenomena*, v.26, n.1 (1982) 65-78.

149. G. Moretti, G. Fierro, M. Lo Jacono, P. Porta, 1989: *Surface and interface analysis*, v.14 (1989) 325-336.

150. U.R. Evans: *The corrosion and oxidation of metals*, London: Edward Arnold Ltd. (1960) p.165.

151. V. Fournier, P. Marcus, I. Olefjord: *Surface and interface analysis*, v.34 (2002) 494-497.

152. R. Lindström, L.G. Johansson, J.E. Svensson: *Materials and corrosion*, v.54 (2003) 587-594.

153. M. Jönsson, D. Persson, D. Thierry: *Corrosion science*, v.49 (2007) 1540-1558.

154. W.B. White: *Environmental geology*, v.30 (1997) 46-58.

155. R. Lindström, L.G. Johansson, G.E. Thompson, P. Skeldon, J.E. Svensson: *Corrosion science*, v.46 (2004) 1141-1158.

156. N. Boshkov, K. Petrov, S. Vitkova, S. Nemska, G. Raichevsky: *Surface and coatings technology*, v.157 (2002) 171-178.

157. Z. Weiss: *Journal of analytical atomic spectroscopy*, v.16 (2001) 1275-1282.

158. M.V. Peláez, J.M. Costa-Fernández, R. Pereiro, N. Bordel, A.Sanz-Medel: *Journal of analytical atomic spectroscopy*, v.18 (2003) 864-871.

159. H.E. Townsend, D.C. McCune, R.J. Neville, R.D. Granata, W.A. Schumacher: *Progress by the automotive and steel industries toward an improved laboratory cosmetic corrosion test*, (1991) Proc. of the 5th automotive corrosion & prevention conference 21/10/91-23/10/91, Michigan,USA: SAE 912275.

160. A. Amirudin, D. Thierry: *Progress in organic coatings*, v.28 (1996) 59-76.

Appendix 1

XRD DATA ANALYSIS

This appendix describes the steps taken to analyse the X-ray diffractograms obtained for each sample. Diffractograms were collected for each material in the uncorroded condition and following different corrosion treatments, as described in Chapters 6 – 8. The JCPDS database identification number for each of the reference diffractograms used is given in Table A1.1. The diffractograms for electrogalvanized steel (EG), hot-dip galvanized steel (HDG) and zinc-magnesium coated steel (ZMG) before corrosion treatment and following 4 weeks of exposure to the Volvo cabinet test method (treatment V4) are shown in Fig. A1.1-A1.3. Fig. A1.4 shows the diffractograms collected for EG and ZMG after 21 and 27 weeks of acid rain treatment respectively. Reference diffractograms are indicated by the coloured vertical lines and show a mixture of corrosion products and metallic species for each corroded sample.

Table A1.1: JCPDS database identification numbers for reference diffractograms used in this work.

Name	Formula	Database ID Number
Zinc	Zn	01-087-0713
Iron	Fe	00-006-0696 or 01-087-0721
Zinc-Magnesium	Zn_2Mg	01-077-1177
Zinc oxide	ZnO	00-036-1451 or 01-079-2205
Zinc hydroxycarbonate	$Zn_4(OH)_6CO_3.H_2O$	00-011-0287
Hydrozincite	$Zn_5(OH)_6(CO_3)_2$	01-072-1100
Simonkolleite	$Zn_5Cl_2(OH)_2.H_2O$	00-007-0155
Magnesium hydroxide	$Mg(OH)_2$	01-078-0316
Magnesium hydroxycarbonate	$Mg_5(OH)_2(CO_3)_4.4H_2O$ $Mg_5(OH)_2(CO_3)_4.5H_2O$	01-070-0361 00-029-0858

(a)

Intensity (a.u.)

2-Theta (Degrees)

◇ Zinc Zn 01-087-0713
▣ Iron Fe 00-006-0696

(b)

Intensity (a.u.)

2-Theta (Degrees)

◼ Simonkolleite Zn5(OH)8Cl2.H2O 00-007-0155
⊞ Zinc hydroxy carbonate hydrate Zn4(OH)6CO3.H2O 00-011-0287
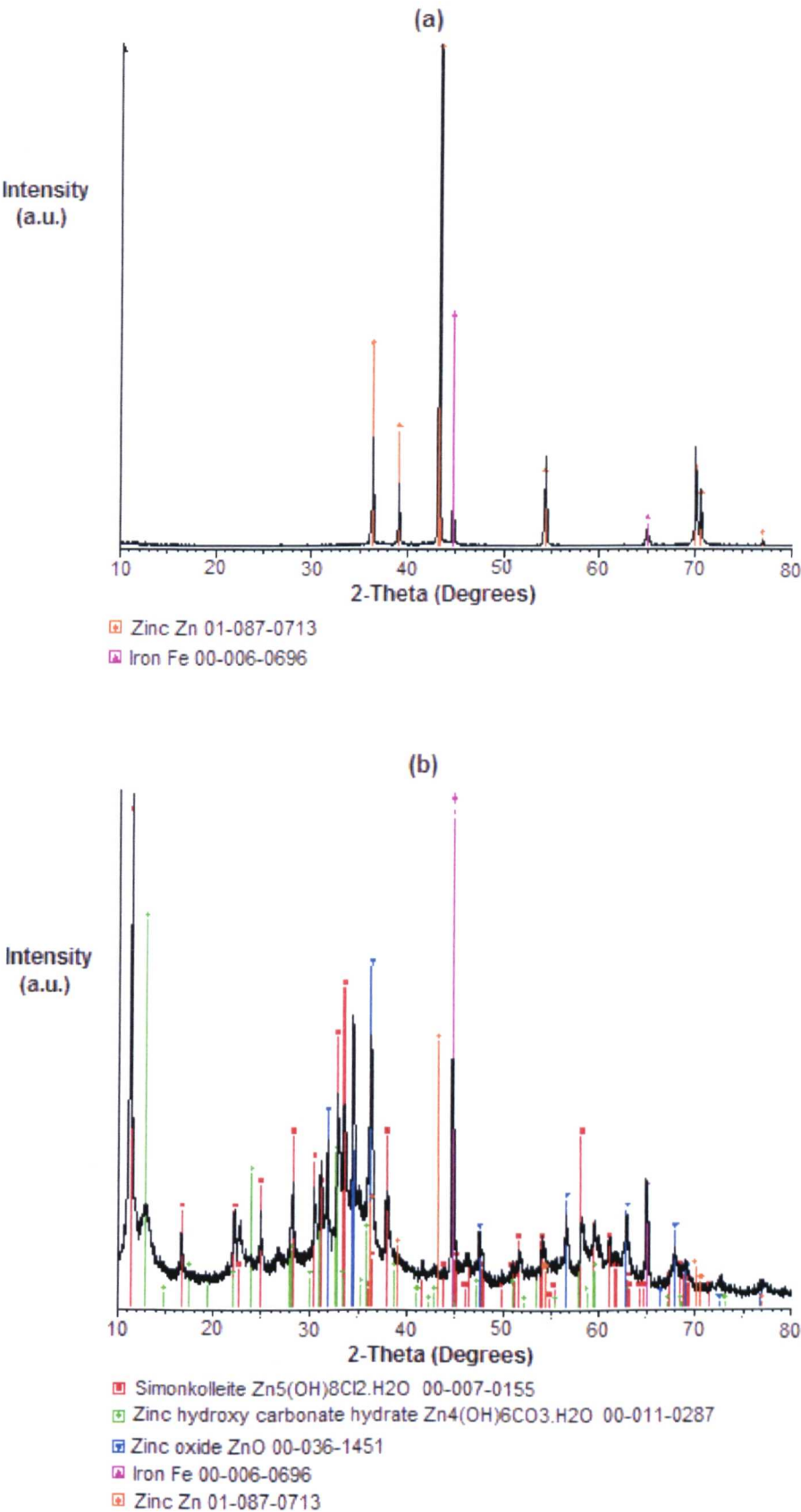⊞ Zinc oxide ZnO 00-036-1451
▣ Iron Fe 00-006-0696
◇ Zinc Zn 01-087-0713

Fig. A1.1: Alignment of reference data to the diffractogram collected for EG (a) before corrosion treatment and (b) following treatment V4.
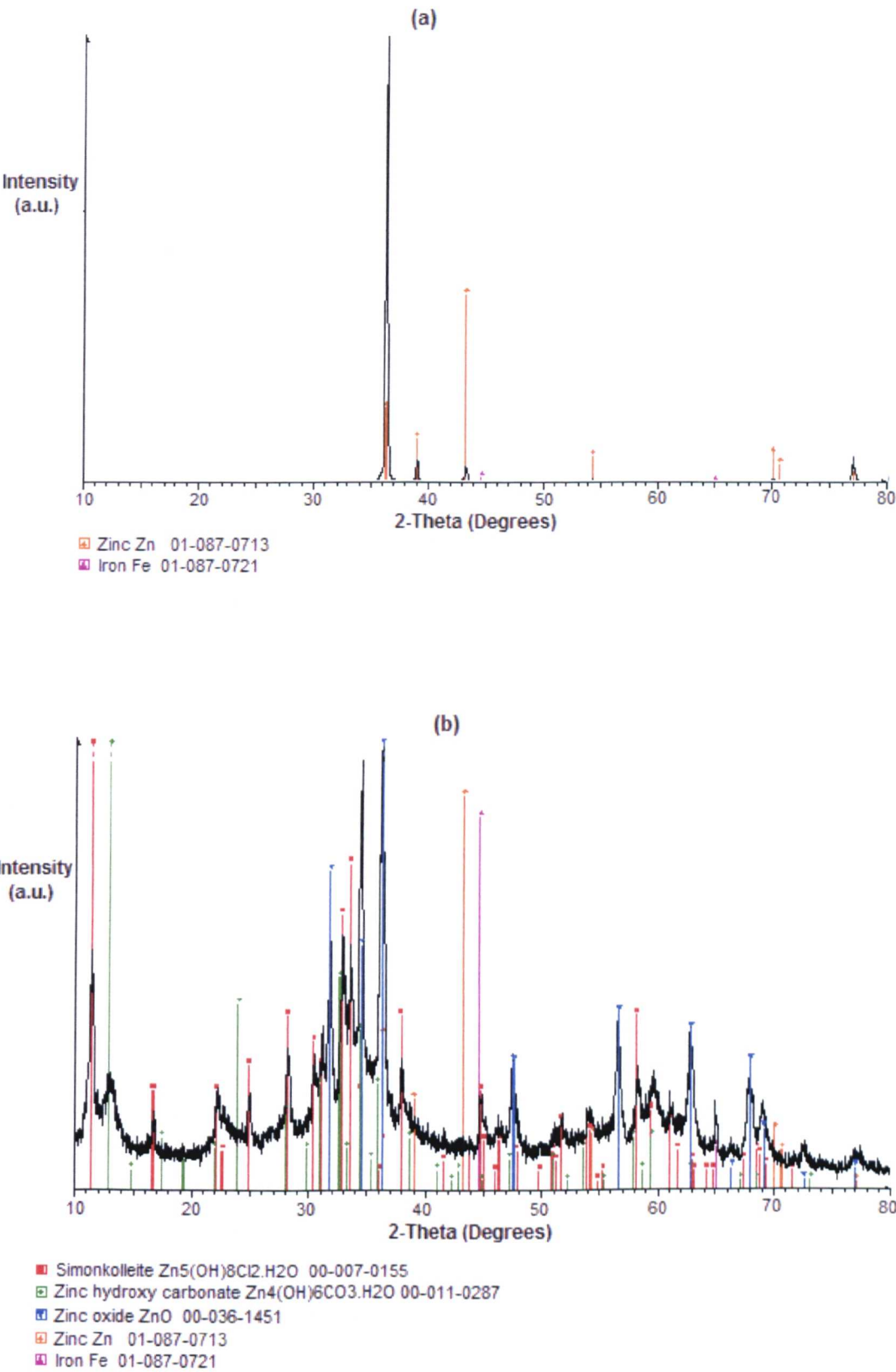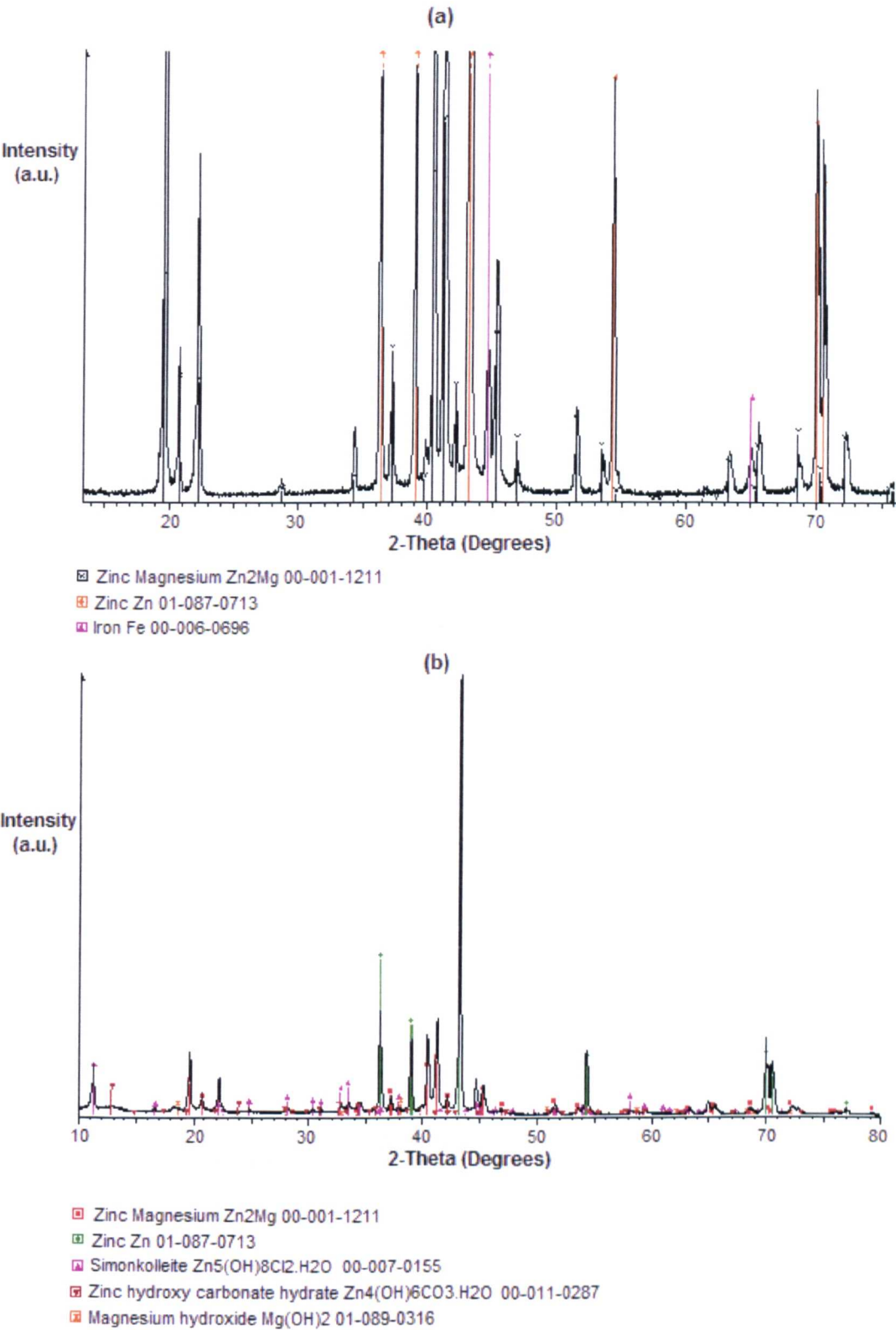
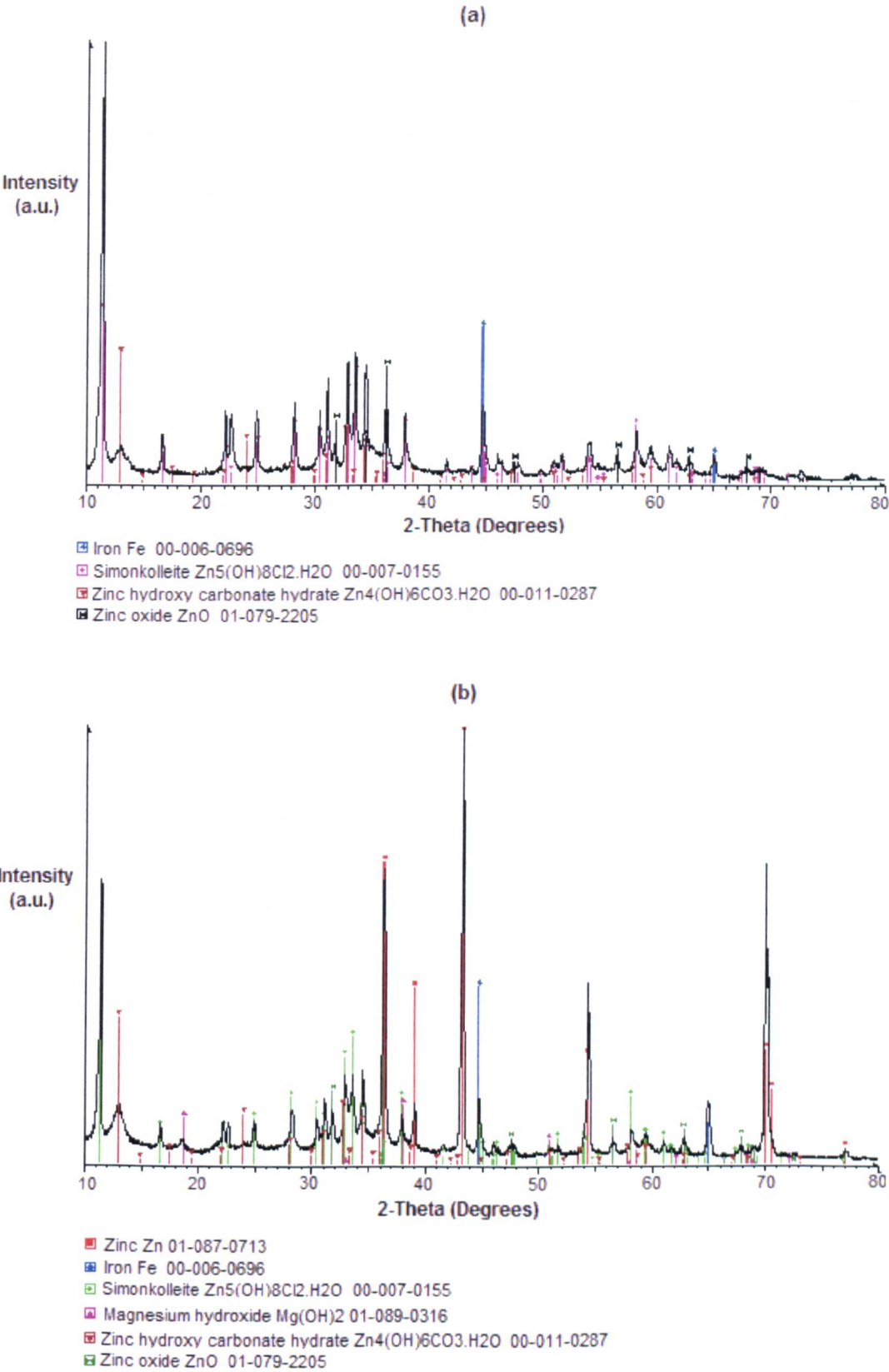Fig. A1.2: Alignment of reference data to the diffractogram collected for HDG (a) before corrosion treatment and (b) following treatment V4.

(a)

Intensity
(a.u.)

2-Theta (Degrees)

☒ Zinc Magnesium Zn2Mg 00-001-1211
⊞ Zinc Zn 01-087-0713
⊡ Iron Fe 00-006-0696

(b)

Intensity
(a.u.)

2-Theta (Degrees)

☐ Zinc Magnesium Zn2Mg 00-001-1211
⊞ Zinc Zn 01-087-0713
⊡ Simonkolleite Zn5(OH)8Cl2.H2O 00-007-0155
⊡ Zinc hydroxy carbonate hydrate Zn4(OH)6CO3.H2O 00-011-0287
⊡ Magnesium hydroxide Mg(OH)2 01-089-0316

Fig. A1.3: Alignment of reference data to the to the diffractogram collected for ZMG (a) before corrosion treatment and (b) following treatment V4.

(a)

Intensity (a.u.)

2-Theta (Degrees)

☒ Iron Fe 00-006-0696
⊡ Simonkolleite Zn5(OH)8Cl2.H2O 00-007-0155
☒ Zinc hydroxy carbonate hydrate Zn4(OH)6CO3.H2O 00-011-0287
☒ Zinc oxide ZnO 01-079-2205

(b)

Intensity (a.u.)

2-Theta (Degrees)

▪ Zinc Zn 01-087-0713
▦ Iron Fe 00-006-0696
⊞ Simonkolleite Zn5(OH)8Cl2.H2O 00-007-0155
▨ Magnesium hydroxide Mg(OH)2 01-089-0316
▣ Zinc hydroxy carbonate hydrate Zn4(OH)6CO3.H2O 00-011-0287
▤ Zinc oxide ZnO 01-079-2205

Fig. A1.4: Alignment of reference data to diffractrogram for (a) EG after 21 weeks of acid rain testing and (b) ZMG after 27 weeks of acid rain testing.

Appendix 2

XPS DATA ANALYSIS

This appendix describes the X-ray photoelectron spectroscopy (XPS) analysis steps. Survey scans indicated the species present on the test sample surface and these are described in Section A2.1. High resolution or narrow scans were conducted for specific elements of interest, e.g. carbon 1s, oxygen 1s and zinc 2p, and these narrow scans are described in Section A2.2. Reference data were also generated from analysis grade samples of various zinc and magnesium compounds and these are presented in Section A2.3 – A2.4.

A2.1. Wide Scans

Wide scans were collected from electrogalvanized steel (EG), hot-dip galvanized steel (HDG) and zinc-magnesium coated steel (ZMG) before and after corrosion treatments, as described in Chapters 6 and 7. Fig. A2.1 shows wide scans for ZMG without any corrosion treatment (ZMG none) and for ZMG following 4 weeks of testing according to the Volvo cabinet test (ZMG V4). Peak identification was achieved by reference to the Kratos library within the CASA XPS software.

Regions of interest were defined for each element as shown in Fig. A2.2, and a suitable background spectrum was defined (e.g. linear background spectrum in Fig. A2.2). The atomic percentage (at.%) of each element was calculated from the peak areas using Kratos sensitivity factors. The at.% calculated from the wide scans was not separated into different chemical species; for example, the carbon at.% reported was the total carbon present on the surface including adventitious carbon (i.e. contamination) and carbonates. Deconvolution of the different chemical species is possible via high resolution narrow scans, as described in Section A2.2.
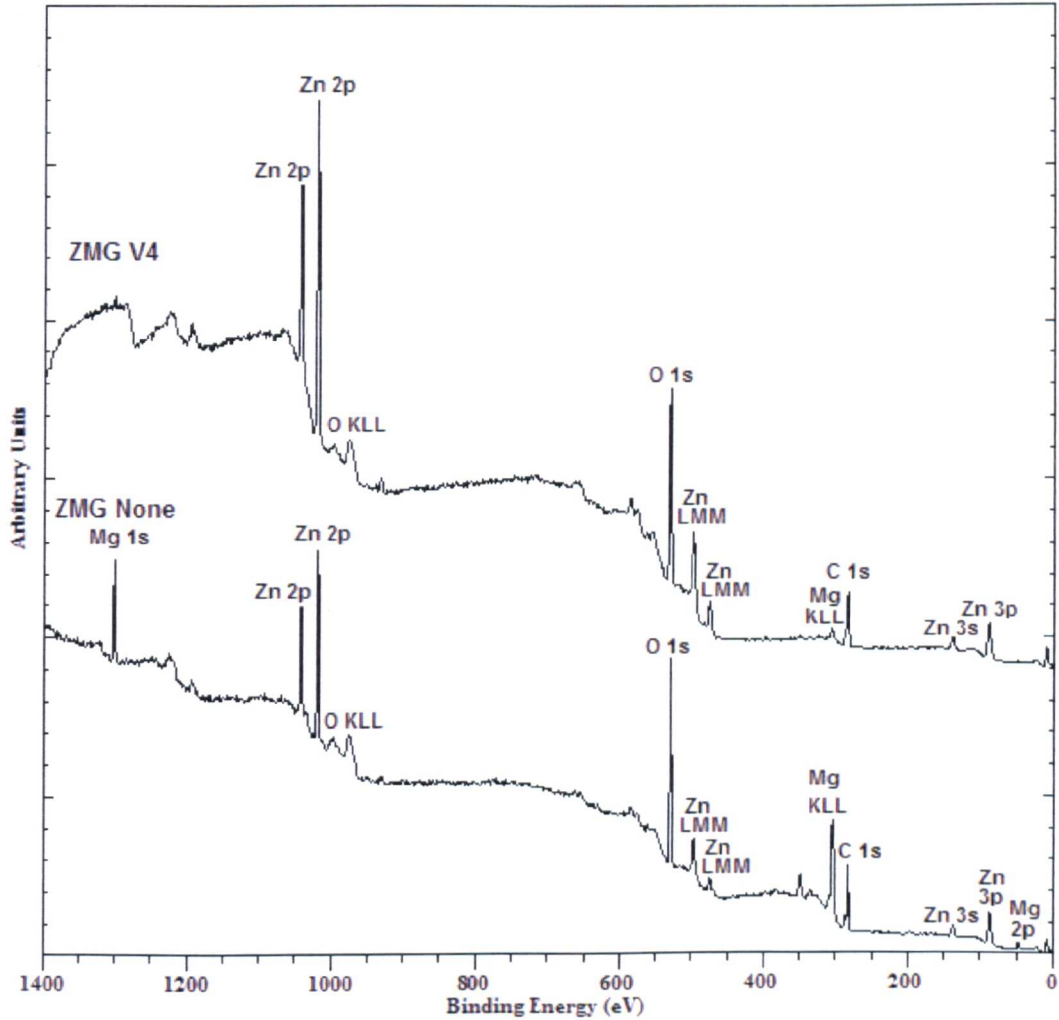
Fig. A2.1: XPS wide scan for ZMG *upper* following 4 weeks of Volvo cabinet test (V4) and *lower* before corrosion testing (none).
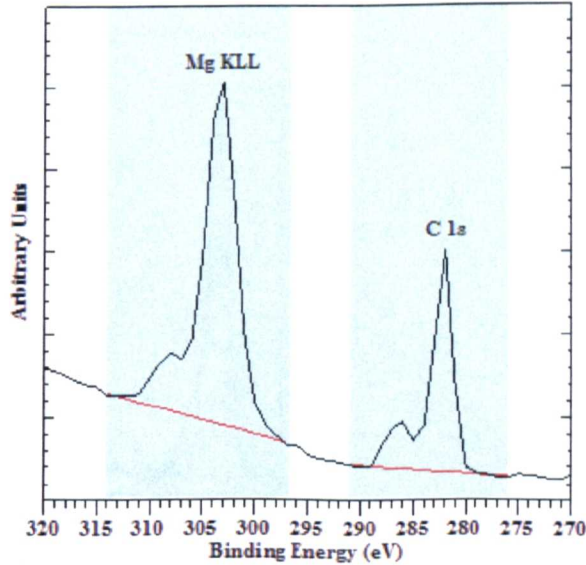

Fig. A2.2: Quantification regions (shaded) for Mg KLL and C 1s collected for ZMG V4. Linear type background spectra (shown in red) were selected for both elements.

A2.2. Narrow Scans

Narrow scans within specific binding energy levels were conducted at 20 eV pass energy to generate high resolution scans for the elements of interest on the test samples. Charge correction to the main carbon 1s peak at 285 eV on the energy scale enabled measurement of the peak positions. Components were fitted to the high resolution scans to estimate the different chemical species present. Fig. A2.3 shows high resolution scans obtained for C 1s, O 1s and Zn 2p on ZMG following 4 weeks of the Volvo cabinet corrosion test (ZMG V4).
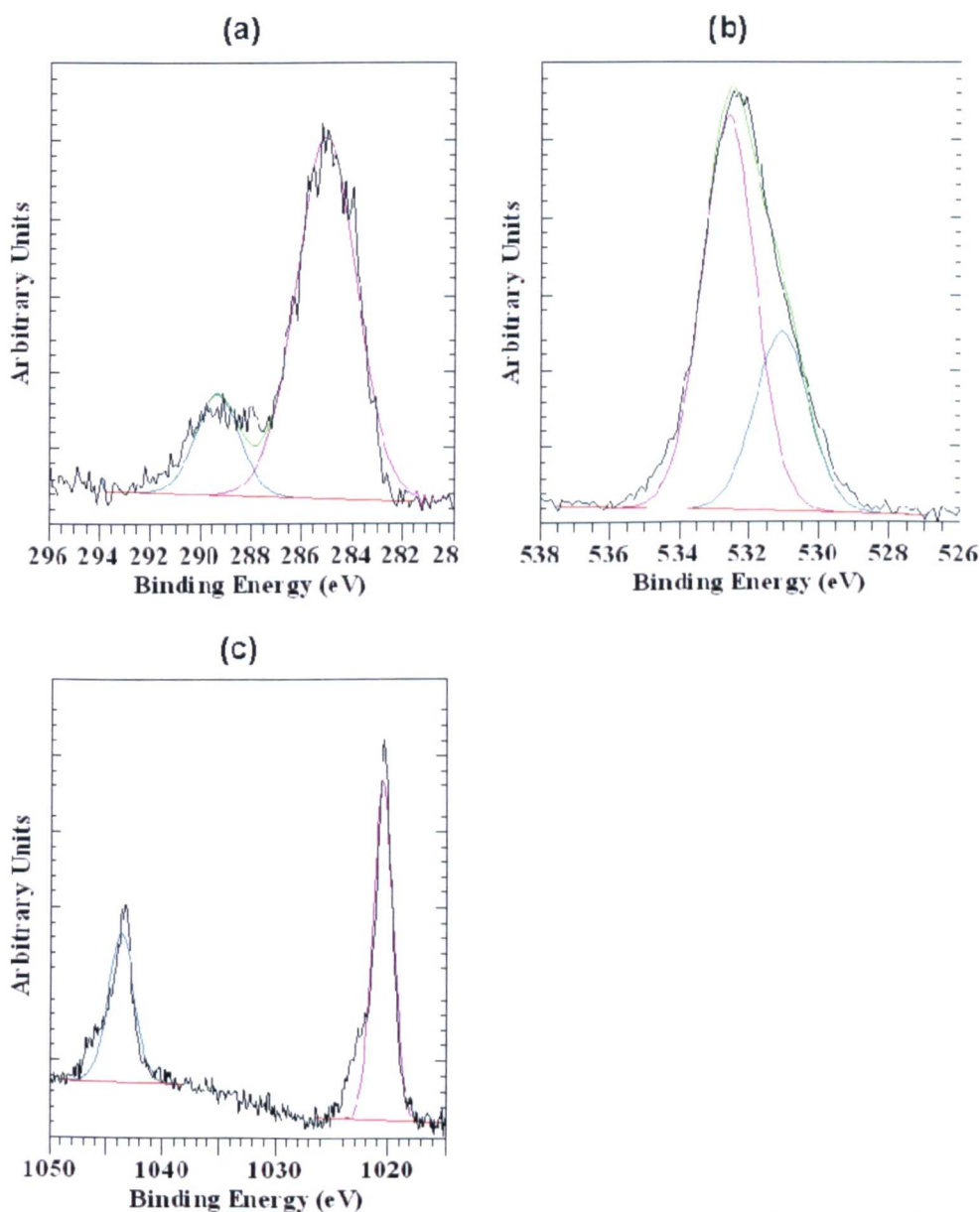
Fig. A2.3: Component fitting (purple and blue lines) to high resolution scans for (a) C 1s (b) O 1s and (c) Zn 2p for ZMG following 4 weeks of Volvo corrosion test (ZMG V4).

A2.3. Reference Data Generated: Wide Scans

Reference data were generated for zinc and magnesium oxides, hydroxides and carbonates. Fig. A2.4 shows the wide scans collected for zinc compounds and Fig. A2.5 shows the wide scans collected for the magnesium compounds.
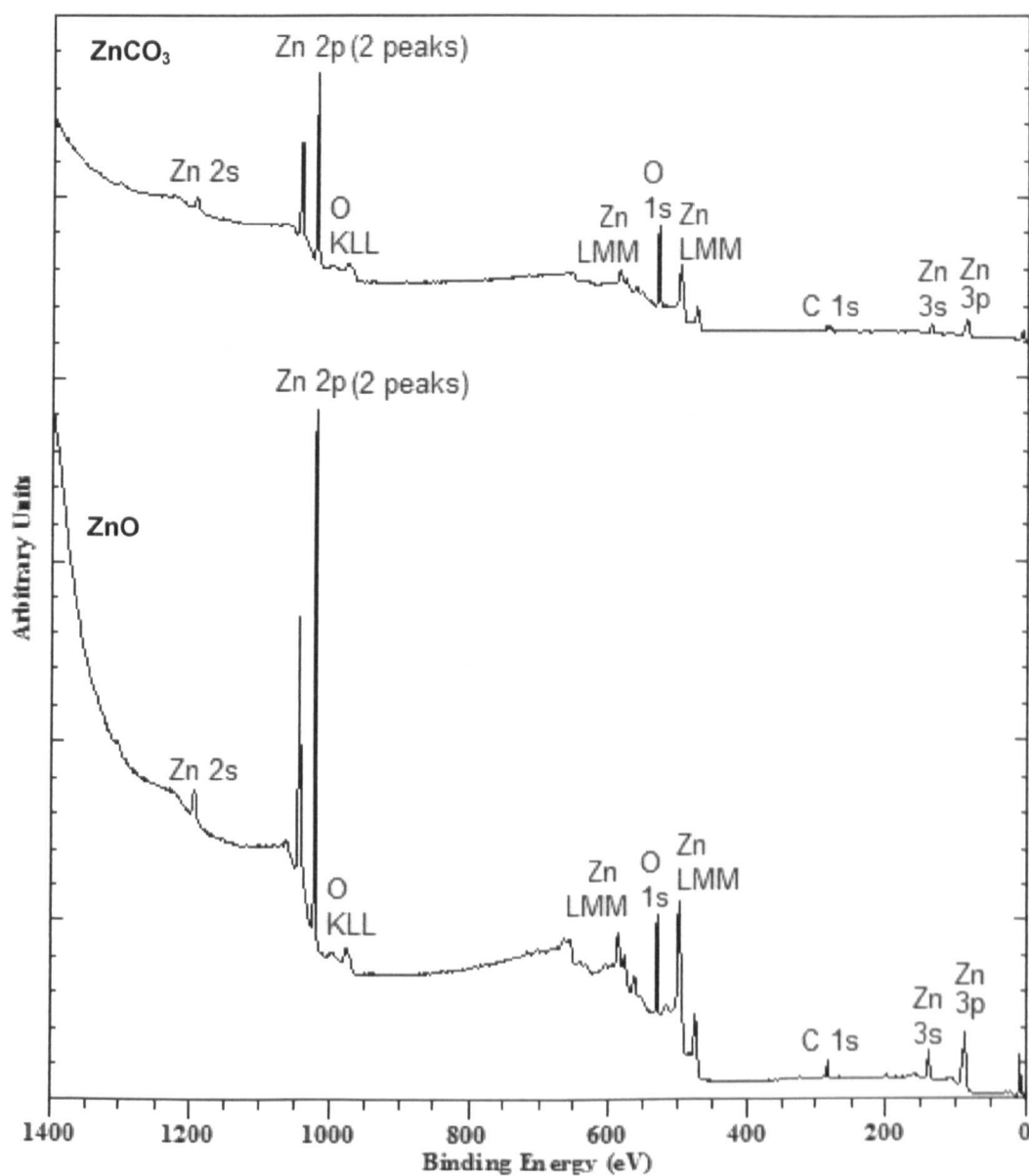

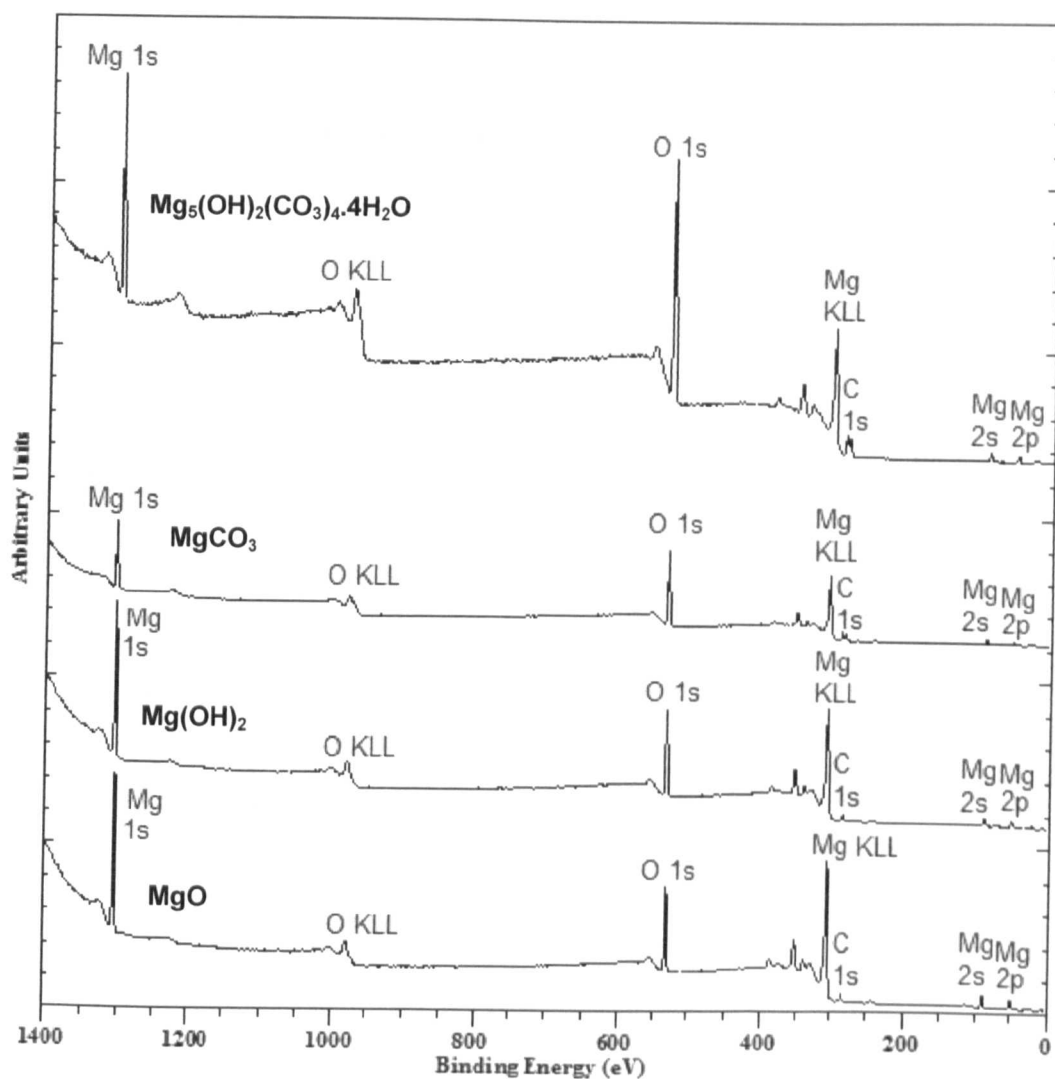Fig. A2.4: Wide scans generated for analysis grade samples of *from top* ZnCO₃ and ZnO.

Fig. A2.5: Wide scans generated for analysis grade samples of *from top* $Mg_5(OH)_2(CO_3)_4.4H_2O$, $MgCO_3$, $Mg(OH)_2$ and MgO.

A2.4. Reference Data Generated: Narrow Scans for Zinc Compounds

Fig. A2.6 – A2.7 show the high resolution (narrow) scans collected for zinc oxide and zinc carbonate respectively.
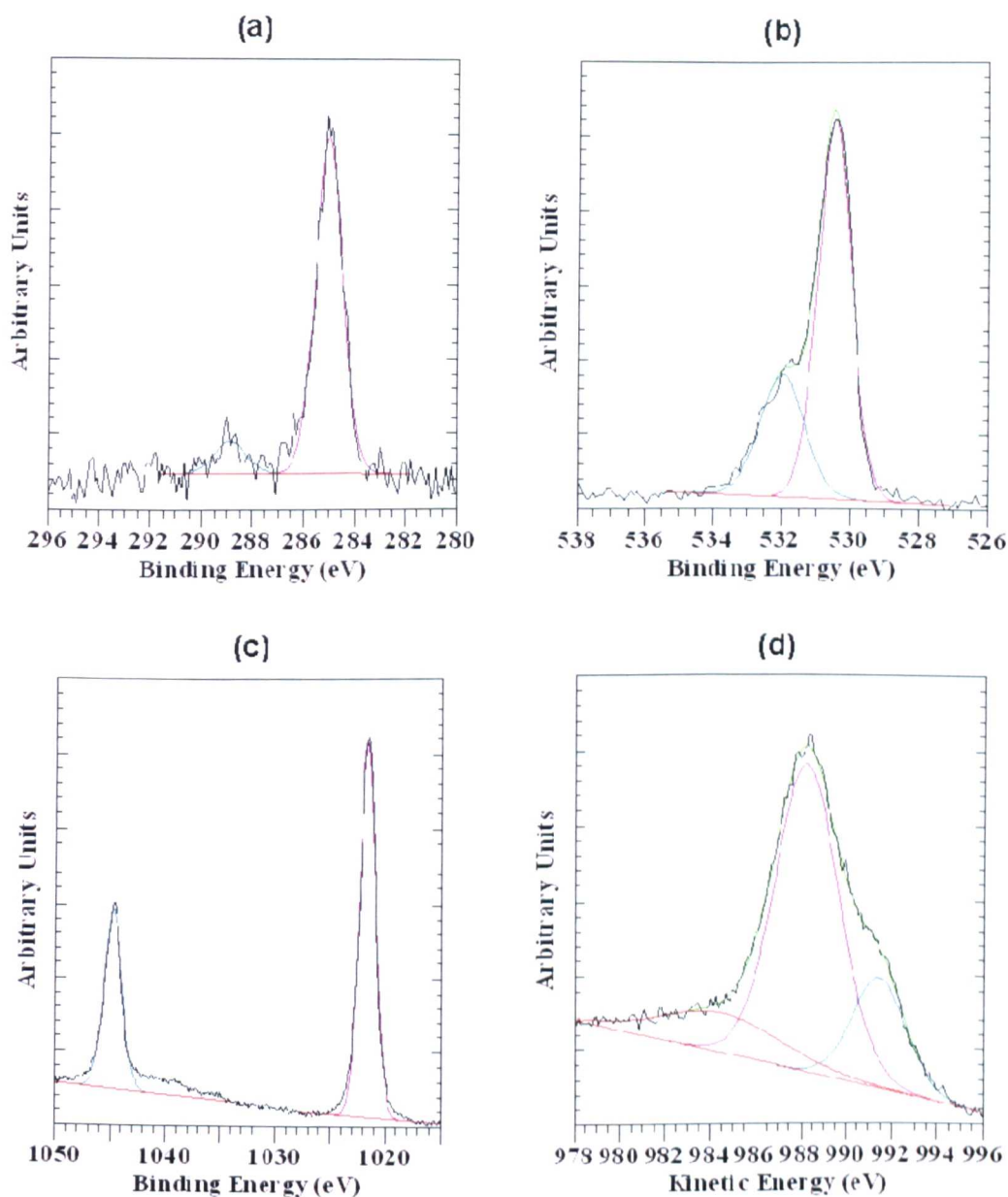

Fig.A2.6: High resolution scans for ZnO (a) C 1s (b) O1s (c) Zn 2p and (d) Zn KLL. Component fitting and linear background spectra shown.
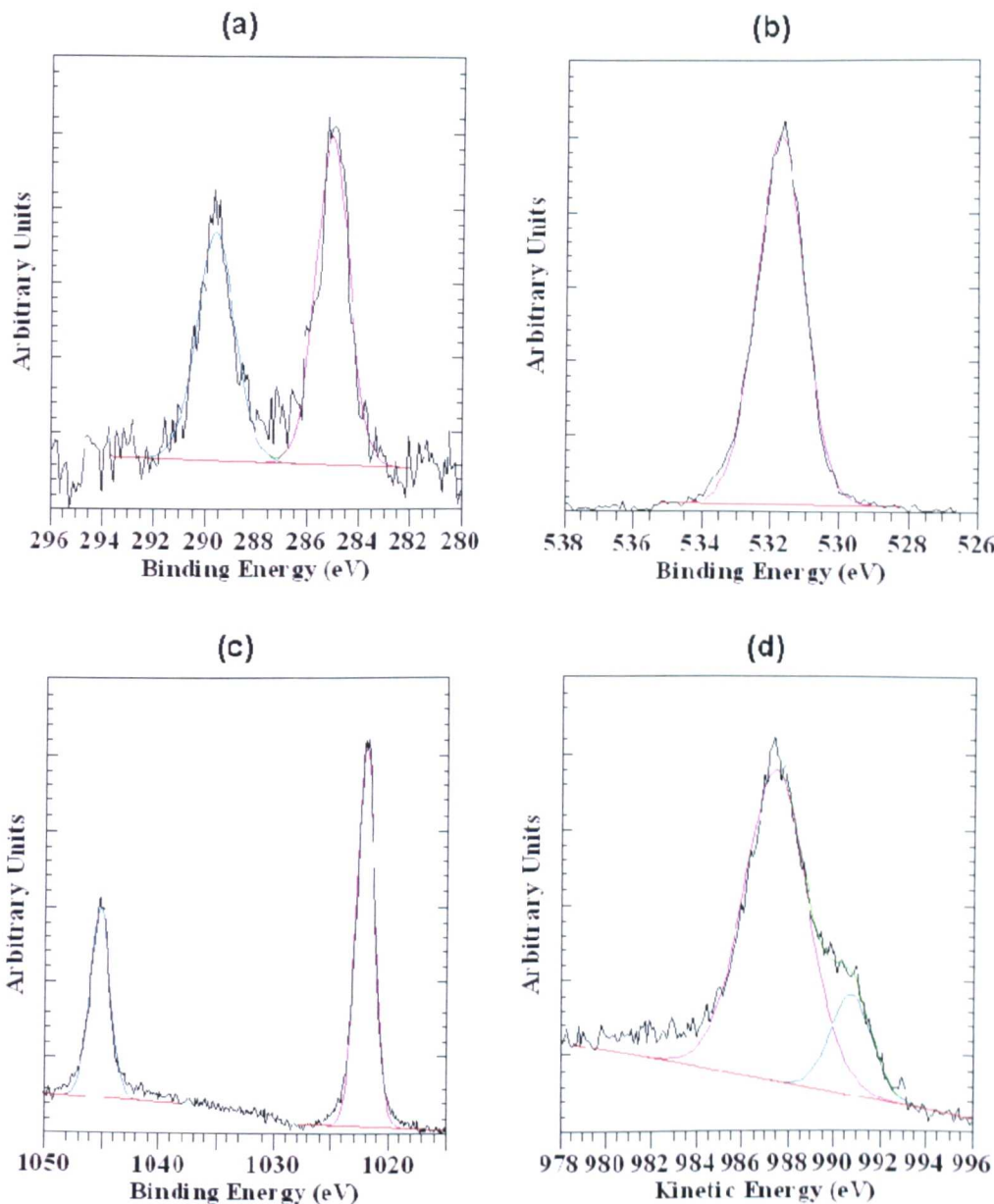
Fig.A2.7: High resolution scans for ZnCO$_3$ (a) C 1s (b) O1s (c) Zn 2p and (d) Zn KLL. Component fitting and linear background spectra shown.

A2.4. Reference Data Generated: Narrow Scans for Magnesium Compounds

Carbon (C 1s) and oxygen (O 1s) spectra for magnesium oxide, magnesium hydroxide, magnesium carbonate and magnesium hydroxy carbonate are given in Fig. A2.8 – A2.9 respectively.
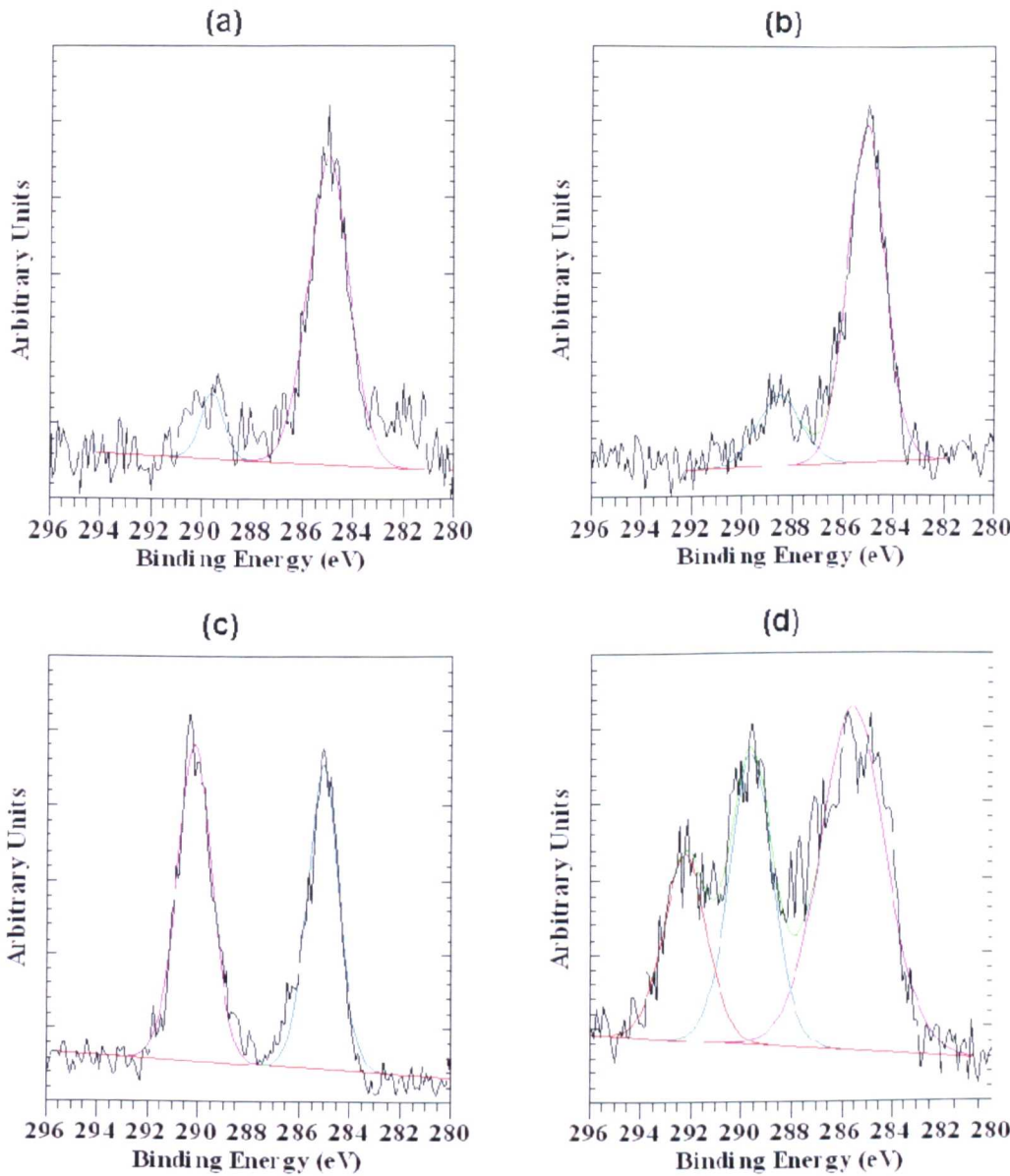

Fig. A2.8: Component fitting to high resolution scans of C 1s for (a) MgO (b) Mg(OH)$_2$ (c) MgCO$_3$ and (d) Mg$_5$(OH)$_2$(CO$_3$)$_2$.H$_2$O. (Linear background spectra shown in red).
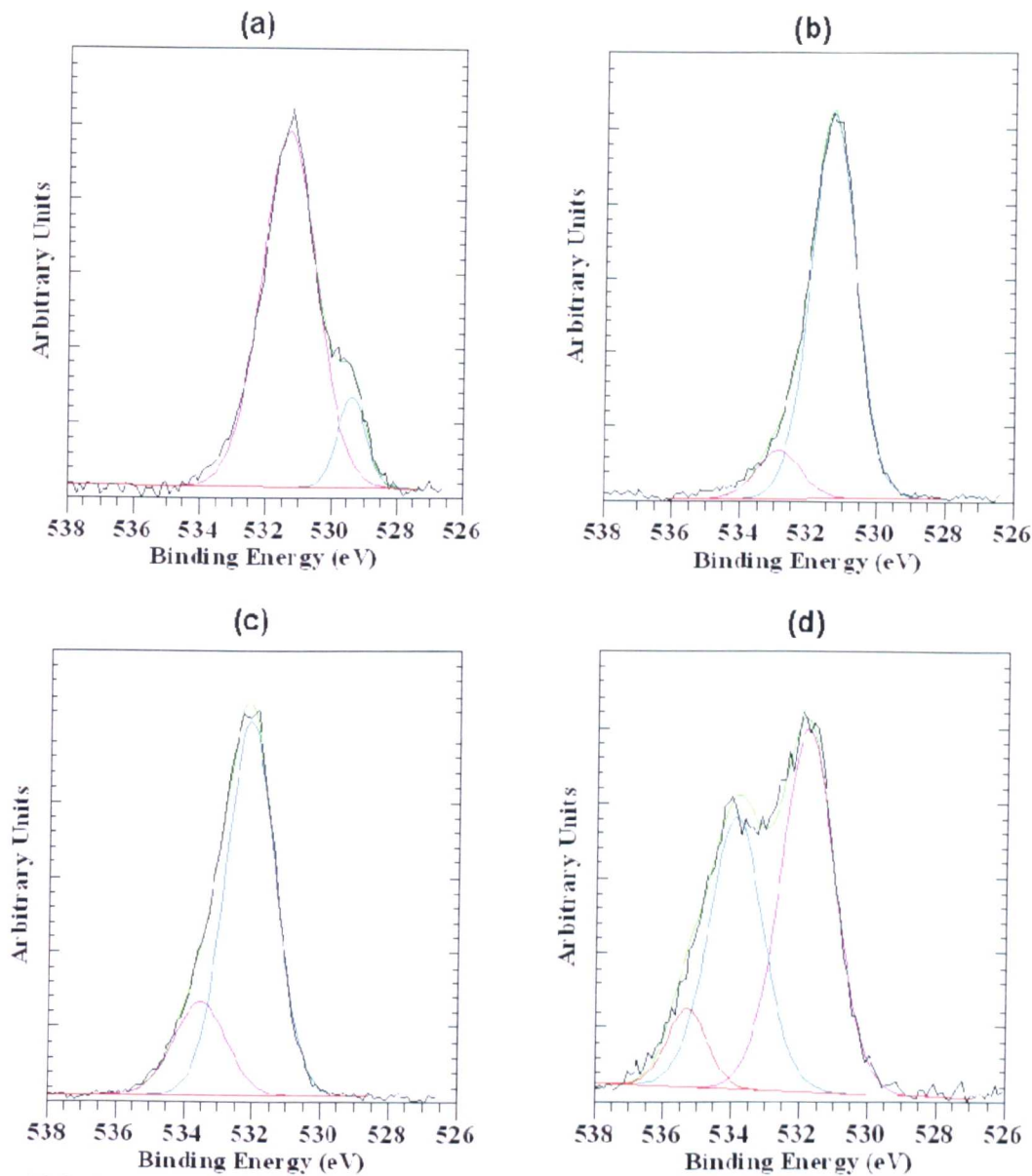
Fig. A2.9: Component fitting to high resolution scans of O 1s for (a) MgO (b) $Mg(OH)_2$ (c) $MgCO_3$ and (d) $Mg_5(OH)_2(CO_3)_2.H_2O$. (Linear background spectra shown in red).